Operating Assistance System for Transitioning between Operating Modes of Molten Salt Receivers

Christian Schwager

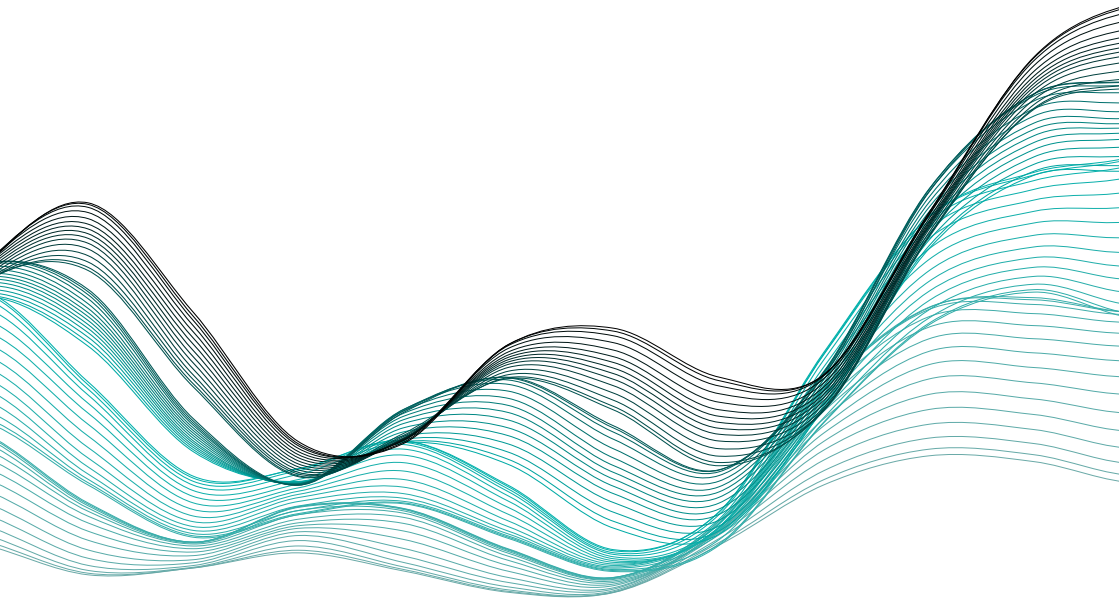

Operating Assistance System for Transitioning between Operating Modes of Molten Salt Receivers

Betriebsassistenzsystem für den Wechsel zwischen Betriebsmodi von Salzschmelze-Receivern

Von der Fakultät für Maschinenwesen der Rheinisch-Westfälischen Technischen Hochschule Aachen zur Erlangung des akademischen Grades eines Doktors der Ingenieurwissenschaften genehmigte Dissertation

vorgelegt von

Christian Schwager

Berichter/in: Univ.-Prof. Dr.-Ing. Bernhard Hoffschmidt
Univ.-Prof. Alexander Mitsos, Ph.D.

Tag der mündlichen Prüfung: 5. Juli 2024

Diese Dissertation ist auf den Internetseiten der Universitätsbibliothek online verfügbar.

Preface

First and foremost, I would like to express my gratitude to my supervisor Univ. Prof. Dr.-Ing. Bernhard Hoffschmidt for giving me the possibility and freedom to work on this thesis, supported by his excellent guidance. I would also like to thank Univ. Prof. Alexander Mitsos Ph.D. for reviewing this thesis and agreeing to co-examining my doctoral examination. Since significant developments supporting this thesis were conducted in the research project DynaSalt-2, I acknowledge the Federal Ministry for Economic Affairs and Climate Action (BMWK) for public funding. Some results of this work were already published in the corresponding project report (Hering et al. 2021b) as well as in research papers (Schwager et al. 2022; Schwager et al.; Schwager et al. 2023).

My special gratitude goes to Dipl.-Ing. Peter Schwarzbözl, Dr.-Ing. Robert Flesch, Prof. Dr.-Ing. Ulf Herrmann and Dipl.-Ing. Cristiano Teixeira Boura for their support, guidance and exceptional collaboration. In addition, I would like to thank my colleagues Florian Angele and Martin May as well as the students Konrad Beeser, Maria Hahn and Veera Varala, whom I had the chance to supervise, for their valuable contributions. Further, I thank my colleagues from DLR, Bijan Nouri, Laurin Oberkirch and Stefan Wilbert, for their support and pleasant collaboration regarding the input data acquisition.

Finally, I would like to express my deepest and sincerest gratitude to my family and friends for their support and guidance leading up to this achievement.

Abstract

Molten salt solar tower (MST) power plants represent a concentrating solar power (CSP) technology already in commercial use. Nevertheless, they still have great potential for efficiency improvements and cost reductions. In contrast to conventional power plants, CSP plants are subject to highly volatile boundary conditions facing components with a wide range of inertias. Hence, to realistically predict and increase the actual yields of an MST, complex simulation models and algorithms are required to pay particular attention to the operation of the receiver system.

Within the scope of this work, it was fundamentally investigated how an operating assistance system can support the receiver operation concerning availability and net yield. An assistance function, which provides model-prediction-based decision proposals for transitioning from normal receiver operation to drained standby, was developed and tested.

As a basis, a detailed dynamic process model of an MST receiver system, including a three-dimensionally discretized receiver, less detailed other components, a distributed control system for start-up and shutdown procedures as well as control loops, was developed and implemented in Modelica. For this purpose, a thermo-hydraulic two-phase model for molten salt and air as well as specific component models, were implemented, which enabled complying with local limits in the receiver during and after flood or drainage of the receiver.

To reduce the computing time of the yield prediction, simplified models and a heuristic decision algorithm were developed and implemented in Modelica and Python, respectively. In this context, a virtual net power approach for the receiver system was developed, which allows realistically predicting the net output while considering the complex dynamic behavior and quickly finding the optimal timing without iterations. This operating assistance function quantifies the yield gain/loss achieved by a temporary receiver standby and serves as the basis for the decision proposal.

The test results show that one single maneuver proposed by this operating assistance function can increase the net yield of a utility scale plant by several megawatt-hours, depending on the cloud situation. Uncertainty analyses show a particular sensitivity for forecasting errors, which is why better forecasting accuracy is needed, especially for larger prediction horizons, compared to the examined data. Furthermore, there is still a need for research on the accurate modeling of the local convective heat loss at such a receiver to predict the thermal losses during start-up and shutdown and thus its duration reliably.

Kurzfassung

Solarturm-Kraftwerke mit Salzschmelze (MST) stellen eine bereits kommerziell eingesetzte konzentrierende Solartechnologie (CSP) dar. Dennoch bergen sie ein großes Potenzial für Effizienzsteigerungen und Kostenreduktionen. Im Gegensatz zu konventionellen Kraftwerken sind CSP-Kraftwerke volatilen Randbedingungen ausgesetzt, welche auf Komponenten mit sehr unterschiedlichen Trägheiten einwirken. Um die Erträge eines MST realistisch vorhersagen und steigern zu können, sind komplexe Simulationsmodelle und Algorithmen erforderlich. Ein besonderes Augenmerk gilt der Betriebsführung des Receiversystems.

Im Rahmen dieser Arbeit wurde untersucht, wie ein Betriebsassistenzsystem den Receiver-Betrieb hinsichtlich Verfügbarkeit und Nettoertrag unterstützen kann. Eine Assistenzfunktion, welche modell-prädiktive Entscheidungsvorschläge für den Übergang vom normalen Receiver-Betrieb zu einem drainierten Standby, wurde entwickelt und getestet.

Als Grundlage wurde ein detailliertes dynamisches Prozessmodell eines MST-Receiversystems inklusive eines dreidimensional diskretisierten Receivers, weniger detaillierten anderen Komponenten und einer automatisierten Prozesssteuerung, welche die umfangreichen An- und Abfahrtprozeduren und Regelkreise beinhaltet, entwickelt und in Modelica implementiert. Dazu wurde ein thermo-hydraulisches Zweiphasen-Modell für Salzschmelze und Luft sowie spezielle Komponenten-Modelle implementiert, die das Einhalten von lokalen Grenzwerten, während und nach dem Befüllen bzw. Entleeren des Receivers ermöglicht.

Um die Berechnungszeit der Ertragsprädiktion zu verkürzen, wurden in zwei Stufen reduzierte Modelle sowie ein heuristischer Entscheidungsalgorithmus entwickelt und in Modelica bzw. Python implementiert. Dazu wurde ein Ansatz für eine virtuelle Nettoleistung des Receiversystems entwickelt, der es erlaubt, den Nettoertrag unter Berücksichtigung des komplexen dynamischen Verhaltens realistisch vorherzusagen und ohne Iterieren das optimale Timing zu finden. Damit wird der durch einen temporären Receiver-Standby erreichte Ertragsgewinn/-verlust quantifiziert als Basis für den Entscheidungsvorschlag.

Die Testergebnisse zeigen, dass ein einzelnes von dieser Betriebsassistenzfunktion vorgeschlagenes Manöver den Nettoertrag einer Großanlage je nach Bewölkungssituation um mehrere Megawattstunden steigern kann. Unsicherheitsanalysen zeigen eine besondere Sensitivität für Vorhersagefehler, weshalb insbesondere für größere Vorhersagehorizonte eine bessere Vorhersagegenauigkeit benötigt wird, als die der untersuchen Daten. Des Weiteren, besteht noch Forschungsbedarf für die genaue Modellierung des lokalen konvektiven Wärmeverlustes an solch einem Receiver, um die thermischen Verluste beim An- und Abfahren und somit dessen Dauer zuverlässig prädizieren zu können.

Table of Contents

Nomenclature

Abbreviations

1P	One-phase
2P	Two-phase
AFD	Allowable flux limit
AI	Artificial intelligence
ANN	Artificial neural network
ASI	All-sky imager
CFD	Computational fluid dynamics
CSI	Clear-sky index
CSP	Concentrating solar power
DLR	German Aerospace Center
DNI	Direct normal irradiation
EPC	Engineering procurement and construction
FEM	Finite element method
FP	Flow path
FS	Forecasting system
GE	General Electric
GHI	Global horizontal irradiation
HTF	Heat transfer fluid
IoT	Internet of things
IPCC	Intergovernmental panel on climate change

LP	Linear programming
LT	Lead time
MAD	Mean-absolute deviation
MAPU	Mean absolute uncertainty prediction
MILP	Mixed integer linear programming
MIQP	Mixed integer quadratic programming
MPC	Model predictive control
MSG	Meteosat second-generation
MST	Molten salt solar tower
OAS	Operating assistance system
P	Proportional
PB	Power block
PCS	Process control system
PI	Proportional-integral controller
PID	Proportional-integral-derivative controller
POI	Point of interest
PT1	First-order delay
PT2	Second-order delay
PTC	Parabolic trough collector
PV	Photovoltaic
RMSD	Root-mean-square deviation
Sc	Scenario
SCADA	Supervisory control and data acquisition

SG	Steam generator
SIJ	Solar Institute Juelich
st.-st.	Steady-state

Latin Symbols

$\dot{E}_{\mathrm{x}}$	Exergy flow rate	W
$\dot{Q}'$	Length-specific heat flow rate	W/m
$\dot{q}''$	Area-specific heat flow rate	W/m^2
Δz^*	Distance between the liquid surface and the center of the discrete element	m
F'	Length-specific friction force	N/m
P^*_{net}	Virtual net power	W
P^{**}_{net}	Actual net power	W
$\dot{Q}$	Heat flow rate	W
$W^{**}_{\mathrm{net,recov}}$	Recoverable net energy (in cold storage tank)	J
c_{p}	Isobaric heat capacity	J/(kg · K)
$e_{\mathrm{forc.}}$	Forecasting error	W/m^2
$e_{\mathrm{pred.}}$	Prediction error	W
$f_{\Delta p_{\mathrm{G}}}$	Pressure drop reduction factor (G/L)	-
$\dot{m}$	Mass flow rate	kg/s
n_{el}	Number of discrete elements (along tube)	-
$n_{\mathrm{tubesPerPass}}$	Number of tubes per receiver pass	-
h	Specific enthalpy	J/kg

R^2	Coefficient of determination	-
s	Specific entropy	$J/(kg \cdot K)$
$\Delta\dot{H}$	Enthalpy flow rate difference (thermal power)	W
Δr	Tube wall thickness	m
Δz	Height discrete fluid element	m
A	Area	m^2
Nu	Nusselt number	-
P	Power	W
Pr	Prandtl number	-
Re	Reynolds number	-
T	Temperature	K
U	Internal energy	J
V	Volume	m^3
c	Flow velocity	m/s
d	Diameter	m
g	Earth gravity acceleration	m/s^2
j	Discrete flow element number (along tube)	-
l	Length	m
m	Mass	kg
p	Pressure	Pa
r	Radial coordinate	m
t	Time	s
u	Flow velocity	m/s

u	Specific internal energy	J/kg
v	Flow velocity	m/s
v	Specific volume	m^3/kg
x	Flow coordinate	m
z	Vertical coordinate	m

Greek Symbols

α	Angle	°
α_{abs}	Absorptivity	-
α_{conv}	Convective heat transfer coefficient	$W/(m^2 \cdot K)$
β	Thermal expansion coefficient	K^{-1}
δ	Relative roughness	-
ε	Emissivity	-
ζ	Wall friction coefficient	-
ζ	Exergy efficiency	-
η	Energy efficiency	-
θ	Relative temperature	°C
κ	Isothermal compressibility	Pa^{-1}
λ	Thermal conductivity	$W/(m \cdot K)$
μ	Dynamic viscosity	$Pa \cdot s$
ξ	Mass fraction	-
ρ	Density	kg/m^3
σ	Stefan-Boltzmann constant	$W/(m^2 \cdot K^4)$

φ	Circumferential coordinate	°
Φ	View factor	-
ϕ	Volume fraction	-

Indices

∞	Ambient
abs	Absorbed
adj	Adjacent
amb	Ambient
B	Back shell
C	Core
conv	Convection
convLoss	Convective heat loss
Cr	Crown
cTank	Cold storage tank
d	Diameter-based
det.	Detailed dynamic 2P model
dev.	Deviation
drain	Draining / drainage
ext	External
F	Front shell
fast	Fast 1P model
FB	Front-back

fill	Filling
flow	Flow
fluid	Fluid
flux	Concentrated solar flux
fr	Frontside
fric	Friction
front	Frontside
fShell	Front shell
G	Gas phase
hTank	Hot storage tank
I	Inner
i	Inner
in	Incoming
int	Internal
L	Liquid phase
lam	Laminar flow
m	Mean
man.	Manifold
mod	Modified
n	Nominal
net	Net
O	Outer
out	Outgoing

Pan.	Receiver panel
PB	Power block
PF1	Flow path 1
pumps	Receiver pumps
Q	Cross-sectional
rad	Radiation
radLoss	Radative heat loss
rampDown	Temperature ramp-down phase
real	Real
rec	Receiver
recy	Recycling
ref	Reference
SG	Steam generator
simp.	Simplified dynamic 2P model
stor	Storage system
tube	Absorbertube
turb	Turbulent flow
vessel	Vessel
W	Wall
wall	Tube wall
η-loss	Loss due to receiver efficiency impairment
j	Discrete flow element number (along tube)
σ	Blackbody radiation

List of Figures

List of Tables

1 Introduction

The expansion of renewable energy was driven mainly by the steep cost reduction of solar photovoltaic (PV) (IRENA 2022). However, storing electrical energy directly or with batteries is still too expensive for broad application in our electrical grids. In contrast, concentrating solar power (CSP) can provide green energy 24/7 at a relatively low cost. Even power production throughout the night is economically feasible due to the relatively inexpensive integrated thermal storage (Hogrefe et al. 2021). Nevertheless, depending on the market other operation strategies often achieve higher profits (Lizarraga-Garcia et al. 2013). Due to the higher investment cost and greater complexity, CSP has not reached a marked penetration as high as PV. Today CSP installations are spread across 23 countries (NREL 2022), and more than 100 CSP plants are in commercial operation (Mehos et al. 2020) with an installed capacity of approx. 6.4 GW in total (IRENA 2022). As illustrated in Figure 1-1, they are primarily located in the Sun Belt regions of the northern and southern hemispheres.

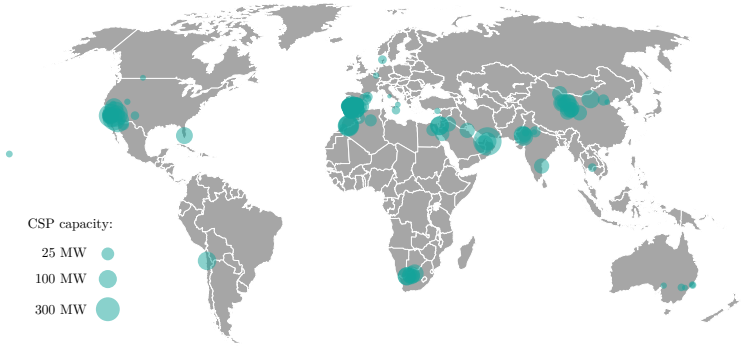

Figure 1-1: Worldwide CSP capacities operational and under construction, data from SolarPACES Network (2021)

In general, CSP technologies are classified into central receiver systems (solar tower systems), parabolic trough systems, linear Fresnel systems and solar dish systems. In the last two decades, parabolic through systems have been

dominating in terms of installed capacities. New installations mostly feature central receiver systems, especially molten salt solar towers (MST), on which this work and the following technology overview focus.

1.1 State of Technology

Molten salt solar towers (MST) represent the most relevant point-focusing technology. These systems are significantly more complex than the previously preferred line-focusing parabolic trough systems. However, the higher concentration, thus higher process temperatures, offer more potential for overall power production efficiency and lower thermal storage cost. Additionally, MST systems achieve higher yields per occupied land area (Ahmadi et al. 2018). Still, the advantages depend on the location and meteorological boundary conditions. On the one hand, the requirement for a clear atmosphere is more significant for MSTs than for parabolic troughs collectors (PTC) because of the long distance between the concentrator (heliostats) and the receiver. On the other hand, as shown in Figure 1-2, MST systems need less land preparation compared to PTC, which can only be erected on even ground (Dersch et al. 2021).

Figure 1-2: Comparative images of PTC (left), MST (center) and heliostat (right) of the Noor II and Noor III power plants in Ouarzazate, Morocco

Apart from the tower, the main identifying feature of an MST plant is the segmented concentrator, also known as the heliostat field, which focusses the

solar radiation onto a receiver placed on top of the tower. Depending on the plant capacity, it comprises hundreds to tens of thousands of heliostats (sun-tracing mirrors). Commercial solar tower systems utilize large heliostats with more than 100 m^2 and small heliostats with less than 20 m^2, which is always a tradeoff between high aiming accuracy and cost. Depending on latitude and receiver type, the heliostat field layout is either north of the tower (northern hemisphere, south if southern hemisphere) or around the tower to maximize annual field efficiency. (Mehos et al. 2020)

The average concentration ratio is usually approx. 1000, with peak flux values up to 1000 kW/m^2. To minimize thermal stresses in the one-sided irradiated absorber tubes and to avoid increased molten salt degradation due to excessive fluid temperatures, the concentrated solar flux must be limited, which is realized by different aiming strategies. The goal is to even out the flux density distribution in peak flux areas by spreading out the aim points of certain heliostats while maintaining a high intercept, thus, low spillage losses. This works better with external receivers than cavity receivers. Hence, external receiver designs have become established quickly for MSTs. (Mehos et al. 2020; Relloso and Gutiérrez 2016)

The flux density distribution is crucial for a well-performing MST and acts as the interface between the heliostat field and the receiver system. This becomes especially relevant if different companies provide these subsystems. They often use raytracing to estimate the flux density distribution based on sun position and predetermined heliostat qualities. However, no commercial method is yet available for mapping the actual flux density distribution on a molten salt central receiver (Mehos et al. 2020; Dersch et al. 2021).

On the one hand, the heliostat field cost still holds the largest share of the overall investment for an MST. On the other hand, the receiver system has proven to be the most challenging subsystem and the most significant cause of unavailability and operational performance losses (Kolb 2011). Since the pioneering MST project SolarTwo, many design features have been adapted in today's commercial plants. The receiver, which absorbs the concentrated solar flux, consists of several flat panels aligned in a horizontal circle forming

a semi-cylindrical receiver surface (see Figure 1-3). Each panel includes numerous adjacent tubes out of high-temperature nickel alloy connected in parallel by headers. The receiver panels are interconnected in series (sometimes in parallel as well) to realize a serpentine flow of the heat transfer medium (HTF).

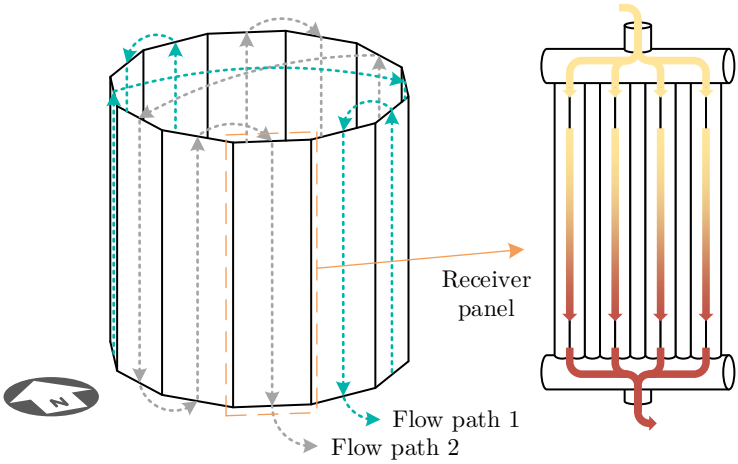

Figure 1-3: Receiver flow path and panel layout of an external molten salt solar tower receiver

Additionally, the receiver is subdivided into two parallel flow paths, which usually are crossed over for a more uniform load distribution during morning and evening hours. The HTF is a mixture of 60 % sodium nitrate and 40 % potassium nitrate, heated in the receiver from 290 °C up to 565 °C. (Zavoico 2001; Dersch et al. 2021)

Due to the allowed temperature range of the HTF between its melting point (liquidus temperature) at approx. 240 °C and the upper limit of approx. 600 °C operating a molten salt receiver system poses a challenging task. On the one hand, falling below would cause freezing and potentially damaging components. One the other hand, exceeding the upper limit would rapidly accelerate the degradation of the HTF, which in turn causes corrosion in wetted components. (Bonk and Bauer 2022; Sötz et al. 2020)

Hence, a complex operating strategy with detailed startup and shutdown procedures is necessary to prevent freezing and overheating. Furthermore, the significant temperature lift and strict flux limitations on the tubular receiver panels lead to a relatively long throughput time of approx. 1 min and in part load anti-proportionally longer. Therefore, the developers of the SolarTwo plant suggested a combined feedforward and feedback control logic to control the outlet temperature in normal operation. In cloudy conditions, the system was operated with a semi-fixed mass flow control based on a clear-sky model, also known as cloud standby. This effectively causes the outlet temperature to drop with every cloud passing the heliostat field, impairing the heat-to-power efficiency. (Pacheco et al. 2002)

The first commercial MST, GemaSolar, adapted and improved the operating and control strategy, but in cloudy conditions, the receiver outlet temperature still decreased significantly, posing performance limitations, especially during partial shading (Burgaleta et al. 2012; Relloso and García 2015). The same applies to the full-scale commercial MST Noor III (Relloso 2019).

The HTF is the direct storage medium in a two-tank thermal storage system. By design, the cold tank holds an inventory of molten salt at 290 °C and the hot tank at 565 °C. However, due to the temperature fluctuations mentioned above, both tanks can take in the molten salt at temperatures that are more than 100 K above or below its bulk inventory temperature. Distribution headers and static mixers minimize temperature gradients inside the tanks. Besides implications for tank engineering, this also affects the efficiency of the connected Rankine cycle power block. (Mehos et al. 2020)

After the first MST plant SolarTwo in the United States with 10 MW_{el} (Zavoico 2001), the technology was scaled up to 20 MW_{el} for the first commercial MST GemaSolar in Spain (García and Calvo 2012), followed by the two full-scale MST plants CrescentDunes in the United States with 110 MW_{el} (Boretti et al. 2017) and Noor III in Morocco with 150 MW_{el} (Relloso and Gutiérrez 2016). With that, the tower height increased from 76 m to 250 m. These plants have/had integrated storage capacities of 3, 15, 10 and 7.5 h for nominal power block operation. More MST installations followed in United

Arab Emirates, Chile and China with similar power production capacities (SolarPACES Network 2021).

After the SolarTwo project has been battling with freezing issues in the receiver and periphery components, today's operators have mostly overcome this problem. Key issues of commercial MST operation are tank leaks, actual radiation (clouds), attenuation, actual flux distribution (field quality) and heat-tracing quality. Moreover, accurate receiver control with advanced flux measurement is essential for adequate receiver performance. Especially during irregular flux distributions at very high or very low levels, receiver operation is critical because of the limited convective heat transfer into the fluid. (Mehos et al. 2020; Rodriguez-Sanchez et al. 2015)

The controllability of a molten salt receiver depends on the temporal and spatial variability of DNI (direct normal irradiation). This alone can lead to approx. 4 % overprediction when being neglected (Schwager et al. 2019). According to Relloso and Gutiérrez (2016), oversimplified commercial simulation software usually neglects actual limitations, which causes up to 11 % overprediction. Hence, more realistic yield prediction tools for MSTs are needed. For example, allowable flux density (AFD) limits must be considered to keep thermal stresses and salt film temperatures below critical levels (Sánchez-González et al. 2020).

Software tools with some prediction methods and online operating assistance are available from companies such as GE General Electric (2022), Siemens AG (2022), ABB Asea Brown Boveri Ltd (2022), STEAG Energy Services GmbH (2022), Aspen Technology Inc. (2022) and others. Many of them are based on digital twins, i.e. a software representation of a physical component, process or system to predict and optimize the operation or to enable early failure detection. Some utilize physical models for process prediction, online optimization or model predictive control (MPC). Others incorporate machine learning respectively artificial intelligence (AI) algorithms for rapid decision-making in complex systems. GE also developed an IoT (internet of things) platform Predix (GE General Electric 2022), to allow third-party software

developers to create online monitoring and optimization applications running in this cloud-based environment.

However, most of the available software tools are suited for broadly established industry processes and systems. CSP plants still are a novelty in this branch. Since there is no significant standardization yet, software operating assistance tools are usually developed by the technology developer explicitly for each plant. For example, SENER, the EPC (engineering procurement construction) contractor of GemaSolar and NoorIII, developed its own plant monitoring and performance supervision program SENSOL (García and Calvo 2012). Also, SolarRecerve, the leading developer of the CrescentDunes plant, developed its own tool for operating the heliostat field (Ayres et al. 2020).

1.2 State of Research

Current research on MST systems is mainly concerned with operational efficiency, availability of the receiver system and cost reduction. One possibility to increase the overall efficiency of an MST plant by design is by raising the upper process temperature, as it is the aim of the research by Puppe et al. (2018) and Frantz et al. (2022a). This is challenging due to the increased decomposition of molten salt at higher temperatures and the resulting corrosion of wetted components. Nevertheless, Bonk et al. (2020) found out that the chemical stability of the used molten salt could be pushed to higher temperatures by closing the system and allowing the reactive gases to build up pressure.

Further overall yield performance improvements have been investigated by operational assistance and optimization. Gall (2012) developed optimized operating strategies for a solar tower with an open volumetric air receiver. He proposed a concept of an operating assistance system (OAS), including an MPC, to optimize the overall performance by predictive field control and storage utilization. Concerning the same solar tower technology, Ahlbrink (2013) proposed to enhance the receiver operational efficiency by aim point

optimization and adjusting the HTF mass flow rate with the help of a dynamic process model. Furthermore, Vinnemeier (2018) developed an OAS for a solar tower with an open volumetric air receiver by means of overall optimal operation and automation. This OAS actively controls the plant while neglecting dynamics mostly. Instead, the OAS optimizes the system's operation with a series of optimal steady states. Alternatively, Ghobeity and Mitsos (2011) optimized the operation of a central receiver concept integrated into a cogeneration plant by applying nonlinear programming on a system-level dynamic model to maximize profit income.

However, some ground laying work has been done to optimize receiver flow patterns fully and panel design in alliance with flux limitations (Rodriguez-Sanchez et al. 2015; Rodríguez-Sánchez et al. 2014; Frantz et al. 2017). Based on allowable flux limit (AFD) definitions by Vant-Hull (2002), numerous studies were conducted on aim point optimization to maximize heliostat field efficiency under normal conditions (Richter and Speetzen 2022; Sánchez-González et al. 2020; Flesch et al. 2017; Acosta et al. 2021; Binotti et al. 2016; Astolfi et al. 2017; Wang et al. 2022).

Furthermore, the transient receiver flux distributions throughout the day and even during cloud passages have been modeled and investigated (Augsburger and Favrat 2013; Schöttl et al. 2018; Ahlbrink et al. 2012). Augsburger and Favrat (2013) proposed a method to reduce transients due to cloud passages by defocusing and slowly ramping up the entire field, which comes with additional yield losses. Moreover, with the help of fast raytracing, Belhomme et al. (2013) developed an aim point optimization algorithm applying an ant colony optimization metaheuristic, which was further improved by Flesch et al. (2017) and Oberkirsch et al. (2021), reaching a performance that allows for online-optimized aiming in cloudy conditions.

Moreover, García et al. (2018) presented a model predictive aiming control method combined with a PI-controller for set point adjustment to prevent cloud-induced temperature overshooting. Moreover, in the field of solar chemical receivers, Oberkirsch et al. (2022) presented an ANN (artificial neural

network) based flux controller to manage alternating flux demands on an array of multiple receivers.

Those flux controllers, respectively aiming optimizers, rely on accurate determination of the resulting flux density distribution, usually done by ray-tracing. A more reliable solution would be to measure the actual flux density distribution on the physical receiver. Methods for online measurement of the flux density distribution on an operating receiver are currently being developed (Offergeld et al. 2019; Ho and Khalsa 2012; Röger et al. 2014).

Besides an optimally controlled heliostat field, receiver control is another crucial factor in overall efficiency. Popp et al. (2023) described an MPC approach for controlling the receiver outlet temperature and limiting local film temperatures by continuously adjusting the control valve of an MST. By assuming well-predicted flux density distributions, the study reveals significant potential for improving control accuracy compared to a PID-based controller. In contrast, García et al. (2022) present a multi-variable control strategy in which intermediate valves along the flow path are utilized to reduce the time delay and quickly respond to cloud-induced fluctuations.

The optimization approaches mentioned above are often based on sophisticated mathematical models and algorithms. Realistic modeling of the receiver and its control system is as important as modeling and controlling the flux density distributions. Due to the fluctuations in the solar flux, dynamic thermo-hydraulic models are usually applied. The level of detail is always adapted to its application. Receiver models with zero-dimensional steady-state absorber tube models (Li et al. 2019) can be used to quickly estimate the overall performance for a long time interval or multiple days.

If local states, such as maximum film or tube wall temperatures, are of interest, discretization is needed. Often the fluid is only discretized in the direction of flow. Additionally, the tube wall is often discretized in the circumferential and radial direction for considering the inhomogeneous irradiation of each absorber tube (Crespi et al. 2018; Losito et al. 2018). For calculating thermomechanical stresses, very fine discretization be means of FEM and CFD

meshing are needed to appropriately describe the three-dimensional structure of the bent tubes (Fritsch et al. 2017; Uhlig et al. 2018; Montoya et al. 2019). For example, Hering et al. (2021a) developed a high-resolution model to predict the lifetime consumption of a receiver due to transient operation.

However, higher discretization expands the differential equations system to be solved for each time step. Hence for control and operation optimization purposes, some absorber tube models are discretized in numerous elements along the direction of flow, but in only two elements along the circumference, i.e. front and back shell, since only the front side is irradiated. By this, Doupis et al. (2016) and Sani et al. (2018) were able to implement drainable receiver models within an outer system model to simulate filling and drainage procedures. Hence, these models also include a two-phase flow model, which brings additional complexity. The disadvantage of only representing a front and a back shell is that the circumferential temperature distribution on the front shell is neglected, leading to an underestimation of the maximum temperature. For this reason, Flesch et al. (2016) introduced an analytical approach to estimate the maximum temperature at the tube crown without additional differential equations. This method was adapted by Popp et al. (2019) and is further developed in Section 3.2.3 for accurate film temperature estimation.

Besides incorporating efficient modeling, an OAS for MST plants can only exploit its full potential when coupled with forecasting data because of their high variability. Nowadays, Meteorological forecasts are applied in the planning, engineering and financing of CSP plants. Among other conditions, DNI is the most crucial parameter. Forecasting methods or technologies are generally distinguished by forecast horizons, respectively lead time. In the energy sector, they range from long-term forecast (several days) to short-term forecasting, respectively nowcasting (up to 6 hours). (Heller 2017)

The latter is most relevant for short-term operational decision-making by means of an OAS. Statistical nowcasting methods use the high autocorrelation of irradiances for very short time periods due to the daily solar cycle. Algorithms such as Kalman filtering, moving average, autoregressive moving

average, autoregressive integrated moving average as well as machine learning algorithms like ANN are implemented in some nowcasting systems. However, statistical nowcasting systems are primarily suitable for GHI (global horizontal irradiation) forecasting and less for DNI since it is much more sensitive to heterogeneous extinction due to clouds (Schroedter-Homscheidt and Wilbert 2017).

Consequently, for CSP systems, the nowcasting methods more often utilize all-sky imagers (ASI), also known as cloud cameras. Most ASI systems monitor the sky using one or two cameras with a fish-eye lens to track the horizontal movements of clouds. The use of multiple ASI allows for determining cloud height and three-dimensional shape. Usually, ASI nowcasting algorithms identify distinct clouds and assume their shape to stay constant. In reality, clouds change in shape and size regularly, but only a few nowcasting systems consider cloud deformation (Huang et al. 2013). Usually, ASI systems are limited to maximal lead times of 10 to 20 min due to the rising measurement error at greater distances, respectively shallow view angels. Blum et al. (2021) proposed a method to overcome this issue by implementing a network of multiple ASI across an area of more than 150 km². This setup increases the accuracy of cloud height measurement and allows for longer lead times. Alternatively, Nouri et al. (2022) combined ASI nowcasting with a persistence forecast. Persistence forecasting assumes the shadings do not change and only considers the sun's movement. This approach avoids any effort to estimate the hardly predictable cloud deformations.

Lastly, satellite image-based forecasting systems are widely used in mid- and long-term forecasting but more and more in nowcasting. The advantage, especially with Meteosat second-generation (MSG) satellites, is that they provide additional images in infrared spectral channels, allowing more profound analysis of aerosols as well as distinguishing between high-altitude ice clouds (cirrus) and lower clouds (e.g. cumulus). However, the spatial and temporal resolution is limited to pixel sizes of more than 1 km and updating intervals of 5 min or longer (Schroedter-Homscheidt and Wilbert 2017; Sirch et al.

2017). Moreover, researchers try to combine ASI with MSG forecasting systems to take advantage of both's strengths (Burgaleta et al. 2012; Yasser et al. 2020).

1.3 Motivation

Due to the limited temperature range in which the HTF, molten salt, can be safely operated and the complex dynamic behavior of the receiver system, operating an MST serves many challenges. The developments mentioned above have successfully brought the technology to market readiness. However, MST plants are mostly underperforming in commercial operation, revealing significant potential for improvements. Most recent research and development aim to optimize normal operation by improving the control accuracy of the receiver by increasing the robustness of aiming strategies. Nevertheless, operators still rely on a learning curve while gaining experience in how to operate the system.

One major drawback of MSTs is the high pumping energy consumption due to lower specific heat caried by the HTF compared to a direct-steam system. In a commercial MST design, the receiver pumps usually consume between 6 and 9 % of the gross power, depending on the system layout and tower height. The tower height increased significantly with the technology development because of its positive effect on field efficiency. Thus, every minute of receiver operation, the system needs to run as efficiently as possible to achieve profitability. More specifically, in cloudy conditions with partial shading, this raises the question of when receiver operation actually is net beneficial and when the receiver should be put in standby instead.

Additionally, there is the continuous risk of the molten salt freezing in the absorber tubes. Hence, transitions between operating modes of an MST, such as normal operation mode and standby, are subject to time-consuming draining, preheating and flooding procedures. This results in a significant loss of productive time and therefore added energy losses, which must also be considered. Practically, it is impossible for a human operator to appropriately

take all these factors into account. Hence, an OAS is needed that can realistically predict net yield and suggest model-predictive decisions to allow the operator of the receiver system to rely less on intuition and more on accurate predictions. Furthermore, the use of prediction models can increase operational safety and reliability. E.g., monitoring local non-measurable states, such as HTF film temperatures in the absorber tubes, can support limiting degradation of the molten salt and thus corrosion of any components in contact with the HTF.

However, newly developed artificial intelligence is often confronted with skepticism and users initially find it difficult to trust such algorithms. Hence, instead of fully automated control, an OAS leaves the final decision to the human operator, benefitting from the human expertise. While this allows for quicker acceptance, such a system can run alongside a commercially operating plant without posing a risk to operational safety. Over time the OAS gains the trust of operational staff while leaving opportunities for improving the algorithms, before they might be applied to a fully automated control system. Also, key will be a well comprehendible visualization for the operators to follow and understand how the OAS gets to the final suggestion.

The Basis of this OAS is physical modeling. The development of very fast and specialized models requires a detailed, fully dynamic model by means of a digital twin to analyze the dynamic system behavior and to derive and validate the reduced model for the process prediction. The receiver model presented by Flesch et al. (2016) poses a suitable approach except for the two-phase (2P) flow modeling, which incorporates a two-fluid modeling approach. The numerical stability is insufficient for more extensive simulation setups, including a whole receiver and periphery. However, the 2P feature is required for an appropriate representation the varying heat transfer during drainage and refill of the receiver tubes, since this affects the cool down rate and therefore how quick the receiver will be ready for operation again. Therefore, the OAS application requires a more efficient 2P modeling approach.

1.4 Scope and Structure of this Dissertation

This dissertation presents the conceptual idea of an operating assistance system (OAS) for a molten salt tower (MST) with different assistance functionalities. Further, it describes the development and validation of a model predictive decision algorithm, including physical modeling.

First, Section 2.1 in Chapter 2 presents the concept of the OAS and the proposed methodology for the technical implementation of the assistance functions. Moreover, Section 2.2 specifies the applied input data by means of nowcasting DNI maps and the considered scenarios.

Chapter 3 follows with in-depth documentation of the modeling. For setting certain boundary conditions, Section 3.1 defines a reference plant. Based on this, a digital twin, respectively detailed dynamic 2P model is implemented as described in Section 3.2. From this, several model reductions are conducted. First, a minor model reduction for predicting (2P) transitions results in the simplified dynamic 2P model in Section 3.3. More drastic reductions lead to the fast 1P model described in Section 3.4 and the most simplified scalar 1P model in Section 3.5. Subsequently, Section 3.6 includes the validation of the detailed model. The validation of the reduced model is documented in Section 3.7.

The Algorithm to determine optimal drainage and refill timing is described in Chapter 4, subdivided into the derivation of the objective function in Section 4.1 and the algorithm part for selecting the actual timing in Section 4.2.

The testing is primarily documented in Chapter 5. Furthermore, an uncertainty analysis is carried out in Section 5.2, followed by some sensitivity studies in Section 5.3.

Finally, Chapter 6 concludes all results and gives an outlook on suggested follow-up research.

2 The Concept of an Operating Assistance System for MSTs

Operating assistance systems (OAS) are used in applications where fully automated operations are not (yet) accepted. Its primary purpose is to enhance the capabilities of human operators by adding awareness or complementing their cognitive capacities. There are numerous variations in how OASs are defined or classified. In this work, an OAS is considered a software component that supports the operator of a partially automated process by providing additional information based on complex algorithms. Three levels of assistance can be defined (Nolteernsting 2020).

First, process prediction based on online measurement data and a physical model, or other algorithms can provide additional information to the operator about the expected course of specific process parameters. Second, a maneuver mode helps to estimate the effect of specific actions, e.g. adjusting a set value or switching to a different operating mode. Both cases, keeping current settings and conducting the maneuver, are predicted for comparison to guide the operator in operational decision-making. Third, a proposal mode combines the process prediction with an optimization algorithm to determine optimal settings or trajectories. Still, the decision to follow the proposal is in the hands of the human operator.

Operating a molten salt receiver poses numerous challenges pushing operators to the limits of their cognitive capabilities. Nowadays, computers are superior in making optimal decisions. However, humans are still more reliable in adjusting to extraordinary situations due to their experience and intuition. Therefore, a fully automated operation is usually not an option in a young technology such as MST with the associated risk. In this case, an OAS allows taking advantage of the added information and intelligence without relying on the innovative algorithms entirely. Using the OAS, the models and algorithms can be further improved while the operators gain trust towards more automation. Figure 2-1 illustrates how the OAS could be integrated into the

control setup of an MST plant. Only the process control system (PCS), also often referred to as supervisory control and data acquisition (SCADA), is directly connected to the hardware by means of sensors, actuators and hardware controllers. The OAS receives current states respectively measurement data from the PCS and forecasting data from the forecasting system (FS). The operator receives predictions and proposals from the OAS through its designated user interface. At the same time, he or she keeps full authority over the plant operation through the user interface of the PCS.

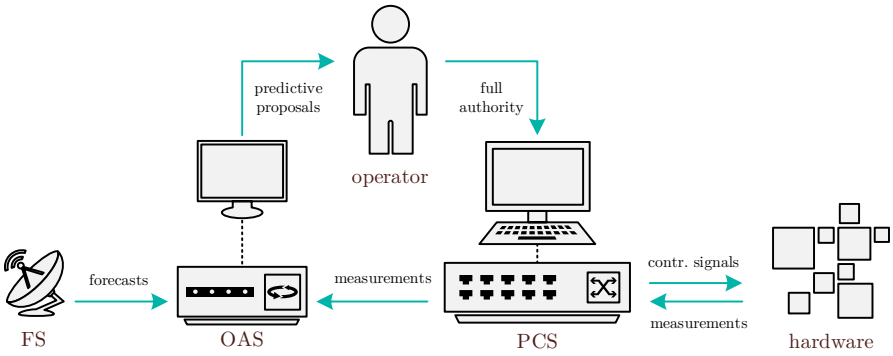

Figure 2-1: Illustration of the OAS integration into an MST plant control setup

In general, the following problems of MST operation were identified as suitable tasks for an OAS with the objective of maximizing overall yield:

Task 1:

Timing startup in non-clear-sky conditions is a demanding task. Usually, the solar subsystem of an MST should start up when the sun reaches a specific elevation. This ensures sufficient solar flux and field efficiency to run the system in clear-sky conditions. However, in hazy or cloudy conditions, it is questionable whether the system actually reaches positive net efficiency because of the high parasitic losses compared to a low heliostat field power. The OAS could predict the duration and parasitic energy consumption during the startup procedure and the achieved net yield. This requires DNI nowcasting data in a quality that allows realistically predicting the concentrated flux distribution during preheating with the help of raytracing or equivalent

algorithms. Furthermore, a dynamic model of the receiver system that allows predicting the system performance during those transitions is essential. Coupled with an optimization algorithm, this could predict the performance and propose the optimal timing to maximize net yield.

Task 2:

The preheat and ramp-up trajectories (compare Section A) can be optimized with the help of an OAS as well. It is desirable to perform the preheat and ramp-up phases as quick as possible since the system does not generate any significant yield. At the same time, parasitic consumptions are high already and solar flux would be available. The relevant constraints are thermal stresses, which are the primary cause of the limited lifetime of the tubular receiver panels. Therefore, the frequency and extend of high thermal stresses must be limited. Hence, maximum rates of change (transients) are usually predetermined for pipe and tube wall temperatures based on thermo-mechanical analysis with conservative assumptions.

Task 3:

During preheat, the one-sided irradiation creates a significant circumferential temperature gradient (front to back) in the empty absorber tubes, causing bending stresses. A **soft sensor** (software sensor) can determine these **gradients** based on a thermal model and help the operator control the trajectory with smaller error margins. The ramp-up phase is less critical because the HTF flow cools the absorber tubes. However, the rising HTF temperature affects the thicker-walled piping downstream of the receiver. To avoid early fatigue due to thermal cycling, the ramp-up must also be performed with a limited temperature transient, which is predetermined with the help of thermo-mechanical modeling. Hence, another soft sensor determining these pipe wall temperature transients (K/s) or even gradients (K/m) would allow for a less conservative trajectory. Ultimately, an OAS could combine these two soft sensor applications with forecasting data and optimization algorithms to directly provide the optimal trajectory meaning flux set values to the operator. This could minimize the startup time and, in turn, maximize the overall yield.

Task 4:
In fluctuating solar conditions, the resulting temperature transients and related thermal stresses significantly impact the **live time consumption of receiver components**. A digital twin of the receiver could be used to determine how much lifetime was consumed during a certain period of operation. This could be realized with a detailed thermo-mechanical model and historical measurement data of the considered system. This information allows the operators to gain experience over time and to avoid (lifetime) costly operations in the future. It could also be integrated into a predictive maintenance program so that, for example, absorber tubes could be replaced as late as possible and safely before they break, minimizing downtime. In a more sophisticated approach, the digital twin would run with forecasting data to predict lifetime consumption. Therefore, indicating to the operator if continuing operation through fluctuation conditions would cost too much in terms of lifetime compared to the expected yield.

Task 5:
Another practical soft sensor application could be **local HTF film temperature and tube wall temperature prediction.** Monitoring local absorber tube wall temperatures would allow for operating the receiver less conservatively, especially if predictions are included. The set values for the (receiver) flow path controllers could be set to higher temperatures, increasing power block efficiency, when the OAS predicts well-controllable conditions for the near future. Otherwise, it could create a warning motivating the operator to decrease the set point or even switch to a less efficient but safer operating mode, such as filled cloud protection (compare Section 3.2.7).

Task 6:
Furthermore, partial shading of the heliostat field during cloudy conditions can affect the **flow distribution** in the parallel tube of a receiver panel. As depicted in Figure 1-3, the HTF flows through the receiver panels in a serpentine pattern. Consequently, in the panels with a downward flow, the driving force results from a combination of gravity and static pressure difference. The latter is dominant at the nominal mass flow rate but not at low mass

flow rates. Nevertheless, depending on the applied aim point strategy of the heliostat field, local shadings are projected blurred on the receiver surface, resulting in higher horizontal flux gradients. Due to such a horizontal flux gradient, the HTF in the absorber tubes of this respective receiver panel with the highest flux heats up more than the others. Since the density of the HTF is highly temperature dependent (see Figure 3-3), a tube (in the same panel) with lower flux contains denser HTF increasing the driving force compared to the tubes with higher flux.

If the pressure difference dominates the driving force, then this has no significant impact on the flow distribution in the parallel tubes. However, if the HTF mass flow rate is relatively low – for example, in the morning – the gravitational force becomes superior. As a result, the flow rate in the less irradiated tube increases. The overall mass flow rate stays constant since the control valve controls it. Consequently, the tube flow on the less shaded side of the receiver panel decreases. This change in flow distribution amplifies the temperature difference (between the tubes with high and low flux) and, in turn, the unevenness in the flow distribution. There is one counteracting force to this self-reinforcing phenomenon because the friction forces increase progressively with the flow rate.

In conclusion, at small horizontal flux gradients, the tube flow rates deviate from each other but reach a stable equilibrium when the difference between the gravitational forces equals the difference between the friction forces. However, suppose the mass flow rate is low and, at the same time, there is a great horizontal flux gradient. In that case (depending on the panel design), the flow may only reach this stable equilibrium after the flow rate on the less shaded site has turned around, resulting in a natural circulation within the respective receiver panel. In between these two extreme cases is the edge case in which the mass flow rate in a tube on the less shaded side stops completely, posing the most critical scenario.

Simulations with the detailed dynamic receiver model revealed this phenomenon and showed that under specific conditions, this phenomenon could even result in thermo-hydraulic oscillations due to thermal inertia. Even in the

regime of uneven but stable flow distribution (without natural circulation), the mass flow rate on the less shaded side of the panel might already be critically low. As a result, the HTF film temperatures would exceed the allowable limit, causing HTF degradation and tube damage. An OAS could incorporate a specialized thermohydraulic receiver panel model to predict this behavior and warn the operator or to determine a minimum mass flow rate that dynamically changes with the flux density distribution. Since this phenomenon can even occur above the typical minimum mass flow rate, such an assistance function would increase operational safety in cloudy conditions, allowing for less conservative and more efficient operation.

Task 7:

Optimized storage charging decisions can increase overall net yield since mixing two fluid flows of different temperatures always comes with an inevitable exergy loss. By design, the HTF should be charged into the hot storage tank. If the flow temperature is below a predefined threshold, it is recycled into the cold storage tank instead. At first sight, since the pumping has been done already, it seems wasteful to put it to the cold tank. Additionally, the related increase in the receiver inlet temperature negatively affects the receiver efficiency. Nevertheless, if the HTF flow temperature is much closer to one of the cold tank inventory than the hot tank, then charging into the hot tank would result in much higher exergy losses. Additionally, recycling the HTF gives the opportunity to increase the stored exergy when the HTF is reheated in the receiver to a higher temperature.

In conclusion, whether charging is more efficient than recycling depends on the current inventory temperatures of both storage tanks and the expected future receiver performance. Therefore, a prediction model that describes the receiver system performance and the storage system combined with an optimization algorithm could be an OAS function to increase net yield effectively.

Task 8:

Finally, in cloudy conditions with high degrees of shading overall net efficiency of the system can become negative due to high parasitic losses. Espe-

cially the receiver pumps of a commercial solar tower consume several megawatts of electricity to provide the necessary pressure and flow rate for lifting the heavy HTF. Additionally, the receiver outlet temperature would drop far below its set point so that the HTF would be recycled into the cold storage tank. As mentioned before, the rising inventory temperature impairs the receiver efficiency in the following time and the need to pump the HTF a second time. With the help of a detailed prediction model that described all these effects, an OAS could predict the overall net efficiency for the near future based on solar nowcasting to inform the operator when the system would produce a negative net yield. Based on this, the operator could make an informed **decision whether a temporary shutdown**, meaning draining and later refilling the receiver, would be beneficial.

However, the transitions from normal operation into a drained cloud protection mode and back take valuable operating time. In addition, before refilling the receiver, the absorber tubes must be preheated, requiring a minimum of solar flux. These implications are difficult to consider just on subjective observations. An OAS can create a benefit by providing a dedicated proposal mode. It should not only point out when the system is running inefficiently but also propose the **optimal decision of when to start receiver shutdown** and when to restart to maximize net yield. In case the loss of operating time would cause more additional losses than the ones that were avoided, it proposes continuing the operation. The following Section describes how the concept of such a proposal mode can be implemented. In the following, this thesis presents the implementation and validation of this proposal mode (Task 8) by an exemplary MST design.

2.1 Implementation of a Proposal Mode for Temporary Shutdowns

The main task of the aspired OAS function is to propose if and when the receiver system should be optimally shutdown to maximize the net yield of the entire MST plant in cloudy conditions. For this, it must quantify the

expected yield for both continuous and interrupted operation, which should also be displayed to the operator for better transparency. This poses an optimization problem in which the objective function can be described as the integrated yield during a specific prediction interval. There are two optimization variables; the time when the shutdown is initialized and the time when the system is restarted. All technical limitations and boundary conditions can be considered constraints of the solution space.

Numerical optimization has already been applied to many different types of energy systems. Especially when an optimization problem has many variables, it can be beneficial to implement a mathematical model to be solved by a dedicated optimization solver (optimizer). Such a solver usually tries to find the quickest path from an initial solution to the optimal solution by following a descending gradient in the solution space of the objective function. If the optimization problem can be modeled in a mathematically simple way, e.g. linear or quadratic modeling, problems with thousands of variables can be handled with acceptable computing effort (Arora 2015).

However, for the validity of the OAS, the modeling must include all relevant dynamic effects. Since the duration of transitions, which include drainage and refill of the receiver, depend on the fluctuating ambient conditions, the associated added losses are very sensitive to that too. Therefore, not only the two operating modes of interest – normal operation and drained cloud protection – but also the transitions must be modeled in detail. The optimization model would include a complex and nonlinear equations system despite the only two-dimensional solution space. A mathematical optimizer, which searched the optimum by iterating, might take too much computing time, since the model would need to be simulated several times. Besides, the resulting solution might not guarantee global optimality. Therefore, a heuristic approach is developed in this work.

To find the optimal time to initialize a shutdown, each iteration of an optimizer includes simulating both transitions and calculating the overall net yield. Hence, the number of iterations must be reduced to a minimum to achieve reasonable solutions within a few minutes. Hence, two main steps are

necessary. First, the overall net power – time derivative of the objective function – is formulated in a way that allows shortening the necessary prediction time interval. For this purpose, time periods are decoupled from each other by moving delayed effects from the time of occurrence to the time of cause. This can be applied to the future losses caused by HTF recycling, as described in more detail in Section 4.1.4. Secondly, this objective function eliminates the need to iterate, as described in Section 4.2. Additionally, even though the objective function resembles the net electric yield, complex power block modeling can be avoided with the help of an exergy-based approach described in Section 4.1.1.

Figure 2-2 illustrates the principal implementation of this assistance function. As a development and validation basis, a detailed dynamic 2P (two phases, molten salt and air) model is implemented in the modeling language Modelica (compare Section 3.2), which is validated by high-resolution CFD/FEM simulations and experiments. It contains a three-dimensionally discretized receiver model with a 2P medium model. The 2P flow modeling also realistically describes the thermohydraulic behavior during the filling and drainage of the absorber tubes. This is important, since it affects the cooling rates during drainage and therefore how quick the receiver can be ready for operation again. The heliostat field performance is pre-simulated with the raytracing software STRAL (Ahlbrink et al. 2012) to predict the flux density distribution on the receiver for every time step. DNI maps from nowcasting or artificial cloud scenarios are used as input data, as presented in Section 2.2.

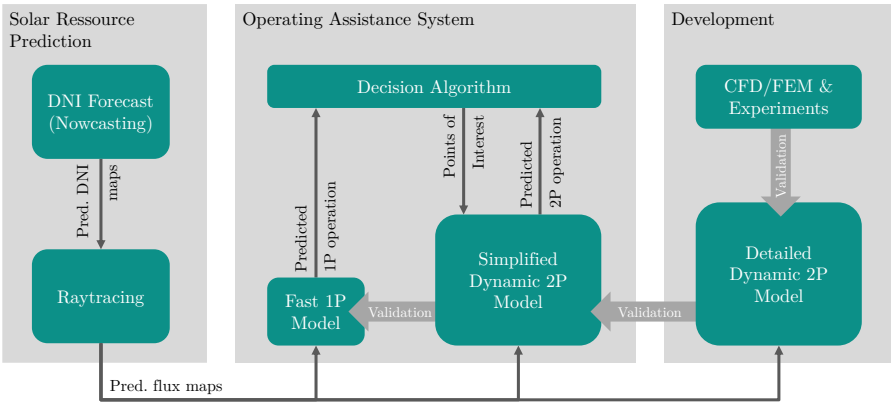

Figure 2-2: Principal implementation of the model-predictive proposal mode

The OAS consists of three main components. The decision algorithm, which is implemented in the universal programming language Python, utilizes two reduced Modelica models, which are simulated in Dymola. A standard Dymola-Python interface it applied for this. The fast 1P model (compare Section 3.4) is a thermal model with only a few differential equations to predict net yield during uninterrupted operation. It is triggered first and can simulate an entire day in a few seconds. Based on those results, the decision algorithm determines the optimal time for a shutdown and triggers a designated simulation of interrupted operation with a simplified dynamic 2P model. This is a simplified version of the detailed dynamic 2P model and therefore describes the 2P behavior during the transitions. After both simulations, the decision algorithm compares the integrated net yield of both simulations. If the predicted gain due to interrupting the operation is higher than its uncertainty (compare Section 5.2), the OAS proposes this maneuver to the operator.

2.2 Input Data and Scenarios

As described before, the heliostat field simulation done by raytracing is not considered part of the OAS but preprocessing instead. The input data of the

prediction model contain the flux density distributions on the receiver. Three exemplary flux density distributions are plotted in Figure 2-3, each with 25 vertical and 34 circumferential elements. The columns of each plot start from the north-facing side of the cylindrical receiver in the anti-clockwise direction.

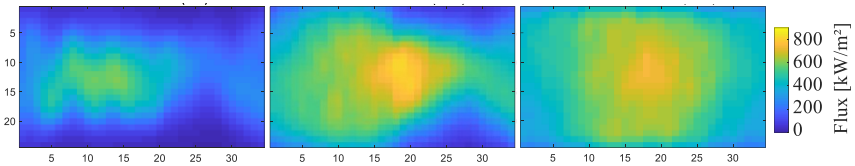

Figure 2-3: Flux density distributions at 07:00 (left), 09:00 (center) and 12:00 (right)

It can be observed that the heliostats mostly aim at the center early in the morning to minimize spillage losses. The vertical aim point offsets are relatively small and correlate with the HTF flow direction resulting in a wavy pattern. Later, in some areas, the flux density reaches the allowable limit. Therefore, the vertical aiming offsets are increased to achieve a more uniform flux density distribution. This happens on the west-facing side earlier since, in the morning, the eastern part of the heliostat field has lower efficiency (higher cosine losses). At noon, the entire receiver has a more uniform flux density distribution with even lower peak flux than during the late morning. This is because there is more solar radiation available than the receiver is capable of, so higher spillage losses are accepted. Hence, more heliostats aim at the outer parts of the receiver and less flux radiates onto the center.

The data are transferred into each model through a format in which this flux density matrix for each time step is flattened into a single column. This also allows for a two-dimensional visualization of this time series as plotted in Figure 2-4 (top). Basically, for each time step, all discrete elements (pixels) of the flux density matrix are stacked into one single column. Starting from the top with the first column of the flux density matrix and following down in the plot corresponds to running counterclockwise around the receiver. Thus, the west-facing receiver half (flow path 1) is shown in the upper half

and the east-facing side in the lower half of the plot. Accordingly, each column of this time series matrix resembles a time step. This visualization also allows observing how the area of the highest flux density moves from west to east throughout one day. The horizontal lines result from lower flux density in the top and bottom areas of each panel. For improved clarity, those lines can be eliminated by plotting the normalized flux density relative to clear-sky flux density, respectively, the clear-sky ratio (CSI), which is done in the bottom plot. This plotting method reveals the impact of local shading on the flux density distribution. For instance, the direction in which the shadows are tilted indicates that the clouds in this scenario move from south to north.

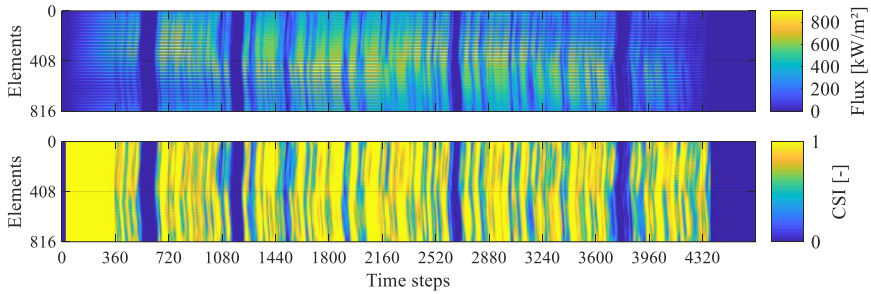

Figure 2-4: Flattened flux density distributions over time; absolute flux density(top) and CSI (bottom)

The time step sizes of the flux density input and the prediction models are independent. The first is usually between 10 and 30 s. Between that, the prediction model performs linear interpolation to avoid additional (unrealistic) transients. The time step size of the prediction models is dynamically adjusted by the solver.

This OAS shall be provided with data from a suitable nowcasting system in the future. The requirements for that are analyzed and discussed in Section 5.2. This work considers three different types of scenarios for testing and validating the different components. Scenarios based on artificial cloud shapes moving across the heliostat field are considered to allow for scenarios

with various cloud characteristics, such as velocity and direction of movement, average cloud coverage, cloud size and variability. Those scenarios are given in the Appendix (section B.1). Furthermore, DNI maps from an ASI-based nowcasting system (Nouri et al. 2022) are applied to the OAS. Apart from the uncertainty analysis in Section 5.2.1, only non-forecasted data (lead time zero) are included in the test scenarios and can be considered measurement data. A selection of the ASI-based scenarios used in this work is given in the Appendix in Section B.2.

In both scenario types, shadow maps are calculated with Matlab scripts and applied to the raytracing simulation, meaning that individual heliostats are deactivated if located in the shaded areas. To account for partial shading (especially at the blurry edges of clouds), the shading map values are clear-sky-discretely randomized. Each heliostat is randomly assigned to a shaded or unshaded state with a probability equal to the CSI of the corresponding DNI map pixel. An exemplary DNI map and the resulting shading map are given in Figure 2-5.

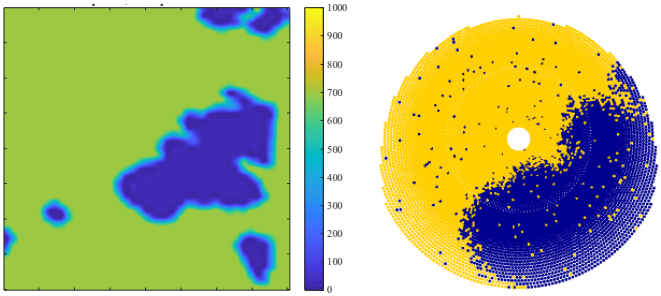

Figure 2-5: DNI map (left) and corresponding heliostat field shading map (right)

Additionally, this work considers designed scenarios for specific testing and validation purposes. They are not based on any spatial shading but on a clear-sky scenario instead. Some stepwise shadings are applied to the flux density distribution homogeneously (across the entire receiver surface), as shown in the Appendix in Section B.3.

3 Modeling

The OAS requires a realistic but numerically efficient representation of the physical receiver system. According to the conceptualized assistance function in Chapter 2, it requires a "real-time-capable" 2P model and a much faster 1P model. As a modeling basis and for testing or developing a feasible operating strategy, a detailed dynamic 2P model of the receiver system, including the storage system, is implemented in the modeling and simulation environment Dymola (compare Section 3.2). Based on this and the findings from simulating this detailed model, a simplified dynamic 2P model (see Section 3.3) is derived for predicting interrupted operation within the OAS. For a more efficient prediction of continuous operation, a fast 1P model (see Section 3.4) is developed with a pseudo-zero-dimensional modeling approach for the receiver panels/passes. Lastly, a more drastic model reduction is conducted and tested, trying to mimic the dynamic behavior of the receiver with only a second-order delay function (scalar 1P model in Section 3.5).

Moreover, the detailed dynamic 2P model is validated by data from high-resolution CFD simulations as well as experimental data (see Section 3.6). Subsequently, the reduced models are validated by the detailed dynamic 2P model (see Section 3.7). All presented models (except validation cases) are parametrized according to a commercial scale reference plant as specified in the following.

3.1 Reference Plant

In the research project DynaSalt-2 a reference plant was defined in collaboration between the Solar Institute Juelich (SIJ), the German Aerospace Center (DLR) and the CSP technology developer and operator General Electric (GE). The plant site is set to the location of the formerly planned Redstone Thermal Power Plant (ACWA POWER 2021) at 28.298 °S and 23.366 °E.

For simplification, the longitude is neglected. Instead, this work considers simulation time as solar time.

The main design parameters of the reference plant are given in Table 3-1. The thermal power of the receiver is rated at 650 MW_{th} using a mixture of 60 % $NaNO_3$ and 40 % KNO_3, also known as Solar Salt (Zavoico 2001), as a heat transfer fluid (HTF) and storage medium. The receiver design developed by General Electric poses an external cylindrical receiver aligned with vertical absorber tube, which are organized in parallel panels as presented by Das et al. (2015). An inlet vessel and an outlet vessel act as buffers providing flexibility. The inlet vessel is pressurized with controlled in and outflow of service air, while the molten salt level is controlled by adjusting the pumps' speed. The outlet vessel is vented to the atmosphere and a control valve at the bottom end of the downcomer line controls the molten salt level. The receiver is subdivided into two parallel flow paths (west and east receiver half, no cross-over). The mass flow rates are individually adjustable to control both outlet temperatures analog to the final control algorithm of the Solar Two test plant (Pacheco et al. 2002). More details about the system layout are given in Section 3.2.6 and the process control system and the considered operating strategy are described in Section 3.2.7.

Table 3-1: Design parameters of the reference plant

Parameter	Value	Unit
Design point	March 21, 12:00 pm solar time	
Thermal receiver output	650	MW_{th}
Lower HTF temperature (cold tank)	290	°C
Upper HTF temperature (rec. outlet)	565	°C
HTF mass flow rate	1,559	Kg/s
Receiver area (absorbing)	~1400	m^2
Inlet vessel pressure	15	barg
Outlet vessel pressure	0	barg
Tower height (receiver center)	191	m
Heliostat reflective area	121	m^2
Heliostat field reflective area	1,335,000	m^2
Flux density on Receiver (mean/max)	~500/~750	kW/m^2
Thermal storage capacity	10	vlh_{PB}

The heliostat field consists of 11,033 heliostats of the Sanlúcar 120 type (Osuna et al. 2006). The effective mirror reflectivity, including cleanliness, is assumed to be approx. 90 %. The field layout, which is illustrated in Figure 3-1, is yield optimized for this site using the DLR tool HFLCAL (Schwarzbözl et al. 2009). The aim point configuration depends on the sun's position and is optimized for maximal thermal output constraint by allowable flux limits and film temperature limits using an aiming optimization algorithm by Flesch et al. (2017).

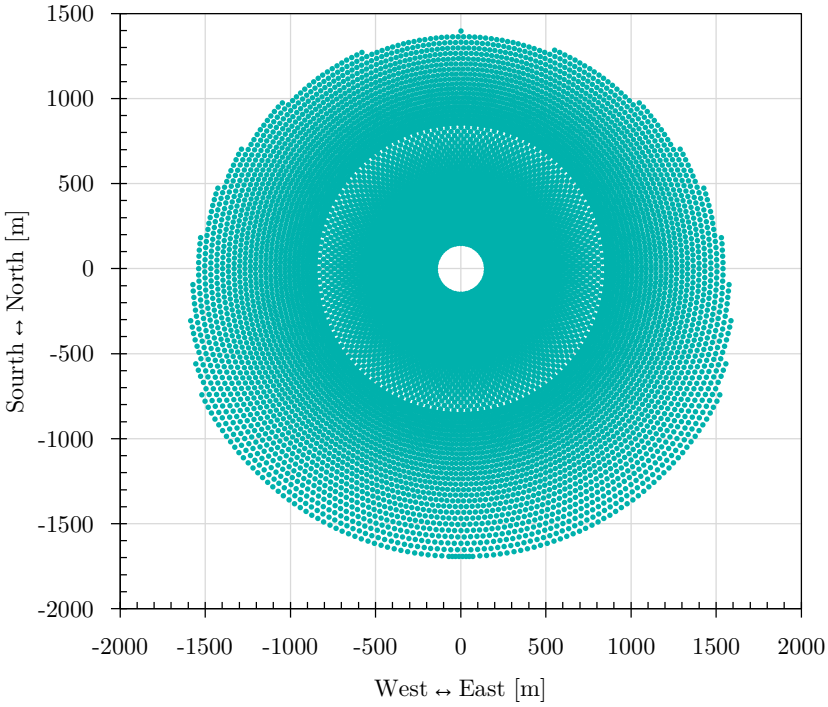

Figure 3-1: Heliostat field layout

Furthermore, the considered operational limits are summarized in Table 3-2. The lower temperature limit prevents freezing in cold spots of the system and the upper temperature limit minimizes the molten salt's degradation. The minimal mass flow rates are derived from the requirement of turbulent flow in the receiver tubes and the lower part load limit for one of the multiple redundant receiver pumps. If the receiver mass flow rate – more precisely, the one in the riser – drops below the minimum mass flow rate of the pumps, a portion of the HTF flow returns through a bypass back into the tank.

Table 3-2: Operational limits

Parameter	Value	Unit
Lower HTF temperature limit	260	°C
Upper HTF (bulk/film) temperature limits:		
- Steady-state	580 / 600	°C
- Transient max. 5 min	602 / 616	°C
Max. bulk temperature transient	20	K/min
Min. receiver mass flow rate	10	%
Min. pumps mass flow rate (before bypass)	20	%

3.2 Detailed Dynamic 2P Model

To analyze the transient operation of an MST and as a basis for the reduced models used in the OAS, a detailed one-dimensional model of the whole receiver system, including the storage system, is implemented in the simulation environment Dymola.

General basic information about molten salt receiver designs and receiver system layouts is available in the literature (Zavoico 2001; Kolb 2011; Rodriguez-Sanchez et al. 2015; Das et al. 2015) as well as concepts for operating such a system (Pacheco et al. 2002; Burgaleta et al. 2012; Relloso and García 2015; Relloso and Gutiérrez 2016).

The following simulation model complies with the above-described reference plant (section 3.1) and is illustrated in Figure 3-2, which shows the first modeling level of the whole physical system and the second modeling level of the receiver (flow path 1 and 2).

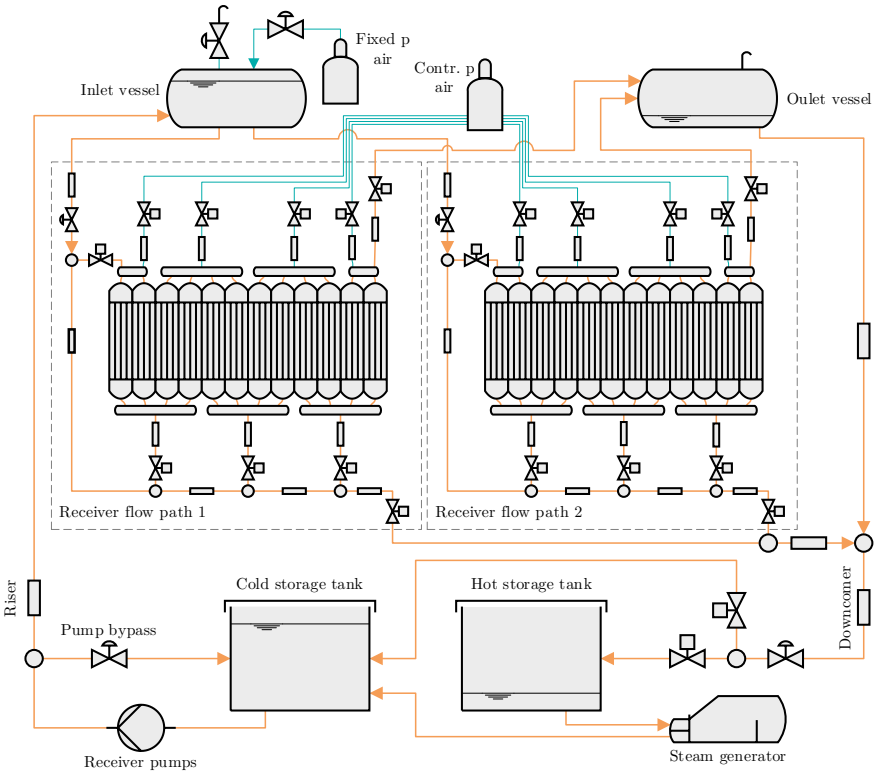

Figure 3-2: First and second modeling levels of the thermohydraulic model

Starting at the cold storage tank, the receiver pumps feed the molten salt up through the riser into the inlet vessel. Parallel to the pumps, a controlled bypass enables a minimum flow rate through the pumps even during lower flow rate demand. The inlet vessel is pressure-controlled by two control valves, which either add air from a fixed pressure source or bleed air out to an ambient pressure sink. The level is controlled by the incoming mass flow rate, respectively, the pumping flow rate. From there, the flow splits into two identical flow paths (compare Figure 3-2) in which a serpentine flow is established during normal operation. The outlet ports of the flow paths lead into the outlet vessel, which directly connects to an ambient pressure boundary. The two HTF flows mix in this vessel and exit into the downcomer line.

At the bottom of the downcomer line, a control valve manipulates the mass flow rate to control the outlet vessel level. Finally, two isolation valves direct the exiting flow either into the hot storage tank or back into the cold storage tank, depending on the bulk temperature at this location. Furthermore, the steam generator (SG) takes HTF out of the hot storage tank and returns it back into the cold storage tank at a fixed return temperature.

As illustrated in Figure 3-2, each receiver flow path includes a complex piping subsystem that realistically describes a commercial-size receiver during flooding and draining transitions. In addition to discretized absorber tubes aggregated in receiver panels and connected through manifolds, each flow path includes drain and vent lines connected to the lower and upper manifolds. Another main drain line also acts as a bypass during transitions, allowing HTF flow directly from the inlet vessel into the downcomer line. Numerous isolation and control valves are considered to realize the different flow patterns, as further described in 3.2.5.

Furthermore, the heliostat field control and a process control system (PCS) are modeled (not shown in Figure 3-2) using linear controllers combined with local conditions and state-machine algorithms to simulate fully automated operations with all relevant transitions during startup, shutdown and production.

More details about the different sub models and the utilized medium and flow model are given in the following sections.

3.2.1 2P Flow model

The 2P flow modeling was developed in collaboration with Robert Flesch and has already been published by Schwager et al. (2022). In general, 2P modeling poses a challenging task. Solving the Navier-Stokes equations for both phases in all details is hardly manageable for today's computers. Brennen (2005) describes the task of solving turbulent two-phase flow as "astronomical".

Hence, certain simplifications are applied to the Navier-Stokes Equations depending on the application and the model's regime. This section presents simplifications suitable for a one-dimensional thermo-hydraulic tube flow model for solar receivers with vertical tubes, which are operated with a liquid and a gas phase. In this case, it is justified to consider the liquid and gas phases in a separated flow, which simplifies the problem compared to a disperse flow.

In this sense, ϕ is introduced as the volume fraction and ξ as the mass fraction of the respective phase. Consequently, for the liquid (molten salt) and gas (air) phases, this leads to

$$\phi_\mathrm{L} + \phi_\mathrm{G} = 1 \tag{3.1}$$

and

$$\xi_\mathrm{L} + \xi_\mathrm{G} = 1 \tag{3.2}$$

To derive one from the other, the following equations apply:

$$\phi_\mathrm{L} = \frac{\frac{\xi_\mathrm{L}}{\rho_\mathrm{L}}}{\frac{\xi_\mathrm{L}}{\rho_\mathrm{L}} + \frac{\xi_\mathrm{G}}{\rho_\mathrm{G}}} \tag{3.3}$$

$$\phi_\mathrm{G} = \frac{\frac{\xi_\mathrm{G}}{\rho_\mathrm{G}}}{\frac{\xi_\mathrm{L}}{\rho_\mathrm{L}} + \frac{\xi_\mathrm{G}}{\rho_\mathrm{G}}} \tag{3.4}$$

$$\xi_\mathrm{L} = \frac{\phi_\mathrm{L}\rho_\mathrm{L}}{\phi_\mathrm{L}\rho_\mathrm{L} + \phi_\mathrm{G}\rho_\mathrm{G}} \tag{3.5}$$

$$\xi_\mathrm{G} = \frac{\phi_\mathrm{G}\rho_\mathrm{G}}{\phi_\mathrm{L}\rho_\mathrm{L} + \phi_\mathrm{G}\rho_\mathrm{G}} \tag{3.6}$$

with the pure substance densities ρ_L and ρ_G.

Often, in system modeling approaches, we use a one-dimensional modeling approach. The 2P modeling approaches can be categorized by the level of detail in which the flow fields of the two phases are resolved: In the case of a two-fluid model, the field variables of velocity and temperature locally differ, resulting in six partial differential equations. Further, closing approximations for impulse exchange and heat transfer between the phases are required (Scheuerer and Scheuerer 1992; Vij and Dunn 1996; Masella et al. 1998; Bauer 1999; Issa and Kempf 2003; Brennen 2005; Akselsen 2012; Hoffmann et al. 2014).

However, in vertical receiver tubes, we can assume locally identical velocities and temperatures of the phases and thus eliminate two differential equations. This leads to a pseudo-homogeneous model, in which the flow is treated like the flow of a single phase (Francke 2014; van Zwieten et al. 2015). The assumption of the identical velocity would not be valid for sections with horizontal flow. However, a detailed representation of the 2P flow is only necessary for the vertical absorber tubes of the receiver. All non-vertical sections in the considered system are slightly angled for drainability, so the separation of liquid and gas is still given. Only the further described heat transfer modeling is not valid in these components. However, since these pipes are insulated and electrically heat-traced, the convective heat transfer is irrelevant. Another limitation of this approach is that if individual tubes are filled quicker or earlier than others and HTF spills over from one tube into another, it would lead to invalid results. Nevertheless, this should be avoided by design and proper operation. In an event like that, the problem could be identified with this simulation model, knowing that local temperature values at this moment would not be applicable.

Accordingly, the homogenous model includes three joint differential equations for the conservation of mass, momentum and energy

$$\frac{\partial}{\partial t}(\rho) + \frac{\partial}{\partial x}(\rho u) = 0 \tag{3.7}$$

$$A\rho\frac{\partial}{\partial t}(u) + A\rho u\frac{\partial}{\partial x}(u) = A\rho g_{|} - A\frac{\partial}{\partial x}(p) + F'_{\mathrm{W}} \tag{3.8}$$

$$A\frac{\partial}{\partial t}(\rho h) + \frac{\partial}{\partial x}(\rho u h A) = \dot{Q}'_{\mathrm{W}} \tag{3.9}$$

plus one additional continuity equation for the liquid phase

$$A\frac{\partial}{\partial t}(\phi_{\mathrm{L}}\rho_{\mathrm{L}}) + \frac{\partial}{\partial x}(\phi_{\mathrm{L}}\rho_{\mathrm{L}}u_{\mathrm{L}}A) = 0. \tag{3.10}$$

All substance properties are determined from a mixture of pure substance properties.

Since the time scales on which the flow adapts to pressure changes are much shorter than those of the considered heat transfer, the flow does not need to be simulated fully dynamically. Hence, the time derivative and the convective term in equation (3.8) can be neglected, resulting in

$$A\frac{\partial}{\partial x}(p) = \xi_{\mathrm{L}}A\rho g_{|} + F'_{\mathrm{W}}. \tag{3.11}$$

With this simplification, it is unnecessary to solve the total mass balance (3.7) as it is only relevant to resolve local velocity gradients. It only stays for numerical purposes. The component mass balance (3.10) is solved to get the receiver filling level, while the energy equation (3.9) provides the fluid temperature. However, to avoid rapid changes in equation (3.7) during filling, the density is kept nearly independent from the composition (see. Section 3.2.2). In order to account for the different gravitational forces on liquid and gas, the mass fraction of the liquid ξ_{L} has been added to the geodetic term in equation (3.11) effectively switching it off if an element is empty.

Regarding the thermal significance of air inside the absorber tubes (with rel. wall thickness $\Delta r/d_{\mathrm{i}} \approx 1/20$), there are three orders of magnitude between the absolute heat capacity of the tube wall and the air volume inside the tube. Consequently, the influence of stagnant air on the wall temperature is negligible.

3.2.2 2P Medium model

With respect to the flow model mentioned above and the associated assumption that the composition has nearly no effect on the density, the differences between volume fraction and mass fraction disappear. Therefore, the substance properties are all defined as a function of temperature T, pressure p and the composition ξ_L. The density is defined as

$$\rho = (1 + (p - p_\mathrm{ref})(\kappa_\mathrm{L}\xi_\mathrm{L} + \kappa_\mathrm{G}\xi_\mathrm{G}) - (T - T_\mathrm{ref})\beta_\mathrm{L})\rho_\mathrm{ref} \tag{3.12}$$

with an artificial compressibility κ_G, which on the one hand, improves numerical stability and on the other hand, still guarantees a solution. The artificial heat capacity of the gas is adjusted so that $\rho c_{\mathrm{p,G}}$ is in the order of magnitude of the real value of air. The isothermal compressibility of the gas poses a trade-off between the requirement that the density should not change too much (because of the assumption $\xi_\mathrm{L} = \phi_\mathrm{L}$) and the numerical stability/performance, since compressible media perform better in Dymola than incompressible media. Furthermore, the specific enthalpy can be described as

$$h = h_\mathrm{ref} + (T - T_\mathrm{ref}) \cdot \left(c_{\mathrm{p,L}} \cdot \xi_\mathrm{L} + c_{\mathrm{p,G}} \cdot \xi_\mathrm{G}\right). \tag{3.13}$$

As shown, the dependency on pressure is neglected. In such a system, the temperature rise due to adiabatic throttling is usually less than 1 K, which justifies this approximation. This also implies that $u = h$. Moreover, since the specific heat capacity of the molten salt varies by only 1.5 % between 290 °C to 565 °C, it is considered constant. Finally, the physical properties are modeled as follows:

$$\lambda = 0.443 + 0.00019 \frac{\mathrm{W}}{\mathrm{m\,K^2}} \cdot \theta \tag{3.14}$$

for the thermal conductivity λ and

$$\begin{aligned} \mu = 10^{-3} \cdot \big[&22.714 + \theta \\ &\cdot \left(-0.12 + \theta \right. \\ &\left. \cdot \left(2.281 \cdot 10^{-4} + \theta \cdot (-1.474) \cdot 10^{-7}\right)\right)\big] \end{aligned} \tag{3.15}$$

for the dynamic viscosity μ using $\theta = (T - 273.15\,\mathrm{K})$ as the temperature value in °C. The assumed values for the mentioned properties are listed in Figure 3-3 and Table 3-3 illustrates the HTF's modeled fluid properties compared to literature data (Zavoico 2001).

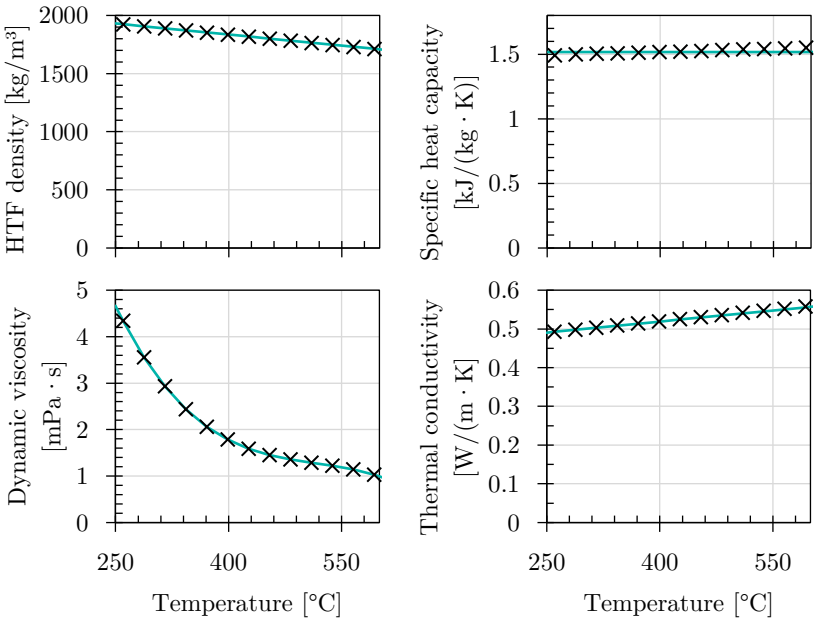

Figure 3-3: Plots of the modeled molten salt density, dynamic viscosity, specific heat capacity and thermal conductivity versus literature data (Zavoico 2001)

Table 3-3: Assumed properties for the 2P medium of molten salt and air

Reference density	ρ_{ref}	1,949.44 $\mathrm{m^3/kg}$
Reference enthalpy	h_{ref}	104,929 J/kg
Specific heat capacity of liquid	$c_{\mathrm{p,L}}$	1,516.53 J/(kgK)
Artificial specific heat capacity of gas	$c_{\mathrm{p,G}}$	1 J/(kgK)
Isothermal compressibility of the liquid	κ_{L}	$1 \cdot 10^{-10}$ 1/Pa
Isothermal compressibility of the gas	κ_{G}	$1 \cdot 10^{-7}$ 1/Pa
Thermal expansion coefficient	β_{L}	3.26247 · 10-4 1/K

3.2.3 Absorber tube model

3.2.3.1 Tube wall

The transient heat conduction in a cylindrical body can be described by this partial differential equation (Martin 2013):

$$\frac{\rho c_{\mathrm{p}}}{\lambda}\frac{\partial T}{\partial t} = \frac{1}{r}\frac{\partial}{\partial r}\left(r\frac{\partial T}{\partial r}\right) + \frac{1}{r^2}\frac{\partial^2 T}{\partial \varphi^2} + \frac{\partial^2 T}{\partial z^2} \tag{3.16}$$

with cylinder coordinates r, φ and z. Analog to the modeling approach previously used by Flesch et al. (2016), the absorber tube wall is discretized into an adjustable number of elements in the direction of flow, which are circumferentially discretized into a front and a back shell. Further radial discretization is represented by three temperatures (compare Figure 3-4). The outer and inner surface temperature $T_{\mathrm{O},j}$ and $T_{\mathrm{I},j}$ are determined by the respective boundary conditions. The core temperature $T_{\mathrm{C},j}$ is defined by a time differential considering the heat capacity of the wall. Based on this and equation (3.16) the core temperature $T_{\mathrm{C},j}$ can be derived from

$$V_j \rho c_\mathrm{p} \frac{\partial T_{\mathrm{C},j}}{\partial t} = \pi \cdot \Delta z \cdot \lambda \cdot \frac{T_{\mathrm{O},j} - T_{\mathrm{C},j}}{\ln\left(\frac{d_\mathrm{O}}{d_\mathrm{C}}\right)} - \pi \cdot \Delta z \cdot \lambda \cdot \frac{T_{\mathrm{C},j} - T_{\mathrm{I},j}}{\ln\left(\frac{d_\mathrm{C}}{d_\mathrm{I}}\right)} + A_\mathrm{FB} \cdot \frac{\lambda}{r_\mathrm{C}} \cdot \frac{\left(T_{\mathrm{FB},j} - T_{\mathrm{C},j}\right)}{\pi} + A_\mathrm{Q} \cdot \lambda \cdot \frac{T_{\mathrm{C},j+1} - T_{\mathrm{C},j}}{\Delta z} - A_\mathrm{Q} \cdot \lambda \cdot \frac{T_{\mathrm{C},j} - T_{\mathrm{C},j-1}}{\Delta z} \tag{3.17}$$

with the volume of the discrete half shell of element j (vertical discretization)

$$V_j = A_\mathrm{Q} \cdot \Delta z = \frac{1}{2} \cdot \frac{\pi (d_\mathrm{O}^2 - d_\mathrm{I}^2)}{4} \cdot \Delta z \tag{3.18}$$

and the contact area between the front and back shell

$$A_\mathrm{FB} = (d_\mathrm{O} - d_\mathrm{I}) \cdot \Delta z. \tag{3.19}$$

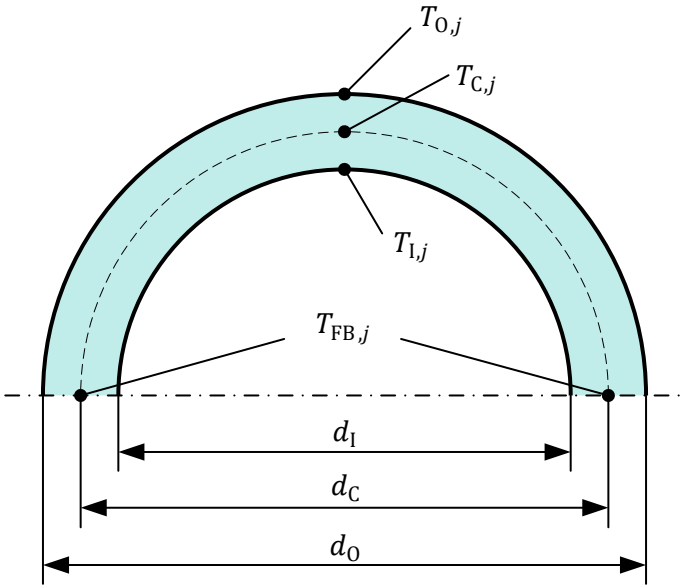

Figure 3-4: Discrete temperatures of a tube shell element

Moreover, the boundary conditions for the outer surface temperatures of the front shell $T_{\mathrm{F,O},j}$ follow as

$$\dot{Q}_{\mathrm{abs},j} - \dot{Q}_{\mathrm{rad},j}\left(T_{\mathrm{O},j}\right) - \dot{Q}_{\mathrm{conv},j}\left(T_{\mathrm{F,O},j}\right) = \pi \cdot \Delta z \cdot \lambda \cdot \frac{T_{\mathrm{F,O},j} - T_{\mathrm{F,C},j}}{\ln\left(\frac{d_{\mathrm{O}}}{d_{\mathrm{C}}}\right)}, \tag{3.20}$$

whereas the corresponding equation for the back shell can be set to zero, considering that heat losses through the backside of the tube can be neglected due to adequate insulation. For the inner surface (film) temperature, the following equation applies for both the front and back shell:

$$\pi \cdot \Delta z \cdot \lambda \cdot \frac{T_{\mathrm{C},j} - T_{\mathrm{I},j}}{\ln\left(\frac{d_{\mathrm{C}}}{d_{\mathrm{I}}}\right)} = \dot{Q}_{\mathrm{fluid},j}(T_{\mathrm{I},j}) \tag{3.21}$$

To further simplify the tube wall model, the heat flow rates in the tube wall are compared with each other. Based on typical temperature gradients, the dominant heat flow, which is in the radial direction through the front shell, lies in the order of 10^4 W, while the thermal conduction in (vertical) flow direction is approximately 10^{-2} W and can consequently be neglected. The heat flow between the front and back shell reaches approximately 10^2 W during normal operation and is therefore less significant as well. However, when the empty tubes are preheated (during startup), the flux density is much lower and the convective heat flow into the fluid (air) is nearly zero so that the front-to-back heat flow becomes dominant (essential mechanism for preheating the whole tube). Besides, the designated temperature sensors are installed on the backside of the absorber tubes. In this case, the vertical gradients are even smaller than during normal operation, so that the vertical heat flow is still insignificant. Consequently, equation (3.17) is reduced to

$$\begin{aligned} V_j \rho c_{\mathrm{p}} \frac{\partial T_{\mathrm{F,C},j}}{\partial t} = {} & \pi \cdot \Delta z \cdot \lambda \cdot \frac{T_{\mathrm{F,O},j} - T_{\mathrm{F,C},j}}{\ln\left(\frac{d_{\mathrm{O}}}{d_{\mathrm{C}}}\right)} - \pi \cdot \Delta z \cdot \lambda \cdot \frac{T_{\mathrm{F,C},j} - T_{\mathrm{F,I},j}}{\ln\left(\frac{d_{\mathrm{O}}}{d_{\mathrm{C}}}\right)} \\ & + A_{\mathrm{FB}} \cdot \frac{\lambda}{r_{\mathrm{C}}} \cdot \frac{\left(T_{\mathrm{FB},j} - T_{\mathrm{F,C},j}\right)}{\pi} \end{aligned} \tag{3.22}$$

for the front shell and

$$V_j \rho c_\mathrm{p} \frac{\partial T_{\mathrm{B,C},j}}{\partial t} = -\pi \cdot \Delta z \cdot \lambda \cdot \frac{T_{\mathrm{B,C},j} - T_{\mathrm{B,I},j}}{\ln\left(\frac{d_\mathrm{c}}{d_\mathrm{i}}\right)} + A_\mathrm{FB} \cdot \frac{\lambda}{r_\mathrm{c}} \cdot \frac{\left(T_{\mathrm{FB},j} - T_{\mathrm{B,C},j}\right)}{\pi} \qquad (3.23)$$

for the back shell while applying the same boundary conditions as above.

3.2.3.2 Crown temperatures

The above-described approach for the receiver tubes only considers two average temperatures (front and back) along the circumference of the absorber tube. In reality, the nearly parallel radiation from the heliostat field is perpendicular to the tube surface only at the crown, whereas the incident angle and therefore the local flux density decreases towards the sides. As a result, the temperature distribution in the front element is highly inhomogeneous. The calculated mean temperature cannot reflect this circumferential profile and is only valid for the energy balance of each element. The maximum temperature at the pipe crown is of particular interest regarding operational limits. Instead of increasing the number of circumferential discrete elements, which would drastically increase the complexity and therefore compromise the computational performance of the model, a different approach is implemented, posing only a few additional algebraic equations.

Flesch et al. (2017) proposed the following: since at the crown of the absorber tube, the temperature gradient $\partial T/\partial \varphi \approx 0$ due to symmetry, the circumferential heat flow in this point is neglected, resulting in two algebraic equations for the associated outer and inner surface temperatures $T_{\mathrm{Cr,O},j}$ and $T_{\mathrm{Cr,I},j}$. However, the circumferential heat flow actually correlates to $\partial^2 T/\partial \varphi^2$, which is less than zero and can be significant – especially at low mass flow rates.

Therefore, an improved approach is based on an (in circumferential direction) infinitely small sub-element at the crown, as shown in Figure 3-5. Its radial and axial extend is the same as the discrete half-shell element of the tube model. A steady state energy balance for this segment is described as

$$0 = \frac{T_{\mathrm{Cr,O},j} - T_{\mathrm{Cr,C},j}}{\ln\left(\frac{d_\mathrm{O}}{d_\mathrm{C}}\right)} - \frac{T_{\mathrm{Cr,C},j} - T_{\mathrm{Cr,I},j}}{\ln\left(\frac{d_\mathrm{C}}{d_\mathrm{I}}\right)} + \frac{2\Delta r}{d_\mathrm{C}} \frac{\partial^2 T}{\partial \varphi^2}\bigg|_{\varphi=0} \tag{3.24}$$

with three additional temperatures $T_{\mathrm{Cr,O},j}$, $T_{\mathrm{Cr,C},j}$ and $T_{\mathrm{Cr,I},j}$ at the crown.

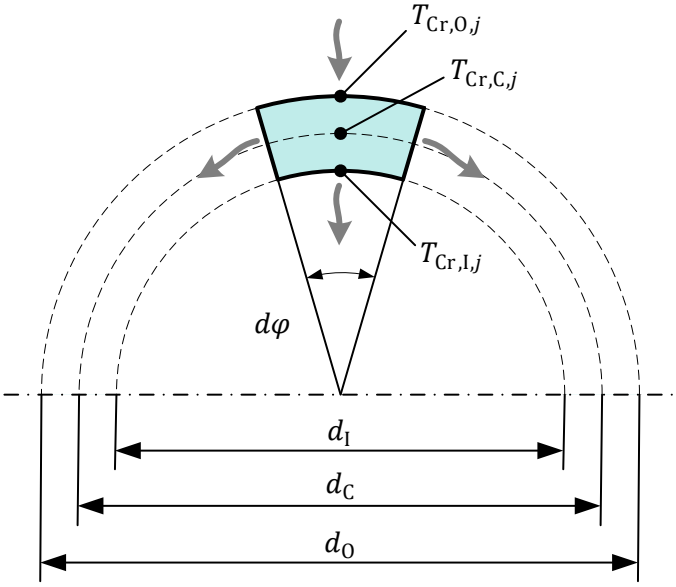

Figure 3-5: Infinitely small tube wall element with crown temperatures

In addition to equation (3.24), the outer surface boundary condition is

$$\lambda \frac{T_{\mathrm{Cr,O},j} - T_{\mathrm{Cr,C},j}}{\ln\left(\frac{d_\mathrm{O}}{d_\mathrm{C}}\right)} = \frac{d_\mathrm{O}}{2} \cdot \left(\dot{q}''_{\mathrm{abs},j} - \dot{q}''_{\mathrm{rad},j}\left(T_{\mathrm{Cr,O},j}\right) - \dot{q}''_{\mathrm{conv},j}\left(T_{\mathrm{Cr,O},j}\right)\right) \tag{3.25}$$

and the absorbed flux density (area-specific heat flow rate)

$$\dot{q}''_{\mathrm{abs},j} = \alpha \cdot \dot{q}''_{\mathrm{flux},j} \tag{3.26}$$

without any view factor since this infinitely small segment only sees the ambient. Accordingly, the radiation losses are determined by

$$\dot{q}''_{\mathrm{rad},j} = \varepsilon \cdot \sigma \cdot \left({T_{\mathrm{Cr,O},j}}^4 - {T_\infty}^4 \right) \tag{3.27}$$

and convective heat losses by

$$\dot{q}''_{\mathrm{conv},j} = \alpha_{\mathrm{conv,O}} \cdot \left(T_{\mathrm{Cr,O},j} - T_\infty \right). \tag{3.28}$$

Moreover, the inner surface boundary condition follows

$$\lambda \frac{T_{\mathrm{Cr,C},j} - T_{\mathrm{Cr,I},j}}{\ln\left(\frac{d_\mathrm{C}}{d_\mathrm{I}}\right)} = \frac{d_\mathrm{I}}{2} \cdot \dot{q}''_{\mathrm{fluid},j}(T_{\mathrm{Cr,I},j}, T_{\mathrm{fluid},j}) \tag{3.29}$$

applying the same convective heat transfer coefficient $\alpha_{\mathrm{conv,I},j}$ as in equation (3.38).

The last unknown in equation (3.24) is $\partial^2 T / \partial \varphi^2$. To avoid introducing more differential equations, an approximation for $T(\varphi)$ is required. Since the tube is irradiated only perpendicular to the crown, the temperature profile is symmetric with a maximum point in the center ($\varphi = 0$) and progressive slopes to the edges. So, a parabola seems appropriate as a functional approach:

$$T_{\mathrm{F,C},j}(\varphi) = T_{\mathrm{Cr,C},j} + \left(T_{\mathrm{FB},j} - T_{\mathrm{Cr,C},j} \right) \left(\frac{2\varphi}{\pi} \right)^2 \tag{3.30}$$

$$\Rightarrow \left. \frac{\partial^2 T_{\mathrm{F,C},j}}{\partial \varphi^2} \right|_{\varphi=0} = \frac{8}{\pi^2} \left(T_{\mathrm{FB},j} - T_{\mathrm{Cr,C},j} \right) \approx 0.81 \cdot \left(T_{\mathrm{FB},j} - T_{\mathrm{Cr,C},j} \right) \tag{3.31}$$

Alternatively, with a cosine approach, the factor 0.81 would be 1.0 instead, resulting in a greater circumferential heat flow, hence lower crown temperature. Hence, the parabola function serves as a more conservative approach. Finally, the equations (3.24), (3.25) and (3.29) pose an equation system from which the three crown temperatures can be determined while the number of differential equations is kept low. The error by assuming a steady-state energy balance in (3.24) is negligible since the dynamics are well represented in the finite element model of the half shell. Making this equation transient would only be necessary if the circumferential temperature profile changes

significantly during operation. This is not expected since it only depends on the (fixed) geometry.

3.2.3.3 Internal radiation

In addition to thermal conduction in the tube wall, radiation exchange in the empty elements between the front and the back shell is considered. In the following, the inner surface area of the tube shell is labeled A_I and the projected area A_d. The front shell is indexed F and the back shell B. Accordingly, the surface brightness of the front shell's inner surfaces is

$$A_\mathrm{I} \cdot \dot{q}''_\mathrm{F} = \varepsilon A_\mathrm{I} \cdot \dot{q}''_{\mathrm{F},\sigma} + \rho A_\mathrm{I} \Phi_{\mathrm{F}\to\mathrm{F}} \cdot \dot{q}''_\mathrm{F} + \rho A_\mathrm{I} \Phi_{\mathrm{B}\to\mathrm{F}} \cdot \dot{q}''_\mathrm{B} \tag{3.32}$$

with the emitted radiation $\varepsilon A_\mathrm{I} \cdot \dot{q}''_{\mathrm{F},\sigma} = \varepsilon A_\mathrm{I} \cdot \sigma T^4_{\mathrm{F,I}}$, the reflection of the self-irradiation $\rho A_\mathrm{I} \Phi_{\mathrm{F}\to\mathrm{F}} \cdot \dot{q}''_\mathrm{F}$ and the reflection of the radiation coming from the back shell $\rho A_\mathrm{I} \Phi_{\mathrm{B}\to\mathrm{F}} \cdot \dot{q}''_\mathrm{B}$. In this context, the view factors can be derived as follows

$$\Phi_{\mathrm{F}\to\mathrm{d}} A_\mathrm{I} = \Phi_{\mathrm{d}\to\mathrm{F}} A_\mathrm{d} \;\;,\;\; \Phi_{\mathrm{d}\to\mathrm{F}} = 1 - \Phi_{\mathrm{d}\to\mathrm{d}} = 1 \tag{3.33}$$

$$\Rightarrow \Phi_{\mathrm{F}\to\mathrm{d}} = \frac{A_\mathrm{d}}{A_\mathrm{I}} = \frac{2}{\pi} = \Phi_{\mathrm{F}\to\mathrm{B}} = \Phi_{\mathrm{B}\to\mathrm{F}} \tag{3.34}$$

$$\Phi_{\mathrm{F}\to\mathrm{F}} = 1 - \Phi_{\mathrm{F}\to\mathrm{B}}. \tag{3.35}$$

Combining equation (3.32) with an analog equation for the back shell concludes to

$$\dot{q}''_\mathrm{F} = \frac{(1-\rho\Phi_{\mathrm{F}\to\mathrm{F}})\varepsilon \cdot \dot{q}''_{\mathrm{F},\sigma} + \rho\Phi_{\mathrm{F}\to\mathrm{B}}\varepsilon \cdot \dot{q}''_{\mathrm{B},\sigma}}{(1-\rho\Phi_{\mathrm{F}\to\mathrm{F}})^2 - (\rho\Phi_{\mathrm{F}\to\mathrm{B}})^2}. \tag{3.36}$$

Further, the net radiative heat exchange between front and back follows

$$\begin{aligned} \Delta\dot{Q}_{\mathrm{rad,FB}} &= A_\mathrm{I}\Phi_{\mathrm{F}\to\mathrm{B}}(\dot{q}''_\mathrm{F} - \dot{q}''_\mathrm{B}) \\ &= A_\mathrm{I}\big(\dot{q}''_{\mathrm{F},\sigma} - \dot{q}''_{\mathrm{B},\sigma}\big)\frac{(1-\rho\Phi_{\mathrm{F}\to\mathrm{F}})\varepsilon - \rho\Phi_{\mathrm{F}\to\mathrm{B}}\varepsilon}{(1-\rho\Phi_{\mathrm{F}\to\mathrm{F}})^2 - (\rho\Phi_{\mathrm{F}\to\mathrm{B}})} \end{aligned} \tag{3.37}$$

$$= A_{\mathrm{I}} \varepsilon \sigma \left(T_{\mathrm{F,I}}^4 - T_{\mathrm{B,I}}^4 \right) \frac{1}{\left(1 - \frac{4}{\pi}\right) \varepsilon + \frac{4}{\pi}}.$$

In addition, this radiative heat flow rate is set to zero when the tube is filled with molten salt with a linear transition proportional to the volume portion of air in each element. Even though the transmissivity of molten salt is greater than zero, this radiative heat exchange is then insignificant in comparison to the convective heat transfer between shell and fluid.

3.2.3.4 Heat transfer into the fluid

To complete equation (3.21), the heat transfer from an absorber tube half-shell element into the fluid is modeled as

$$\dot{Q}_{\mathrm{fluid},j}\left(T_{\mathrm{I},j}\right) = \alpha_{\mathrm{conv,I},j} \cdot \frac{\pi d_{\mathrm{I}}}{2} \Delta z \cdot \left(T_{\mathrm{I}} - T_{\mathrm{fluid},j}\right) \tag{3.38}$$

with the convective heat transfer coefficient derived from

$$Nu_{\mathrm{I},j} = \frac{\alpha_{\mathrm{conv,I},j} \cdot d_{\mathrm{I}}}{\lambda_j}. \tag{3.39}$$

For the Nusselt number, two different correlations for laminar and turbulent flow are implemented based on general correlations for a constant heat flux boundary (Gnielinski 2013a), which were confirmed by specific experiments with Solar Salt (Frantz et al. 2022b). The modified laminar Nusselt number follows

$$Nu_{\mathrm{lam},j} = \left((Nu_1)^3 + 1 + \left(Nu_{2,j} - 1\right)^3 + \left(Nu_{3,j}\right)^3 + \left(Nu_{\mathrm{fill},j}\right)^3 \right)^{1/3} \tag{3.40}$$

with

$$Nu_1 = 4.364 \tag{3.41}$$

$$Nu_{2,j} = 1.302 \cdot \left(Re_j \, Pr_j \, \frac{d_{\mathrm{I}}}{z_j} \right)^{1/3}. \tag{3.42}$$

$$Nu_{3,j} = 0.462 \cdot Pr^{1/3} \left(Re_j \ \frac{d_I}{z_j} \right)^{1/2}. \tag{3.43}$$

In addition, $Nu_{\text{fill},j}$ accounts for increased heat transfer during filling right below the rising liquid surface due to radial fluid flow (in the not yet developed flow). Based on the results from Flesch et al. (Flesch et al. 2016) it is modeled as follows

$$Nu_{\text{fill},j} = 0.822 \cdot \left(Re_j \, Pr_j \frac{d_I}{\Delta z^*} \right)^{0{,}434}, \tag{3.44}$$

where Δz^* represents the distance between the liquid surface and the center of the element j. However, this approach is only valid at a constant flow rate. In case of turbulent flow, the Nusselt number conventionally follows

$$Nu_{\text{turb},j} = \frac{\left(\xi_j^*/8\right) Re_j \, Pr_j}{1 + 12.7\sqrt{\xi_j^*/8}\left(Pr_j^{\,2/3} - 1\right)} \cdot \left(1 + \frac{1}{3} \cdot \left(\frac{d_I}{z_j} \right)^{2/3} \right) \tag{3.45}$$

with

$$\xi_j^* = \left(1.8 \cdot \log\left(Re_j\right) - 1.5\right)^{-2}. \tag{3.46}$$

In the range $Re_j = 2300 \ldots 10000$ the model performs a smooth transition between $Nu_{\text{lam},j}$ and $Nu_{\text{turb},j}$.

3.2.3.5 Heat input and losses

The absorbed heat flow $\dot{Q}_{\text{abs},j}$ in equation (3.20) is calculated according to

$$\dot{Q}_{\text{abs},j} = \alpha_{\text{abs}} \cdot d_O \cdot \Delta z \cdot \dot{q}''_{\text{flux}}. \tag{3.47}$$

The projected surface area of a tube serves as the effective area since the incidence of the concentrated solar flux can be assumed to be nearly parallel. This accounts for the reduction of the flux density on the edge of the tube due to the cosine effect.

For calculating radiative heat losses, the radiative heat exchange between adjacent tubes needs to be considered. The corresponding view factor can be determined by (Vortmeyer and Kabelac 2013):

$$\Phi_{\mathrm{O}\to\mathrm{adj}} = \frac{1}{\pi}\left[\pi + \sqrt{\left(2+\frac{2\Delta r}{d_\mathrm{o}}\right)^2 - 4} - \left(2+\frac{2\Delta r}{d_\mathrm{o}}\right) - 2\arccos\left(\frac{2}{2+\frac{2\Delta r}{d_\mathrm{o}}}\right)\right], \quad (3.48)$$

which for thin-walled tubes ($\Delta r \ll d_o$) is approximately $\Phi_{\mathrm{O}\to\mathrm{adj}} = 1 - \frac{2}{\pi}$. Assuming that the temperature differences between adjacent tubes are small and the absorptivity high, only the radiation into the ambient needs to be considered with the corresponding view factor

$$\Phi_{\mathrm{O}\to\infty} = 1 - \Phi_{\mathrm{O}\to\mathrm{adj}} = \frac{2}{\pi}. \quad (3.49)$$

Consequently, the radiative heat loss of a tube element can be modeled as

$$\dot{Q}_{\mathrm{rad},j}\left(T_{\mathrm{F,O},j}\right) = d_\mathrm{O}\cdot\Delta z\cdot\varepsilon\sigma\left(T_{\mathrm{F,O},j}^4 - T_\infty^4\right). \quad (3.50)$$

Moreover, the convective losses can be determined by

$$\dot{Q}_{\mathrm{conv},j}\left(T_{\mathrm{F,O},j}\right) = d_\mathrm{O}\cdot\Delta z\cdot\alpha_{\mathrm{conv,O}}\left(T_{\mathrm{F,O},j} - T_\infty\right). \quad (3.51)$$

Applying the actual surface area $\frac{\pi}{2} d_\mathrm{O}\Delta z$ would significantly overestimate the convective losses due to a cavity effect in the corner between two adjacent tubes. In this sense, an appropriate α_{conv} correlation for cross-flow cylinders (Gnielinski 2013b) can be used.

Generally, for high-temperature solar receivers, convective losses are significantly lower than radiative losses. However, convection is more relevant in the lower temperature range, especially during startup.

3.2.3.6 Implementation in Modelica

The above-described modeling approach is implemented in the modeling language Modelica using the commercial modeling and simulation environment Dymola (Dassault Systèmes 2021). The Modelica Standard Library includes

a pseudo-homogeneous two-phase medium model named `PartialMedium`, which is adapted in this work. The state of the medium is defined by pressure p, specific enthalpy h and composition ξ. Other properties such as temperature T, density ρ, dynamic viscosity μ, thermal conductivity λ and specific heat capacity c_p are derived from those according to the equations in Section 3.2.2.

For the **correlation between pressure drop and mass flow rate** in the absorber tube model, the class `PartialGenericPipeFlow` has been modified to account for the very different flow properties of the two phases, which can cause numerical issues. The total mass flow rate results from a combination of both phases

$$\dot{m}_j = \xi_{\mathrm{flow},j}\, \dot{m}_{\mathrm{L},j} + \left(1 - \xi_{\mathrm{flow},j}\right) \dot{m}_{\mathrm{G},j}, \tag{3.52}$$

which is understood as the mass flow rate from element j into the next element above $j+1$ (opposite direction if negative), as illustrated in Figure 3-6. Since in the applied staggered flow discretization, the volume elements of the medium model are offset compared to the states of the flow model, a conversion of the mass fraction is done as follows:

$$\xi_{\mathrm{flow},j} = \min\left\{max\left\{\xi_j - 0.5\,, 0\right\}\,, 0.5\right\} + \min\left\{max\left\{\xi_{j+1}\,, 0\right\}\,, 0.5\right\} \tag{3.53}$$

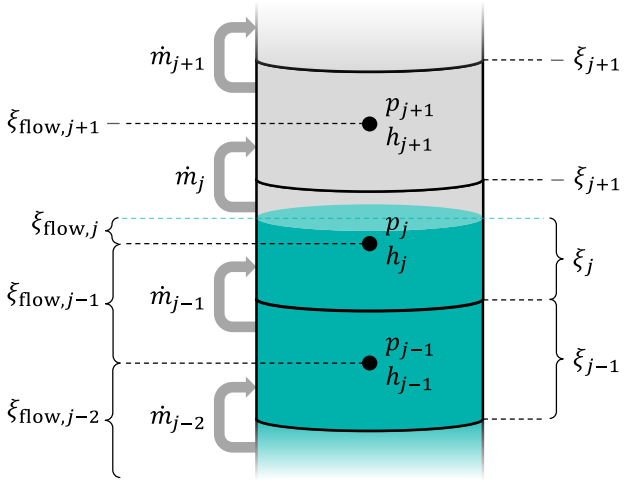

Figure 3-6: Schematic of the staggered flow discretization in the 2P flow model

During normal operation and even flood and drainage, the liquid component's hydraulic behavior dominates the flow rate in the absorber tubes. Therefore, the model is modified to primarily derive the pressure loss based on the molten salt flow. The mass flow portion of the gas phase (in an empty element) is defined by a straightforward equation

$$\dot{m}_{\mathrm{G},j} = \frac{\dot{m}_{\mathrm{n}}}{f_{\Delta p_{\mathrm{G}}} \cdot \Delta p_{\mathrm{n}}} \cdot \Delta p_j \tag{3.54}$$

with the pressure drop reduction factor $f_{\Delta p_{\mathrm{G}}} = 5 \cdot 10^{-4}$ making it easier for the solver (enhancing numerical performance) and insignificantly small so that it does not affect the results. Thus, there is no need to consider the geostatic pressure of the gas phase. The driving pressure difference follows:

$$\Delta p_j = \left(p_j - p_{j+1}\right). \tag{3.55}$$

In contrast, the dominant mass flow rate (liquid phase) is calculated according to the detailed pipe flow characteristic (…`WallFriction.Detailed`)

from the Modelica Standard Library (version 3.2.3) in dependence of the friction-related pressure loss by subtracting the geostatic pressure difference:

$$\Delta p_{\mathrm{fric},j} = \Delta p_j - \xi_{\mathrm{flow},j}\, g\, \Delta z_j\, \rho_j \tag{3.56}$$

With this, the wall friction function `massFlowRate_dp` determines the mass flow rate of the liquid phase according to

$$\dot{m}_{\mathrm{L},j} = \frac{A_{\mathrm{Q}}}{d_{\mathrm{I}}}\, \mu_{j-1} \cdot \begin{cases} Re_j\,, & \Delta p_{\mathrm{fric},j} \geq 0 \\ -Re_j\,, & \Delta p_{\mathrm{fric},j} < 0 \end{cases} \tag{3.57}$$

Where the Reynolds number in the laminar and turbulent regime is determined as

$$Re_j = \begin{cases} Re_{j,\mathrm{lam}}\,, & Re_{j,\mathrm{lam}} < Re_1 \\ Re_{j,\mathrm{turb}}\,, & Re_{j,\mathrm{lam}} > Re_2 \end{cases} \tag{3.58}$$

with $Re_2 = 4000$ and

$$Re_1 = \min\left\{\left(745 \cdot e^{\min\left\{\frac{0.0065}{\delta_{\mathrm{I}}}, 1\right\}}\right)^{0.97}, Re_2\right\}. \tag{3.59}$$

The values of both regimes are defined as

$$Re_{j,\mathrm{lam}} = \frac{\zeta_j}{64} \tag{3.60}$$

and

$$Re_{j,\mathrm{turb}} = -2\sqrt{\zeta_j} \cdot \lg\left(\frac{2.51}{\sqrt{\zeta_j}} + 0.27\, \delta_{\mathrm{I}}\right) \tag{3.61}$$

With the modified wall friction coefficient

$$\zeta_j = \left|\Delta p_j\right| \cdot 2\, d_{\mathrm{I}}^3 \frac{\rho_j}{l_j\, \mu_j^2} \tag{3.62}$$

Additionally, smooth interpolation is implemented between Re_1 and Re_2.

Furthermore, the class `PartialTwoPortFlow`, from which the absorber tube model extends, is modified to eliminate a phenomenon that can be described as diffusive propagation of mass fraction. It means that in an ordinary homogeneous mixture model, the fluid flow from a partially filled element into the next would have the same composition $\xi_{\mathrm{flow},j}$ as the originating element. Practically explained, during filling, small but increasing amounts of molten salt would be lifted into the upper elements long before the lower elements are filled. Since the model primarily represents vertical tubes that are always filled from the bottom up, this would result in a blurred level and therefore incorrect convective heat transfer between HTF and tube wall.

Consequently, the class `PartialTwoPortFlow` is modified to describe a sequentially filling behavior. This is achieved by introducing

$$\xi_{\mathrm{fill},j} = \begin{cases} 1\,, & \xi_j > 1 - tol_{\xi,trans} + blend_{\xi,trans} \\ 0\,, & \xi_j < 1 - tol_{\xi,trans} - blend_{\xi,trans} \end{cases} \tag{3.63}$$

which transitions around $tol_{\xi,trans} = 5 \cdot 10^{-3}$ within an interval of $\pm blend_{\xi,trans} = 2 \cdot 5 \cdot 10^{-3}$ from 0 to 1 with the help of the `regStep` function, performing a smooth and differentiable transition based on a 3rd-order polynomial. Analog for the reverse flow during drainage applies

$$\xi_{\mathrm{drain},j} = \begin{cases} 1\,, & \xi_j > 0 + tol_{\xi,trans} + blend_{\xi,trans} \\ 0\,, & \xi_j < 0 + tol_{\xi,trans} - blend_{\xi,trans} \end{cases} \tag{3.64}$$

with the same smooth transition. Finally, this is incorporated into the definition of the liquid phase mass flow rate

$$\dot{m}_{\mathrm{L},j} = \begin{cases} \dot{m}_j\, \xi_{\mathrm{fill},j}\,, & \dot{m}_j > 0 \\ \dot{m}_j\, \xi_{\mathrm{drain},j+1}\,, & \dot{m}_j < 0 \end{cases} \tag{3.65}$$

with a smooth transition around zero by using the Modelica build-in function `semiLinear`. This also implies that this model has a fixed orientation concerning gravity. Hence `port_b` must always be higher than `port_a`, independently from the flow direction.

It should be noted that for better clarity, the indexing above is kept consistently corresponding to the indexing of the flow model. In the actual Modelica code, the $\xi_{\mathrm{fill},j}$ and $\xi_{\mathrm{drain},j}$ correspond to the medium model, which is offset to the flow model by one. This is because the medium model considers n_{el} discrete volume elements, whereas the flow model considers $n_{\mathrm{el}} + 2$ states, including the ports of the tube. Therefore, the indices of $\xi_{\mathrm{fill},j}$ and $\xi_{\mathrm{drain},j+1}$ in equation (3.65) are implemented as $j - 1$ and j respectively.

Finally, the heat transfer between the 2P medium and the tube wall is manipulated. In particular, the convective heat flow equation (3.38), which is implemented in the base class `PartialPipeFlowHeatTransfer`, is adapted to a modified heat transfer coefficient

$$\alpha_{\mathrm{mod},j} = \max\left(\min\left(\xi_j\,,1\right),0\right) \cdot \alpha_{\mathrm{conv,I},j}\,, \tag{3.66}$$

which fades out with the mass fraction of the liquid phase. The use of min and max functions provides additional robustness in case ξ_j exceeds the intended range due to numerical noise.

3.2.4 Receiver panel model

The above-described absorber tube model is embedded in a composed model for a receiver panel according to a typical external molten salt receiver design. This panel design comprises a bottom and top header connected to a bundle of adjacent absorber tubes. Accordingly, Figure 3-7 depicts the model structure. The central absorber tube model only represents the irradiated portion of the absorber tubes. Two connected pipe models account for the non-radiated parts of the absorber tubes. These pipe models are based on the class `DynamicPipe` from the Modelica Standard Library with the same modifications described in the previous section. By this, the delayed propagation of the phase interface can be simulated appropriately.

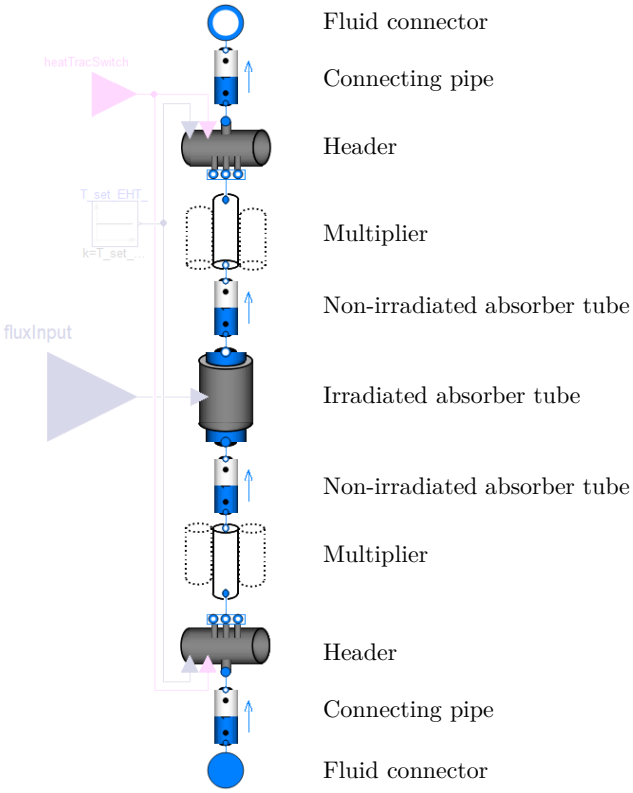

Figure 3-7: Diagram view of the receiver panel model in Dymola

To achieve manageable computing time, the model is set up to only solve the differential-algebraic equations for fewer absorber tubes than there are in the physical design based on the assumption that adjacent tubes in parallel flow have similar states (at the same height). The number of modeled tubes can be adjusted to any integer divisor of the real number (incl. one). Hence, the absorber tube models are implemented as horizontal vector instances. Combined with their vertical discretization, it results in a matrix of tube elements in alignment with the flux input matrix. To account for the combined mass flow rate of the real number of tubes, the top and bottom multipliers convert

between the simulated and actual combined mass flow rates. Independently from that, the discretization in flow direction is adjustable as well.

The top and bottom headers are both represented by a generic header model class with different parameter settings to account for their orientation. For the correct filling and draining behavior, the class `PartialLumpedVolume` from the Modelica Standard Library is extended with specialized mass and energy balances. The hydrostatic pressure difference is considered, but pressure losses due to friction are neglected. Furthermore, this model includes temperature-controlled heat tracing considering the thermal capacities and resistances of header walls and insulation. Because of the great thermal resistance of the tube wall and insulation combined, the convective thermal resistance is neglected. Hence the wall's inner surface temperature equals the medium temperature. The heat tracing is placed between the wall and insulation and connected to a semi-on-off controller. The latter includes a `regStep` function to achieve a smooth transition around the set point and, therefore, better numeric performance than a strict on-off controller. The wall and insulation sub-models include transient thermal conduction equations analog to the absorber tube model but without discretization.

Finally, the connecting pipe models represent the lines connecting headers to the manifolds. They are instances from the same model class as the non-radiated tube models.

3.2.5 Two-phase receiver model

The receiver design considered in this work originates from General Electric (GE) and resembles the one presented by Das et al. (2015). Like other commercial designs, this receiver is subdivided into two parallel flow paths, which can operate independently. Accordingly, a flow path class is implemented comprising all components of one flow path between the inlet vessel and the outlet vessel. As depicted in Figure 3-8, it comprises panels, manifolds, connecting lines, valves and sensors necessary to run different operating modes/transitions such as normal operation, flood and drainage. Notably, it

has an irregular number of parallel panels to realize different flow velocities for adapted materials.

The inlet line is placed in the top left corner and is connected to the inlet vessel of the receiver system (compare Section 3.2.6). From there, the salt runs through the main control valve, continuing either through an isolation valve to the receiver panels or down into the main drain line. The latter is for bypassing and filling the receiver. During normal operation, however, the HTF follows a serpentine pattern through the receiver panels, which can be seen in the center. The receiver panels are connected in series and parallel by five manifolds, resulting in three downwards and three upwards passes, each consisting of multiple panels in parallel. For these manifolds three different manifold model classes are implemented with the same basic modelling as the header class but with different fluid ports.

Besides, header and manifold models both consider the above-described non-diffusive transport of composition, meaning salt only exits the top connectors if the volume is almost filled. In turn, air only exits the bottom connectors if the volume is nearly empty. This allows for determining flood and drainage durations accurately. Finally, another isolation valve connects the flow path outlet line with the outlet vessel (compare Section 3.2.6) in the top right corner.

To simulate startup and shutdown procedures, the flow path model includes drain and vent lines with corresponding isolation valves. During flooding, the main drain line guides the HTF below the receiver, from where three drain valves allow the HTF to enter the bottom manifolds. At the same time, any displaced air in the receiver exits through four vent valves, which are placed above the upper manifolds. For numerical reasons, any joining of the vent lines is neglected. Hence, they are directly connected to the outlet vessel through a multiport. During drainage, another isolation valve connects the main drain line to the downcomer line to allow for dumping the HTF into the outlet vessel or directly down to the storage system. During transitions, the HTF can bypass the receiver through the main drain line into the downcomer.

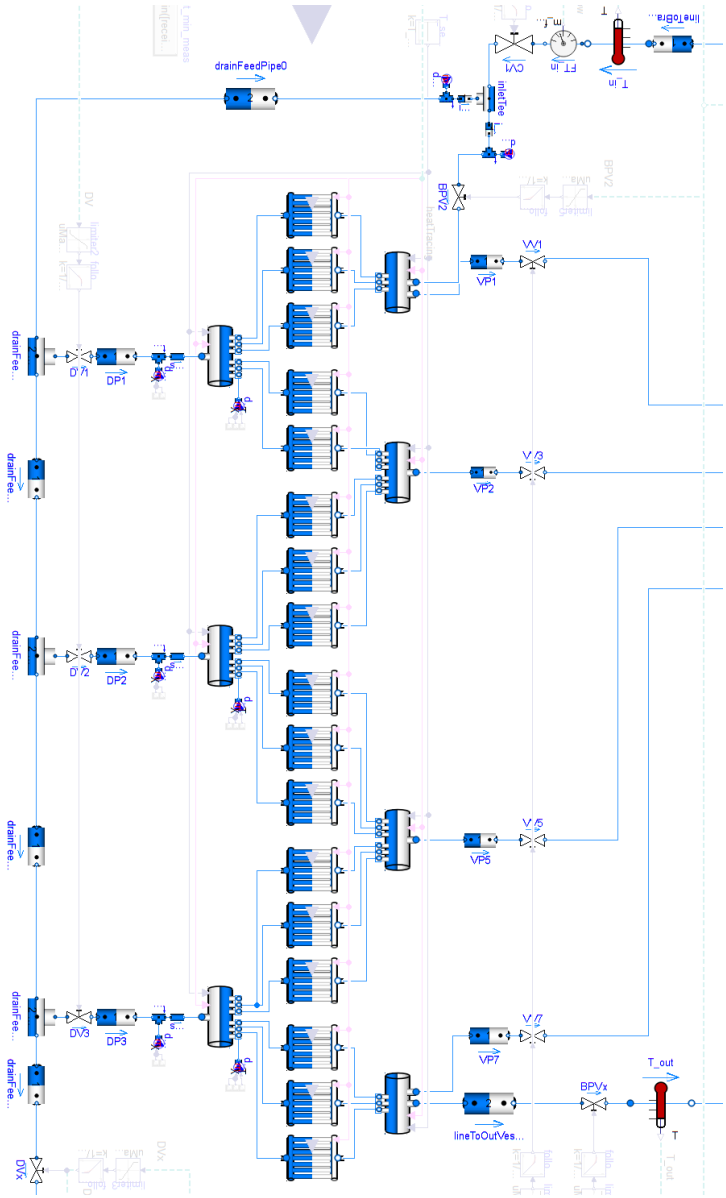

Figure 3-8: Diagram view of the receiver flow path model in Dymola

All valves implemented in this model consider appropriate actuation speed and leakage. Especially, the large-size isolation valves actuate significantly slower, affecting control performance during transitions. The leakage mainly serves the numeric stability and performance of the simulation model due to the avoidance of zero mass flow rates. These leakages are usually in the order of 0.1 % of the corresponding nominal mass flow rate and therefore insignificant for overall performance evaluation.

An undesirable side effect of these leakages is that HTF can flow into the empty manifolds and receiver panels when drain valves are (fully) closed. To avoid this premature filling of the receiver, mass flow sources and sinks are connected to the lower manifolds, which create a small but sufficient counter flow of air always when the drain valves are closed and the manifolds are less than 90 % filled. Furthermore, during drainage with pressurized air, it is possible that small amounts of air leak from the empty panels through the isolation valve (inlet side) into the main drain line creating unnecessary difficulties for the solver respectively rapid fluid property transients. For this reason, a constant flush current of molten salt opposing the air leakage flow is implemented around the inlet tee duct. These flush currents are in the order of approx. 0.5 % of nominal mass flow rate and have no significant impact on the relevant simulation results of the receiver system. However, they are essential for acceptable numerical stability and performance of the simulation model.

The flux density distribution on the receiver surface is given to the flow path model as an array, which correlates with the number of discrete flow elements in the vertical direction and around the circumference of the cylindrical receiver. Each simulated absorber tube element receives its corresponding flux density value from the heliostat field model through this time-varying array.

3.2.6 Periphery modeling and solar input

Since the control of a molten salt receiver is complex and significantly affects the receiver system's overall efficiency, it is necessary to model an appropriate representation of all relevant periphery components and the control system. However, the level of detail in the periphery models can be much lower compared to the receiver model. Figure 3-9 depicts the reference setup in top-level view, including the receiver pumps, the inlet vessel, one flow path the outlet vessel, control and isolation valves, HTF transport lines, storage tanks and a heliostat field component. Non-physical objects such as the process control system (PCS) and the human operator as well as configuration units such as the system block, the wind boundary conditions and the plant design data are placed in the top left corner. Measurement and control signals are organized by a bi-directional expandable bus system with three separate lines (system, receiver flow path 1 and flow path 2).

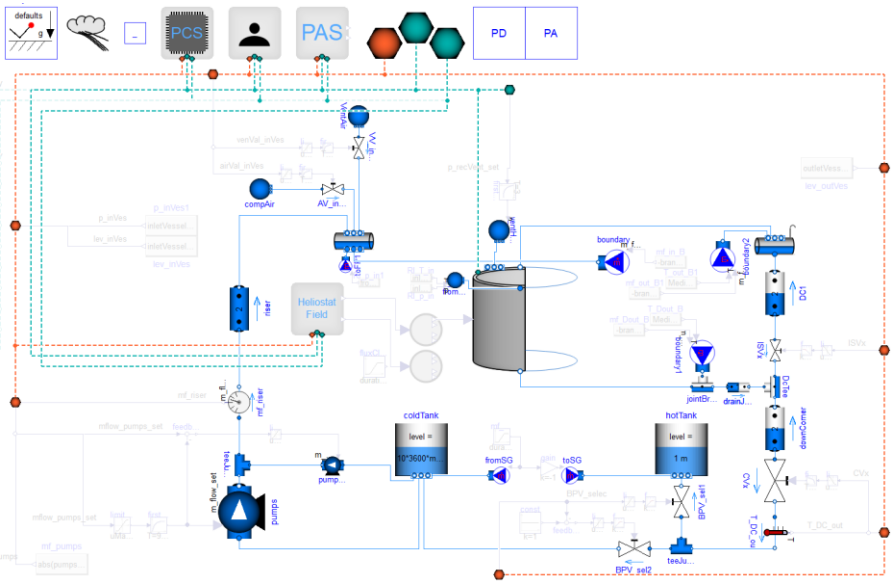

Figure 3-9: Top-level diagram view in Dymola of the detailed dynamic 2P model

3.2.6.1 Receiver pumps and bypass

In MST, multiple vertical shaft pumps are typically submerged in the molten salt inside the storage tank with the motor mounted on top. A bypass, which ensures a minimum mass flow rate, can either be integrated within the housing of each multistage centrifugal pump or run through a controlled valve.

In the detailed dynamic 2P simulation model, the receiver pumps are represented by the class `ControlledPump` of the Modelica Standard Library. It describes a set of parallel centrifugal pumps with an ideally controlled (total) mass flow rate. By this, the actual mass flow rate of the pump strictly follows the control signal. Hence, this model neglects a typical pump characteristic, such as the mass flow rate decreasing with a rising head (pumping pressure). This simplification is justified since the pumping head is mainly defined by the static head plus a well-controlled inlet vessel pressure and therefore nearly constant. Moreover, this reduces the complexity and therefore enhances numerical performance of the overall model.

Moreover, since the pumps are used to maintain a molten level in the inlet vessel, the dynamics of these pumps significantly impact the control quality. For this reason, a first-order delay (PT1) unit at the control signal input mimics the transient behavior, as seen in Figure 3-10. It shows the pumps' actual mass flow rate as a response to a step and a following ramp in the control signal. The time constant is set so that the pumps reach 95 % of the step height after 90 s, which is a typical value for a centrifugal pump of this size.

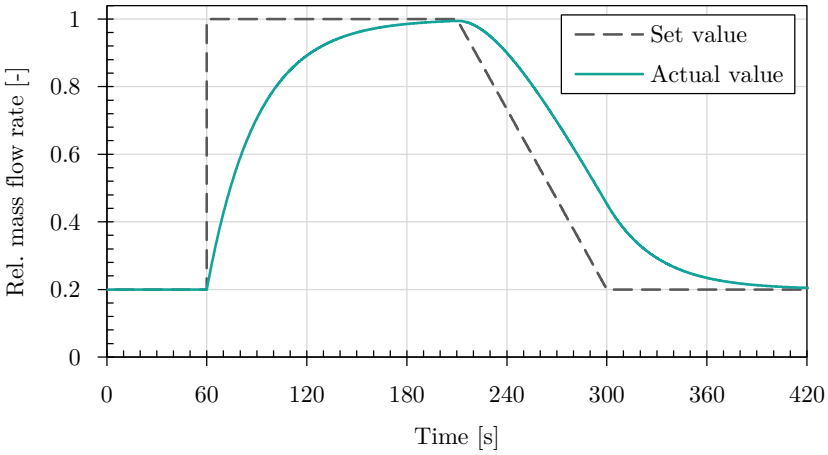

Figure 3-10: Transient behavior of the pumps' model in the detailed dynamic 2P model

Furthermore, the pumping power consumption is calculated inside the component model based on hydraulic power and constant efficiency accounting for mechanical and hydraulic friction losses. The implemented energy balance also accounts for the resulting temperature lift of approx. 3.4 K (at 62 bar pressure difference).

The aforementioned minimal flow rate and bypass are modeled with a control signal limiter and an additional pump model parallel to the primary pump model redirecting a controlled mass flow rate equal to the difference between the actual pumps' mass flow rate and the control signal back into the cold storage tank.

3.2.6.2 Outlet vessel

The outlet vessel resembles an unpressurized/vented and insolated vessel which on one hand regulates temperature transients in the fluid flow to protect the thick-walled downcomer pipes and on the other hand acts as a buffer to absorb HTF when the downcomer flow capacity might be compromised

either during quick receiver drainage or in case of malfunctioning control valves.

Hence, a generic volume model is applied analog to the header model (comp. Section 3.2.4) but vented to an atmospheric pressure source. In the real plant, the vessel's HTF level is measured and functions as a control signal. However, the simulation model needs to calculate the level based on the volume fraction of the liquid phase. Since the vessel's shape resembles a horizontal cylinder, the correlation is nonlinear (see Figure 3-11).

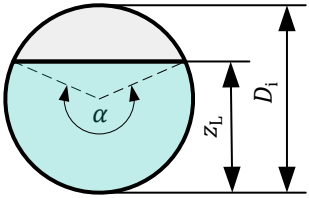

Figure 3-11: Geometry of HTF level in a horizontal cylinder-shaped vessel

Accordingly, the following two equations are implemented to determine the relative level $\frac{z_L}{D_i}$ from the liquid volume fraction ϕ_L:

$$\frac{z_L}{D_i} = \frac{1 - \cos\left(\frac{\alpha}{2}\right)}{2} \tag{3.67}$$

$$\alpha - \sin(\alpha) = 2\,\pi\,\phi_L \tag{3.68}$$

with $\phi_L = \zeta_L$. The liquid volume is considered as ideally mixed with constant heat transfer coefficients from HTF to wall and from wall to ambient.

3.2.6.3 Inlet vessel

The inlet vessel of a molten salt receiver system decouples the receiver HTF flow rate from the mass flow rate in the riser, allowing to dynamically vary the receiver mass flow rate despite the pumps' slow transient behavior and the immense inertia of the molten salt mass in the riser. It also acts as an emergency buffer in case of a blackout or other pump failures. Suppose for

any reason, the riser mass flow rate diminishes. In that case, the inlet vessel can still provide enough HTF and pressure to cool the receiver for 60 s while the heliostat field defocuses. The model therefore needs to describe a closed volume, in which the air portion of the 2P medium is modeled compressible, replicating the changes in pressure due to expansion or compression when the salt level varies.

This model is based on the same base class as the outlet vessel, considering an ideal mixture in each phase and constant heat transfer coefficients as well as the nonlinear HTF-level of a horizontal cylinder-shaped vessel. In addition, instead of venting to ambient pressure, the outlet vessel model is considered closed. Since the 2P medium model does not describe the compressibility of the gas phase realistically, the vessel volume is made pseudo-variable. The ullage pressure is calculated based on the ideal gas model (Lucas 2008) as follows

$$p_{\mathrm{G}} = \frac{m_{\mathrm{G}}\, R_{\mathrm{G}}\, T_{\mathrm{G}}}{V_{\mathrm{G,real}}} \tag{3.69}$$

with the real compressed volume

$$V_{\mathrm{G,real}} = V_{\mathrm{vessel}} - \frac{m_{\mathrm{L}}}{\rho_{\mathrm{L}}}. \tag{3.70}$$

Since, in this case, the volume of the medium model is different from the real volume, the HTF level cannot be directly determined from the mass fraction ζ_{L} but from the real volume fraction instead

$$\phi_{\mathrm{L,real}} = 1 - \frac{V_{\mathrm{G,real}}}{V_{\mathrm{vessel}}} \tag{3.71}$$

Besides, equations (3.67) und (3.68) apply for the inlet vessel as well.

3.2.6.4 Receiver vents

By design, the receiver vent lines connect the vent valves to a vent header connected to the outlet vessel. For better numerical stability, this vent header

is neglected without a significant effect on the simulation results. Moreover, since the outlet vessel directly connects to ambient pressure, all drain valves of the receiver are directly connected to an ambient pressure boundary to improve numerical performance.

3.2.6.5 Transport lines

The major HTF transport lines, such as the riser and downcomer, are modeled with the same modified version of the `DynamicPipe` class (from the Modelica Standard Library) as connecting pipes in the receiver panel model (see Section 3.2.4) in order to replicate the delayed transport of thermodynamic state and properties. Due to the large dimensions hence the inertia of the fluid mass, quick changes in mass flow rate can actually cause significant pressure peaks. Nevertheless, the pumps operate with moderately slow transients, so this effect is less significant in the application of the model. Consequently, for a reasonable tradeoff between accuracy and performance, the transport lines are implemented with steady-state momentum balances but transient energy and mass balances.

3.2.6.6 Storage system

Since this work focuses on operating the receiver system, the storage system is modeled leanly. In this sense, both storage tanks are represented by the `OpenTank` class from the Modelica Standard Library, describing an ideally mixed isobaric volume (see Figure 3-9). They are both connected to the downcomer via designated isolation valves, which are controlled by the flow selection station inside the process control system. This allows for the simulation of the development of storage temperatures under the influence of the variable receiver outlet temperature.

In addition, the interface to the steam generator (SG) is represented by two mass flow boundaries to account for the moderating effect of the constant return temperature of the steam generator. In most simulations, the SG mass flow rate is ramped up (before noon) and set to half of the nominal receiver mass flow rate, assuming a solar multiple of two.

3.2.6.7 Heliostat field

The interface between the receiver and the solar concentrator, i.e. heliostat filed, is defined as the flux density distribution. Its spatially integral value, the intercept power, and the spatial distribution of flux on the receiver strongly influence the receiver efficiency, local temperature distribution and (in transient operations) the outlet temperature trend. Therefore, an appropriate representation of the heliostat field is essential.

With the help of raytracing, the physics of the solar concentrator is modeled and simulated in STRAL (Ahlbrink et al. 2012), which considers internal losses of the heliostat field such as shading, blocking, cosine losses, extinction and spillage losses. It incorporates a solar position and clear-sky DNI model, the heliostat field specifications (see Section 3.1) as well as a field- and time-specific aim point configuration. The latter specifies where each heliostat points at the receiver surface, significantly affecting the flux density distribution field efficiency.

Using a recently developed optimization algorithm (Flesch et al., 2017), optimal aim point configurations are determined for every 5 min of one day (March 21). This optimization is set to maximize the thermal power while complying to constraints such as maximum film temperature and maximum allowable flux density. Figure 3-12 visualizes how the optimal aim point configurations vary between different times of the day. Early at 7 am, most heliostats aim very centered, minimizing spillage losses. Heliostats that are very close to the receiver, and therefore achieve small images, aim further up or down depending on the flow direction of the receiving panel to put more flux on the colder part of the absorber tubes. At 9 am the field efficiency of the western half is already high enough to allow for a more even flux distribution. Hence, most heliostats have significant vertical offsets. At 12 pm, however, the heliostat field can provide more intercept power than the receiver could handle. Consequently, the aim point optimizer accepts more spillage losses and assigns more aim points towards the upper and lower edge of the receiver surface. Especially the heliostats in the inner circle mostly have vertical offsets of more than 5 m, which results in a more even flux density distribution.

Horizontal aim point offsets are not considered to minimize computational effort.

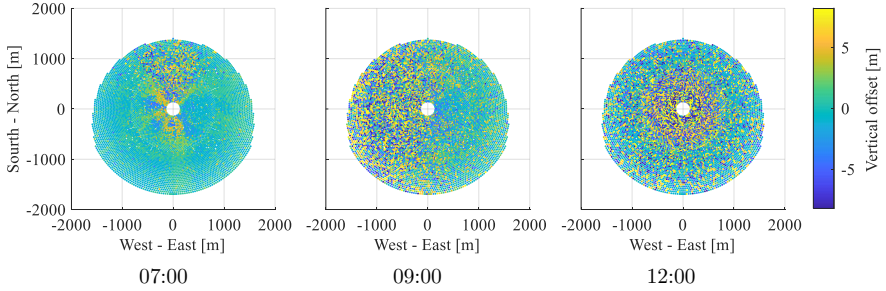

Figure 3-12: Vertical aim point offsets for each heliostat on March 21 at different times

In addition, the raytracing in STRAL also considers individual heliostat shading due to cloud passages. This allows for realistically simulating cloud passages based on shading maps and the resulting flux density distribution are saved as a time series, which acts as data input for the detailed dynamic model in Dymola. The shading maps are generated either from artificial cloud shapes (see B.1) or based on DNI-maps from a nowcasting system (see B.2).

For this purpose, the heliostat field is represented as a separate component in the periphery model declared as `heliostatField`. This includes code to load the flux file as well as a simplified field controller. Depending on the field mode, which is prescribed by the `humanOperator`, the `heliostatField` creates corresponding flux density distributions. During **night preservation** mode and **standby,** the flux is set to zero.

In **gentle warming** mode, the heliostat field is usually controlled in a way to produce a nearly homogeneous flux distribution with only a small number of heliostats being used. The number of focused heliostats needs to be constantly adapted to control the rate at which the empty absorber tubes heat up. A detailed representation of this would require a co-simulation of Dymola and STRAL with a feedback control loop between both. Since this would cause

poor computing performance hence excessively long simulation times, a simplified approach is chosen. For each receiver panel, there is a P controller that continuously adjusts the flux density on the corresponding panel controlling the measured back wall temperatures of this panel while the temperature set point is ramped up. Based on the assumption that a real field controller could function with relatively little delay, the flux value from the controller is projected evenly onto the receiver panel. In addition, the flux on each panel is limited to the actually available flux density according to the flux input data.

In **optimized aiming** mode, the `heliostatField` model directly transmits the flux distribution from the flux file to the receiver model. A limitation is not required since the aim point optimization already considers allowable flux density limits and the maximum thermal power of the receiver. During **temperature ramp** mode, the heliostat field mimics a linear transition between the gentle warming and the optimized aiming mode. Furthermore, the `heliostatField` includes an algorithm that confirms to the process control system when the desired mode has been reached. In the case of the transition between night preservation mode and standby, the confirmation is programmed with a fixed delay of 60 s to mimic the transition between stow position and standby aiming.

3.2.7 Process control system

To achieve a realistic process prediction, a comprehensive process control system is implemented in the detailed dynamic 2P model. It is hierarchically structured, as illustrated in Figure 3-13. The operator has master authority over the whole plant and gives commands to the field control, receiver control, and storage control. The power block is not considered because the thermal storage decouples the power block operation from the solar system. The OAS is on the same level as the operator since it is provided with all measurement and control signals, but it cannot control any control units directly.

Instead, it provides proposals to the operator. The receiver control is represented by the component `modeOperator` within the PCS and the storage control is represented by the `flowSelectionStation`.

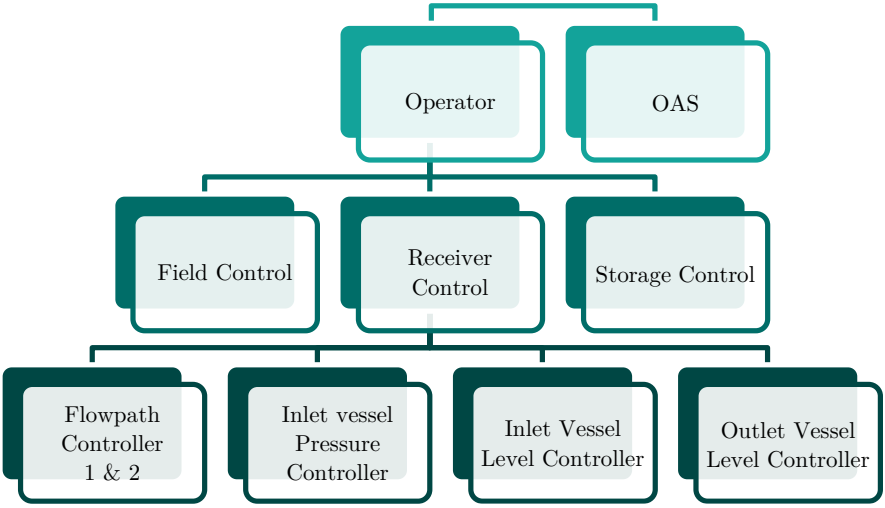

Figure 3-13: Hierarchy of the process control system in the MST

The field control is considered a separate control unit and therefore implemented in the component `heliostatField` (comp. Section 3.2.6). The Receiver controller handles the entire receiver system by setting different controllers and setpoints according to predefined operating modes and automated transitions. The storage control manages the feed of the heated HTF into the two storage tanks.

The implemented overall operating strategy is based on a suggestion made by the project partner GE (compare Das et al. 2015) and further refined with the help of test simulations on the detailed dynamic 2P model. Figure 3-14 draws out the operating modes of the overall system considered for the operator and the OAS (green), the operating modes for the receiver control (yellow) and the operating modes for the field control (blue). Furthermore, the

errors indicate the data exchanged during the different modes. The specifications of these operating modes and the transition between them are further described in the following.

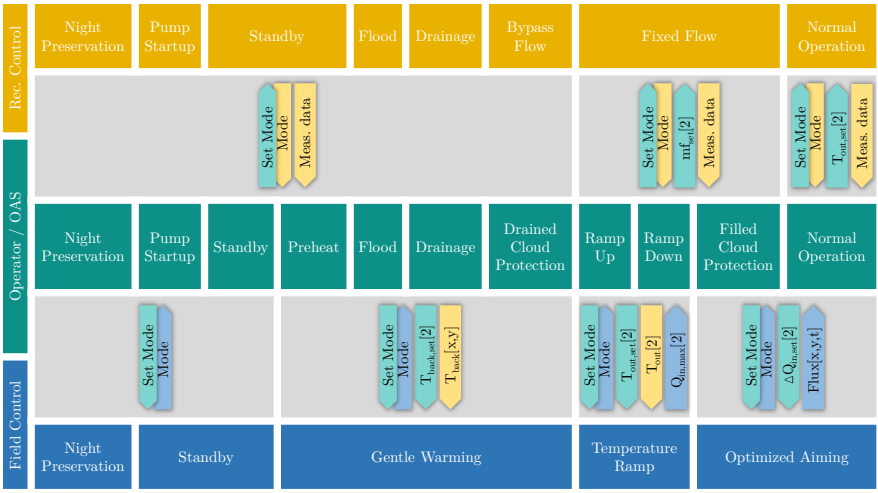

Figure 3-14: Overview of the operating modes for the overall system (Operator / OAS), the receiver modes (receiver) control and the field modes (field control)

3.2.7.1 Human operator

In the detailed dynamic 2P model, the human operator is represented by the component `humanOperator`. It includes an automatic state machine algorithm utilizing the open-source Modelica library StateGraph2. Its purpose it to decide when to activate which operating mode depending on prescribed conditions. It then sends commands through a bus system to the control units. The transitions that are implemented in the `humanOperator` as visualized in Figure 3-15. The dark grey arrows indicate the daily routine for startup and shutdown, whereas the light grey arrows represent transitions to temporarily put the receiver out of operation, which is relevant for the assistance function of the OAS developed and tested in this work. The red arrow marks an emergency shutdown of the receiver and the thin dashed arrows

indicate that the receiver control can automatically switch between normal operation and filled cloud protection.

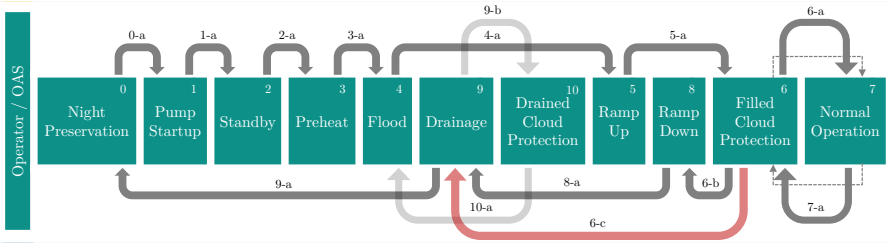

Figure 3-15: Transitions between the operating modes of the human operator

Explanations of the operating modes and transitions used in the daily routine as well as details about specific set points and valve positions in Appendix Section A.

3.2.7.2 Mode Operator

The `modeOperator`, which represents the receiver control, is implemented as a subcomponent inside the process control system (PCS). As illustrated in Figure 3-16, the `modeOperator` is connected to the bidirectional data bus system (hexagons) to send and receive control and measurement signals. Via dedicated control signals, it has direct authority over the different control circuits described in the following subsection. According to the receiver mode commanded by the `humanOperator` the `modeOperator` performs predefined transitions by setting valves, activating control circuits and adjusting set points. This algorithm is implemented in an event-oriented Modelica code, which describes the transition table in Appendix Section A.

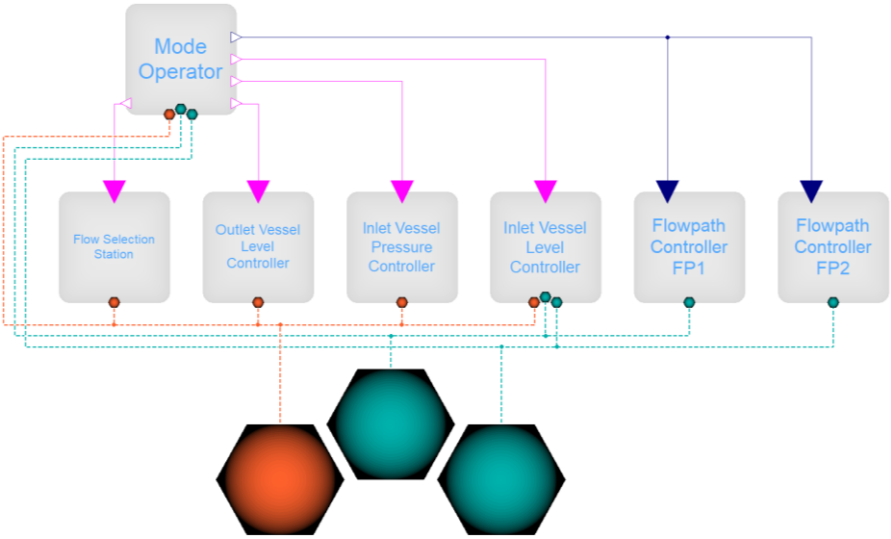

Figure 3-16: Graphical implementation of subcomponents inside the PCS

3.2.7.3 Flow path controller

The receiver is subdivided into two flow paths, which are controlled independently. Therefore, the PCS includes two components of the same class, `FlowpathController`. It describes an automated control circuit according to the control algorithm tested at the SolarTwo test plant (Pacheco et al. 2002). The diagram view of its implementation is shown in Figure 3-17. The `FlowpathController` can operate in four modes: Offline, (constant) mass flow control, (forced) clear-sky control and automatic control.

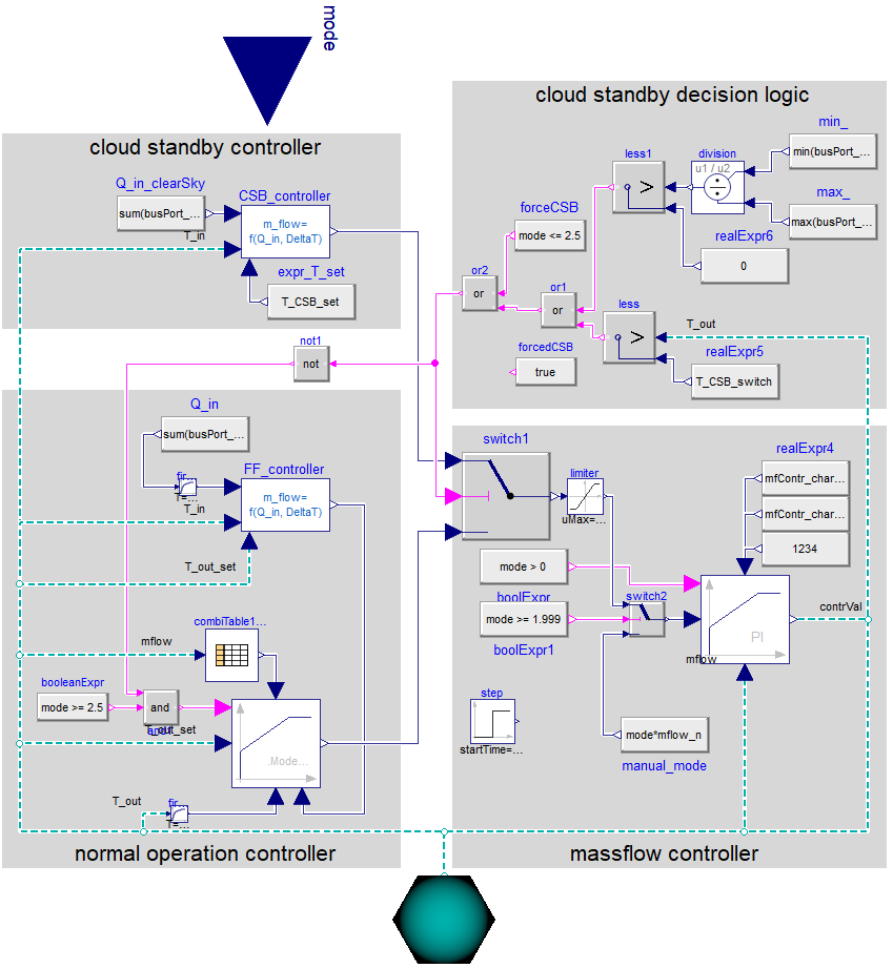

Figure 3-17: Graphical implementation of the flow path controller

In mass flow control mode, only the mass flow controller, a limited PI controller, is active adjusting the control valve according to a fixed set point for the mass flow rate given by the `modeOperator`. In clear-sky control mode, the cloud standby controller provides a semi-constant set point for the mass flow rate, a feedforward controller, that determines the required mass flow

rate to achieve the set temperature under clear-sky conditions hypothetically. The `modeOperator` activates this mode during filled cloud protection. For this purpose, the flux files include the clear-sky flux distribution besides the actual flux.

In automatic control mode, the `FlowpathController` decides whether the mass flow controller uses the floating set point signal from the normal operation controller or the cloud standby controller based on a decision logic. This decision is based on a lower outlet temperature threshold and a flux skewness threshold. The normal operation controller combines a feedforward with actual flux measurements and a feedback controller for the measured outlet temperature of the flow path. Besides, the controller parameters of the feedback controller, a PID controller (Schneider and Heinrich 2017), constantly adapt to the mass flow rate to account for the variable delay time of the controlled system. Before any simulation, these parameters are optimized for five different mass flow rates. In the actual simulation, the `FlowpathController` interpolates between those optimized values according to the measured mass flow rate in the simulation.

3.2.7.4 Inlet vessel pressure controller

To maintain constant boundary conditions for both `FlowpathController`, the `inletVesselPressureController` actuates a pressurized air inlet and an outlet valve on top of the inlet vessel to control the ullage pressure. As shown in Figure 3-18, it includes a limited P controller. The control signal is transmitted to the inlet or the outlet valve, depending on its sign. In this case, the controller parameters are optimized based on a heuristic algorithm without adaptation during operation.

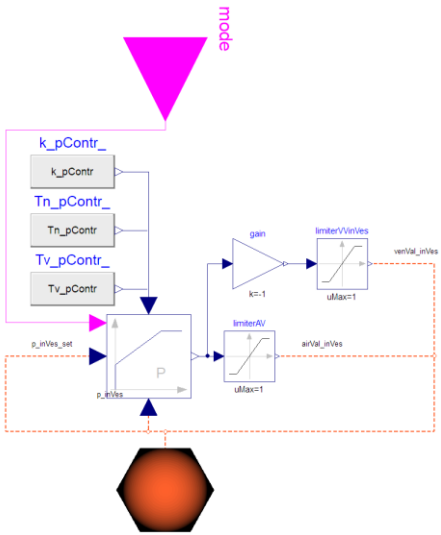

Figure 3-18: Graphical implementation of the inlet vessel level controller

3.2.7.5 Inlet vessel level controller

Furthermore, to ensure a sufficient reservoir of HTF in the receiver system, the level in the inlet vessel is controlled by adjusting the mass flow rate of the pumps. For this purpose, the `inletVesselLevelController` uses a PID controller with optimized (constant) parameters. In addition, it utilizes the measured inlet mass flow rates of both flow paths as a feedforward signal to improve the control performance when mass flow rates change quickly (see Figure 3-19).

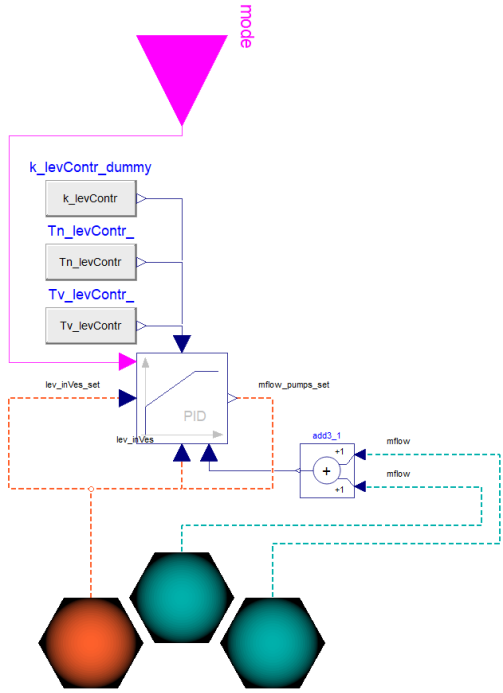

Figure 3-19: Graphical implementation of the inlet vessel level controller

3.2.7.6 Outlet vessel level controller

The outlet vessel's level must be controlled to prevent the vessel from spilling over and draining completely, which could cause high mechanical stresses in the downcomer due to plunging HTF. Therefore, the `outletVesselLevelController` uses a PID controller with fixed parameters (see Figure 3-20) to control the HTF level in the outlet vessel by adjusting a control valve at the bottom end of the downcomer line.

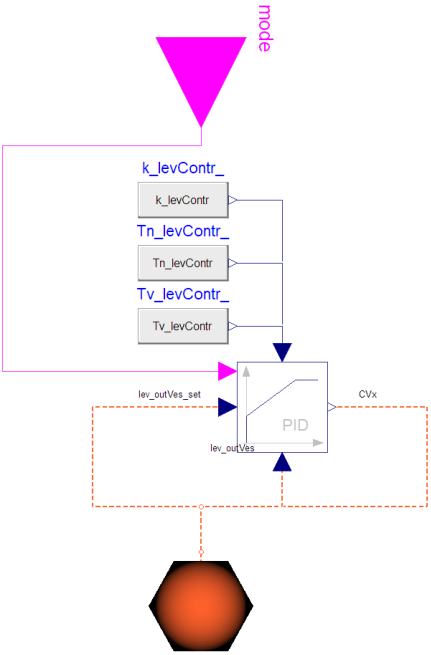

Figure 3-20: Graphical implementation of the outlet vessel level controller

3.2.7.7 Flow selection station

The `flowSelectionStation` includes a simple logic switch that decides which of the two storage tanks the HTF that exits the downcomer is fed into. If the bulk temperature measured at the outlet of the downcomer is below a certain threshold, the HTF is recycled into the cold storage tank. For this purpose, it actuates the corresponding two isolation valves.

3.3 Simplified Dynamic 2P Model

For the process prediction in the OAS, a model that simulates faster than real-time is required. However, the prediction of interrupted operation still requires a model that realistically describes dynamic behavior and parasitic

losses during the transition between filled and drained operating modes. Test simulations and numerical analysis done by Dymola revealed that most computing time is used to solve the interconnected differential equations for the fluid discretized flow in the absorber tubes. A grid dependency study presented by Schwager et al. (2022) shows that the number of vertical elements in significantly impacts the computing time but also the accuracy of the model. Therefore, a different model reduction is made to the detailed dynamic 2P model. Instead of modeling and solving the differential equations for all 17 panels per branch, each pass consisting of two or three parallel panels is represented by only one panel model, as illustrated in Figure 3-21. Since the mass flows of the parallel panels (in each pass) mix in the manifolds this simplification is expected to result in a reasonably small loss of accuracy.

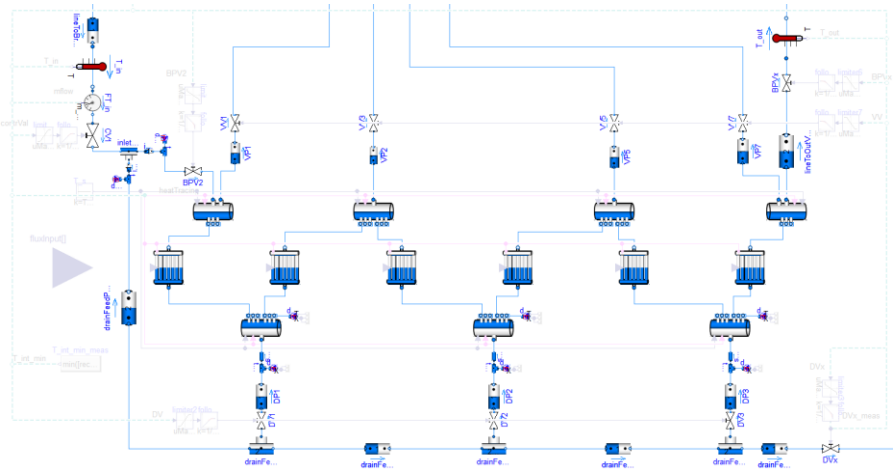

Figure 3-21: Diagram view of the simplified 2P flow path model in Dymola

For physical compensation, the header volumes and the number of “real” tubes are increased by the respective reduction factor (two or three). This effectively reduces the flow path model to only six individual absorber tubes for which differential equations need to be solved. The parallel tubes in each pass are considered to have the same states, which causes deviations in local

temperature distribution but only insignificant changes in the overall dynamic behavior (see Section 3.7).

Additionally, the discretization of the simplified 2P model is set to a low value of six. Hence, each flow path is discretized in only six by six flow elements (excluding non-radiated tubes). Since the two flow paths can be operated independently, the reduced models only consider one flow path to minimize computing time. In the real application, when both flow paths should be considered, this could easily be parallelized with almost no performance penalty. The top-level model setup remains nearly unchanged. However, further model reductions are possible if faster computing performance is required.

3.4 Fast 1P Model

The fast 1P model is supposed to predict the continuous operation of the receiver system in cloudy conditions. Not only for the yield comparison between continuous and interrupted operation but also to quickly predict the net power trend for a much more extended period, based on which the decision algorithm can identify any points of interest that should be simulated with the more complex 2P model. Accordingly, a highly efficient modeling approach is required to achieve minimal computational effort.

Instead of further incremental model reduction on the simplified 2P model, a fast 1P model is developed from scratch. First, the sub-model for each receiver pass poses a dynamic but only thermal zero-dimensional model without any hydraulic equations. This prohibits calculating any pressure losses but drastically improves the computing performance since the mass flows in all components in one series share the same mass flow rate. Moreover, compared to the SolarTwo test plant referenced above, commercial plants are usually operated more conservatively with a clear-sky mass flow control. Hence, the mass flow rate can be determined with a simple clear-sky model (as in the Flow path controller) and prescribed to the thermal model without any feedback loop.

In turn, the receiver pass model only needs to calculate one dynamic energy balance as well as heat transfer and losses, as illustrated in Figure 3-22. Specifically, the intercept flux on one receiver pass is described as

$$\dot{Q}_{\text{in}} = \dot{q}''_{\text{in}} A_{\text{abs}} \tag{3.72}$$

with the incoming mean solar flux density $\dot{q}''_{\text{in}}$ and corresponding aperture area

$$A_{\text{abs}} = \left(d_{\text{i,tube}} + 2\,\Delta r_{\text{tube}}\right) l_{\text{rad}}\, n_{\text{tubesPerPass}}\,. \tag{3.73}$$

Based on this, the absorbed (gross) heat flux follows

$$\dot{Q}_{\text{abs}} = \dot{Q}_{\text{in}}\, \alpha_{\text{abs}} \tag{3.74}$$

with the effective absorptivity of the tube coating α_{abs}.

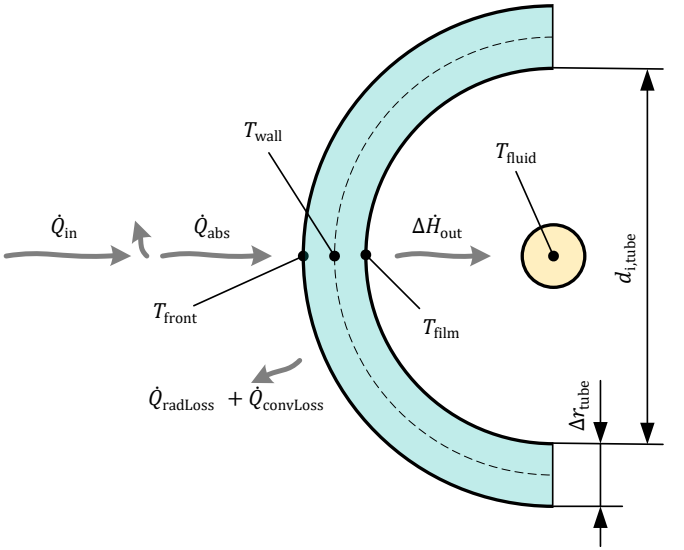

Figure 3-22: Schematic of the zero-dimensional energy flow and thermal states in each receiver pass of the fast 1P model

For modeling thermal losses, the longitudinal temperature profile of an absorber tube is examined with the help of the simplified 2P model in Figure 3-23. In this context, a reasonably accurate approximation of the surface temperature is essential because the thermal losses strongly depend on it with a significant nonlinearity. The diagram clarifies that the outer surface temperature (T_{front}) has a curved profile because of the higher flux density in the mid-section compared to the outer parts of the receiver tubes. The staggered flow approach usually applied in a discretized 1D model assumes each element to be ideally mixed so that the bulk temperature of each discrete volume equals the outlet temperature of this element. In a model with very coarse discretization, this would lead to a significant overestimation of the fluid temperature. Since the surface temperature is linked to the fluid temperature by thermal convection and conduction equations, the thermal losses would also be significantly overestimated.

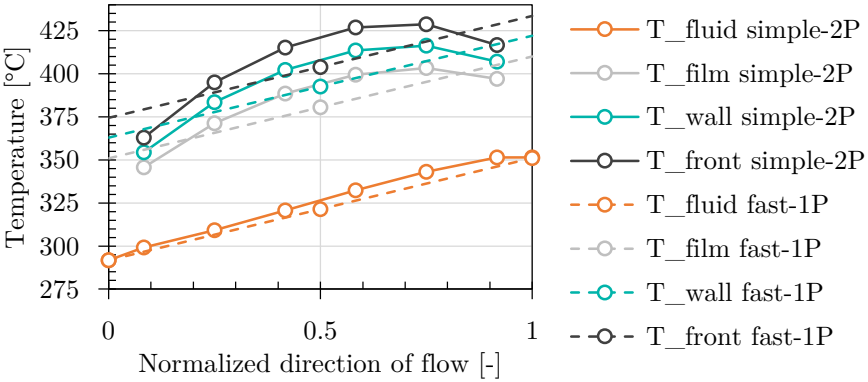

Figure 3-23: Longitudinal temperature profiles of the simplified 2P model and in comparison to the pseudo-zero-dimensional receiver pass of the fast 1P model

Instead, the fast 1P model assumes a linear temperature profile, where the mean fluid temperature follows

$$T_{\text{fluid}} = \frac{(T_{\text{out}} + T_{\text{in}})}{2} \tag{3.75}$$

Nevertheless, due to its nonlinearity, the radiation losses should not only be calculated based on this average temperature to avoid additional deviations. Instead, the radiation losses can be analytically integrated along the linear temperature profile:

$$\dot{Q}_{\mathrm{radLoss}} = \varepsilon\ \sigma\ A_{\mathrm{abs}}\ \frac{\int_0^{l_{\mathrm{rad}}} (T(x)^4 - T_\infty^4)\ dx}{l_{\mathrm{rad}}} \tag{3.76}$$

For this, the profile of the surface temperature is simplified to be linear as well and parallel to the fluid temperature profile so that the temperature range at the inner and outer tube surfaces and in the fluid are the same, meaning

$$T_{\mathrm{fr,out}} - T_{\mathrm{fr,in}} = \Delta T_{\mathrm{fr}} = \Delta T_{\mathrm{fluid}} = T_{\mathrm{out}} - T_{\mathrm{in}} \tag{3.77}$$

from which follows

$$T_{\mathrm{fr,in}} = T_{\mathrm{in}} + T_{\mathrm{front}} - T_{\mathrm{fluid}}\,. \tag{3.78}$$

With this assumption, equation (3.76) is transformed to

$$\begin{aligned} \Rightarrow \dot{Q}_{\mathrm{radLoss}} = \varepsilon\, A_{\mathrm{abs}}\, \sigma \Big[& \frac{1}{5}\, \Delta T_{\mathrm{fluid}}^4 + \Delta T_{\mathrm{fluid}}^3\, T_{\mathrm{fr,in}} + 2\, \Delta T_{\mathrm{fluid}}^2\, T_{\mathrm{fr,in}}^2 \\ & + 2\, \Delta T_{\mathrm{fluid}} T_{\mathrm{fr,in}}^3 + T_{\mathrm{fr,in}}^4 - T_\infty^4 \Big] \end{aligned} \tag{3.79}$$

Detailed derivation is printed out in Appendix Section D.1.

Finally, with the convection loss

$$\dot{Q}_{\mathrm{convLoss}} = \alpha_{\mathrm{conv,ext}}\, A_{\mathrm{abs}}\, (T_{\mathrm{front}} - T_\infty) \tag{3.80}$$

the net heat input into the tube wall can be defined as

$$\dot{Q}_{\mathrm{in,net}} = \dot{Q}_{\mathrm{abs}} - \dot{Q}_{\mathrm{radLoss}} - \dot{Q}_{\mathrm{convLoss}}\,. \tag{3.81}$$

As indicated in Figure 3-22 the backside of the wall (back shell), which is not irradiated, is neglected since it has almost no impact on the dynamic behavior. In this sense, the unknown surface mean temperature T_{front} results from

the cylindrical thermal conduction equation for the outer half of the wall (of the front shell)

$$\dot{Q}_{\mathrm{in,net}} = \pi\, l_{\mathrm{rad}}\, \lambda_{\mathrm{wall}} \frac{(T_{\mathrm{front}} - T_{\mathrm{wall}})}{\log\left(\frac{d_{\mathrm{i,tube}} + 2\, s_{\mathrm{tube}}}{d_{\mathrm{i,tube}} + s_{\mathrm{tube}}}\right)}\, n_{\mathrm{tubesPerPass}}\,. \tag{3.82}$$

The mean wall temperature is calculated based on a transient energy balance for the wall (front shell)

$$\frac{d(T_{\mathrm{wall}})}{dt} = \frac{\left(\dot{Q}_{\mathrm{in,net}} - \Delta\dot{H}_{\mathrm{out}}\right)}{c_{\mathrm{p,wall}}\, m_{\mathrm{fShell}}} \tag{3.83}$$

and the mean film temperature T_{film} is defined by the cylindrical conduction equation of the inner half of the wall (of the front shell)

$$\dot{Q}_{\mathrm{fluid}} = \pi\, l_{\mathrm{rad}}\, \lambda_{\mathrm{wall}} \frac{(T_{\mathrm{wall}} - T_{\mathrm{film}})}{\log\left(\frac{d_{\mathrm{i,tube}} + 2\, s_{\mathrm{tube}}}{d_{\mathrm{i,tube}} + s_{\mathrm{tube}}}\right)}\, n_{\mathrm{tubesPerPass}} \tag{3.84}$$

Finally, the heat flow into the fluid results from

$$\dot{Q}_{\mathrm{fluid}} = \alpha_{\mathrm{conv,int}}\, (T_{\mathrm{film}} - T_{\mathrm{fluid}})\, l_{\mathrm{rad}}\, \frac{\pi\, d_{\mathrm{i,tube}}}{2}\, n_{\mathrm{tubesPerPass}} \tag{3.85}$$

With the convective heat transfer coefficient

$$\alpha_{\mathrm{conv,int}} = \frac{Nu_{\mathrm{m}}\, \lambda_{\mathrm{fluid}}}{d_{\mathrm{i,tube}}} \tag{3.86}$$

based on the mean Nusselt number for pipe flow (Gnielinski 2013a)

$$Nu_{\mathrm{m}} = \frac{\frac{\xi_{\mathrm{Nu}}}{8}\, Re\, Pr}{1 + 12.7\sqrt{\frac{\xi_{\mathrm{Nu}}}{8}}\left(Pr^{\frac{2}{3}} - 1\right)} \left[1 + \left(\frac{d_{\mathrm{i,tube}}}{l_{\mathrm{rad}}}\right)^{\frac{2}{3}}\right] \tag{3.87}$$

with

$$\xi_{\mathrm{Nu}} = (1.8 \log_{10} Re - 1.5)^{-2} \tag{3.88}$$

and the Reynolds number

$$Re = \frac{\rho_{\text{fluid}}\, v_{\text{tube}}\, d_{\text{i,tube}}}{\eta_{\text{fluid}}} \tag{3.89}$$

with the flow velocity

$$v_{\text{tube}} = \frac{|\dot{m}|}{\rho_{\text{fluid}}\, \frac{d_{\text{i,tube}}^2}{4}\, \pi\, n_{\text{tubesPerPass}}}. \tag{3.90}$$

In addition, one dynamic energy balance for the fluid is implemented by a lumped volume model, which is connected to the heat flow $\dot{Q}_{\text{fluid}}$ as shown in Figure 3-24. By this, the pseudo-zero-dimensional receiver pass model has only two differential equations while considering the heat capacities of the fluid and the wall and assuming a linear temperature profile regarding thermal losses.

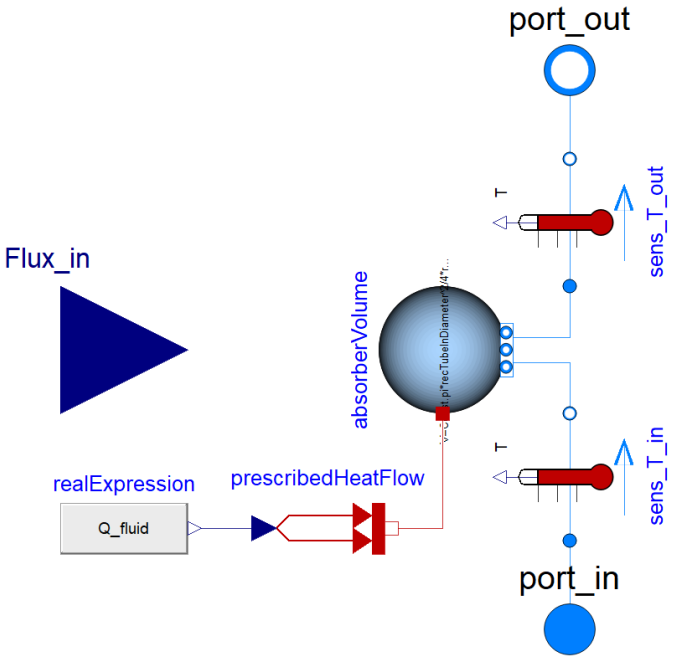

Figure 3-24: Graphical implementation part of the pseudo-zero-dimensional receiver pass sub-model in the fast 1P model

Furthermore, one receiver flow path comprises six receiver pass components connected in series with several additional lumped volume models to resemble the time delay behavior of headers and connecting pipes (see Figure 3-25).

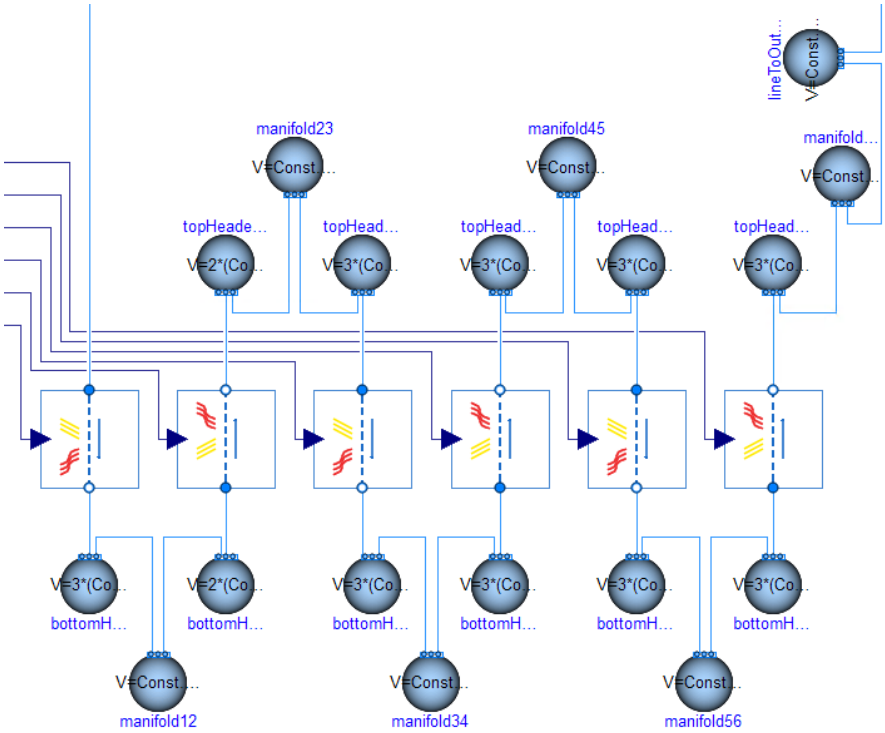

Figure 3-25: Graphical implementation of a receiver flow path in the fast 1P model

In contrast to the simplified dynamic 2P model, the top-level model setup of the fast 1P model is drastically simplified. As shown in Figure 3-26, the flow path model is directly connected to a mass flow boundary and a pressure boundary resembling the inlet and outlet vessel with only two additional lumped volumes in between. The other periphery is modeled without flow modeling components to reduce complexity.

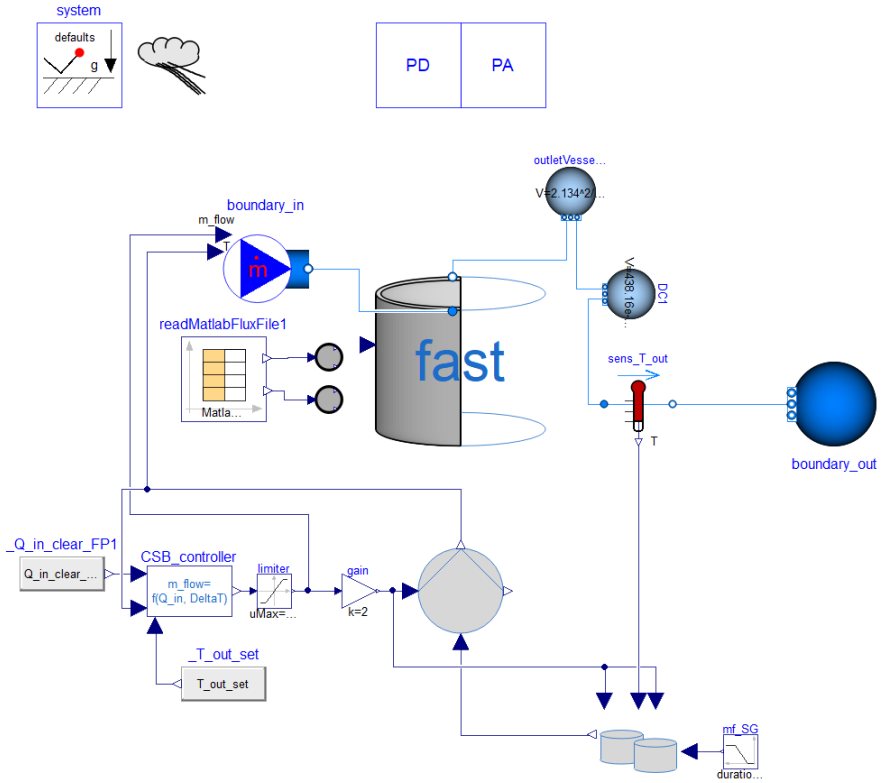

Figure 3-26: Graphical implementation of the fast 1P model setup

Instead of the whole PCS, only the cloud standby controller is implemented since this model only describes the filled cloud protection mode. A simple pump model calculates the receiver inlet temperature based on the cold storage tank temperature and the temperature rise due to pumping efficiency losses. The pumping power is based on geostatic pressure neglecting the comparably low friction losses in pipes and fittings. Delayed transport of Temperature through the riser and inlet vessel is neglected as well. The storage model only includes two dynamic mass and two dynamic energy balances while neglecting any pressure changes.

3.5 Scalar 1P Model

The scalar 1P model is a zero-dimensional steady-state receiver model for testing to what extent model reductions are reasonable for use in the OAS. The same pseudo-zero-dimensional approach as in the fast 1P model is used, but for the whole receiver flow path. Consequently, besides inlet and outlet temperature, the scalar model only considers one mean temperature for each radial state (wall, fluid, surface, etc.) in the whole flow path. Additionally, the energy balances for fluid and wall are implemented without differentials meaning steady-state. The outlet temperature signal of the flow path is manipulated with a second order delay function (PT2) to approximate the transient behavior.

The Periphery is modeled analog to the fast 1P model so that the entire scalar 1P model includes only four simple differential equations for the storage system and one second-order differential equation for the PT2 block.

3.6 Validation of the Detailed Dynamic 2P Model

The detailed dynamic 2P Model includes the entire receiver system of which the receiver – especially the absorber tubes – incorporate novel modeling approaches that require validation. This model is an improved derivative of the one presented by Flesch et al. (2016). The main distinctions lie in the two-phase modeling approach and the crown temperature approximation. Hence, despite the crown temperatures, the validations by Flesch et al. (2016) with experiment and CFD data are still valid for the detailed dynamic 2P model in the 1P flow regime. Consequently, for optimal comparability, this work validates the modified crown temperature approximation by the same CFD data.

First, local tube wall and HTF film temperatures in steady-state flow in a single tube are examined. For this purpose, the simulations of the detailed dynamic 2P model (Dymola) and the CFD model are conducted with the same homogeneous solar flux with respect to the receiver surface (not tube

surface) and the same HTF mass flow rate. As a result, Figure 3-27 presents the circumferential temperature profiles at two vertical positions. Both the temperature profile on the inner (black) and outer surface (green) match on the back side (90 ° to 180 °) since there is no significant redial heat flow. However, at the front side (0 °), the CFD data reveal a great temperature difference between the outer and inner surface as well as a significant circumferential gradient due to the different angles of incidence. The Dymola model resembles the radial temperature difference well, but the coarse discretization obviously cannot reflect the circumferential gradient. Without the crown temperature approximation, the Dymola model would underestimate the peak surface temperature by approx. 27 K. However, the approximated crown temperatures of the outer and inner tube surface are overestimated by only 4 K and therefore hold as a slightly conservative approximation.

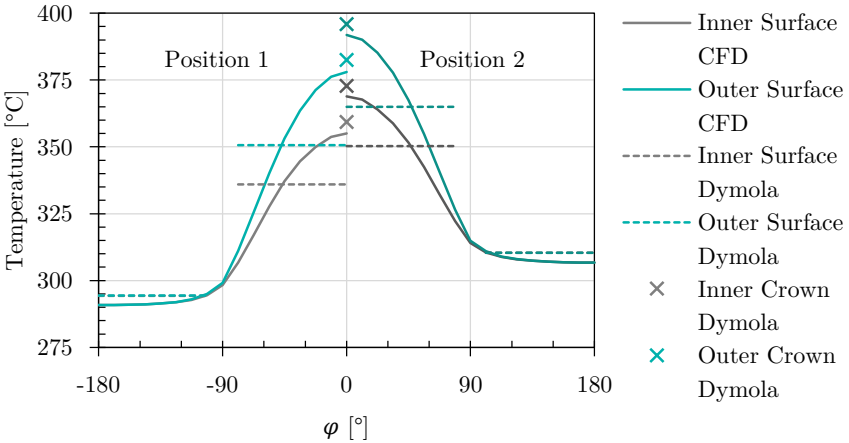

Figure 3-27: Circumferential tube wall temperature distribution at two heights in the Dymola model versus the CFD model

Regarding the 2P flow representation, the absorber tube model is validated with CFD simulations of a single empty absorber tube being filled at a constant mass flow rate. Before the simulation sequence examined, the tube is

preheated with constant solar flux. When it has reached a steady state, the filling is started. At this point, the plotted simulation time is reset to zero.

The resulting plot in Figure 3-28 reveals that even though this homogeneous 2P model includes significantly fewer differential equations than the two-fluid model by Flesch et al. (2016), it still provides a good representation of the hydraulic behavior during filling. It appears that the course of the molten salt level and the inlet pressure, which results from the geostatic pressure and friction in the filled elements, match with the CFD results very well, with only minor deviations of less than 0.2 %.

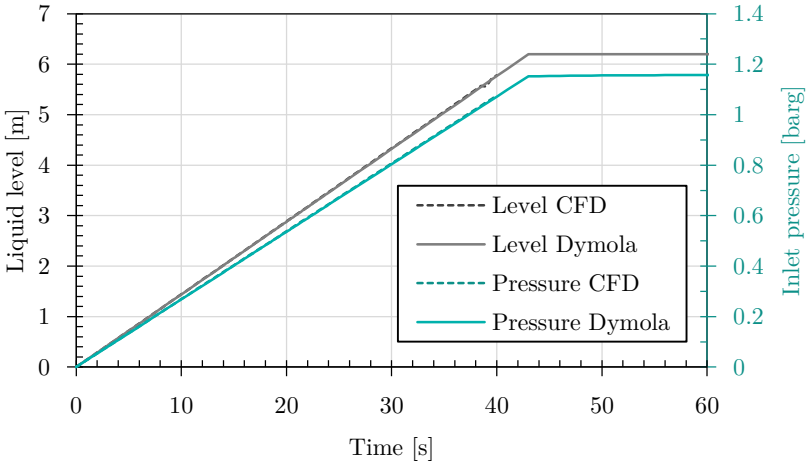

Figure 3-28: Trends of molten salt level and inlet pressure during filling

Finally, to validate the impact of varying convective heat transfer from the tube wall into the fluid (air vs. molten salt) during filling, Figure 3-29 depicts the front and backside wall temperatures at two different heights during filling from both Dymola and CFD simulation. These results confirm that this homogeneous 2P modeling approach achieves a satisfactory representation of the transient filling behavior of the preheated absorber tube.

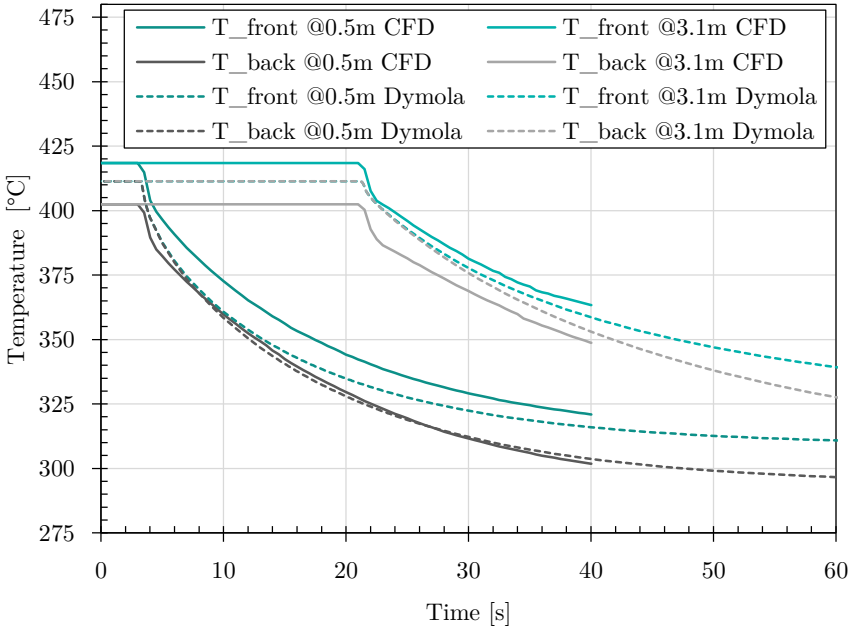

Figure 3-29: Front and back shell temperature trends at two different heights during absorber tube filling

The most significant deviation is observed in the temperature difference between tube front and back sides of the empty tube. The back shell is considered adiabatic to the environment due to well insulation and the heat flow into the medium (air) is zero when the preheating has reached steady-state. Consequently, the Dymola model shows the same temperature for the front and back shell. However, the CFD model considered the circumferential temperature profile caused by the much higher flux at the crown than at the edges. The plotted temperature is the average of the front half shell at a specific height. Therefore, it is higher than the edge temperature and thus higher than the adiabatic back shell. This only applies as long as the considered portion of the tube is empty. As soon as the forced convection in the molten salt starts at the respective tube position, the temperature difference between the front and back sides develops. Then the heat flow from the back

shell into the fluid causes a front-to-back temperature difference, which seems to converge to the same level as in the CFD model, as the trends in Figure 3-29 indicate. The overall trends of these temperatures during and after filling achieve satisfactory similarity between the Dymola and CFD models.

3.7 Validation of the Reduced Models

3.7.1 Semi-steady state operation

First, the receiver and system performance are validated for normal operation in a semi-steady state. For this, the scenario Sc_Clear_10s_-80%-50%_0800-1000, which is based on a clear-sky day, is simulated. The solar flux is stepwise reduced from a clear sky index (CSI) of 100 % to 20 %, 50 % and back to 100 %. These steps are spaced with 1 h intervals to allow the system to reach a semi-steady state. Figure 3-30 focuses on the resulting temperature trends of the detailed dynamic 2P model (reference) in comparison to the simplified dynamic 2P model, the fast 1P model and the scalar 1P model. In addition to the bulk temperatures in all seven manifolds (shades of green), the maximum film temperature (red) is plotted for the 2P models.

The corresponding deviations between the reduced models and the reference are plotted in Figure 3-31. For improved clarity, the bulk temperature deviations are plotted for only the first and last manifold. As expected, the simplified 2P model only shows small bulk temperature deviations between 0 K and 0.2 K, since it only contains a mild model reduction. The fast 1P model and the scalar 1P model perform quite similarly in this regard. They both deviate from the reference by approx. -0.8 K at low load (20 %), between -1.8 K and -2.8 K at full load. The (higher) deviations during the transitions between two semi-steady states are discussed in Section 3.7.2.

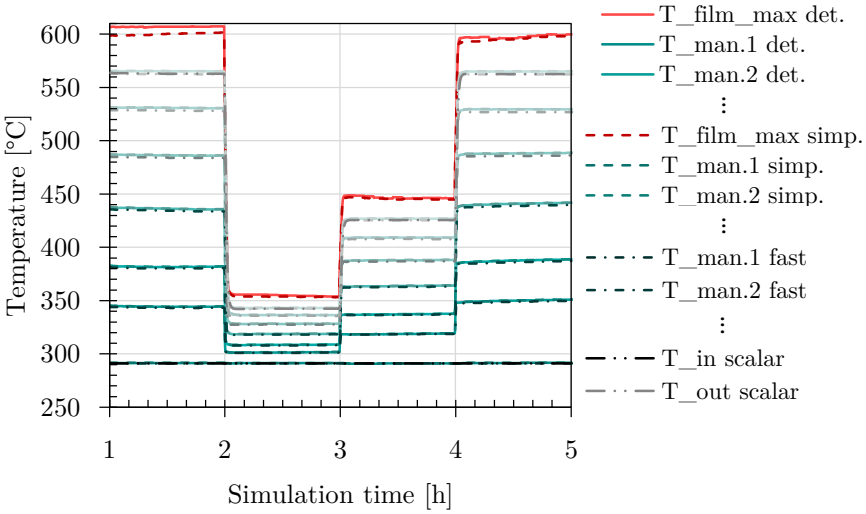

Figure 3-30: Receiver bulk and film temperature trends in the semi-steady-state validation

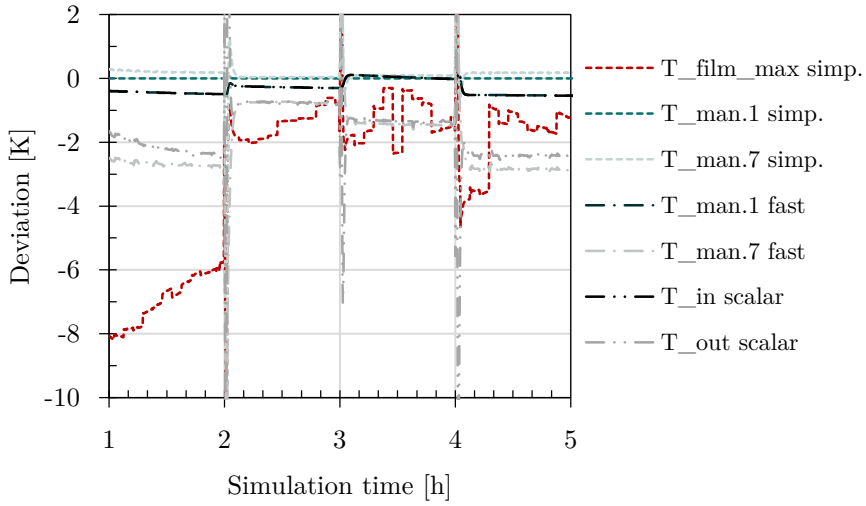

Figure 3-31: Deviations of temperature values in the semi-steady-state validation

The maximum film temperature, which is only considered in the 2P models, is more affected by the model reduction. Especially in the first shown interval between, which represents 07:00 to 08:00 in the morning, the simplified 2P model underestimated the maximum film temperature by approx. 8 K. This is due to averaging up to three flux values into one to represent parallel panels by only one tube. Since the flux distribution is less uniform in the morning, this is when this effect is most relevant. The minor stepwise variations are caused by updating the aim point configuration every 5 min.

Furthermore, Figure 3-32 compares the corresponding thermal receiver power and virtual net power trends of the reduced model to the reference. Besides the excellent alignment in this view, Figure 3-33 quantifies the relative deviations. The simplified 2P model miscalculates both the thermal power and the virtual net power by less than 0.04 %. However, the fast 1P model and scalar 1P model both underestimate the power values by less than 0.7 %.

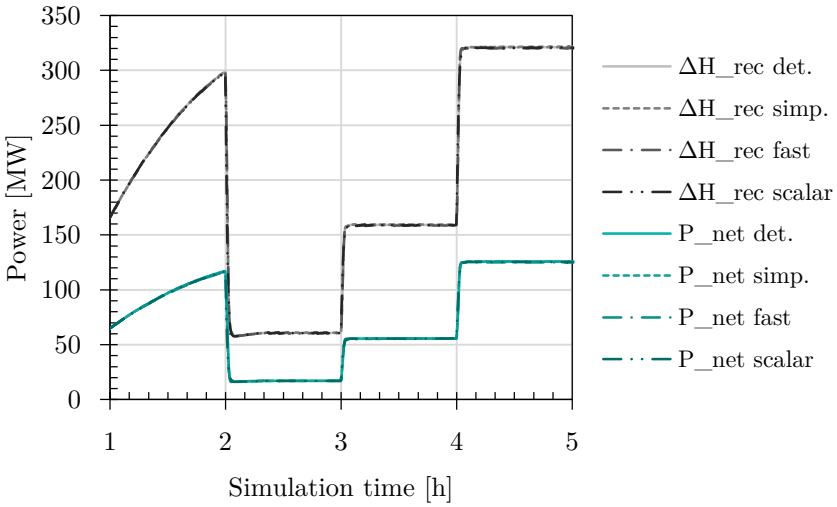

Figure 3-32: Thermal receiver power and virtual net power trends in the semi-steady-state validation

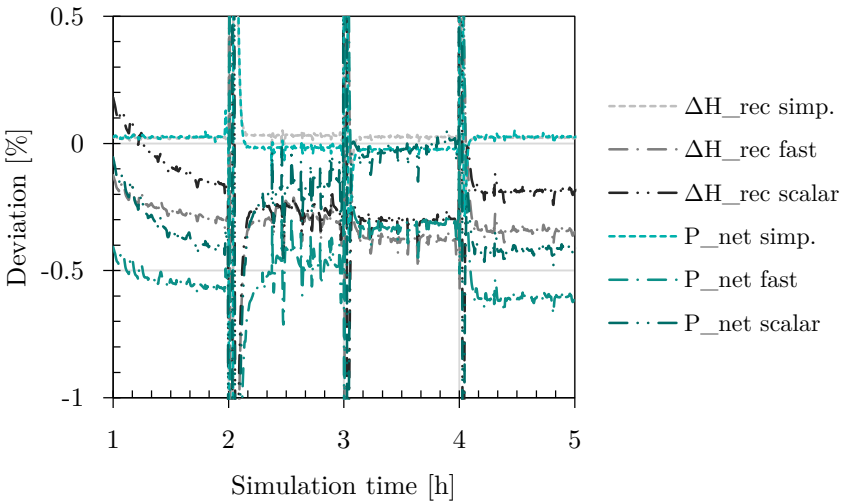

Figure 3-33: Deviations of thermal and virtual net power values in the semi-steady-state validation

3.7.2 Transient operation

3.7.2.1 Step response

The step response of the receiver system gives a good indication of how the system performs under fluctuating solar conditions. For this, the transition between two different semi-steady states in the scenario mentioned above Sc_Clear_10s_-80%-50%_0800-1000 is analyzed on a smaller time scale. As revealed in Figure 3-34 (step from 100 to 20 % CSI), the three most detailed models align quite well, whereas the scalar model deviates significantly. According to the relative deviations in Figure 3-35, the scalar model miscalculates by more than twice as much as the fast 1P model and even during higher absolute values, which therefore weighs more in the overall yield prediction. Also, the initial response of the scalar model is way too quick compared to the reference, which becomes more evident in fluctuating conditions in the subsequent section.

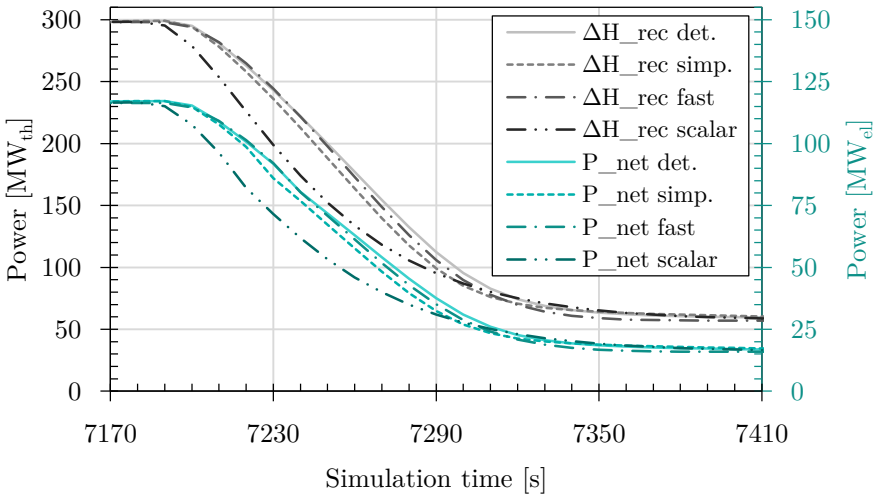

Figure 3-34: Thermal receiver power and virtual net power trends in the step response validation

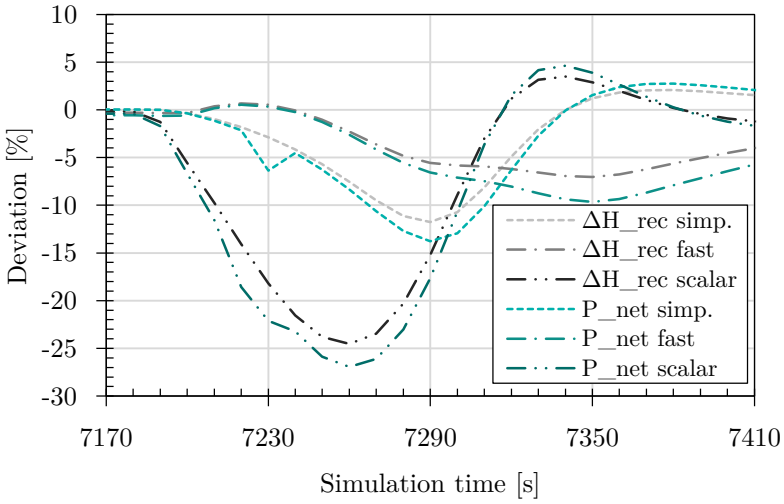

Figure 3-35: Deviations of power trends in the step response validation

Moreover, to put this into perspective, Figure 3-36 and Figure 3-37 show analog results for the smaller step from 50 % to 100 %. The net power deviation from the simplified 2P model shortly peaks at -13.7 % during the large step (dashed green line in Figure 3-35), respectively 7.4 % during the smaller step (dashed green line in Figure 3-37). In the same cases, the fast 1P model peaks at -9.6 %, respectively 2.4 %. Regarding the time integral during the large step response (Figure 3-35), the simplified 2P model deviates from the reference by 3.3 %, the fast 1P model by 2.3 % and the scalar model by 10.9 %. The corresponding integral errors for the smaller step response (Figure 3-37) are 1.2 %, 0.6 % and 2.0 %.

In conclusion, during large transients, the integral deviation from the scalar model is approx. five times higher than the fast 1P model. Hence, the fast 1P model is preferred for continuous operation prediction within the OAS.

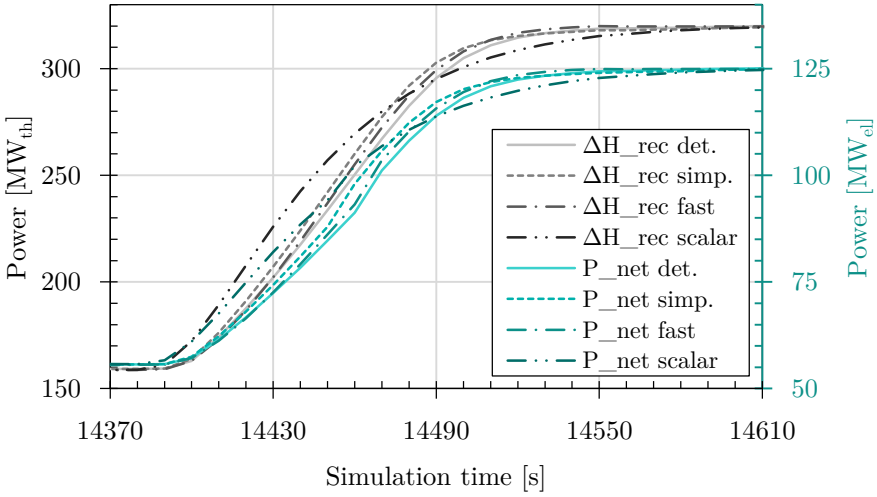

Figure 3-36: Thermal receiver power and virtual net power trends in the step response validation

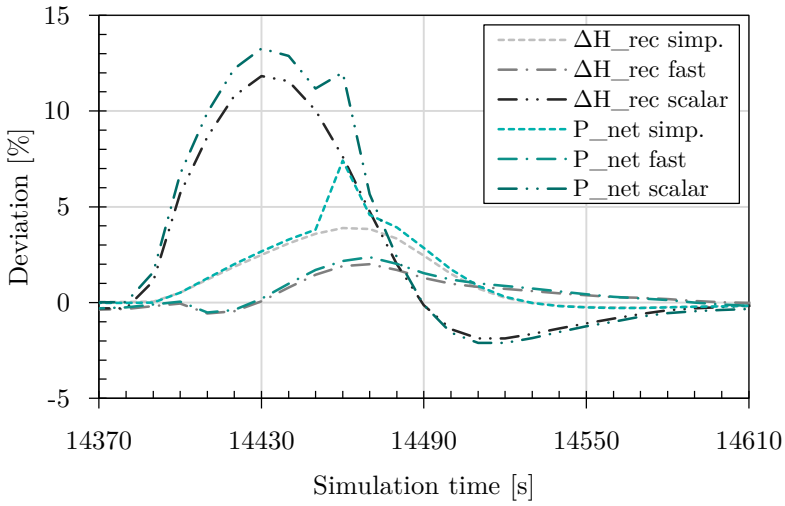

Figure 3-37: Deviations of power trends in the step response validation

3.7.2.2 Fluctuating conditions

To validate the reduced model in more realistic fluctuating conditions, the synthetic cloudy passage scenario Sc_7750 is simulated accordingly. As illustrated in Figure 3-38, the simplified 2P model and fast 1P model represent the bulk temperature trends between the receiver panels (in the manifolds) well without apparent deviations. More clarity is provided by Figure 3-39, revealing outlet temperature (manifold 7) deviations in both reduced models of up to approx. 7 K. The other bulk temperature deviations are less significant and excluded from this plot for better visibility.

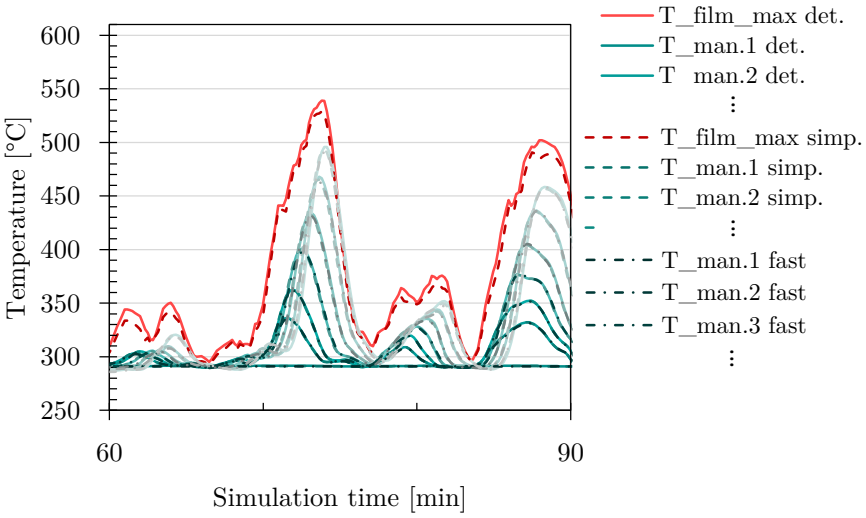

Figure 3-38: Receiver bulk and film temperature trends in fluctuating conditions

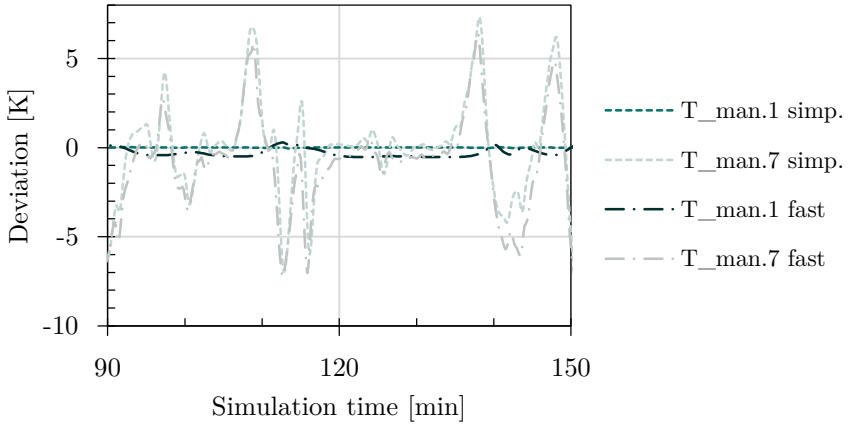

Figure 3-39: Bulk temperature deviations in fluctuating conditions

The maximum film temperature, however, is more affected by the model reduction. As presented in Figure 3-40, the simplified 2P model mainly underestimates this value by up to approx. 19 K. This can be traced back to averaging two to three flux values to reduce parallel panels to one single pipe. By this, the variety of flux values and therefore peak values decrease. For the OAS function developed in this work, the maximum film temperature is not a relevant result. However, for predicting the maximum film temperature, a different model reduction method would be recommended, similar to one published by Popp et al. (2019).

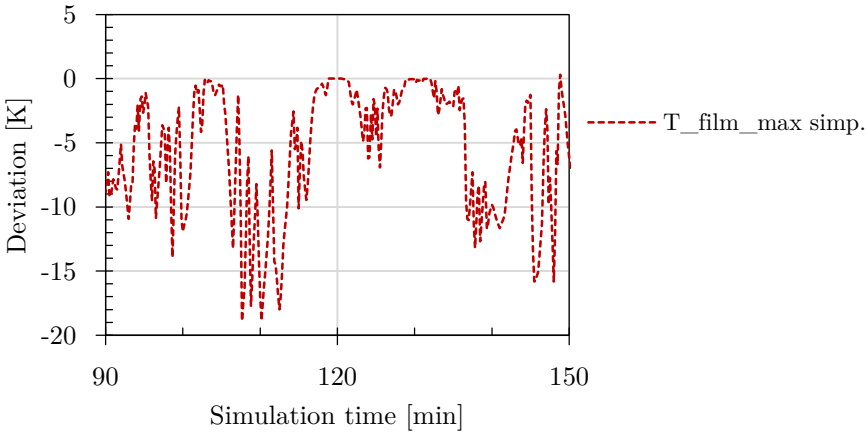

Figure 3-40: Maximum film temperature deviations in fluctuating conditions

Finally, the virtual net power of the same scenario is plotted in Figure 3-41. Analog to the temperatures also, these net power trends show well alignment between the reduced models and the detailed reference model. The deviation plot in Figure 3-42 mostly has small single-digit values with some peaks up to approx. 6 K deviation. This is because the time when the system switches between storage charging and recycling into the cold storage tank is slightly shifted. Therefore, the different models operate in different modes with different efficiencies for a short period and therefore deviate more decisively regarding net power.

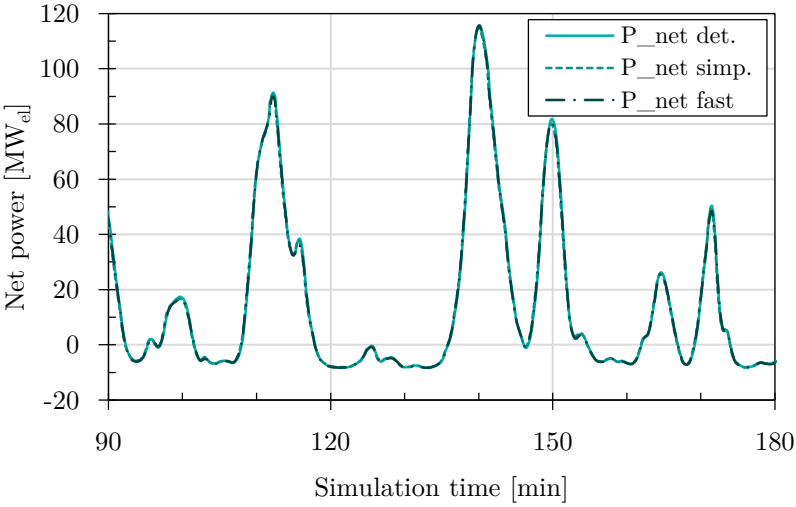

Figure 3-41: Virtual net power trends in fluctuating conditions

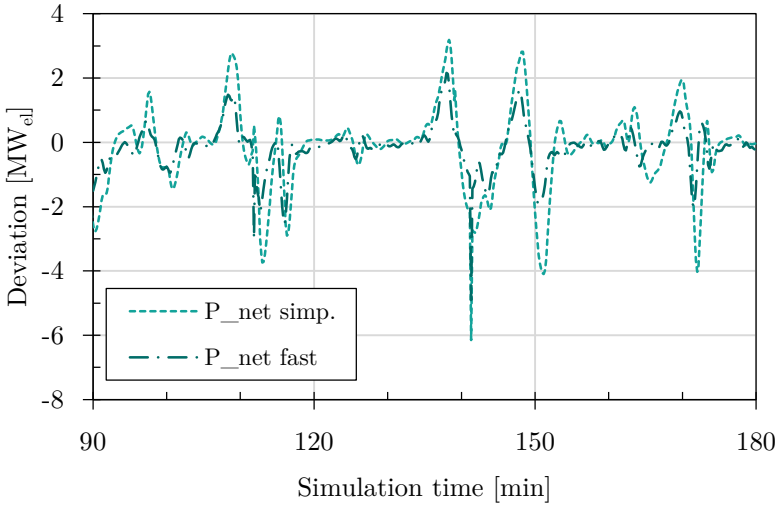

Figure 3-42: Net power deviations in fluctuating conditions

Since this effect only occurs for very short times and spike in both positive and negative directions, those peaks have a low impact on the integral value, hence the net energy output. This is illustrated in Figure 3-43, which indicates a small growing deviation between the two reduced models and the reference. The corresponding deviation plot in Figure 3-44 clarifies that the absolute deviation, despite some fluctuations, increases linearly with time at a rate of 0.15 MWh_{el}/h, which is approx. 0.12 % of the nominal net power. However, due to the low average yield during this sequence, the relative deviations of both reduced models converge to approx. 1 %.

In conclusion, both reduced models deviate by up to 1 % and are more accurate in conditions with less heavy and less volatile shadings. Since they agree even better with each other than with the reference, this indicates well suitability for the intended comparison of net yield predictions from the two models (within the decision algorithm).

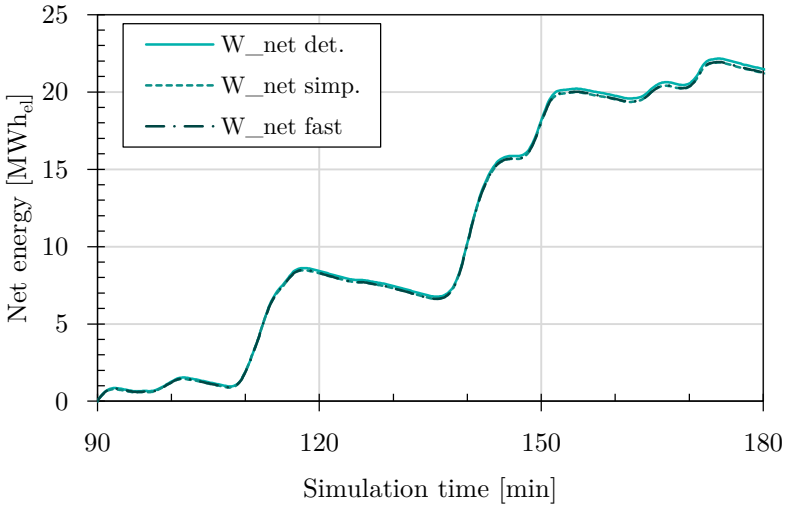

Figure 3-43: Virtual net energy output in fluctuating conditions

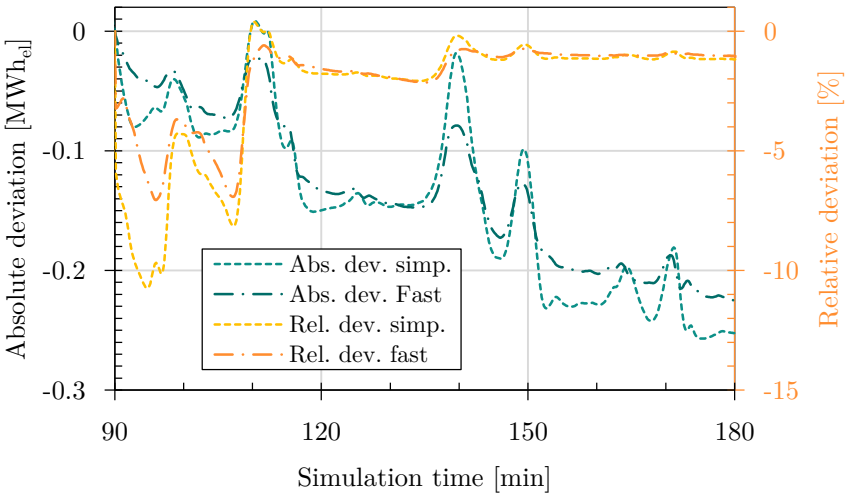

Figure 3-44: Virtual net energy deviations in fluctuating conditions

3.7.3 Startup procedure

Lastly, the simplified dynamic 2P model is validated regarding the startup procedure. Hence, a daily startup procedure at sunrise is simulated with the simplified and detailed dynamic 2P models. In Figure 3-45, the max. tube wall temperature trends reveal a gap between the first three and other panels during the solar preheating of the empty tubes. This is due to a flush flow, which was added for numerical stability and should not significantly affect the yield prediction. However, the excellent alignment of the two models reflects their similarity.

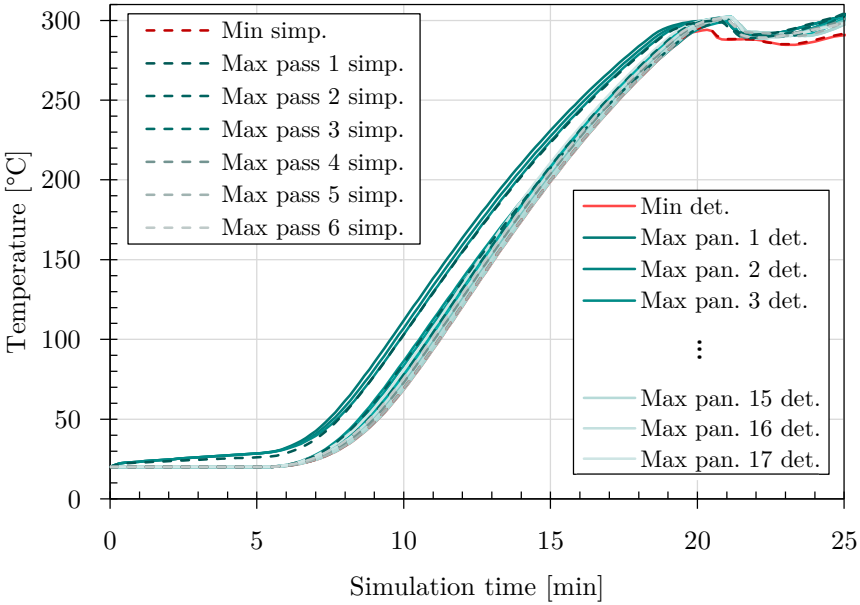

Figure 3-45: Min. and max. temperature trends of the absorber tube back wall for each panel during preheating and flood phase.

According to the corresponding deviations plot in Figure 3-46, the max values, which the preheat controller uses, deviate by -9 K to +5 K. Nevertheless, the total min. value, which is relevant for the timing of the next transition, deviates by less than 1 K during the preheat phase. As a result, the time at which the receiver flood phase is initiated is offset by less than 10 s. The peaks after 20 min simulation time are due to the incoming molten salt and are irrelevant to the yield prediction.

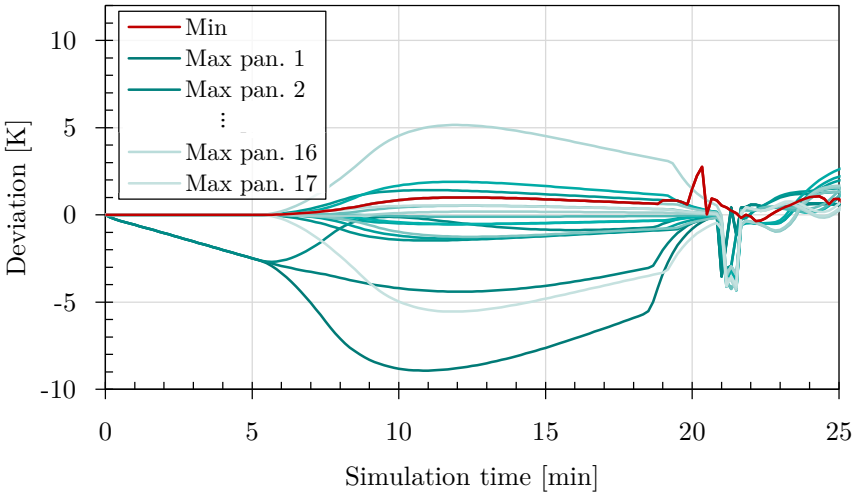

Figure 3-46: Deviations of wall temperature values during preheating and flood phase

Figure 3-47 shows the bulk temperatures between the panels (in manifolds) as well as the maximum film temperature during the subsequent ramp-up phase. Similar to the transient validation, the simplified model describes the bulk temperature trends well with deviations of less than 9 K during the ramp-up phase. The max. film temperature deviates less in this case because of the less dynamic flux density distribution (clear sky). The prominent peak at approx. 19 min is irrelevant since the underlying crown temperature approach is only supposed to be valid during normal flow conditions.

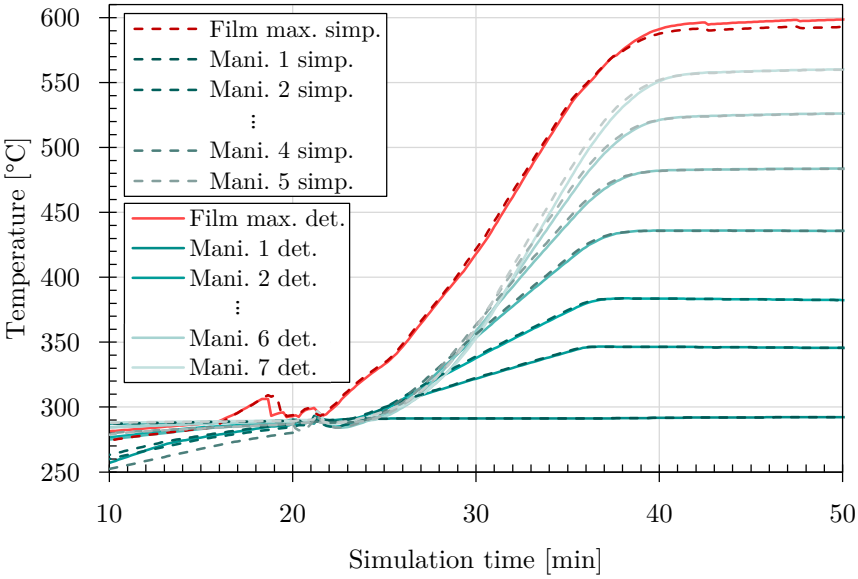

Figure 3-47: Trends of bulk temperatures between receiver panels (in manifolds) and the maximum film temperature during the flood and ramp-up phase

Lastly, the simulated thermal and electric power trends are plotted in Figure 3-49 and the corresponding deviations in Figure 3-50. The solar input only significantly deviates during the ramp-up phase since this start in the simplified model simulation approx. 10 s earlier. This also explains the thermal power deviation of up to 2.4 MW_{th} as well as the pumping power deviation of up to 0.6 MW_{el}.

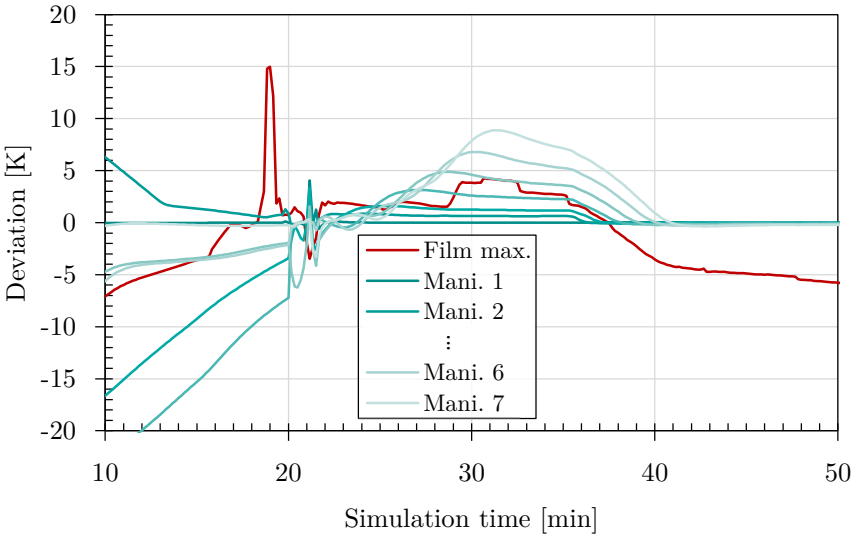

Figure 3-48: Deviations of bulk temperatures between receiver panels (in manifolds) and the maximum film temperature during the flood and ramp-up phase

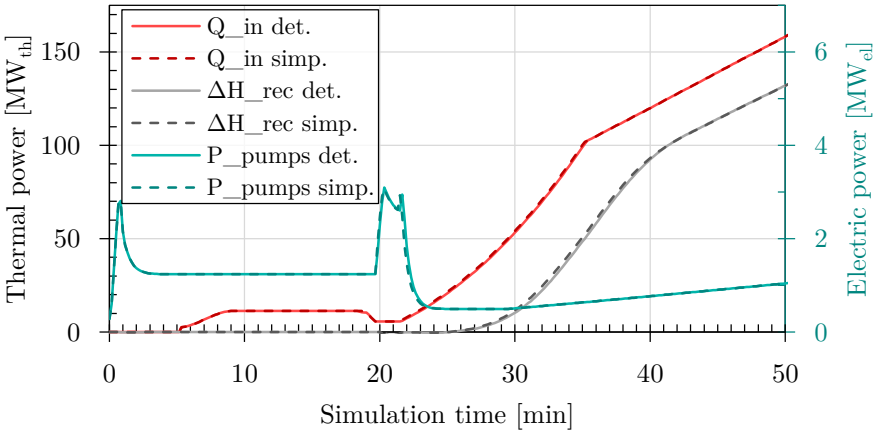

Figure 3-49: Thermal and electric power trends during the entire startup phase

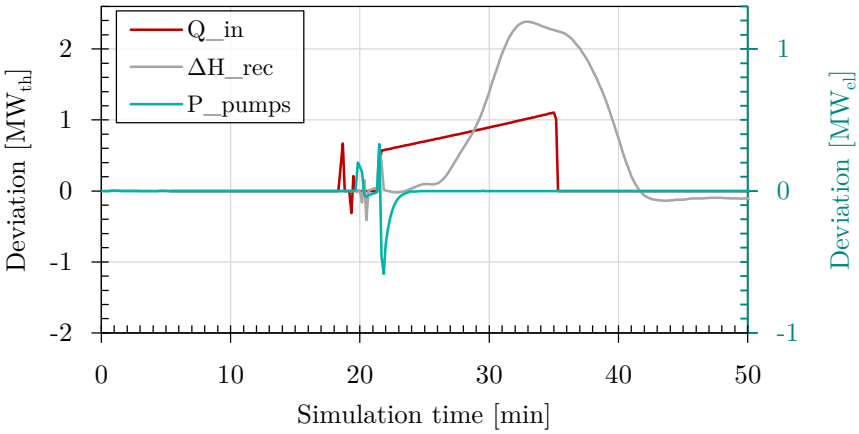

Figure 3-50: Power deviations during the entire startup phase

4 Decision Algorithm

The purpose of the decision algorithm is to determine when the MST can increase net yield by interrupting the receiver operation and to predict the expected gain by such a maneuver. At first glance, this poses an optimization problem with three variables, the time to shut the receiver operation down, the time to reinitiate its operation and the binary decision whether to perform this maneuver at all. Constraints are defined by the available solar resources, other ambient conditions as well as the physics of the system.

A possible methodology is to formulate the objective function, which would be the net yield, with certain constraints by means of optimization modeling and solving the resulting system of equations with the help of a dedicated optimization solver. The lower the mathematical complexity, the faster an optimization problem can be solved. One of the most efficient methods is linear programming (LP) and also quite efficient is mixed integer linear programming (MILP). Non-linear problems are manageable when the model is convex, because they have only one local minimum. There are solvers for other nonlinear problems, but without convexity, there is no guarantee for optimality and computing times increase drastically. (Anand et al. 2017; Arora 2015)

The optimization problem in this work is nonlinear. Theoretically, any model can be linearized with limited accuracy by applying segmented linearization on each nonlinear function, which increases the number of integer variables but allows applying MILP solvers. However, in this work a heuristic approach is developed instead. The objective function is formulated so that delayed impacts on net efficiency are shifted from the time of occurrence to the time of cause. This modification allows for the hypothesis the optimal time for a temporary shutdown is when the time derivative of the objective function becomes negative, whereas the optimal time for restarting is when it becomes positive. The derivation of such an objective function is carried out in the following.

4.1 Objective Function

4.1.1 Heat-to-power conversion

To optimize the MST receiver operation for maximum yield, the objective function needs to correlate with the net electricity production of the overall power plant. A lean approach is chosen to avoid a complex representation of the power block. In general, the net electricity output of the power block can be described as

$$P_{\mathrm{PB,net}} = \dot{Q}_{\mathrm{PB,in}}\,\eta_{\mathrm{PB}}\,, \tag{4.1}$$

in which the input heat flow rate can be replaced with the difference of in and outgoing enthalpy flow rates at the steam generator

$$\dot{Q}_{\mathrm{PB,in}} = \Delta\dot{H}_{\mathrm{SG,in}} = \left(\dot{H}_{\mathrm{SG,in}} - \dot{H}_{\mathrm{SG,out}}\right) \tag{4.2}$$

assuming that all heat losses of the steam generator are taken into account by the heat-to-power efficiency η_{BP}. This, however, highly depends on the temperature at which the heat is provided. Since the outlet temperature of a commercial molten salt receiver is often subject to fluctuations, even after mixing in the hot storage tank, there are some temperature variations, which can significantly influence this efficiency.

In this regard, the results of a sensitivity study are presented in Figure 4-1. For this, a state-of-the-art power block with intermediate superheating and five intermediate taps for regenerative preheating is simulated in EBSILON Professional (STEAG Energy Services GmbH 2020). The life steam temperature is varied while keeping the feed water mass flow rate constant. As a result, the thermal power intake decreases with lower temperatures and the net power output even more because the energy efficiency η_{net} decreases. In contrast, the exergy efficiency ζ_{net} shows no significant temperature dependency in the relevant range.

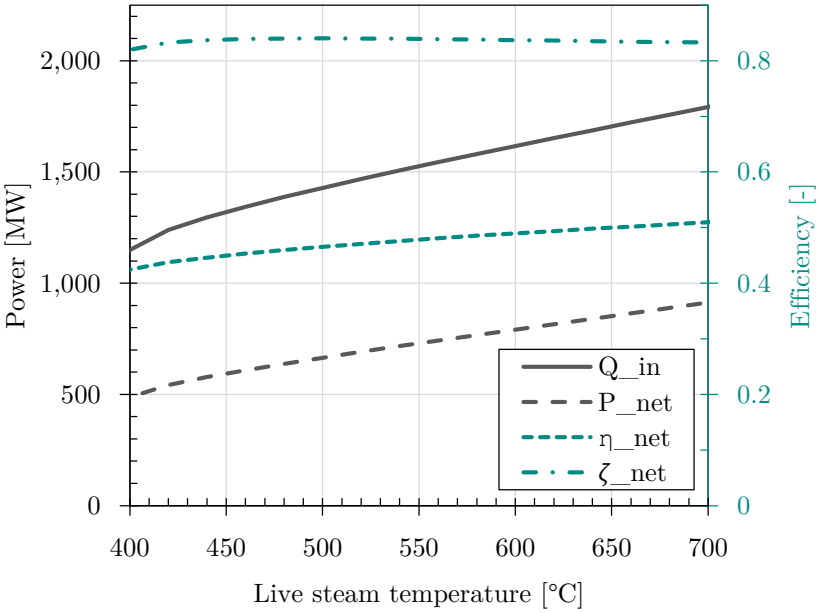

Figure 4-1: Temperature dependency of power block output and efficiency

Consequently, the exergy efficiency is assumed to be constant and defined as

$$\zeta_{\mathrm{PB}} = \frac{P_{\mathrm{PB,net}}}{\Delta \dot{E}_{\mathrm{x,SG,in}}} = \mathrm{const.} \tag{4.3}$$

with the difference between in and outgoing exergy flow rate $\Delta \dot{E}_{\mathrm{x,SG,in}}$ corresponding to $\Delta \dot{H}_{\mathrm{SG,in}}$. To determine the ζ_{PB} equation (4.1) with (4.2) can be applied to nominal operation resulting in

$$P_{\mathrm{PB,net,n}} = \Delta \dot{H}_{\mathrm{SG,in,n}}\, \eta_{\mathrm{PB,n}} \tag{4.4}$$

and combined with equation (4.3) to

$$\Rightarrow \zeta_{\mathrm{PB}} = \zeta_{\mathrm{PB,n}} = \frac{\mathrm{P_{PB,net,n}}}{\Delta \dot{E}_{\mathrm{x,SG,in,n}}} = \eta_{\mathrm{BP,n}} \frac{\Delta \dot{H}_{\mathrm{SG,in,n}}}{\Delta \dot{E}_{\mathrm{x,SG,in,n}}} \tag{4.5}$$

According to the general definition of the enthalpy of incompressible fluids (Schmidt 2019)

$$\Delta h = \overline{c_\mathrm{p}}\,\Delta T + v\,\Delta p \tag{4.6}$$

and the assumption that pressure changes in the steam generator are negligible, the enthalpy input can be formulated as

$$\begin{aligned}\Delta \dot{H}_{\mathrm{SG,in}} &= \dot{m}_{\mathrm{SG}}\,\overline{c_\mathrm{p}}\,\left[\left(T_{\mathrm{SG,in}} - T_{\mathrm{amb}}\right) - \left(T_{\mathrm{SG,out}} - T_{\mathrm{amb}}\right)\right] \\ &= \dot{m}_{\mathrm{SG}}\,\overline{c_\mathrm{p}}\left(T_{\mathrm{SG,in}} - T_{\mathrm{SG,out}}\right).\end{aligned} \tag{4.7}$$

The exergy describes how much working capability thermal energy contains (Schmidt 2019, p. 348) and is defined for a fluid flow as

$$\dot{E}_{\mathrm{x,h}} = \dot{m}\left[h - h_{\mathrm{amb}} + \frac{1}{2}\,c^2 + g\,z - T_{\mathrm{amb}}(s - s_{\mathrm{amb}})\right]. \tag{4.8}$$

with the specific entropy defined as

$$s - s_{\mathrm{amb}} = \overline{c_\mathrm{p}} \cdot \ln\frac{T}{T_{\mathrm{amb}}} \tag{4.9}$$

$$\Rightarrow \dot{E}_{\mathrm{x,h}} = \dot{m}\left[h - h_{\mathrm{amb}} - \overline{c_\mathrm{p}}\,T_{\mathrm{amb}}\,\ln\frac{T}{T_{\mathrm{amb}}}\right] \tag{4.10}$$

Based on this and the assumption that changes in kinetic and potential energy in a steam generator are negligible, the nominal exergy input through the molten salt flow can be formulated as

$$\begin{aligned}\Delta \dot{E}_{\mathrm{x,SG,in}} &= \dot{m}_{\mathrm{SG}}\left[h_{\mathrm{SG,in}} - h_{\mathrm{amb}} - \overline{c_\mathrm{p}}\,T_{\mathrm{amb}}\,\ln\frac{T_{\mathrm{SG,in}}}{T_{\mathrm{amb}}}\right] \\ &\quad - \dot{m}_{\mathrm{SG}}\left[h_{\mathrm{SG,out}} - h_{\mathrm{amb}} - \overline{c_\mathrm{p}}\,T_{\mathrm{amb}}\,\ln\frac{T_{\mathrm{SG,out}}}{T_{\mathrm{amb}}}\right] \\ &= \Delta \dot{H}_{\mathrm{SG,in}} - \dot{m}_{\mathrm{SG}}\,\overline{c_\mathrm{p}}\,T_{\mathrm{amb}}\,\ln\frac{T_{\mathrm{SG,in}}}{T_{\mathrm{SG,out}}}\end{aligned} \tag{4.11}$$

Finally, with equations (4.7) and (4.11), equation (4.5) results in

$$
\begin{aligned}
\Rightarrow \zeta_{\mathrm{PB}} &= \eta_{\mathrm{PB}} \cdot \left. \frac{\Delta \dot{H}_{\mathrm{SG,in}}}{\Delta \dot{H}_{\mathrm{SG,in}} - \dot{m}_{\mathrm{SG}}\, \overline{c_{\mathrm{p}}}\, T_{\mathrm{amb}}\, \ln \frac{T_{\mathrm{SG,in}}}{T_{\mathrm{SG,out}}}} \right|_{\mathrm{n}} \\
&= \eta_{\mathrm{PB}} \cdot \left. \frac{\dot{m}_{\mathrm{SG}}\, \overline{c_{\mathrm{p}}}\, \left(T_{\mathrm{SG,in}} - T_{\mathrm{SG,out}}\right)}{\dot{m}_{\mathrm{SG}}\, \overline{c_{\mathrm{p}}}\, \left(T_{\mathrm{SG,in}} - T_{\mathrm{SG,out}}\right) - \dot{m}_{\mathrm{SG}}\, \overline{c_{\mathrm{p}}}\, T_{\mathrm{amb}}\, \ln \frac{T_{\mathrm{SG,in}}}{T_{\mathrm{SG,out}}}} \right|_{\mathrm{n}} \\
&= \eta_{\mathrm{PB}} \cdot \left. \left(1 - \frac{T_{\mathrm{amb}}\, \ln \frac{T_{\mathrm{SG,in}}}{T_{\mathrm{SG,out}}}}{\left(T_{\mathrm{SG,in}} - T_{\mathrm{SG,out}}\right)} \right)^{-1} \right|_{\mathrm{n}}
\end{aligned}
\tag{4.12}
$$

Aligning with a previous study for commercial scale MST (Puppe et al. 2018), the nominal heat-to-power efficiency $\eta_{\mathrm{PB,n}}$ is assumed to be 41.6 %.

4.1.2 Parasitic losses

In addition, since the power block efficiency η_{PB} respectively ζ_{PB} only includes parasitic loss of the power block, the power consumption of the non-conventional part of the MST needs to be considered. Since the purpose of the described net power calculation is to derive optimal decisions for temporary receiver standby, it is assumed that the heliostat field tracking would need to stay active and its power consumption would not significantly differ between continuous and interrupted receiver operation. Therefore, parasitics of the heliostat field are neglected. Thus, only the energy consumption of the receiver pumps plays a relevant role. Hence, the overall plant net power output follows

$$
P_{\mathrm{net}} = P_{\mathrm{PB,net}} - P_{\mathrm{pumps}} = \Delta \dot{E}_{\mathrm{x,SG,in}} \cdot \zeta_{\mathrm{PB}} - P_{\mathrm{pumps}} \tag{4.13}
$$

Moreover, the current power production of the power block is usually prescribed by specific load demands and schedules. However, the overall electrical energy the power plant can generate is limited by the exergy effectively

stored in the thermal storage system. Even if the solar receiver and the steam generator operate simultaneously, the HTF always passes through the hot storage tank first to minimize temperature variation in the steam generator. Thus, the objective function must link the receiver output to the rate of change of available exergy in the storage system.

4.1.3 Stored exergy

In this regard, the different flow patterns between the receiver and the storage system are illustrated in Figure 4-2. Subfigure (a) describes the "normal" case in which the temperature of the HTF arriving at the storage system is sufficiently high to be charged into the hot storage tank. This directly contributes to gaining available exergy $\Delta E_{\mathrm{x,hTank}}$ while variations in the flow temperature change the hot tank (inventory) temperature T_{hTank} and with it the associated power block efficiency η_{PB}. The steam generator is assumed to return the HTF at a fixed temperature so that the cold tank (inventory) temperature is not affected when it has nominal value.

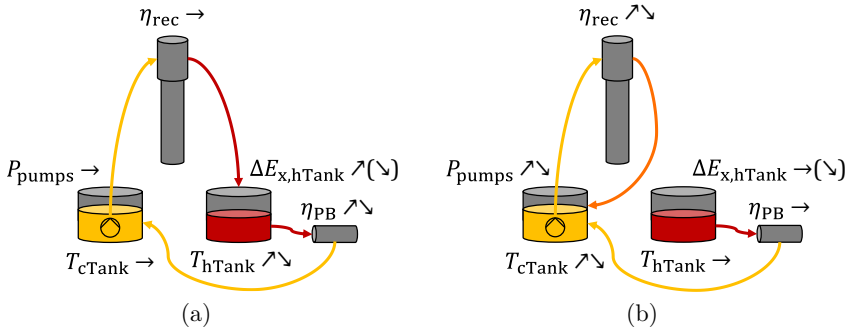

Figure 4-2: Different flow patterns between receiver and storage system at high (a) and low (b) receiver outlet temperatures

In contrast, when the receiver can only provide relatively low flow temperatures during low solar irradiation, the partially heated HTF is recycled into the cold storage tank, thus not available for the steam generator. However, it usually causes a temperature rise in the cold storage tank. The associated

rise in the receiver inlet temperature results in lower receiver efficiency. Additionally, due to the decreased receiver temperature spread, a higher HTF mass flow rate is required resulting in additional pumping energy consumption. In the case of nearly zero DNI (full cloud cover), the thermal losses of the receiver effectively cool the molten salt inventory down, causing opposite effects on the receiver efficiency and pumping energy consumption.

In order to derive how the rate of change of available exergy in the storage system depends on the receiver output, the exergy content of the hot storage tank is analyzed. The molten salt thermal storage system stores internal energy of the medium. In general, the exergy contained within a closed system can be described based on the internal energy as: (Schmidt 2019, p. 348)

$$E_{\mathrm{x,u}} = m\left[u - u_{\mathrm{amb}} + \frac{1}{2}c^2 + gz - T_{\mathrm{amb}}(s - s_{\mathrm{amb}}) + p_{\mathrm{amb}}(v - v_{\mathrm{amb}})\right] \tag{4.14}$$

Changes in kinetic and potential energy in the storage tanks are negligible. Even though molten salt can be considered incompressible, it experiences significant changes in specific volumes with varying temperatures. Still, in the relevant temperature range of 290 to 565 °C the environment work

$$p_{\mathrm{amb}}\left(v_{\mathrm{SG,in,n}} - v_{\mathrm{SG,out,n}}\right) \approx 1 \cdot 10^5\ \mathrm{Pa}\ (5.79 - 5.25) \cdot 10^{-4}\ \frac{\mathrm{m^3}}{\mathrm{kg}} \approx 6\ \frac{\mathrm{J}}{\mathrm{kg}} \tag{4.15}$$

is more than four orders of magnitude smaller than the reversible transferred heat

$$T_{\mathrm{amb}}\left(s_{\mathrm{SG,in,n}} - s_{\mathrm{SG,out,n}}\right) \approx 293\ \mathrm{K} \cdot 1.521\ \frac{\mathrm{kJ}}{\mathrm{kg\ K}} \cdot \ln\frac{838\ \mathrm{K}}{563\ \mathrm{K}} \approx 177\ \frac{\mathrm{kJ}}{\mathrm{kg}} \tag{4.16}$$

and is therefore negligible. Hence, equation (4.14) is reduced to

$$E_{\mathrm{x,u}} = m[u - u_{\mathrm{amb}} - T_{\mathrm{amb}}(s - s_{\mathrm{amb}})] \tag{4.17}$$

with the specific internal energy (Schmidt 2019, p. 229)

$$u - u_{\mathrm{amb}} = \overline{c_{\mathrm{p}}}\,(T - T_{\mathrm{amb}}) \tag{4.18}$$

and entropy according to equation (4.9). This concludes (4.17) to

$$\Rightarrow E_{\mathrm{x,u}} = m\,\overline{c_{\mathrm{p}}}\left[(T - T_{\mathrm{amb}}) - T_{\mathrm{amb}}\ln\frac{T}{T_{\mathrm{amb}}}\right] \tag{4.19}$$

with the inventory mass of molten salt m, the temperature of the ideally mixed molten salt T, and its mean specific heat capacity $\overline{c_p}$.

In order to determine how incoming and outgoing flows affect the stored exergy in the molten salt tanks, the time derivative of the exergy is derived as follows:

$$\begin{aligned}\frac{dE_{\mathrm{x,u}}}{dt} = \frac{dm}{t}\,\overline{c_{\mathrm{p}}}\left[(T - T_{\mathrm{amb}}) - T_{\mathrm{amb}}\ln\frac{T}{T_{\mathrm{amb}}}\right]\\ + m\,\overline{c_{\mathrm{p}}}\left[\frac{d}{dt}(T - T_{\mathrm{amb}}) - T_{\mathrm{amb}}\frac{d}{dt}\left(\ln\frac{T}{T_{\mathrm{amb}}}\right)\right]\end{aligned} \tag{4.20}$$

Combined with a transient mass balance for the considered tank

$$\frac{dm}{dt} = (\dot{m}_{\mathrm{in}} - \dot{m}_{\mathrm{out}}) \tag{4.21}$$

it results in

$$\begin{aligned}\Rightarrow \dot{E}_{\mathrm{x,u}} &= (\dot{m}_{\mathrm{in}} - \dot{m}_{\mathrm{out}})\,\overline{c_{\mathrm{p}}}\left[(T - T_{\mathrm{amb}}) - T_{\mathrm{amb}}\ln\frac{T}{T_{\mathrm{amb}}}\right]\\ &\quad + m\,\overline{c_{\mathrm{p}}}\left[\frac{dT}{dt} - T_{\mathrm{amb}}\frac{1}{T}\cdot\frac{dT}{dt}\right]\\ &= (\dot{m}_{\mathrm{in}} - \dot{m}_{\mathrm{out}})\,\overline{c_{\mathrm{p}}}\left[(T - T_{\mathrm{amb}}) - T_{\mathrm{amb}}\ln\frac{T}{T_{\mathrm{amb}}}\right]\\ &\quad + m\overline{c_{\mathrm{p}}}\,\frac{dT}{dt}\left[1 - \frac{T_{\mathrm{amb}}}{T}\right]\end{aligned} \tag{4.22}$$

The last remaining unknown $\frac{dT}{dt}$ can be derived from a transient energy balance for the considered tank:

$$\frac{dU}{dt} = \dot{m}_{\mathrm{in}}\left(h_{\mathrm{in}} + \frac{1}{2}c_{\mathrm{in}}^2\right) - \dot{m}_{\mathrm{out}}\left(h_{\mathrm{out}} + \frac{1}{2}c_{\mathrm{out}}^2\right) \tag{4.23}$$

for which the specific enthalpy can be determined by equation (4.6). As before, changes in kinetic energy and pressure changes are insignificant. Hence, with

$$h - h_{\mathrm{amb}} = \overline{c_{\mathrm{p}}}\,(T - T_{\mathrm{amb}}) \tag{4.24}$$

equation (4.23) is transformed to

$$\frac{d}{dt}\left(m \cdot \overline{c_{\mathrm{p}}}(T - T_{\mathrm{amb}})\right) = \dot{m}_{\mathrm{in}}\overline{c_{\mathrm{p}}}(T_{\mathrm{in}} - T_{\mathrm{amb}}) - \dot{m}_{\mathrm{out}}\overline{c_{\mathrm{p}}}(T_{\mathrm{out}} - T_{\mathrm{amb}}) \tag{4.25}$$

$$\Leftrightarrow \frac{dm}{dt}(T - T_{\mathrm{amb}}) + m\frac{dT}{dt} = \dot{m}_{\mathrm{in}}(T_{\mathrm{in}} - T_{\mathrm{amb}}) - \dot{m}_{\mathrm{out}}(T_{\mathrm{out}} - T_{\mathrm{amb}}) \tag{4.26}$$

With the help of equation (4.21), some more conversions

$$\begin{aligned} \Leftrightarrow (\dot{m}_{\mathrm{in}} - \dot{m}_{\mathrm{out}})(T - T_{\mathrm{amb}}) + m\frac{dT}{dt} \\ = \dot{m}_{\mathrm{in}}(T_{\mathrm{in}} - T_{\mathrm{amb}}) - \dot{m}_{\mathrm{out}}(T_{\mathrm{out}} - T_{\mathrm{amb}}) \end{aligned} \tag{4.27}$$

$$\begin{aligned} \Leftrightarrow m\frac{dT}{dt} = \dot{m}_{\mathrm{in}}(T_{\mathrm{in}} - T_{\mathrm{amb}}) - \dot{m}_{\mathrm{out}}(T_{\mathrm{out}} - T_{\mathrm{amb}}) \\ - (\dot{m}_{\mathrm{in}} - \dot{m}_{\mathrm{out}})(T - T_{\mathrm{amb}}) \end{aligned} \tag{4.28}$$

$$\begin{aligned} \Leftrightarrow \frac{dT}{dt} = \frac{\dot{m}_{\mathrm{in}}}{m}(T_{\mathrm{in}} - T_{\mathrm{amb}} - T + T_{\mathrm{amb}}) \\ - \frac{\dot{m}_{\mathrm{out}}}{m}(T_{\mathrm{out}} - T_{\mathrm{amb}} - T + T_{\mathrm{amb}}) \end{aligned} \tag{4.29}$$

and considering that in an ideally mixed mass of molten salt $T_{\mathrm{out}} = T$, it finally concludes to

$$\Rightarrow \frac{dT}{dt} = \frac{\dot{m}_{\mathrm{in}}}{m}(T_{\mathrm{in}} - T) \tag{4.30}$$

Consequently, combining equations (4.22) and (4.30) results in

$$\begin{aligned} \Rightarrow \dot{E}_{\mathrm{x,u}} = (\dot{m}_{\mathrm{in}} - \dot{m}_{\mathrm{out}})\overline{c_{\mathrm{p}}}\left[(T - T_{\mathrm{amb}}) - T_{\mathrm{amb}}\ln\frac{T}{T_{\mathrm{amb}}}\right] \\ + \dot{m}_{\mathrm{in}}\overline{c_{\mathrm{p}}}(T_{\mathrm{in}} - T)\left[1 - \frac{T_{\mathrm{amb}}}{T}\right] \end{aligned} \tag{4.31}$$

$$= f(\dot{m}_{\mathrm{in}}, \dot{m}_{\mathrm{out}}, T_{\mathrm{in}}, T)$$

with the first part representing convective exergy gains and the second part accounting for exergy gain due to temperature change. By this, the rate of change of the exergy of the internal energy inside a closed vessel depends on the in and outgoing mass flow rates, the inlet temperature and the current inventory temperature.

Furthermore, the exergy is relative to the ambient temperature, which means that it represents the amount of work that can potentially be extracted by energy conversion if the medium is cooled down to ambient temperature. However, only a portion of this is effectively fed into the power block because the exergy of the return flow must be considered as well. With respect to the stored exergy, this means that the remaining exergy of the HTF, after it was used and cooled down through the steam generator and returned to the cold storage tank, needs to be subtracted. In this sense, the exergy extracted by the SG is derived by applying equation (4.19) to the hot storage tank inventory before and after it will have passed through the SG:

$$\begin{aligned} \Delta E_{\mathrm{x,hTank}} = {} & m_{\mathrm{hTank}}\,\overline{c_{\mathrm{p}}}\left[(T_{\mathrm{hTank}} - T_{\mathrm{amb}}) - T_{\mathrm{amb}} \ln\frac{T_{\mathrm{hTank}}}{T_{\mathrm{amb}}}\right] \\ & - m_{\mathrm{hTank}}\,\overline{c_{\mathrm{p}}}\left[\left(T_{\mathrm{SG,out}} - T_{\mathrm{amb}}\right) - T_{\mathrm{amb}} \ln\frac{T_{\mathrm{SG,out}}}{T_{\mathrm{amb}}}\right] \end{aligned} \tag{4.32}$$

This is transformed into the rate of change of the usable exergy stored in the hot storage tank analog to the transformation of equations (4.20) to (4.31) resulting in

$$\begin{aligned} \Delta \dot{E}_{\mathrm{x,hTank}} = {} & (\dot{m}_{\mathrm{in}} - \dot{m}_{\mathrm{out}})\overline{c_{\mathrm{p}}}\left[\left(T_{\mathrm{hTank}} - T_{\mathrm{SG,out,n}}\right) - T_{\mathrm{amb}} \ln\frac{T_{\mathrm{hTank}}}{T_{\mathrm{SG,out,n}}}\right] \\ & + \dot{m}_{\mathrm{in}}\overline{c_{\mathrm{p}}}\left(T_{\mathrm{hTank,in}} - T_{\mathrm{hTank}}\right)\left[1 - \frac{T_{\mathrm{amb}}}{T_{\mathrm{hTank}}}\right] \end{aligned} \tag{4.33}$$

One final modification is necessary to account for the two receiver flow paths. Since they can be operated independently, the decision proposal from the

OAS should also be derived for each flow path individually. Thus, the objective function needs to consider the effect of the output of one single flow path. Actually, both HTF flows are mixed together in the outlet vessel and the joint flow reaches the storage system after descending through the downcomer. Due to the conservation of energy and negligible thermal losses along the downcomer, it is assumed that the sum of exergy losses by mixing different temperatures in the inlet vessel and in the storage tank is the same as if both flows would descend unmixed and only mix in the storage tank. This justifies utilizing the flow path outlet temperature instead of the storage tank inlet temperature. Besides, the outgoing mass flow rate is equal to the one of the SG. The portion of exergy change in the hot storage tank that is caused by the output of the first receiver flow path can then be formulated as follows:

$$\begin{aligned}\Delta\dot{E}_{\mathrm{x,hTank,FP1}} = &\left(\dot{m}_{\mathrm{FP1\rightarrow hTank}} - \frac{\dot{m}_{\mathrm{SG}}}{2}\right)\overline{c_{\mathrm{p}}} \\ &\cdot\left[\left(T_{\mathrm{hTank}} - T_{\mathrm{SG,out,n}}\right) - T_{\mathrm{amb}}\ln\frac{T_{\mathrm{hTank}}}{T_{\mathrm{SG,out,n}}}\right] \\ &+\dot{m}_{\mathrm{FP1\rightarrow hTank}}\,\overline{c_{\mathrm{p}}}\left(T_{\mathrm{FP1,out}} - T_{\mathrm{hTank}}\right)\left[1 - \frac{T_{\mathrm{amb}}}{T_{\mathrm{hTank}}}\right] \\ &= f\left(\dot{m}_{\mathrm{FP1\rightarrow hTank}}, \dot{m}_{\mathrm{SG}}, T_{\mathrm{FP1,out}}, T_{\mathrm{hTank}}\right)\end{aligned} \tag{4.34}$$

Strictly speaking, this equation implies mixing the flow path outlet temperature with the current storage tank temperature, even though the latter might change during the time it takes for the HTF to travel from the receiver to the storage system. This is neglected since the storage temperature usually changes relatively slowly due to the large size of the thermal storage system. Finally, the mass flow rate into the hot storage tank is linked to the flow path mass flow rate depending on the flow temperature:

$$\dot{m}_{\mathrm{FP1\rightarrow hTank}} = \begin{cases}\dot{m}_{\mathrm{FP1,out}}, & T_{\mathrm{FP1,out}} > T_{\mathrm{switch}} \\ 0, & T_{\mathrm{FP1,out}} \leq T_{\mathrm{switch}}\end{cases} \tag{4.35}$$

4.1.4 Virtual net power

To sum up, sections 4.1.1 and 4.1.2 present the mathematics to determine the actual net power output of the whole power plant from the exergy input at the steam generator. The metric of interest is the net power equivalent of the current output of one receiver flow path. In the net power equation (4.13), the exergy input of the steam generator $\Delta\dot{E}_{\mathrm{x,SG,in}}$ cannot just be replaced by the exergy output of the flow path $\Delta\dot{E}_{\mathrm{x,FP1,out}}$ because by this the exergy losses due to mixing different temperatures in the storage tank would be falsely neglected. Therefore, the rate of exergy change caused by FP1 in the hot storage tank $\Delta\dot{E}_{\mathrm{x,hTank,FP1}}$ is added to the equation. In turn, the actual net power equivalent of the first receiver flow path can be defined as

$$P_{\mathrm{net,FP1}} = \left(\Delta\dot{E}_{\mathrm{x,hTank,FP1}} + \frac{\Delta\dot{E}_{\mathrm{x,SG,in}}}{2}\right)\cdot\zeta_{\mathrm{PB}} - P_{\mathrm{pumps}}\,\frac{\dot{m}_{\mathrm{FP1,out}}}{\dot{m}_{\mathrm{pumps}}}. \qquad (4.36)$$

Here, the exergy input to the steam generator is halved ($\frac{\Delta\dot{E}_{\mathrm{x,SG,in}}}{2}$). Actually, this and the $\frac{\dot{m}_{\mathrm{SG}}}{2}$ in equation (4.34) cancel each other out. Thus, it has no impact on the resulting net power but is kept in the equation to maintain clarity among the other variables. Also, the pumping energy consumption is scaled down to the portion corresponding to this receiver flow path.

At first glance, since only the flow going into the hot storage tank is incorporated in this net power definition, it might give the impression that any HTF respectively energy that is recycled into the cold storage tank could be considered a loss of yield. However, Figure 4-3 presents the resulting solar input and net power output trends according to this approach. It is evident that at low outlet temperatures (compare Figure 4-4), the net power drops below zero because no exergy is charged into the hot storage tank while the receiver pumps still consume power.

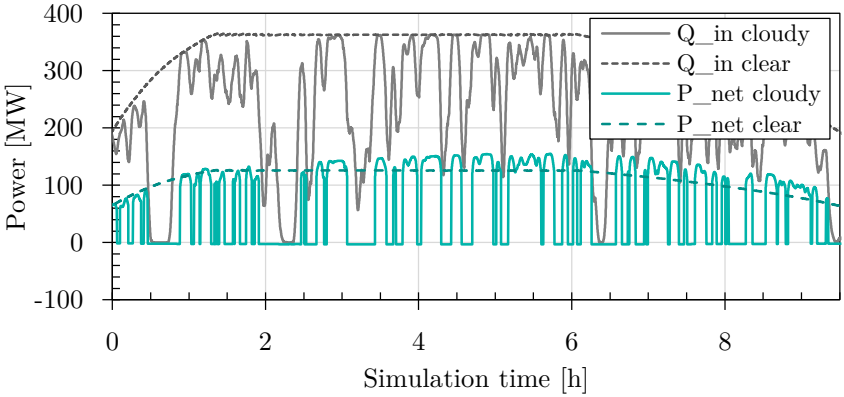

Figure 4-3: Power trends based on equation (4.36) on a cloudy day compared to a clear day

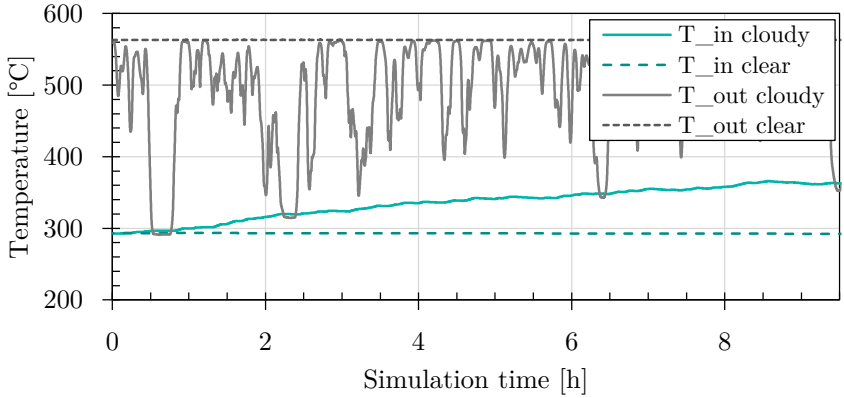

Figure 4-4: Receiver (flow path) in and outlet temperature trends on a cloudy day compared to a clear day

It is also noticeable that after significant times of heavily shaded conditions, thus HTF recycling, the net power values between the shaded periods increase beyond the clear-sky values. As initially discussed by Schwager et al. (2019) this phenomenon is due to the temperature rise in the cold storage tank and therefore higher receiver inlet temperature, which can be observed in Figure 4-4. Since this net power metric is based on exergy flow relative to

SG return temperature, it results in elevated net power compared to if no recycling has happened before. By this, the temporarily lost yield, which is withheld in the cold storage tank, is later recovered and, therefore, available for net power production. Hence, this phenomenon is fully taken into account if the simulation runs until either the cold storage temperature normalizes again or the tank is fully drained. Then by integrating the net power over the entire simulation time, this dynamic effect could be fully covered.

For the OAS, which is supposed to predict net yield within a short computing time, this approach is impractical since each decision proposal would require simulating at least a whole day. Instead, an alternative approach is developed to incorporate energy recovery, including associated losses in the net power value at the time at which it is initially provided by the receiver. This **virtual net power** approach is illustrated in a Sankey diagram in Figure 4-5. The top portion of the diagram refers to the energy flow during nominal operation (clear sky). The thermal power provided by the receiver contains about 70 % exergy, while the remaining anergy poses pure energy loss. Further conversion losses occur in the heat-to-power conversion process, resulting in equivalent electric power. From that, the parasitic power consumption by the receiver pumps is subtracted, leaving the (virtual) net power as the effective yield of the power plant. This is understood as the net power equivalent of the actual thermal power output of the receiver. It distinguishes it from the actual net power since the thermal storage allows the power block to operate independently from the solar part of the plant.

In cloudy conditions, the proportions change as follows. The middle part in Figure 4-5 illustrates the case when the HTF temperature has dropped but is still fed into the hot storage tank. Not only does the thermal power decrease, but also the exergy portion can drop down to less than 50 %, due to the decreased outlet temperature. Hence, the heat-to-power efficiency decreases as well. Therefore, if the outlet temperature of the receiver drops below a defined threshold, the energy is usually recycled and withheld in the cold storage tank to reuse the HTF and lift the thermal energy to a higher

temperature later. By this, the exergy portion, thus the heat-to-power efficiency, is increased, as shown in the bottom part of Figure 4-5.

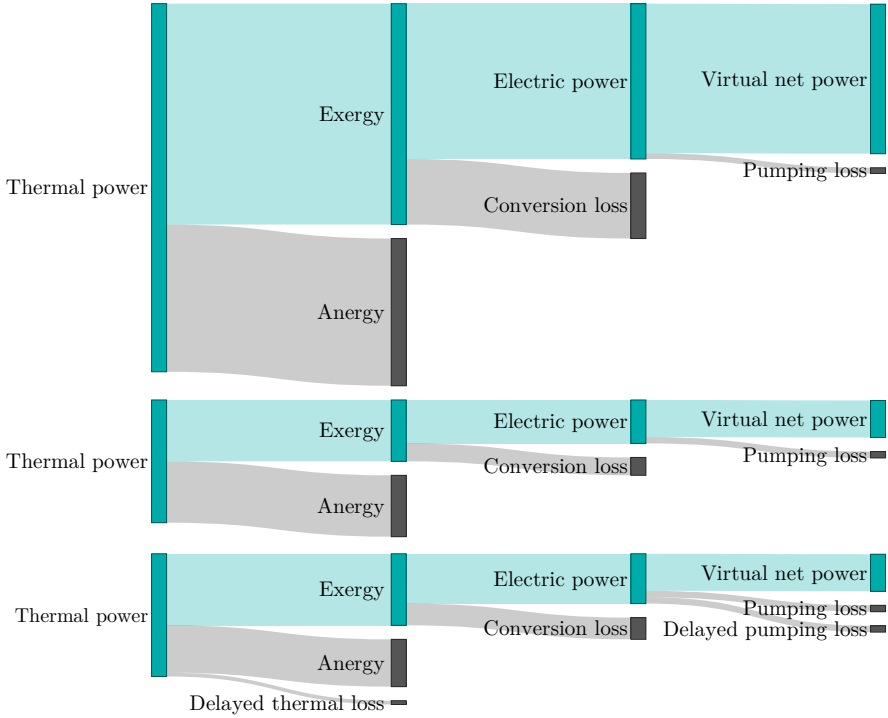

Figure 4-5: Energy flow at clear (top) and cloudy (middle and bottom) conditions from thermal receiver output to virtual net power; with (bottom) and without recycling (top and middle)

However, the delayed losses mentioned above affect the net yield as well. Therefore, the effect of impaired receiver efficiency due to elevated inlet temperatures is deducted from the actual thermal receiver output as delayed thermal energy loss. Furthermore, additional pumping power consumption is deducted from the electric power to account for the need to pump the HTF up to the receiver a second time to make the recycled energy available. By

this, the virtual net power approach accounts for all thermal losses at the time of causation instead of the time of occurrence.

Accordingly, equation (4.36) is extended as follows:

$$P^*_{\mathrm{net,FP1}} = \left(\Delta\dot{E}_{\mathrm{x,hTank,FP1}} + \frac{\Delta\dot{E}_{\mathrm{x,SG,in}}}{2} + \Delta\dot{E}_{\mathrm{x,recy,FP1}} \right) \cdot \zeta_{\mathrm{PB}} - P_{\mathrm{pumps}} \frac{\dot{m}_{\mathrm{FP1,out}}}{\dot{m}_{\mathrm{pumps}}} - P_{\mathrm{pumps,recy}} \tag{4.37}$$

with $\Delta\dot{E}_{\mathrm{x,recy,FP1}}$ representing the exergy from the actual receiver output after deducting the delayed losses due to receiver efficiency impairment. The additional pumping energy consumption is described by

$$P_{\mathrm{pumps,recy}} = P_{\mathrm{pumps}} \frac{\dot{m}_{\mathrm{FP1\rightarrow cTank}}}{\dot{m}_{\mathrm{pumps}}} \tag{4.38}$$

and scales with the mass flow rate into the cold storage tank. It can be calculated from

$$\dot{m}_{\mathrm{FP1\rightarrow cTank}} = \dot{m}_{\mathrm{FP1,out}} - \dot{m}_{\mathrm{FP1\rightarrow hTank}} \,. \tag{4.39}$$

Accordingly, equation (4.37) concludes to

$$P^*_{\mathrm{net,FP1}} = \left(\Delta\dot{E}_{\mathrm{x,hTank,FP1}} + \frac{\Delta\dot{E}_{\mathrm{x,SG,in}}}{2} + \Delta\dot{E}_{\mathrm{x,recy,FP1}} \right) \cdot \zeta_{\mathrm{PB}} - P_{\mathrm{pumps}} \frac{\dot{m}_{\mathrm{FP1,out}} + \dot{m}_{\mathrm{FP1\rightarrow cTank}}}{\dot{m}_{\mathrm{pumps}}} \tag{4.40}$$

In order to determine the recycled exergy $\Delta\dot{E}_{\mathrm{x,recy,FP1}}$ the following hypothesis is proposed: The thermal energy that is recycled into the cold storage tank is fully recovered due to the conservation of energy. The increasing cold tank temperature and, therefore, receiver inlet temperature only impairs the efficiency of future solar energy harvesting. However, the virtual power should incorporate these losses at the time of causation. Therefore, it is assumed that the currently recycled flow of energy minus the delayed losses will pro-

vide exergy in the hot storage tank analog to the non-recycled flow in equation (4.34). But this recycled energy is combined with later harvested energy and the temperature at which both are delivered to the storage is unknown. Hence, as a simplification, it is assumed that the outlet temperature will be nominal to avoid having to predict/simulate the whole day. For the same reason, the hot tank temperature is assumed to be nominal. Therefore, the recycled exergy is potentially overestimated in cloudy periods that are followed by more cloudy conditions throughout the day, which favors decisions toward the (conservative) uninterrupted operation. Consequently, the recycled exergy flow follows

$$\begin{aligned}\Delta\dot{E}_{\mathrm{x,recy,FP1}} = \dot{m}_{\mathrm{recy,FP1}}\,\overline{c_{\mathrm{p}}} \\ \cdot\left[\left(T_{\mathrm{hTank}} - T_{\mathrm{SG,out,n}}\right) - T_{\mathrm{amb}}\ln\frac{T_{\mathrm{hTank,n}}}{T_{\mathrm{SG,out,n}}}\right] \\ +\dot{m}_{\mathrm{recy,FP1}}\,\overline{c_{\mathrm{p}}}\left(T_{\mathrm{FP1,out,n}} - T_{\mathrm{hTank,n}}\right)\left[1 - \frac{T_{\mathrm{amb}}}{T_{\mathrm{hTank,n}}}\right]\end{aligned} \tag{4.41}$$

$$\Rightarrow \Delta\dot{E}_{\mathrm{x,recy,FP1}} = \Delta\dot{H}_{\mathrm{recy,FP1}} - \dot{m}_{\mathrm{recy,FP1}}\,\overline{c_{\mathrm{p}}}\,T_{\mathrm{amb}}\ln\frac{T_{\mathrm{hTank}}}{T_{\mathrm{SG,out,n}}} \tag{4.42}$$

with the effectively recyclable portion of the thermal receiver output

$$\Delta\dot{H}_{\mathrm{recy,FP1}} = \Delta\dot{H}_{\mathrm{FP1,out}} - \Delta\dot{H}_{\mathrm{\eta-loss,FP1}} \tag{4.43}$$

and the corresponding HTF mass flow rate

$$\dot{m}_{\mathrm{recy,FP1}} = \frac{\Delta\dot{H}_{\mathrm{recy,FP1}}}{\overline{c_{\mathrm{p}}}\left(T_{\mathrm{hTank}} - T_{\mathrm{SG,out,n}}\right)}\,, \tag{4.44}$$

which concludes to

$$\Delta\dot{E}_{\mathrm{x,recy,FP1}} = \frac{\dot{m}_{\mathrm{FP1\to cTank}}}{\dot{m}_{\mathrm{FP1,out}}}\cdot\begin{bmatrix}\left(\Delta\dot{H}_{\mathrm{FP1,out}} - \Delta\dot{H}_{\mathrm{\eta-loss,FP1}}\right) \\ -T_{\mathrm{amb}}\left(\dfrac{\Delta\dot{H}_{\mathrm{FP1,out}} - \Delta\dot{H}_{\mathrm{\eta-loss,FP1}}}{\overline{c_{\mathrm{p}}}\left(T_{\mathrm{hTank}} - T_{\mathrm{SG,out,n}}\right)}\right) \\ \cdot\,\overline{c_{\mathrm{p}}}\,\ln\dfrac{T_{\mathrm{hTank}}}{T_{\mathrm{SG,out,n}}}\end{bmatrix} \tag{4.45}$$

Finally, the thermal energy loss due to receiver efficiency impairment can be approximated based on the absolute efficiency loss multiplied by the amount of concentrated solar energy that would be harvested with impaired efficiency. Again, to avoid integration over a long period of time, it is approximated with nominal in- and outlet temperatures of the receiver. Derivated over time, this leads to

$$\Delta\dot{H}_{\eta-\mathrm{loss,FP1}} = \frac{m_{\mathrm{cTank}}\,\overline{c_{\mathrm{p}}}\left(T_{\mathrm{rec,out,n}} - T_{\mathrm{rec,in,n}}\right)}{\eta_{\mathrm{rec,n}}} \cdot \frac{d\eta_{\mathrm{rec}}}{dt} \tag{4.46}$$

in which the rate of efficiency change can be derived from

$$\frac{d\eta_{\mathrm{rec}}}{dt} = \frac{\partial}{\partial T_{\mathrm{rec,in}}}(\eta_{\mathrm{rec}}) \cdot \frac{\partial}{\partial t}\left(T_{\mathrm{rec,in}}\right) \tag{4.47}$$

This concludes to

$$\Delta\dot{H}_{\eta-\mathrm{loss,FP1}} = \frac{m_{\mathrm{cTank}}\,\overline{c_{\mathrm{p}}}\left(T_{\mathrm{rec,out,n}} - T_{\mathrm{rec,in,n}}\right)}{\eta_{\mathrm{rec,n}}} \cdot \frac{\partial}{\partial T_{\mathrm{rec,in}}}(\eta_{\mathrm{rec}}) \cdot \frac{\partial}{\partial t}(T_{\mathrm{cTank}}) \tag{4.48}$$

Since $\frac{\partial}{\partial t}(T_{\mathrm{cTank}})$ is already calculated in the storage model, the only remaining unknown is the inlet temperature sensitivity of the receiver efficiency $\frac{\partial}{\partial T_{\mathrm{rec,in}}}(\eta_{\mathrm{rec}})$, which is approximated in the following.

Determining the temporal derivative of the receiver efficiency can either be done analytically based on the scalar 1P model or numerically with any receiver model. In this sense, the detailed dynamic 2P model is simulated with constant intercept flux of 100 % and 50 % part load and active outlet temperature control while varying the inlet temperature. The resulting temperature trends are plotted in Figure 4-6. Especially in part load, the trends reveal limited control quality. For this reason, the inlet temperature ramp is conducted in ascending and descending directions.

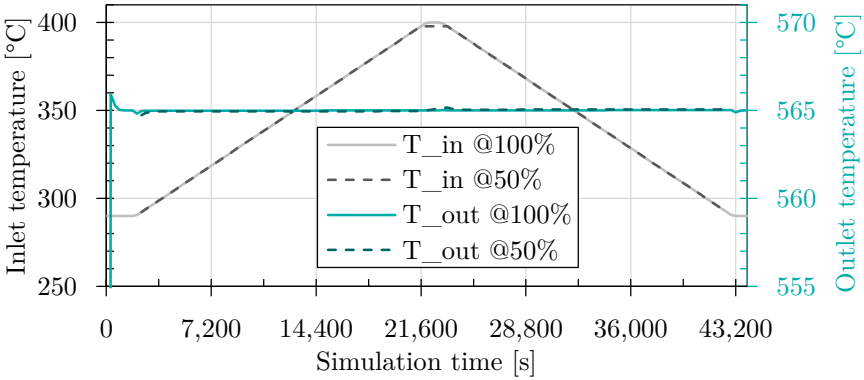

Figure 4-6: Temperature trends of the detailed dynamic 2P model simulation with constant intercept flux and varying inlet temperature

After selecting only the data with inlet temperatures between 291 °C and 399 °C (to focus on the semi-steady-state sequences), the corresponding receiver efficiency is calculated and plotted against the inlet temperature in Figure 4-7. The inlet temperature sensitivity of the receiver efficiency $\frac{\partial}{\partial T_{\mathrm{rec,in}}}(\eta_{\mathrm{rec}})$ is then derived from a second-order fit polynomial. Between 300 °C and 400 °C respectively, 50 % and 100 % it ranges from 0.58 % to 1.54 % per 100 K inlet temperature increase.

To sum up, Figure 4-8 illustrates the impact of each loss mechanism on net power depending on relative shading. It considers clear-sky control. Hence, the outlet temperature decreases nearly proportionally with shading. The storage tank temperatures are assumed to be nominal. All net power graphs include the additional pumping loss due to recycling, which explains the step down at approx. 19 % shading. The first graph describes a net power metric that is just based on the thermal receiver power with a constant heat-to-power efficiency while neglecting any temperature-related losses. In contrast, the second graph represents a net power metric based on the exergy flow provided by the receiver. Therefore, it takes into account the temperature-dependent heat-to-power efficiency but still neglects the exergy losses due to mixing in the storage tanks. Moreover, the third graph results from a net

power metric based on the rate of exergy change in the storage system. This results in a much deeper step down at the transition from storage charging to HTF recycling due to the much higher temperature difference to the cold storage tank. Finally, the fourth graph depicts the virtual net power approach presented above, which additionally considers delayed losses.

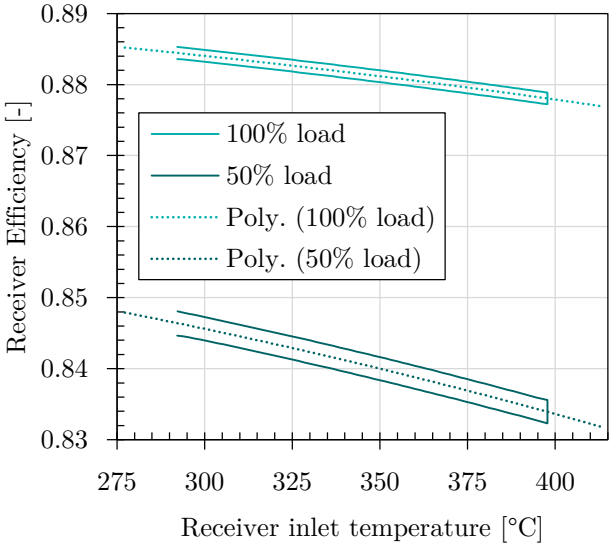

Figure 4-7: Receiver efficiency in dependence of the inlet temperature with fit polynomials

It also must be noted that by using the virtual net power approach without any adjustment to the model, the delayed losses and energy recovery would be accounted for twice because of the increasing receiver inlet temperature. Hence, when the performance analyzer is set to virtual power calculation, the inlet temperature of the receiver pumps is decoupled from the cold tank temperature and set to the nominal value instead. By this, the delayed energy recovery and related losses are effectively shifted from the time of occurrence to the time of causation.

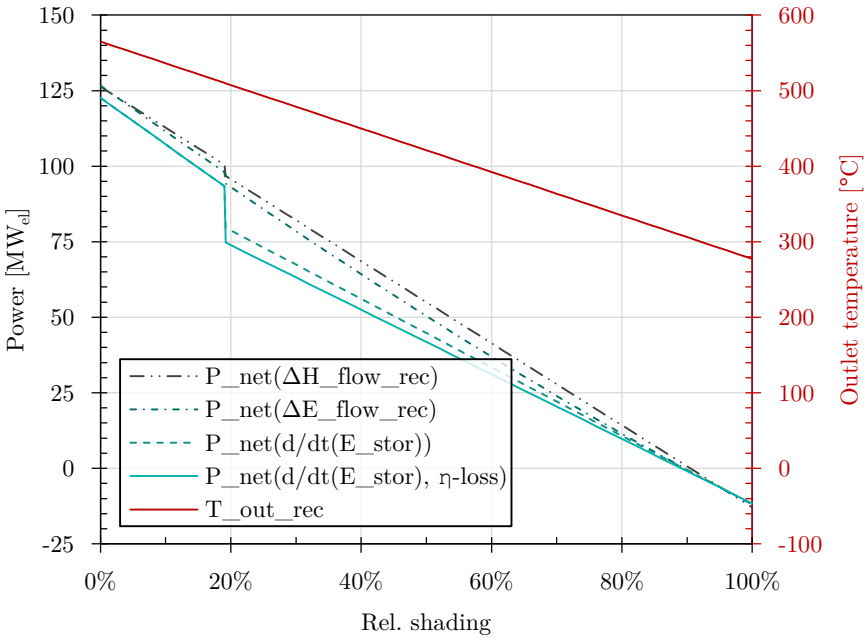

Figure 4-8: Comparison of different net power approaches and their sensitivity to the receiver outlet temperature

4.1.5 Validation of the virtual net power approach

To confirm the theory described above, this virtual net power metric is validated against the conventional approach for actual net power. In contrast to the virtual net power $P^{*}_{\mathrm{net,FP1}}$, the actual net power $P^{**}_{\mathrm{net,FP1}}$ does not instantly consider the recycled exergy. Instead, actual power is only based on the exergy gain in the hot tank and the steam generator feed:

$$P^{**}_{\mathrm{net,FP1}} = \left(\Delta\dot{E}_{\mathrm{x,hTank,FP1}} + \frac{\Delta\dot{E}_{\mathrm{x,SG,in}}}{2}\right) \cdot \zeta_{\mathrm{PB}} - P_{\mathrm{pumps}} \tag{4.49}$$

As a result, Figure 4-9 illustrates the two different net power trends plotted throughout the semi-steady-state scenario Sc_Clear_10s_-80%-50%_0800-1000. As expected from Figure 4-8, the system is in recycling mode during

the 2 h long shading period, which leads to negative actual net power. However, after the shading has passed, the actual net power exceeds its nominal value of 125 MW_{el} due to the elevated receiver inlet temperature (compare Figure 4-10), resulting in a higher mass flow rate. In contrast, the virtual net power only drops down to approx. 14 % and returns to nominal value right after the shading has passed. Most importantly, the integrals of these two trends shown in the diagram below converge throughout the day, confirming the theory.

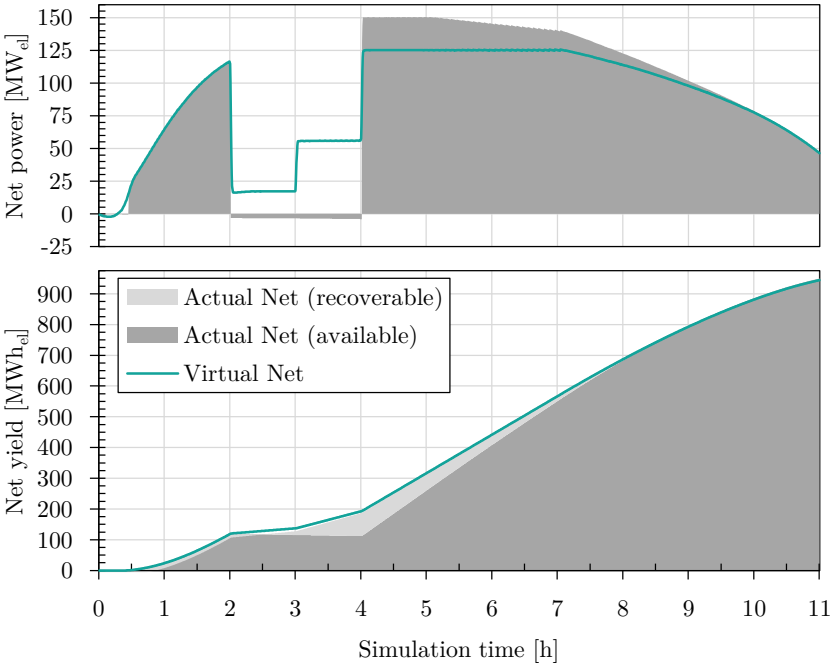

Figure 4-9: Comparison between actual and virtual net power/yield in semi-steady-state conditions

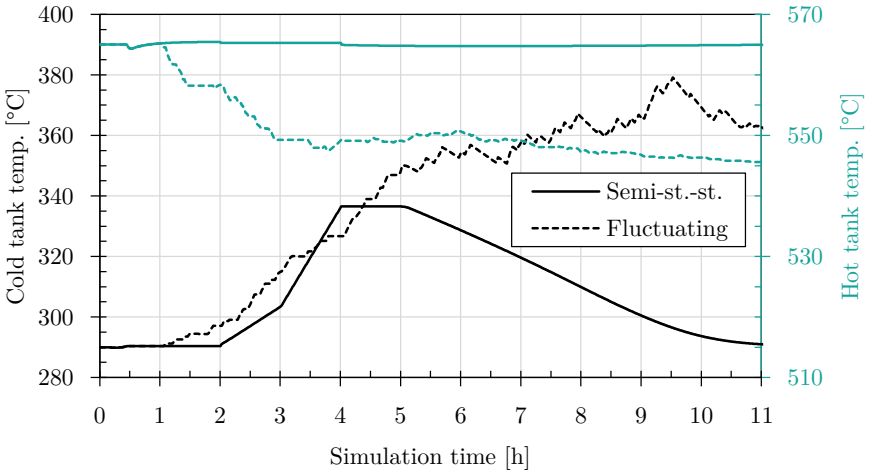

Figure 4-10: Storage medium temperature trends in semi-steady-state and fluctuating conditions

In this validation, it must be noted that there might be non-available but recoverable sensible heat left in the cold storage tank. Therefore, the recoverable but not yet available net yield equivalent is calculated based on the exergy (relative to SG return) stored in the cold tank:

$$W^{**}_{\mathrm{net,recov,FP1}} = \Delta E_{\mathrm{x,cTank,FP1}} \cdot \zeta_{\mathrm{PB}} - P_{\mathrm{pumps}} \tag{4.50}$$

Adding this to the actual net yield allows direct comparison with the virtual net yield, as illustrated by the stacked areas in Figure 4-9. The deviation between the two different net yield metrics remains at 0.38 % by the end of this scenario.

Finally, the same validation is performed with the cloud camera-based scenario Sc_7710 and presented in Figure 4-11 accordingly. Due to more overall shading in this scenario, a significant amount of recoverable energy remains. However, the virtual net power aligns well with the sum of actual and recov-

erable yield throughout the day. The deviation between both metrics converges to 1.11 %. Hence, the virtual net power is a suitable approach to model the net yield over time.

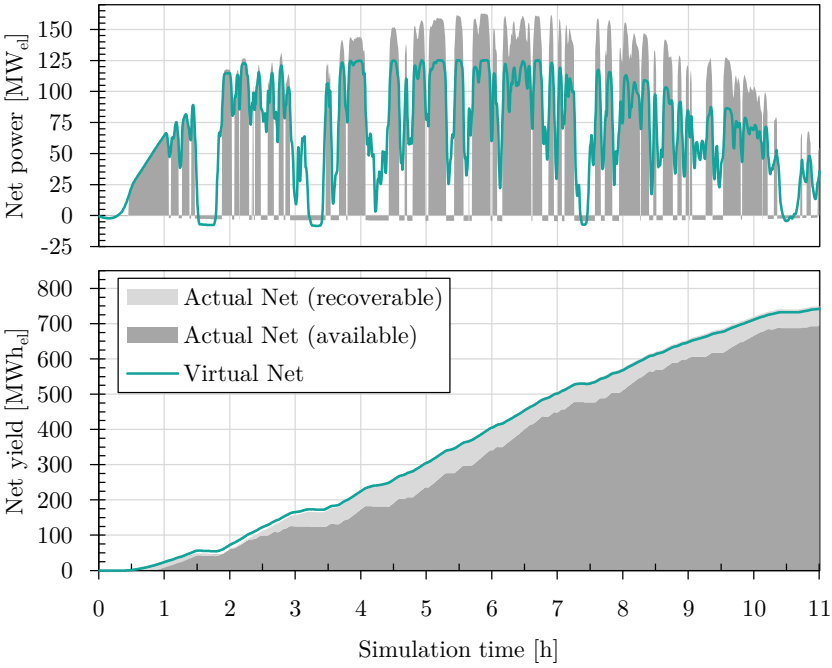

Figure 4-11: Comparison between actual and virtual net power/yield in fluctuating conditions

4.2 Selection and Timing for Shutdown Maneuvers

The decision algorithm determines if and when the receiver operation should be interrupted to maximize net yield. More specifically, the time at which the temporary shutdown should be initiated and the time at which the system should be restated is determined based on forecasted flux density distribution. Figure 4-12 clarifies with a simplified example how critical this timing is. In continuous operation at a certain degree of shading, the net power

becomes negative due to relatively high thermal and parasitic losses (grey line). If, instead, the receiver is shut down (green line), the parasitic losses are reduced by a certain amount (green shaded area) but the shutdown and restart cause additional losses (grey shaded area). Only if these additional losses are significantly smaller than the saved parasitic losses the temporary shutdown actually increases the overall net yield.

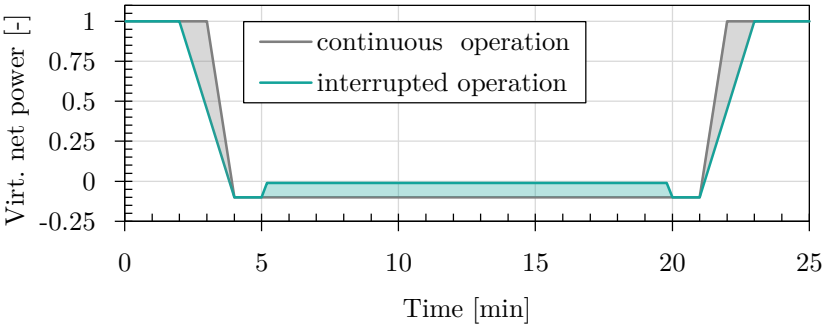

Figure 4-12: Simplified trends of virtual net power during a cloud passage with continuous and interrupted receiver operation

The central part of the decision algorithm is implemented in the Python programming language and interacts with the prediction models in Dymola via a dedicated interface. The general workflow is illustrated in Figure 4-13. The pre-processing of the DNI forecasting data is implemented in Matlab and STRAL does the raytracing for calculating the flux density distributions. Both are considered independently from the decision algorithm and are part of the pre-processing of the OAS tests.

The decision algorithm itself starts with a request from the user. First, it initializes the fast 1P model for predicting net power during continuous operation throughout the entire forecasted period. In parallel, based on the available flux, it determines at which times the flux density would be sufficient for gentle warming (compare Section 3.2.7) on each receiver panel in order to know when the system could be safely drained and refilled. After Dymola has finished the 1P simulation, the algorithm loads the predicted net

power trend from the results file. Next, it determines points of interest at each time step when the net power becomes negative (POI_{down}) and when it becomes positive again (POI_{up}), since these would be the ideal times to shut down and restart. However, certain delays due to transitions must be considered as well.

Thus, the following is then conducted for each POI_{down}. The drainage would ideally start at each $POI_{down,}$ on the one hand, to harvest as much of the positive net power as possible and, on the other hand, to reduce the parasitic losses as early as possible. Besides that, the receiver must be kept warm by means of gently warming mode to avoid freezing during drainage. Consequently, the algorithm initially sets the drainage start t_{drain} to $\Delta t_{\mathrm{drain}}$ before the POI_{down} and then moves it to an earlier time as far as needed, so that sufficient flux is available during the whole drainage period.

Next, the algorithm needs to consider the required outlet temperature ramp-down prior to the receiver drainage. For this, it loads the predicted outlet temperature trend from the 1P simulation. If $T_{\mathrm{out}}(t_{\mathrm{drain}})$ is below T_{drain}, the threshold for initializing drainage, then the ramp-down is neglected. Otherwise, since the ramp-down mode ends with the drainage, the algorithm sets the endpoint of the temperature ramp at t_{drain} with T_{drain} and the maximum allowable slope. The last intersection between this ramp and the predicted trend before t_{drain} is chosen as the shutdown time t_{rampDown}.

Subsequently, the algorithm must verify whether this temporary shutdown actually results in higher net yield compared to uninterrupted operation. For this, it initializes the simplified 2P model with the determined shutdown time and the POI_{up} as aspired restart time. The actual restart depends on how long the preheat takes and will result from this simulation. Accordingly, Dymola simulates the interrupted operation for only a limited period from shortly before t_{rampDown} until a sufficient time after POI_{up}. Finally, the algorithm compares the predicted net power trends of both cases and calculates the gain of net yield by integrating the difference between both trends over

an appropriate period. If the gain is greater than the uncertainty of the prediction, the OAS will propose this maneuver. Otherwise, it would propose continuous operations.

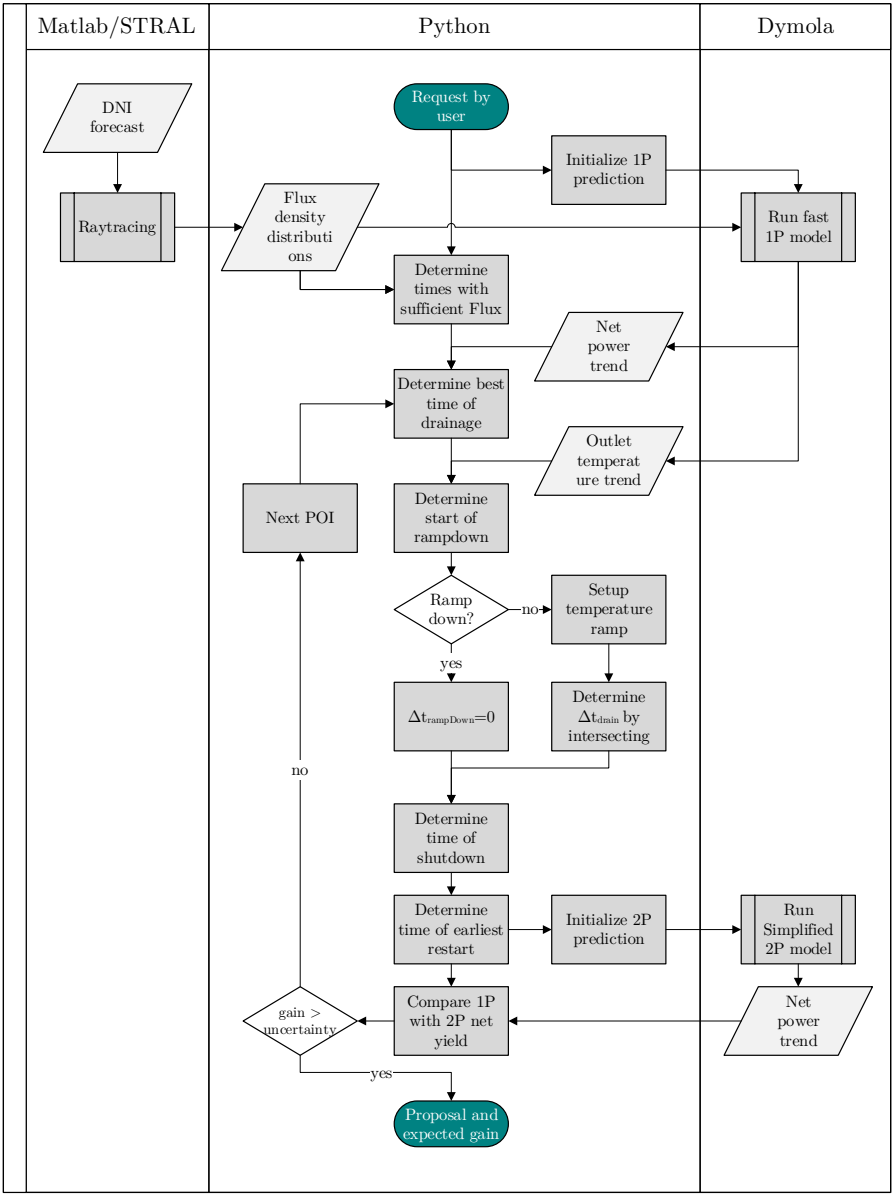

Figure 4-13: Flow chart of the decision algorithm

5 Results and Discussion

5.1 OAS Testing

For testing the OAS functionality, test runs are conducted with different scenarios based on artificial cloud movements or DNI maps from ASIs. For instance, Figure 5-1 shows the OAS output for POI number 11 in the artificial cloud scenario Sc_7750. The top plot presents the flattened flux density distribution over time, revealing heavy cloud coverage in the middle part of the displayed sequence. The black graph in the central diagram reveals the resulting virtual net power for continuous operation and the green graph for interrupted operation. The green and grey shaded areas represent the saved and lost yield due to the maneuver of interrupting the receiver operation.

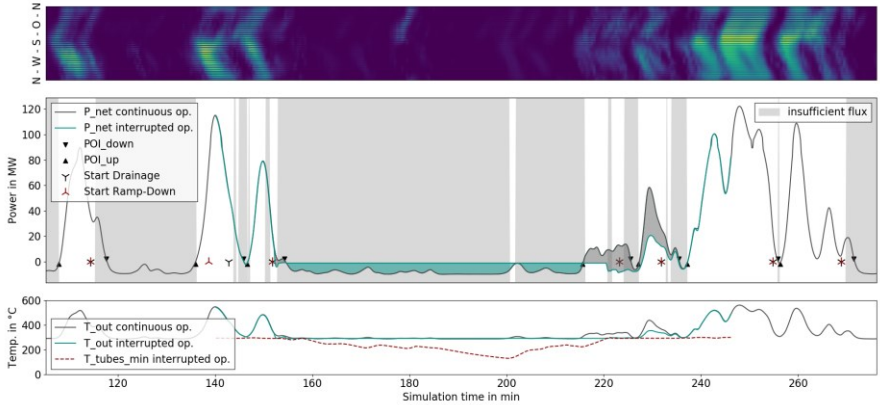

Figure 5-1: OAS test results for POI 11 in scenario Sc_7750 saving 2.3 MWh_{el}

Based on this, the OAS concludes that the maneuver achieves a net yield gain of 2.3 MWh_{el}. At first glance, it seems this could easily be optimized by restarting the system earlier to reduce the added losses (grey area). However, the OAS actually commands to the PCS to restart the system at the next POI_{up} at approx. 215 min. Since the absorber tubes have been cooled down significantly (see bottom diagram) due to insufficient flux, the PCS must

wait a few minutes until preheating is completed. This results in a delayed restart and therefore additional losses.

Moreover, the timing of the shutdown is examined. For this, the initialization of the shutdown is varied in one-minute increments around the proposed time. The resulting net power and HTF level trends of the receiver are plotted in Figure 5-2 accordingly. As expected, an earlier shutdown results in reduced yield, but in this example, it does not significantly change the time at which the receiver drains, because it mainly prolongs the ramp-down phase. This phenomenon is due to the higher power at which the shutdown is initiated; therefore, a longer ramp-down is necessary. In contrast, delaying the shutdown results in later drainage accordingly.

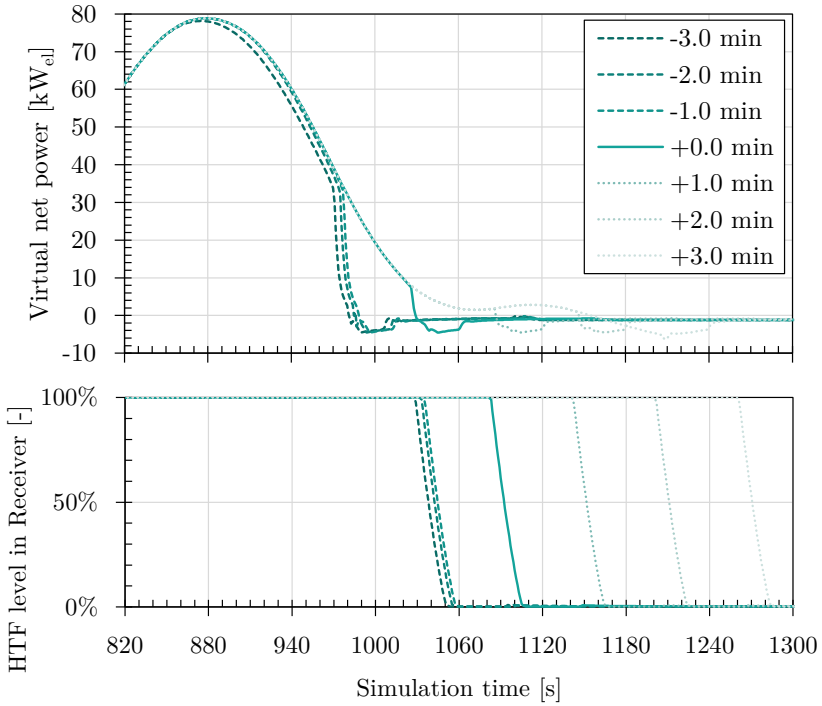

Figure 5-2: Virtual net power (top) and HTF level (bottom) trends with different shutdown timings

The resulting net yield benefits due to the interruption of operation are plotted in Figure 5-3. It reveals an optimum at approx. 2 minutes later as proposed disregarding the necessity of sufficient preheating flux. Thus, in theory, the net yield could be optimized up to this point but with the risk that the molten salt might freeze in the absorber tubes during drainage. Therefore, the timing proposed by the OAS poses the optimum considering realistic constraints.

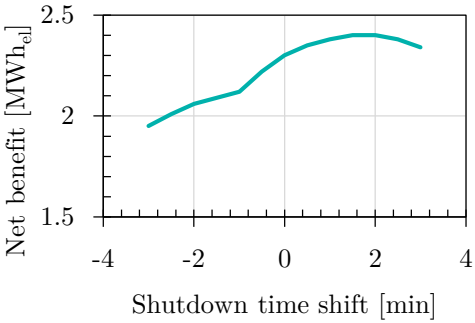

Figure 5-3: Net benefit from the maneuver proposed by the OAS depending on the shutdown timing

Lastly, for this exemplary case, the accuracy and performance of the OAS is compared to the detailed dynamic 2P model. For this purpose, Figure 5-4 includes plots of the virtual net power during interrupted and continuous operation as calculated by the OAS (fast 1P model and simplified 2P model) and the detailed dynamic 2P model with various receiver flow discretizations. The continuous and interrupted operations both only show visible deviations during the transitions. The overall alignment, however, is excellent. Moreover, the resulting net benefits are given in Figure 5-5 by the grey columns. Compared to the highest discretized model, the OAS underestimates the net benefit by 0.14 MWh_{el}, but this might vary depending on the scenario. Furthermore, Figure 5-5 presents the different models' overall computing time for this case. The OAS obtains this result in less than 10 min, whereas the detailed model uses between 1 and 15 h of computing time.

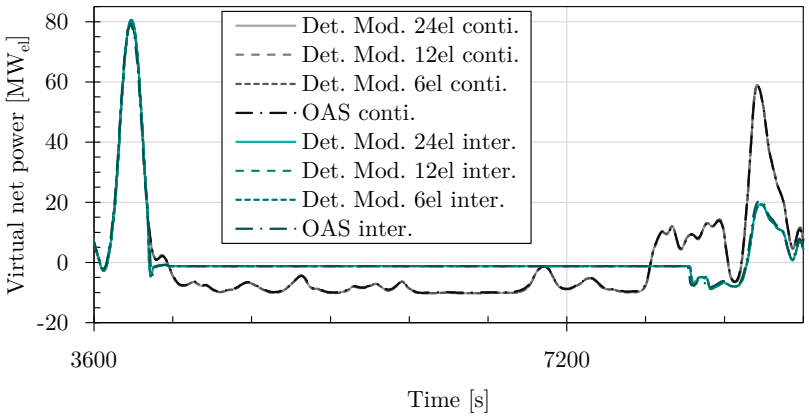

Figure 5-4: Comparison of continuous and interrupted net power trends from the OAS and the detailed dynamic 2P model at different levels of receiver discretization

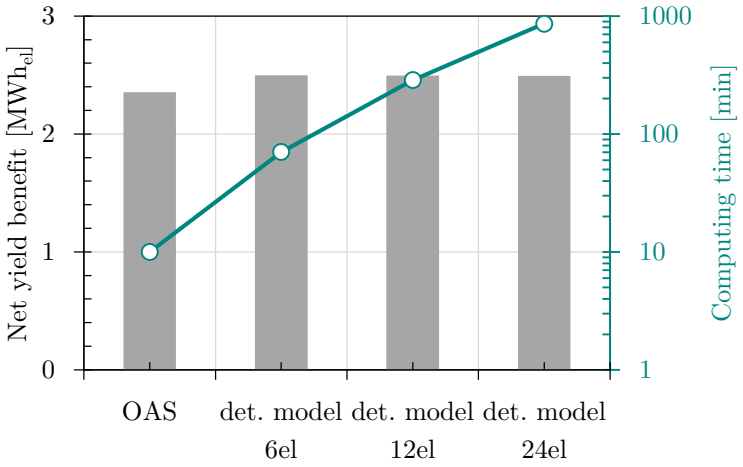

Figure 5-5: Net benefit based on the prediction with the OAS and the detailed dynamic 2P model at different levels of receiver discretization as well as the corresponding computing time

A different example case is shown in Figure 5-6, which emphasizes the importance of the ability to return to normal operation quickly. Here, the flux returns very quickly so that a large amount of net yield is lost due to the comparably slow restart of the receiver system. Higher allowable transients could shorten the startup time and increase the net yield significantly. Nevertheless, with the considered allowable transients, the OAS would propose to continue the operation since interrupting it would cost 6.12 MWh_{el} of net yield.

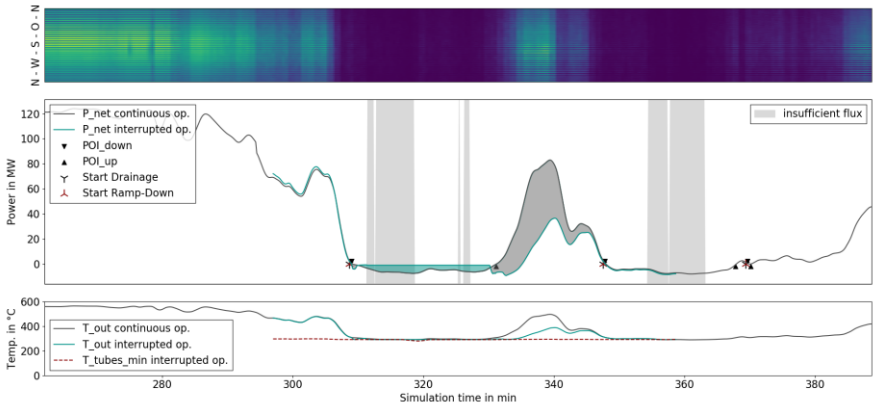

Figure 5-6: OAS test results for POI 15 in scenario Sc_PSA_191126_realBlur costing 6.12 MWh_{el}

Finally, Figure 5-7 reveals a case in which the OAS proposes interrupting receiver operation, predicting a net benefit of 15.91 MWh_{el}. This can be further increased if the receiver is kept in drained cloud protection mode even longer. Restarting at the second-next POI_{up} results in what is shown in Figure 5-8. Because of the long and heavy shading, it is beneficial to delay the restart. In addition, there is sufficient preheat flux for a while before the time of restart. Therefore, the receiver can immediately be filled without further delay for preheating. This results in an even higher net benefit of 18 MWh_{el}.

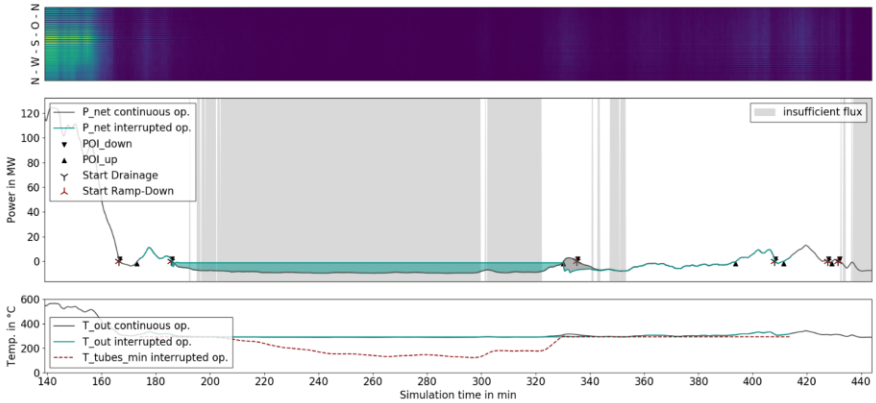

Figure 5-7: OAS test results for POI 1 in scenario Sc_PSA_191101_realBlur saving 15.91 MWh_{el}

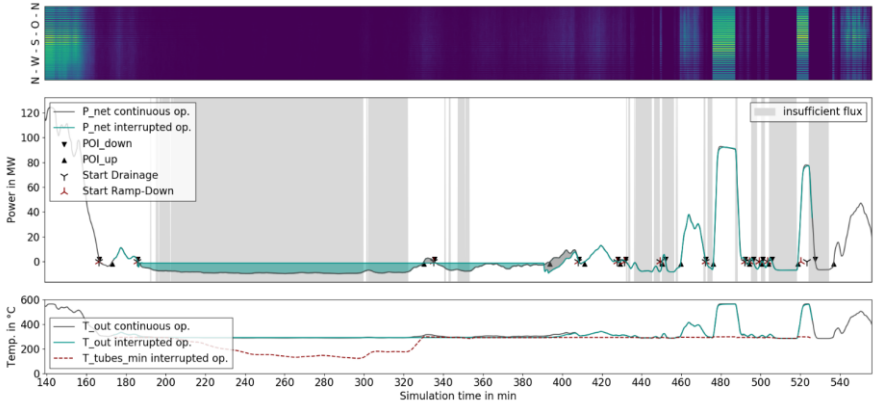

Figure 5-8: OAS test results for POI_{down} 1 and POI_{up} 2 in scenario Sc_PSA_191101_realBlur saving 18 MWh_{el}

Other interesting cases of the OAS tests are provided in the Appendix in Section C.

5.2 Uncertainty Analysis

The uncertainty of the process prediction must be considered for the reliable function of the OAS. The prediction error must always be significantly smaller than the predicted benefit from a proposed maneuver to ensure actual gain of performance respectively yield. Therefore, this Section examines the uncertainty of the prediction and its relation to the quality as well as the uncertainty of the forecasted input data. Available DNI (direct normal irradiation) forecasting data are usually based on satellites or all-sky imagers (ASI) and differ in temporal and spatial resolution, the forecasting horizon and the forecasting uncertainty. For the following analysis, measured and forecasted DNI maps from an ASI-based system (Nouri et al. 2022) are preprocessed, composing different scenarios (compare Section B.2).

5.2.1 Input data quality impact

In order to determine the required quality of the input data for the OAS, meaning DNI forecasting data, the detailed dynamic model is simulated with input data of different spatial quality. In this sense, the resolution of a series of DNI maps is artificially coarsened with two different clustering methods, as illustrated in Figure 5-9. The original maps (a) have a pixel size of 20 m by 20 m. For every 30 s of the day, these data include a set of DNI maps from lead time 0 (LT00), which is considered as reference, up to 20 min lead time (LT20) with 1 min increments. In this section, only the reference maps (LT00) are applied.

Since the available forecasting methods provide maps with different resolutions of square pixels, the Cartesian clustering method (Figure 5-9 b) enlarges the original 20 m by 20 m pixels to a multiple. Different enlargement factors are considered to replicate different forecasting methods, such as all-sky imager (high resolution) or satellite-based (lower resolution) systems. The clustering is done by averaging the values in each cluster to keep the integral within each cluster and across the entire DNI map consistent.

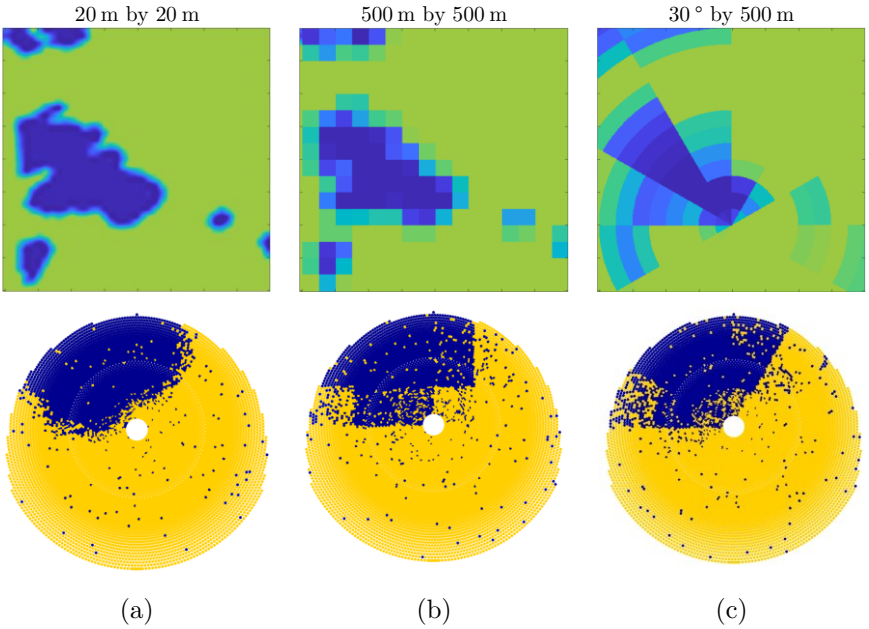

Figure 5-9: Clustered DNI maps (a: original; b: Cartesian; c: polar) and corresponding heliostat field shading

For comparison, the polar clustering method is introduced, which better suits the heliostat field layout and allows for differentiating between radial and circumferential sensitivities. It averages values across clustered areas as well, but the aggregation is done on a polar-coordinate-based pattern (compare Figure 5-9 c). The origin of the polar coordinate system is located at the tower position respectively in the center and symmetry axis of the heliostat field. The polar radial and circumferential cluster sizes are varied independently.

As a result, an excerpt of the predicted intercept and virtual net power trends based on different input data resolutions (Cartesian method) is plotted in Figure 5-10. Significant deviations can be observed, especially with cluster sizes of more than 500 m. This is primarily due to averaging across areas that

only partially overlap with the heliostat field so that outsider DNI values manipulate the simulated irradiance in the heliostat field.

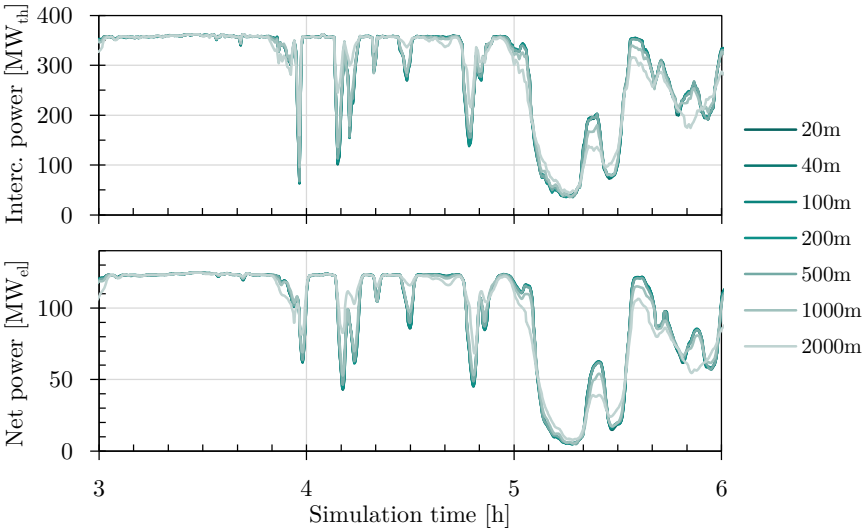

Figure 5-10: Excerpt of simulated intercept (top) and net (bottom) power based on different Cartesian cluster/pixel sizes

In order to eliminate short-term deviations, which are irrelevant for predicting yield over several minutes, a 20 min moving average is applied to the net power trends before calculating statistic metrics throughout a full operation day (10.5 h). The resulting mean-absolute deviation (MAD) and root-mean-square deviation (RMSD) are graphed in Figure 5-11 against the cluster size with (right) and without (left) applying the 20 min moving average. As expected, the RMSD rises progressively up to 5.4 MW_{el} at 2000 m wide clusters, but with decreasing cluster sizes, it converges to approx. 0.08 MW. Peak deviations (not shown in the diagram) reach from 0.25 MW_{el} to 16.15 MW_{el}. With respect to the model accuracy and the order in which prediction-based operational decisions can increase yield, it seems appropriate to aim for an RMSD of less than 1 % of the nominal power. Hence, a pixel size of less than 960 m is required to keep the RMSD below 1.2 MW_{el}. This excludes any state-

of-the-art satellite-based forecasting technology, but the resolution of now-casting maps from all-sky imager-based systems (ASI) is sufficient for such a yield prediction application.

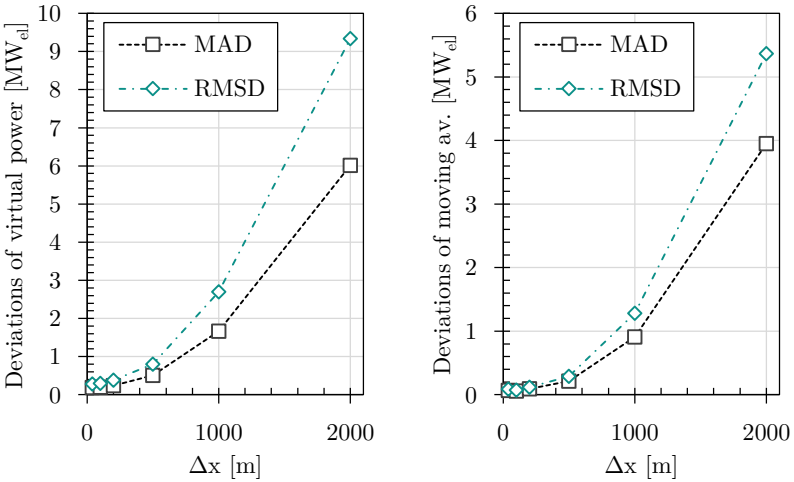

Figure 5-11: Statistics of the net power (left) and of the corresponding 20 min moving average (right) depending on the Cartesian cluster size

Furthermore, the same statistical analysis is conducted for the polar clustering method to examine the influence of the heliostat field layout. The resulting MAD and RMSD values are plotted in Figure 5-12 against the circumferential (left) and radial (right) cluster size. In each parameter variation, the other parameter is kept constant at the smallest value considered. Hence, the deviations are smaller compared to the Cartesian clustering. However, depending on the radial cluster size, the RMSD varies between 0.09 MW_{el} and 1.47 MW_{el} with a progressive trend, while peak deviations lie between 0.28 MW_{el} and 4.08 MW_{el}.

In contrast, in the range of 0.09 MW_{el} to 1.48 MW_{el}, the RMSD correlates almost linearly with the circumferential cluster size with peak deviations between 0.28 MW_{el} and 4.47 MW_{el}. In comparison, at small cluster sizes, the net power prediction is more affected by the circumferential resolution since the

field efficiency and the receiver efficiency both vary around the circumference significantly, whereas the radial DNI gradients only interfere with the field efficiency and not with the receiver efficiency. However, at larger cluster sizes, the aforementioned impact of outsider DNI values (outside of the heliostat field but still within the cluster) explains the progressive increase in the dependency from Δr. With one additional parameter sweep for $\Delta\varphi$ at $\Delta r = 500\,\text{m}$, it can be concluded that an appropriate cluster size of 500 m by 90 ° results in an RMSD of 0.79 MW_{el}.

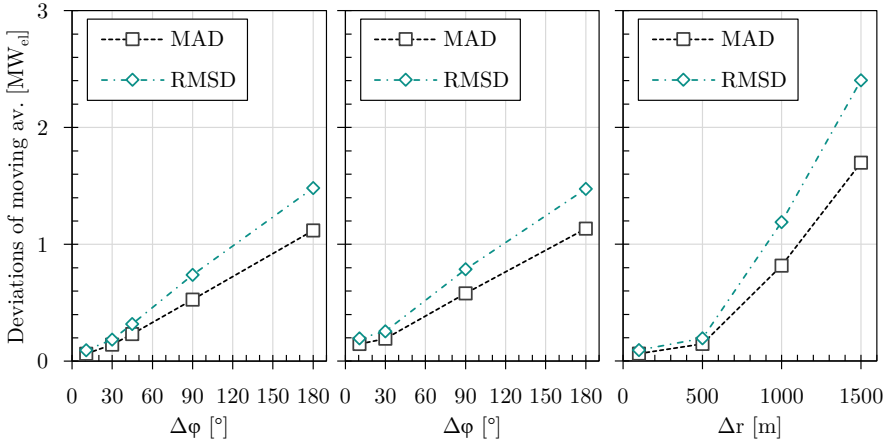

Figure 5-12: Statistics of the net power (20 min moving average) depending on the polar cluster size ($\Delta\varphi$ at $\Delta r = 100\,\text{m}$, $\Delta\varphi$ at $\Delta r = 500\,\text{m}$ and Δr at $\Delta\varphi = 10.6\,°$)

The same analysis for the controlled outlet temperature and maximum film temperature (only relevant for other OAS and MPC functions) will be published separately.

5.2.2 Forecasting and prediction uncertainty

To analyze how the dynamic simulation model performs with forecasted input data, including associated forecasting errors, designated forecasting scenarios are composed for the same day as above. In this context, Figure 5-13

gives an excerpt of the DNI maps for 6 September 2019 with 5 of the 21 available lead times. Based on this, forecasting scenarios are composed of the forecasted DNI maps for each lead time (>0) and compared to the reference scenario (LT00). For example, in scenario LT20 each time step represents a forecast based on ASI measurement data from 20 min before, whereas LT00 is considered as (auto validation) reference.

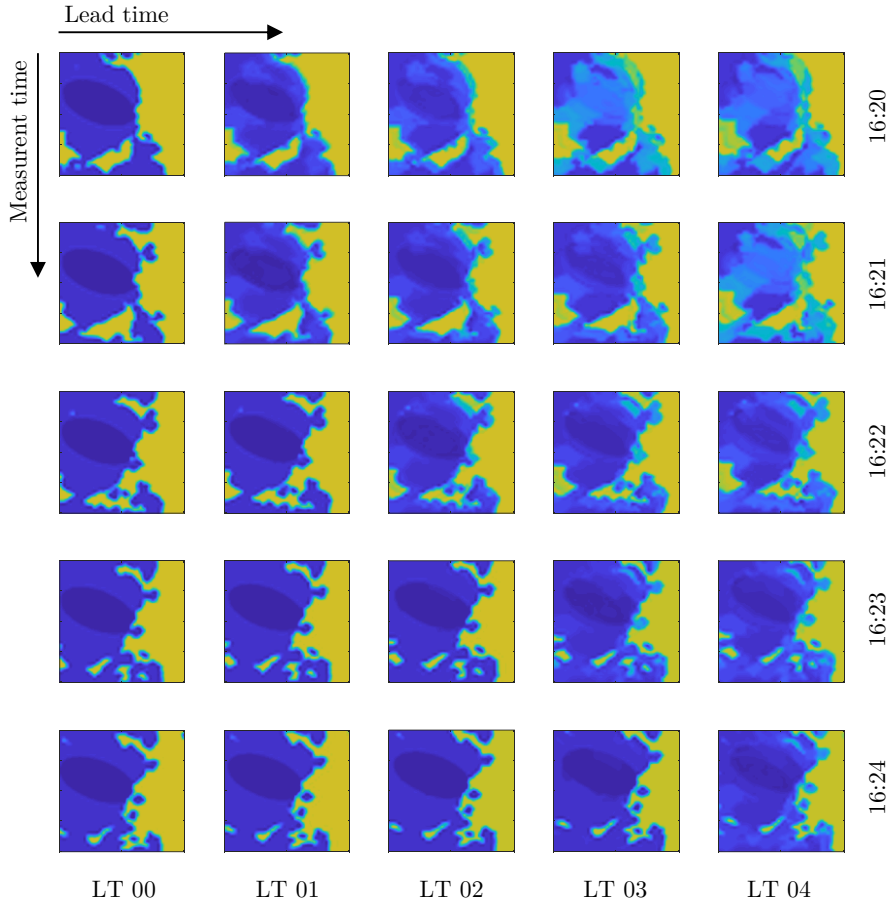

Figure 5-13: Excerpt of applied nowcasting DNI maps with different lead times

Figure 5-14 shows an excerpt of the simulated intercept and virtual net power trends for LT00 to LT10. Apparently, the shadow-induced drop-downs in the forecast scenarios are shifted to the right with increasing lead time. This is due to some shadows rather appearing and disappearing than moving across the heliostat field, making it difficult to forecast. Hence, the earlier the forecast is done, the older the data it is based on; therefore, the forecast lags behind.

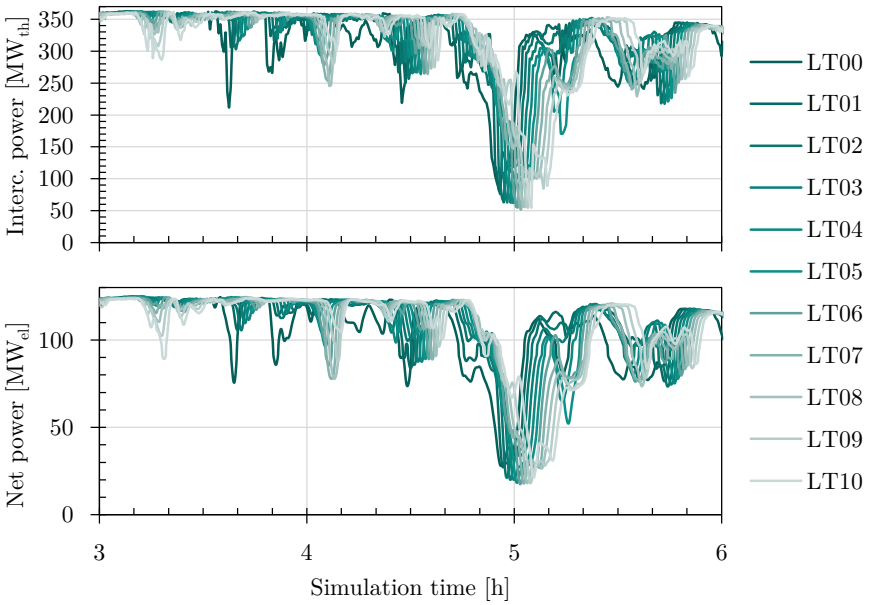

Figure 5-14: Excerpt of predicted intercept (top) and net (bottom) power based on forecasted DNI maps with different lead times

The discrepancy between predicted and actual power becomes clearer in Figure 5-15, where the predicted (LT01) data is plotted against the actual (LT00) data. The predicted intercept power scatters significantly, especially with longer lead times. Ideally, all points would follow the dotted linear line. According to the plot below, the RMSD (over time) of the intercept power lies around 35.8 MW_{th} with 1 min lead time but 82 MW_{th} with 20 min lead

time, while occasional deviations reach up to 300 MW_{th}. The same plots for the virtual net power are shown in Figure 5-16. In contrast, due to the system's thermal inertia, the net power data points agglomerate along curved paths. The RMSD of the virtual net power is 11.2 MW_{el} with 1 min lead time and 30 MW_{el} with 20 min lead time, while occasional deviations reach up to 100 MW_{el}.

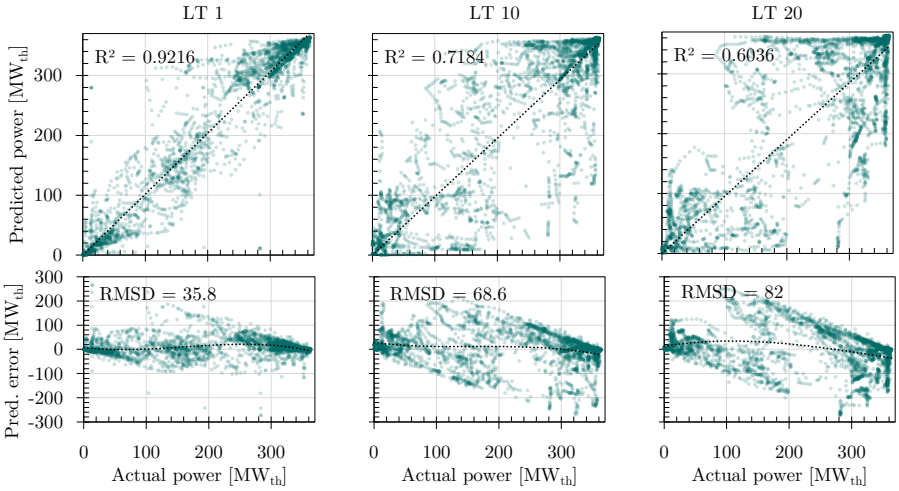

Figure 5-15: Predicted intercept power and corresponding prediction errors scattered over actual power for three different lead times

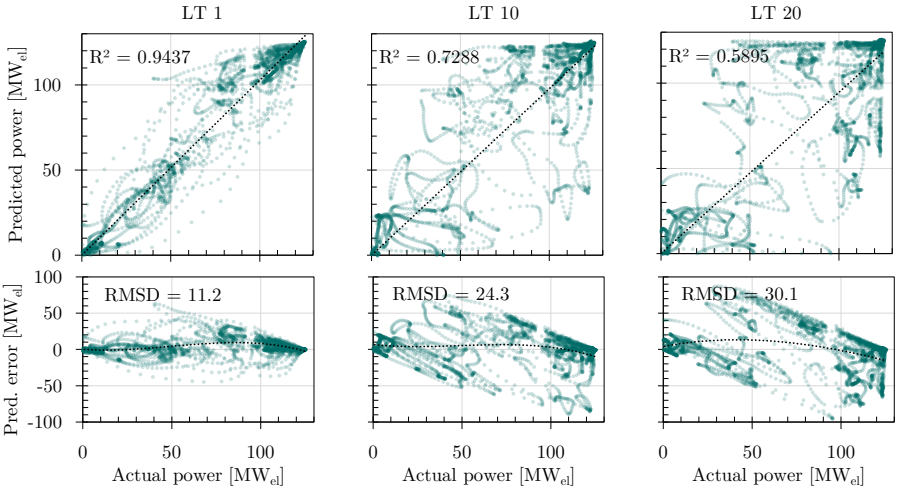

Figure 5-16: Predicted net power and corresponding prediction errors scattered over actual power for three different lead times

Furthermore, applying a moving average on the forecasted and predicted data decrease average deviations, which is appropriate when the uncertainty of yield prediction for a certain period is of interest. In this regard, Figure 5-17 presents the sensitivity of the RMSD (of the net power) regarding the lead time and the moving average interval length.

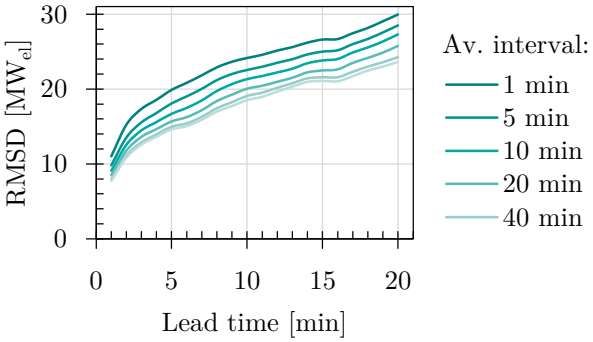

Figure 5-17: Sensitivity of the RMSD of the net power prediction over lead time with different moving average intervals

However, those results only represent one specific scenario and strongly depend on the achieved forecasting accuracy. A correlation between prediction and forecasting uncertainty must be determined to exclude this dependency. The following study examines prediction errors depending on the corresponding forecast errors. The considered nowcasting system can provide the uncertainty for each pixel of the DNI map, which the OAS could make use of.

Usually, forecasting methods are validated with different scalar error metrics such as mean absolute deviation (MAD) or root mean square deviation (RMSD). This study considers four different forecast error metrics in order to find the one that correlates with the prediction error best. Since the OAS integrates the yield predictions over periods of several minutes, momentary errors can be neglected. Hence, a 5 min moving average is applied to the forecast and prediction data before calculating the errors. In addition, all forecast errors are calculated only based on pixels inside the heliostat field. First, the root-mean-square deviation (RMSD) over the heliostat field area is considered, as it is common in nowcasting validations. Second, the RMSD is applied on polar clustered (500 m by 90 °) DNI maps. Third, the absolute value of the bias (|bias|) is considered, which is the absolute value of the mean deviation. Lastly, bias is considered while being the only signed error metric in this study. The definitions of those forecasting error metrics follow:

$$e_{\text{forc.}}^{\text{MAD}} = \frac{\sum |e_{x,y}|}{N} \tag{5.1}$$

$$e_{\text{forc.}}^{\text{RMSD}} = \sqrt{\frac{\sum \left(e_{x,y}\right)^2}{n}} \tag{5.2}$$

$$e_{\text{forc.}}^{|\text{bias}|} = \left| \frac{\sum e_{x,y}}{N} \right| \tag{5.3}$$

$$e_{\text{forc.}}^{\text{bias}} = \frac{\sum e_{x,y}}{N} \tag{5.4}$$

with $e_{x,y}$ representing the error of each pixel.

Accordingly, forecast and prediction errors are calculated for each time step over 10 h of varying conditions (scenario Sc_PSA_190906_realBlur) and for all 20 lead times resulting in 24.020 data points for each forecast error metric. Figure 5-18 presents corresponding scatter plots with 95 % transparency and including a linear fit (dotted line) with the respective coefficient of determination (R^2). In addition to the net power prediction errors (bottom diagrams), the intercept power prediction errors (top diagrams) are given, allowing us to distinguish between the raytracing and the dynamic prediction model. Apparently, the prediction errors correlate poorly with the RMSD, as indicated by the low R^2. The clustered RMSD only achieves a minor improvement, whereas the (signed) bias results in the highest R^2. Moreover, for the net power, the absolute and especially the signed bias correlate significantly better, with almost 60 % determination and approx. 78 % for the intercept power.

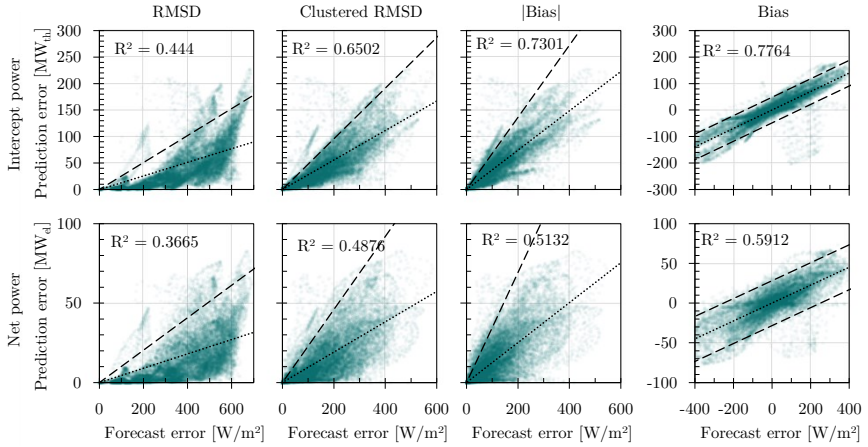

Figure 5-18: Prediction errors of the 5 min moving average of the intercept (top) and net power (bottom) values for all 20 lead times over different DNI map forecast error metrics

However, due to the strong scattering of these data, reliably estimating the uncertainty of the net power prediction is not possible only based on a fit

function. Instead, a linear 95 % confidence threshold is determined as depicted by the dashed line in Figure 5-18. This allows for predicting the uncertainty of power predictions at any time based on the corresponding forecast error in the following manner: With 95 % confidence

$$e_{\text{pred.}} < a \cdot e_{\text{forc.}} \tag{5.5}$$

with unsigned forecast error metrics and respectively

$$a \cdot e_{\text{forc.}} - b < e_{\text{pred.}}^{\text{bias}} < a \cdot e_{\text{forc.}} + b \tag{5.6}$$

with the signed bias. The corresponding uncertainty parameters a and b are given in Table 5-1. Moreover, the parameter b decreases with the mean average interval length. Hence, not only does the prediction error decrease with longer averaging intervals, but its uncertainty can also be predicted more precisely. Finally, as a performance indicator for the uncertainty prediction, the mean absolute value of the predicted uncertainties (MAPU) is given in Table 5-1 for the considered scenario and all lead times. In conclusion, bias as a forecasting error metric results in the lowest MAPU and is, therefore, best suited for predicting the uncertainty of the net power prediction.

Table 5-1: Parameters of the 95 % confidence threshold and resulting mean absolute uncertainty prediction (MAPU) for the net power prediction

	$\tau_{\text{mov.av.}}$	a [MW/(W/m²)]	b [MW]	MAPU [MW]
RMSD-based	5 min	0.1020	–	38.2
	20 min	0.0823	–	31.1
	60 min	0.0755	–	29.1
CRMSD-based	5 min	0.2300	–	37.7
	20 min	0.1752	–	29.0
	60 min	0.1620	–	27.6
|Bias|-based	5 min	0.3465	–	40.6
	20 min	0.2310	–	27.4
	60 min	0.2084	–	25.5
Bias-based	5 min	0.1127	28.3	28.6
	20 min	0.1223	16.4	17.0
	60 min	0.1119	7.8	8.0

5.2.3 Variability of convection losses

In contrast to the well-predictable radiation losses, convection losses are subject to highly variable wind conditions. Even though radiation losses dominate the receiver efficiency at normal surface temperatures, as seen in Figure 5-19, the convective heat losses become significant at lower temperatures. This is especially relevant during the preheating of the empty absorber tubes during startup. Hence, accurate prediction of the convective losses seems necessary to predict the startup time realistically.

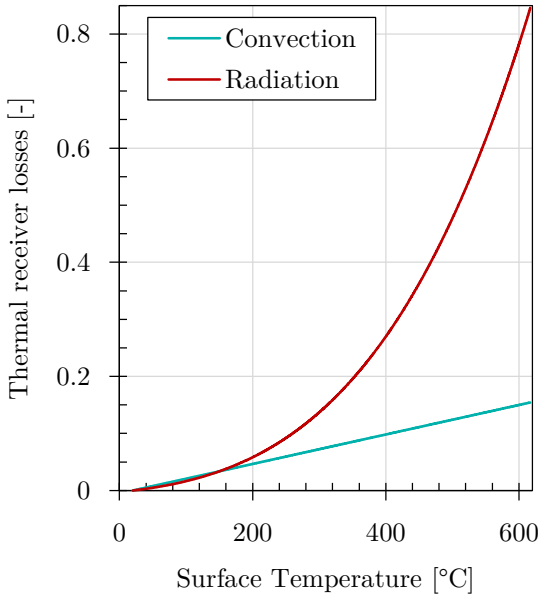

Figure 5-19: Comparison of convection and radiation losses of an external receiver depending on the surface temperature

Not only does the amount of convective heat loss depend on the ambient temperature and wind speed, but it also depends on the panel orientation in relation to the wind direction. For instance, a panel on the windward side has much higher convective losses than a panel on the lee side. Thus, a windward-facing panel requires more flux and potentially more time for preheating. Sanitjai and Goldstein (2004), W.Ezzat and W. Zghaer (2013) and Dhiman et al. (2017) have conducted CFD simulations as well as experiments to determine local Nusselt numbers and convective heat transfer coefficients on a cylinder in cross flow. As shown in Figure 5-20, the local Nusselt number decreases from the windward surface (0°) to the sides until the flow transitions to turbulent flow. Behind that point, the Nusselt number increases towards the lee side (180°).

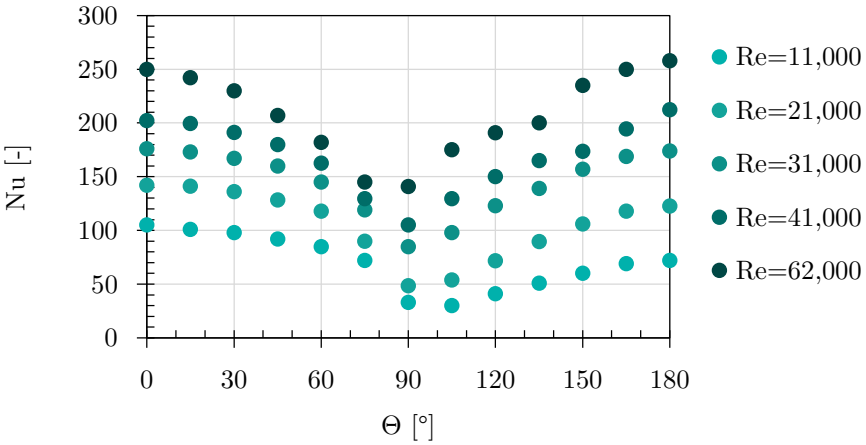

Figure 5-20: Local Nusselt numbers along the circumference of a cross-flow cylinder (modified from Dhiman et al. 2017)

Based on this, Figure 5-21 presents the relative range of how much the local Nusselt number deviates from the mean value depending on the Reynolds number. Actually, the rage becomes smaller with higher Reynolds numbers (-32 % to +24 %). However, for a commercial-scale external Receiver, the Reynolds number is one to two orders of magnitude higher than in the data available in the literature. For instance, at a wind speed of 5 m/s, the considered receiver has a Reynolds number of $8 \cdot 10^6$. In addition, no suitable correlation has yet been developed, leaving the uncertainty of the actual convection losses during preheating.

Additionally, the receiver shape is not as smooth as the cylinders examined in the mentioned studies. The influence of the polygonal shape with 34 corners is considered negligible in comparison to a cylinder. Still, the surface roughness of the receiver panels due to the shape of the adjacent absorber tubes should be considered. Uhlig et al. (2016) investigated how this surface roughness as well as the three-dimensional shape of the Solar Two receiver affect the thermal losses hence the receiver efficiency. Both effects act in

opposite directions, but compared to cylinder-based correlations, deviations of up to 15 % can be expected in wind speeds of up to 20 m/s.

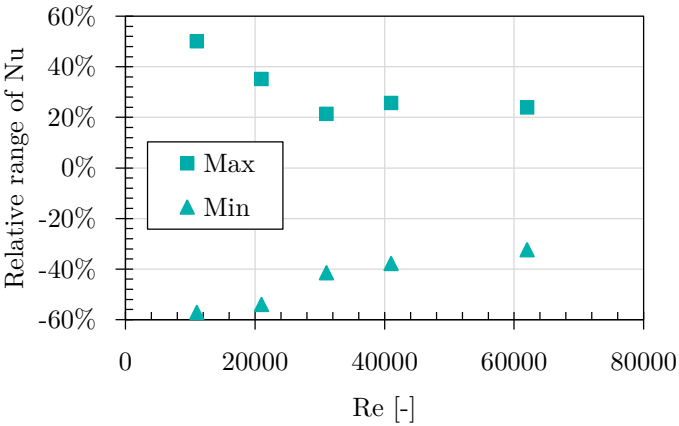

Figure 5-21: Range of the Nusselt number relative to the average along the circumference of a cylinder in cross flow

In order to investigate the impact of those uncertainties on the preheating time and net yield, the temporary shutdown maneuver is simulated with different convective heat transfer coefficients for the convective losses. The resulting minimal backside temperatures and net power trends are plotted in Figure 5-22. It shows that doubling α_{conv} (from 10 to 20 W/(m²K)) causes the respective temperature to drop about 50 K deeper, delaying the restart by 2 min. As shown in Figure 5-23, this reduces the net yield by approx. 1.2 MWh_{el}. The trend suggests a nearly linear correlation between the convective heat transfer coefficient and the predicted net yield, but its dependency on the available flux should not be neglected.

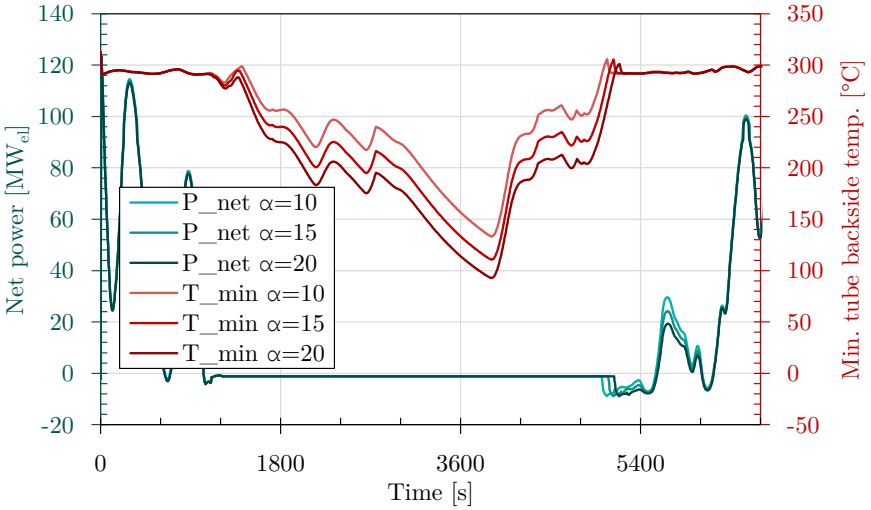

Figure 5-22: Trends of the net power and minimal absorber backside temperature during temporary shutdown with different convective heat loss coefficients (α_{conv} in W/(m²K))

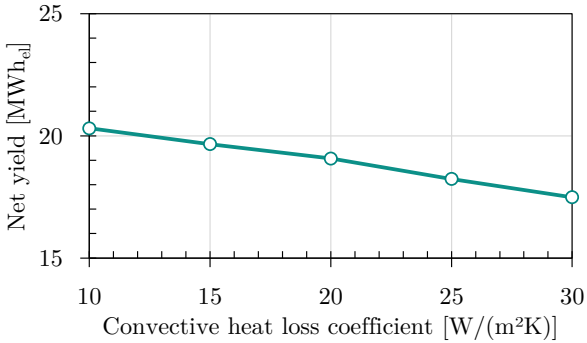

Figure 5-23: Net yield of an exemplary interrupted operation sequence in dependence on the convective heat loss coefficient

5.3 Sensitivity Studies

The following sensitivity studies investigate how some design parameters of an MST influence the outcome of the OAS.

5.3.1 Tower height

The height of the solar tower mainly defines the pumping energy consumption since the most significant portion of the pumping pressure is due to geodetic pressure. The heliostat field efficiency usually benefits from a higher solar tower because blocking and shading losses decrease. Therefore, in the course of the commercialization of MSTs, the height of the constructed towers increased significantly from less than 100 m to up to 250 m. In this regard, the OAS is tested with different tower heights to quantify its impact on the predicted net yield benefit. The results are plotted in Figure 5-24 accordingly.

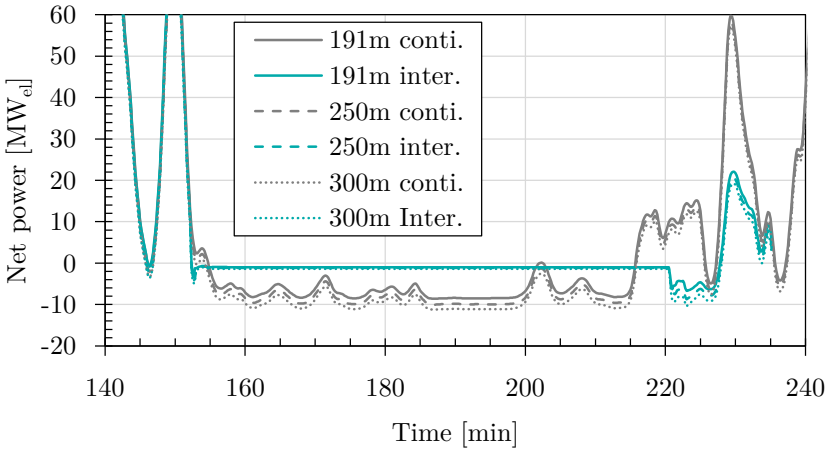

Figure 5-24: Predicted net power trends of continuous and interrupted operation with different tower heights

They clearly show how parasitic losses increase with greater tower height, especially in times of negative net power. Moreover, Figure 5-25 presents the

resulting net benefits that can be achieved by the proposed maneuver of a temporary shutdown. The tower height influences the parasitic losses much more when the receiver is in operation. Therefore, it has more impact on the continuous operation. In turn, the achievable net benefit due to the maneuver increases with the greater tower height significantly. This leads to the conclusion that this OAS function becomes more and more relevant the taller an MST is designed.

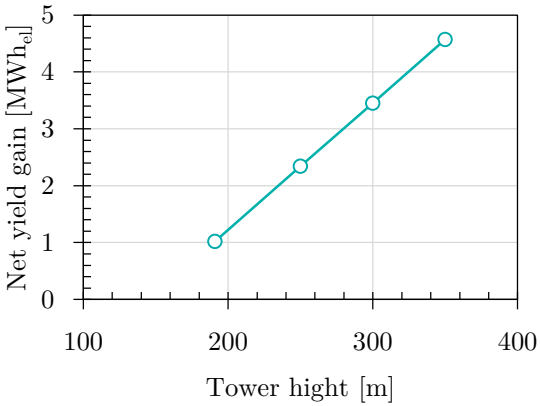

Figure 5-25: Predicted net power benefit due to a temporary shutdown with different tower heights

5.3.2 Allowable transients

In high-temperature components of a molten receiver, the occurring transients, respectively, rates of temperature change are critical for the lifetime of the receiver. Doupis et al. (2016) suggest that the transients during startup should not exceed a rate of 20 K/min (0.33 K/s) to prevent early fatigue at the joints between absorber tubes and headers. However, allowing only slow transients prolongs startup time and reduces the overall yield. The following study puts this into perspective compared to the simulated transients during cloud passages and quantifies the effect of the allowable transients on net yield during a temporary shutdown maneuver.

First, Figure 5-26 presents simulated transients during the artificial cloud scenario Sc_7750. As expected, the tube wall temperature transients show the most significant amplitudes since they are directly connected to the fluctuating solar flux. Still, the bulk temperature transients in the manifolds and the outlet pipe often reach more than 1 K/s and sometimes more than 2 K/s. However, those artificial clouds have sharp edges, which obviously cause higher transients than more realistic blurry edges. It can be considered as a theoretical extreme case instead. Hence, another simulation is performed with the ASI data-based scenario Sc_PSA_190906_realBlur, as shown in Figure 5-27. This simulation reveals significantly milder transients. The highest bulk temperature transient peak can be observed at 7.8 h, which poses a non-realistic outlier. This becomes clear in the CSI distribution plot in Figure 0-3. Apparently, the entire flux map instantly changes from fully shaded to clear-sky and back, which is considered a false measurement. Apart from that, the bulk temperature transients stay below 2 K/s and only sometimes exceed 1 K/s. However, the proposed limit of 0.33 K/s is violated quite often.

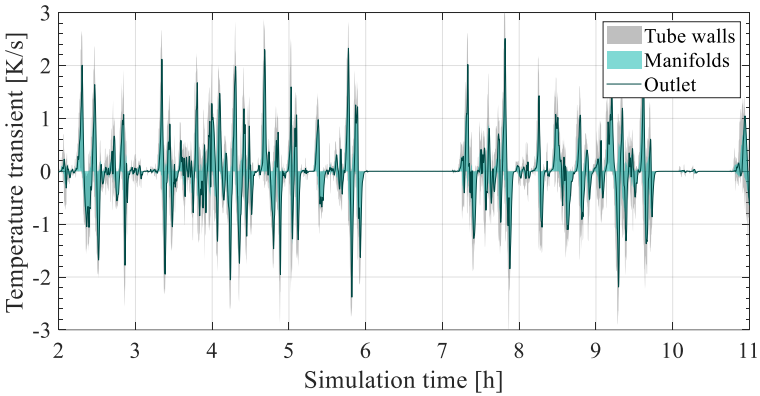

Figure 5-26: Transients of the tube wall, manifold and outlet bulk temperatures during artificial cloud passages

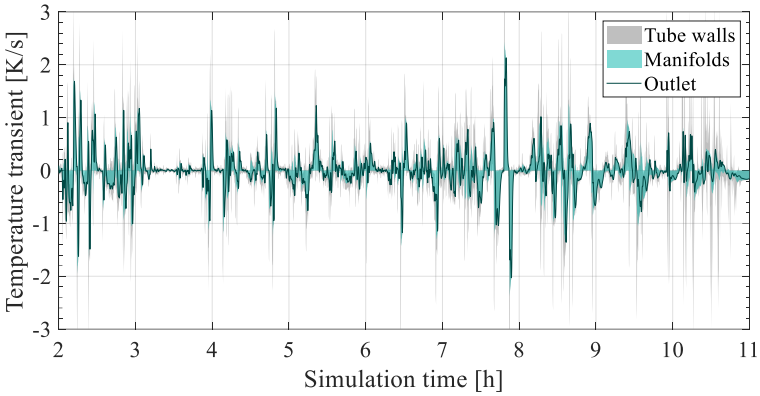

Figure 5-27: Transients of the tube wall, manifold and outlet bulk temperatures during cloudy conditions based on ASI data

Moreover, Figure 5-28 reveals the receiver outlet temperature trends during a restart with different limits for the allowable transient during preheating and ramp-up. It confirms that the allowable transient significantly impacts how long it takes after a temporary shutdown until the outlet temperature returns to the same level as if the system was operated continuously. Especially between 20 and 40 K/min, it reveals a significant gap.

Moreover, Figure 5-29 gives the predicted net yield values for the above-mentioned cases. It leads to the conclusion that the allowable transients significantly impact the net yield during such a transition. The net yield gain from this maneuver could be doubled by allowing higher transients. This would have to be compared to the additional cost for higher material quality or earlier replacement of critical components.

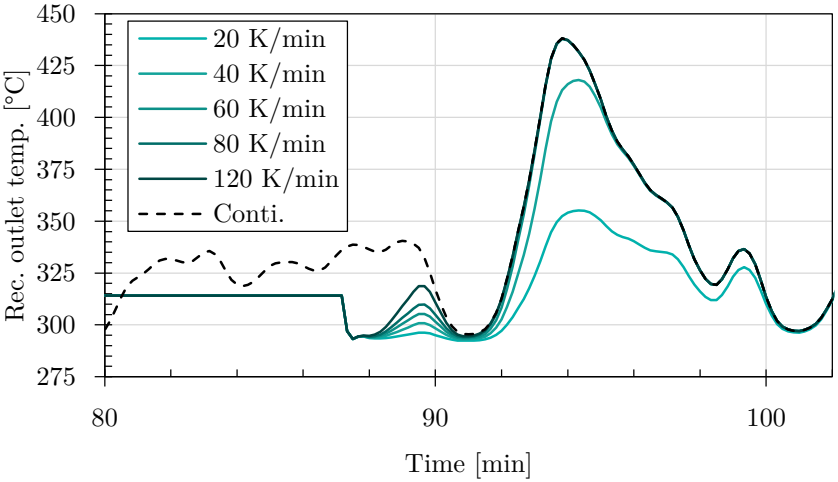

Figure 5-28: Receiver outlet temperature trends with different limits for the temperature transients during restart and continuous operation

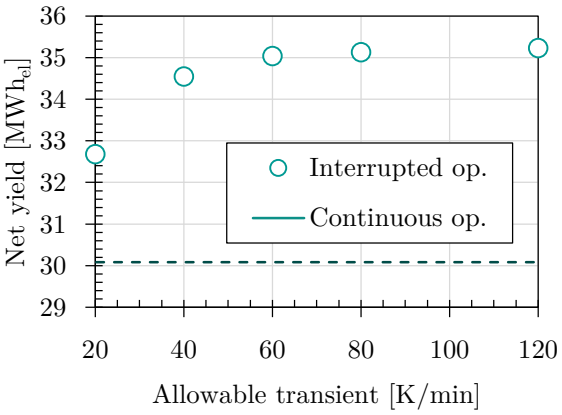

Figure 5-29: Predicted net yield during a temporary shutdown maneuver depending on the allowable temperature transients.

6 Conclusion and Outlook

The presented work's objective was an **operating assistance system** (OAS) for the transition between operation modes of molten salt receivers. This should allow for increased operational net yield with the help of model-predictive assistance without any equipment modification. Based on the state of the technology of molten salt solar towers (MST) and previous research, this thesis presents the concept of an appropriate OAS.

A variety of **assistance functions** was proposed and conceptualized on how they could be implemented, such as optimizing startup timing (task 1) and ramp-up trajectories (task 2) with the help of process prediction, soft sensor application for monitoring critical temperatures/-gradients (task 3 and 5) and predicting actual flow distributions to derive dynamic minimal mass flow rates to prevent overheating during partial shading (task 6). Finally, one assistance function that supports the decision of whether the receiver system should continue or interrupt operation during heavy cloud coverage (task 8) was developed, implemented and tested throughout the central part of this thesis.

The proposed implementation method includes dynamic models of different levels of detail, a heuristic decision algorithm and solar flux distribution forecasts as input data. With the perspective of applying nowcasting data in the future, numerous test scenarios were created based on all-sky imager (ASI) records and artificial cloud movements. As a basis for developing specialized reduced models, a **detailed dynamic two-phase (2P) model** of the receiver system was developed and implemented in the modeling language Modelica. With the help of a novel 2P medium and flow modeling approach and specific tweaks in the system modeling, it was possible to give the detailed 2P model the numerical stability to simulate all operating modes and transitions like a

digital twin. This model was laid out and parameterized according to a commercial-scale reference plant.

With this setup, the dynamic behavior of the receiver system in codependence with the thermal storage system was analyzed to derive model reductions to achieve shorter computing times in the OAS application. First, the detailed modeling of the tubular molten salt receiver was simplified by representing multiple panels (tube bundles) with only one absorber tube model, reducing the difficulty of solving the thermo-hydraulic differential-algebraic equation (DAE) system significantly. This **simplified dynamic 2P model** was applied in the OAS to describe the interrupted operation, including drainage, preheat and refill.

Second, a more drastic model reduction was conducted to create a **fast one-phase (1P) model** to describe the continuous operation of the receiver system. For this, a semi-zero-dimensional modeling approach was developed to represent each receiver pass (parallel connection of multiple receiver panels) while maintaining an appropriate representation of the highly nonlinear thermal losses. Combined with minimalistic periphery modeling, this allows for predicting dynamic system performance during several hours of continuous operation within only a few seconds of computing time.

Both reduced models were **validated** against the detailed dynamic 2P model, which holds validity against high-resolution CFD simulations and experimental data. In contrast, a scalar receiver modeling approach with second-order delay (PT2) characteristics revealed an unsatisfactory representation of transients.

Furthermore, in contrast to conventional mathematical optimization methods, a **heuristic decision algorithm** was developed and implemented in the universal programming language Python. This algorithm determines the optimal timing for a temporary shutdown and quantifies the net benefit of this maneuver with the help of the fast 1P model and the simplified dynamic 2P model. For this, a **virtual net power** approach was developed as a measure

that includes all relevant dynamic effects. By shifting delayed effects from the time of occurrence to the time of cause, the decision algorithm can utilize this as an objective function eliminating the need for iterations. Hence, both models only need to be solved once to determine the optimal time for the shutdown and to quantify the net benefit. The virtual net power validation confirmed that it results in nearly the same overall net yield. However, in contrast to a conventional (actual) power approach, it is unnecessary to simulate the entire day to account for delayed energy recycling and similar effects.

Finally, the test results show satisfactory functionality of the OAS. The applied test scenarios cover cases where the OAS proposes a temporary shutdown predicting a net benefit of several megawatt-hours of electricity. In contrast, the OAS proposes continuing receiver operation in other cases where the added losses due to the transitions would be higher than the avoided parasitic losses.

Moreover, three different **uncertainty analyses** were conducted. First, the input data quality impact was investigated, showing that DNI (direct normal irradiance) maps with pixels significantly smaller than 1000 m are needed to represent the dynamic behavior appropriately. Secondly, the impact of forecasting errors on the predicted net yield was investigated. The statistical results revealed that the accuracy of the examined nowcasting system would need significant improvement for the OAS application. However, by applying a confidence threshold to these data, the uncertainty of any net yield prediction could be estimated.

Third, the convective heat losses, especially at low temperatures, pose another uncertainty. Based on experiments and CFD simulations, the literature shows that compared to the mean value of the convective heat transfer coefficient, its local value can vary by more than 30 % depending on the wind direction and speed and the three-dimensional shape and macroscopic surface roughness. This significantly affects the required flux density for preheating and, therefore, the duration of a restart procedure, as demonstrated in the corresponding sensitivity study.

Two further sensitivity studies were conducted, showcasing how the height of the solar tower and allowable limits for temperature transients affect the net yield, especially the net benefit from a temporary shutdown.

In conclusion, this thesis proves the feasibility of the proposed OAS function provided the availability of appropriate DNI forecasts. The introduced model reductions allowed for manageable computing times while maintaining validity in the designated regimes. The heuristic decision algorithm and the incorporated virtual net power approach enabled this. However, uncertainties about the achieved process predictions are significant, primarily due to the uncertainty of input data. Further research is necessary to increase the forecasting accuracy or more extended lead times. Besides, appropriate modeling of the local heat transfer coefficient in dependence on wind direction, wind speed, three-dimensional shape and surface roughness needs to be developed to predict restart durations realistically. Finally, testing this OAS on an actual receiver system would allow for further learning on how this system can realistically be integrated into commercial operations.

7 Bibliography

ABB Asea Brown Boveri Ltd (2022): Advanced control and optimization. Available online at https://new.abb.com/life-sciences/services/advanced-control-and-optimization.

Acosta, David; Garcia, Jesus; Sanjuan, Marco; Oberkirsch, Laurin; Schwarzbözl, Peter (2021): Flux-feedback as a fast alternative to control groups of aiming points in molten salt power towers. In *Solar Energy* 215, pp. 12–25. DOI: 10.1016/j.solener.2020.12.028.

ACWA POWER (2021): Redstone CSP IPP. Available online at https://www.acwapower.com/en/projects/redstone-csp-ipp/, checked on 12/19/2021.

Ahlbrink, Nils (2013): Modellgestützte Bewertung und Optimierung der offenen Luftreceivertechnologie. Dissertation.

Ahlbrink, Nils; Belhomme, Boris; Flesch, Robert; Quinto, Daniel Maldonado; Rong, Amadeus; Schwarzbözl, Peter (2012): STRAL. Fast Ray Tracing Software With Tool Coupling Capabilities for High-Precision Simulations of Solar Thermal Power Plants. In : Proceedings of the SolarPACES Conference 2012. SolarPACES. Marrakech, Marokko. Available online at elib.dlr.de/78440/.

Ahmadi, Mohammad Hossein; Ghazvini, Mahyar; Sadeghzadeh, Milad; Alhuyi Nazari, Mohammad; Kumar, Ravinder; Naeimi, Abbas; Ming, Tingzhen (2018): Solar power technology for electricity generation: A critical review. In *Energy Sci Eng* 6 (5), pp. 340–361. DOI: 10.1002/ese3.239.

Akselsen, Andreas Holm (2012): Simulation of Unstable Two-phase Flows in Long Risers.

Anand, Rimmi; Aggarwal, Divya; Kumar, Vijay (2017): A comparative analysis of optimization solvers. In *Journal of Statistics and Management Systems* 20 (4), pp. 623–635. DOI: 10.1080/09720510.2017.1395182.

Arora, Rajesh Kumar (2015): Optimization: Chapman and Hall/CRC. DOI: 10.1201/b18469.

Aspen Technology Inc. (2022): Solutions for Power Generation, Transmission & Distribution. Available online at https://www.aspentech.com/en/industries/power-generation-transmission-and-distribution?src=web-home-industries.

Astolfi, Marco; Binotti, Marco; Mazzola, Simone; Zanellato, Luca; Manzolini, Giampaolo (2017): Heliostat aiming point optimization for external tower receiver. In *Solar Energy* 157, pp. 1114–1129. DOI: 10.1016/j.solener.2016.03.042.

Augsburger, Germain; Favrat, Daniel (2013): Modelling of the receiver transient flux distribution due to cloud passages on a solar tower thermal power plant. In *Solar Energy* 87, pp. 42–52. DOI: 10.1016/j.solener.2012.10.010.

Ayres, Mark; Dunn, Rebecca; Raczka, Gary; Speir, Mark; Buck, Roger; Anderson, Greg (2020): Heliostat aiming corrections with bad data detection. In *AIP Conference Proceedings* 2303 (1), p. 30004. DOI: 10.1063/5.0028603.

Bauer, Olaf (1999): Modelling of Two-Phase Flows with Modelica. Master thesis. Lund Institute of Technology, Lund, Sweden. Department of Automatic Control.

Belhomme, Boris; Pitz-Paal, Robert; Schwarzbözl, Peter (2013): Optimization of Heliostat Aim Point Selection for Central Receiver Systems Based on the Ant Colony Optimization Metaheuristic. In *J. Sol. Energy Eng* 136 (1). DOI: 10.1115/1.4024738.

Binotti, Marco; Giorgi, Paolo de; Sanchez, David; Manzolini, Giampaolo (2016): Comparison of Different Strategies for Heliostats Aiming Point in Cavity and External Tower Receivers. In *J. Sol. Energy Eng* 138 (2). DOI: 10.1115/1.4032450.

Blum, Niklas Benedikt; Nouri, Bijan; Wilbert, Stefan; Schmidt, Thomas; Lünsdorf, Ontje; Stührenberg, Jonas et al. (2021): Cloud height measurement by a network of all-sky imagers. In *Atmos. Meas. Tech.* 14 (7), pp. 5199–5224. DOI: 10.5194/amt-14-5199-2021.

Bonk, Alexander; Bauer, Thomas (2022): Solar Salt - Thermal Property Analysis - Extended Version: Report on thermo-physical properties of binary NaNO3-KNO3 mixtures in a range of 55-65 wt% NaNO3. Available online at https://elib.dlr.de/185795/. DOI: 10.57676/3rea-p782.

Bonk, Alexander; Braun, Markus; Sötz, Veronika A.; Bauer, Thomas (2020): Solar Salt – Pushing an old material for energy storage to a new limit. In *Applied Energy* 262, p. 114535. DOI: 10.1016/j.apenergy.2020.114535.

Boretti, Albert; Castelletto, Stefania; Al-Zubaidy, Sarim (2017): Concentrating Solar Power Tower: Latest Status Report and Survey of Development Trends. DOI: 10.20944/preprints201710.0027.v2.

Brennen, Christopher Earls (2005): Fundamentals of Multiphase Flow. Cambridge: Cambridge University Press. DOI: 10.1017/CBO9780511807169.

Burgaleta, Juan Ignacio; Ternero, Antonio; Vindel, David; Salbidegoitia, Ibon; Azcarrraga, Gonzalo (2012): Gemasolar, Key Points for the Operation of the Plant. In : Proceedings of the SolarPACES Conference 2012. SolarPACES. Marrakech, Marokko.

Crespi, Francesco; Toscani, Andrea; Zani, Paolo; Sánchez, David; Manzolini, Giampaolo (2018): Effect of passing clouds on the dynamic performance of a CSP tower receiver with molten salt heat storage. In *Applied Energy* 229, pp. 224–235. DOI: 10.1016/j.apenergy.2018.07.094.

Das, A. K.; Iñigo, P.; Terdalkar, R. J.; Joshi, A.; Wang, C.; Clark, M. M. et al. (2015): Design Features and Control Concepts of ALSTOM Molten Salt Receiver. In *Energy Procedia* 69, pp. 350–359. DOI: 10.1016/j.egypro.2015.03.040.

Dassault Systèmes (2021): Dymola®. Version 2021: Dassault Systèmes. Available online at https://www.3ds.com/products-services/catia/products/dymola/key-advantages/.

Dersch, Jürgen; Paucar, Jaime; Polkas, Thomas; Schweitzer, Axel; Stryk, Alexander (2021): Blueprint for Molten Salt CSP Power Plant. Final report of the project "CSP-Reference Power Plant" No. 0324253. Available online at https://elib.dlr.de/141315/.

Dhiman, S. K.; Prasad, J. K.; Kumar, Arbind (2017): Unsteady convective heat transfer in cross flow past two tandem cylinders: an inverse heat conduction approach. In *Heat Mass Transfer* 53 (5), pp. 1761–1775. DOI: 10.1007/s00231-016-1927-x.

Doupis, Dimitri; Wang, Chuan; Carcorze-Soto, Jorge; Chen, Yen-Ming; Maggi, Andrea; Losito, Matteo; Clark, Michael (2016): Transient simulation of molten salt central receiver. In *AIP Conference Proceedings* 1734 (1), p. 30013. DOI: 10.1063/1.4949065.

Flesch, Robert; Frantz, Cathy; Maldonado Quinto, Daniel; Schwarzbözl, Peter (2017): Towards an optimal aiming for molten salt power towers. In *Solar Energy* 155, pp. 1273–1281. DOI: 10.1016/j.solener.2017.07.067.

Flesch, Robert; Högemann, Daniel; Hackmann, Jonas Michael; Uhlig, Ralf; Schwarzbözl, Peter; Augsburger, Germain; Clark, Michael (2016): Dynamic

modeling of molten salt power towers. In : Proceedings of the SolarPACES Conference 2016. SolarPACES. Abu Dhabi. Available online at http://elib.dlr.de/108542/. DOI: 10.1063/1.4984359.

Francke, Henning (2014): Thermo-hydraulic model of the two-phase flow in the brine circuit of a geothermal power plant [PhD thesis].

Frantz, Cathy; Binder, Matthias; Busch, Konrad; Ebert, Miriam; Heinrich, Andreas; Kaczmarkiewicz, Nadine et al. (2022a): Basic engineering of a high performance molten salt tower receiver system. In *AIP Conference Proceedings* 2445 (1), p. 110002. DOI: 10.1063/5.0085895.

Frantz, Cathy; Buck, Reiner; Röger, Marc; Hoffschmidt, Bernhard (2022b): Experimental Analysis of Forced Convective Heat Transfer of Nitrate Salt in a Circular Tube at High Reynolds Numbers and Temperatures. In *SSRN Journal*. DOI: 10.2139/ssrn.4126906.

Frantz, Cathy; Fritsch, Andreas; Uhlig, Ralf (2017): ASTRID© – Advanced Solar Tubular ReceIver Design: A powerful tool for receiver design and optimization. In. SOLARPACES 2016: International Conference on Concentrating Solar Power and Chemical Energy Systems. Abu Dhabi, United Arab Emirates, 11–14 October 2016: Author(s) (AIP Conference Proceedings), p. 30017. DOI: 10.1063/1.4984360.

Fritsch, Andreas; Uhlig, Ralf; Marocco, Luca; Frantz, Cathy; Flesch, Robert; Hoffschmidt, Bernhard (2017): A comparison between transient CFD and FEM simulations of solar central receiver tubes using molten salt and liquid metals. In *Solar Energy* 155, pp. 259–266. DOI: 10.1016/j.solener.2017.06.022.

Gall, Jan (2012): Betriebsführung und -optimierung eines solarthermischen Turmkraftwerkes. Dissertation. Rheinisch-Westfälische Technische Hochschule Aachen, Aachen. Institut für Regelungstechnik.

García, Elvira; Calvo, Roberto (2012): One Year Operation Experience of Gemasolar Plant. In : Proceedings of the SolarPACES Conference 2012. SolarPACES. Marrakech, Marokko.

García, Jesús; Barraza, Rodrigo; Soo Too, Yen Chean; Vásquez-Padilla, Ricardo; Acosta, David; Estay, Danilo; Valdivia, Patricio (2022): Transient simulation of a control strategy for solar receivers based on mass flow valves adjustments and heliostats aiming. In *Renewable Energy* 185, pp. 1221–1244. DOI: 10.1016/j.renene.2021.12.008.

García, Jesús; Soo Too, Yen Chean; Padilla, Ricardo Vasquez; Beath, Andrew; Kim, Jin-Soo; Sanjuan, Marco E. (2018): Dynamic performance of an aiming control methodology for solar central receivers due to cloud disturbances. In *Renewable Energy* 121, pp. 355–367. DOI: 10.1016/j.renene.2018.01.019.

GE General Electric (2022): IOT Platform Predix. Available online at https://www.ge.com/digital/iiot-platform, checked on 2022.

Ghobeity, Amin; Mitsos, Alexander (2011): Optimal Operation of a Concentrated Solar Thermal Cogeneration Plant. In E. N. Pistikopoulos, M. C. Georgiadis, A. C. Kokossis (Eds.): Computer Aided Chemical Engineering : 21 European Symposium on Computer Aided Process Engineering, vol. 29: Elsevier, pp. 1974–1978. Available online at https://www.sciencedirect.com/science/article/pii/B9780444542984501732. DOI: 10.1016/B978-0-444-54298-4.50173-2.

Gnielinski, Volker (2013a): G1 Durchströmte Rohre. In VDI e.V. (Ed.): VDI-Wärmeatlas. Berlin, Heidelberg: Springer Berlin Heidelberg, pp. 785–792. Available online at https://link.springer.com/referenceworkentry/10.1007/978-3-642-19981-3_42. DOI: 10.1007/978-3-642-19981-3_42.

Gnielinski, Volker (2013b): G6 Querumströmte einzelne Rohre, Drähte und Profilzylinder. In VDI e.V. (Ed.): VDI-Wärmeatlas. Berlin, Heidelberg: Springer Berlin Heidelberg, pp. 817–818. Available online at https://link.springer.com/referenceworkentry/10.1007/978-3-642-19981-3_47. DOI: 10.1007/978-3-642-19981-3_47.

Heller, Peter (Ed.) (2017): The performance of concentrated solar power (CSP) systems. Analysis, measurement and assessment. Duxford, Cambridge, MA, Kidlington: Elsevier (Woodhead Publishing series in energy). Available online at http://www.sciencedirect.com/science/book/9780081004470. DOI: 10.1016/C2014-0-03695-7.

Hering, D.; Binder, M.; Schwarzbözl, P.; Schwaiger, R.; Pitz-Paal, R. (2021a): Monitoring of service life consumption for tubular solar receivers: Review of contemporary thermomechanical and damage modeling approaches. In *Solar Energy* 226, pp. 427–445. DOI: 10.1016/j.solener.2021.08.022.

Hering, D.; Iding, K.; Schwarzbözl, Peter; Popp, R.; Enste, U.; Schwager, C.; Angele, F. (2021b): Unterstützung des dynamischen Betriebs von Salzschmelereveivern - DynaSalt-2. öffentlicher Abschlussbericht : Laufzeit des Vorhabens: 01.08.2017 bis 31.12.2020. DLR. Köln. Available online at https://www.tib.eu/de/suchen/id/TIBKAT%3A1783514469.

Ho, Clifford K.; Khalsa, Siri S. (2012): A Photographic Flux Mapping Method for Concentrating Solar Collectors and Receivers. In *J. Sol. Energy Eng* 134 (4), p. 315. DOI: 10.1115/1.4006892.

Hoffmann, A.; Merk, B.; Hirsch, T.; Pitz-Paal, R. (2014): Simulation of thermal fluid dynamics in parabolic trough receiver tubes with direct steam generation using the computer code ATHLET. In *Kerntechnik* 79 (3), pp. 175–186. DOI: 10.3139/124.110419.

Hogrefe, Jürgen; Hinsch, Juliane, (ed.); Krüger, Joachim, (ed.) (2021): CSP - Solar power around the clock. German Association for Concentrated Solar Power.

Huang, Hao; Xu, Jin; Peng, Zhenzhou; Yoo, Shinjae; Yu, Dantong; Huang, Dong; Qin, Hong (2013): Cloud motion estimation for short term solar irradiation prediction. In : new 2013 IEEE International Conference on Smart Grid Communications (SmartGridComm). IEEE International Conference on Smart Grid Communications (SmartGridComm). Vancouver, BC, Canada: IEEE, pp. 696–701. DOI: 10.1109/SmartGridComm.2013.6688040.

IRENA (2022): Renewable Energy Statistics 2022. Abu Dhabi: International Renewable Energy Agency.

Issa, R. I.; Kempf, M.H.W. (2003): Simulation of slug flow in horizontal and nearly horizontal pipes with the two-fluid model. In *International Journal of Multiphase Flow* 29 (1), pp. 69–95. DOI: 10.1016/S0301-9322(02)00127-1.

Kolb, Gregory J. (2011): An Evaluation of Possible Next-Generation High-Temperature Molten-Salt Power Towers. Sandia National Laboratories. Albuquerque, New Mexico. DOI: 10.2172/1035342.

Li, Zhi; Wang, Zhifeng; Zhang, Qiangqiang; Bai, Fengwu (2019): A fast molten salt receiver model in MATLAB. In *AIP Conference Proceedings* 2126 (1), p. 30034. DOI: 10.1063/1.5117546.

Lizarraga-Garcia, Enrique; Ghobeity, Amin; Totten, Mark; Mitsos, Alexander (2013): Optimal operation of a solar-thermal power plant with energy storage and electricity buy-back from grid. In *Energy* 51, pp. 61–70. DOI: 10.1016/j.energy.2013.01.024.

Losito, Matteo; Maggi, Andrea; Sani, Alessandro; Flesch, Robert; Schwarzbözl, Peter (2018): Dynamic analysis of extraordinary operations of molten

salt central receiver. In *AIP Conference Proceedings* 2033 (1), p. 210008. DOI: 10.1063/1.5067210.

Lucas, Klaus (2008): Thermodynamik. Berlin, Heidelberg: Springer Berlin Heidelberg. DOI: 10.1007/978-3-540-68648-4.

Martin, Holger (2013): E2 Instationäre Wärmeleitung in ruhenden Körpern. In VDI e.V. (Ed.): VDI-Wärmeatlas. Berlin, Heidelberg: Springer Berlin Heidelberg, pp. 727–752. Available online at https://link.springer.com/referenceworkentry/10.1007/978-3-642-19981-3_36. DOI: 10.1007/978-3-642-19981-3_36.

Masella, J. M.; Tran, Q. H.; Ferre, D.; Pauchon, C. (1998): Transient simulation of two-phase flows in pipes. In *International Journal of Multiphase Flow* 24 (5), pp. 739–755. DOI: 10.1016/S0301-9322(98)00004-4.

Mehos, Mark; Price, Hank; Cable, Robert; Kearney, David; Kelly, Bruce; Kolb, Gregory; Morse, Frederick (2020): Concentrating Solar Power Best Practices Study. National Renewable Energy Laboratory (NREL). DOI: 10.2172/1665767.

Montoya, Andrés; Rodríguez-Sánchez, M. R.; López-Puente, Jorge; Santana, Domingo (2019): Thermal stress variation in a solar central receiver during daily operation. In *AIP Conference Proceedings* 2126 (1), p. 30038. DOI: 10.1063/1.5117550.

Nolteernsting, Felix (2020): Operation assistance for concentrating solar power plants to increase efficiency based on control engineering methods. RWTH Aachen University. DOI: 10.18154/RWTH-2021-02120.

Nouri, Bijan; Blum, Niklas; Wilbert, Stefan; Zarzalejo, Luis F. (2022): A Hybrid Solar Irradiance Nowcasting Approach: Combining All Sky Imager Systems and Persistence Irradiance Models for Increased Accuracy. In *Solar RRL* 6 (5), p. 2100442. DOI: 10.1002/solr.202100442.

NREL (2022): Concentrating Solar Power Projects. Available online at https://solarpaces.nrel.gov, checked on 22.08.22.

Oberkirsch, Laurin; Grobbel, Johannes; Maldonado Quinto, Daniel; Schwarzbözl, Peter; Hoffschmidt, Bernhard (2022): Controlling a solar receiver with multiple thermochemical reactors for hydrogen production by an LSTM neural network based cascade controller. In *Solar Energy* 243 (C), pp. 483–493. DOI: 10.1016/j.solener.2022.08.007.

Oberkirsch, Laurin; Maldonado Quinto, Daniel; Schwarzbözl, Peter; Hoffschmidt, Bernhard (2021): GPU-based aim point optimization for solar tower power plants. In *Solar Energy* 220, pp. 1089–1098. DOI: 10.1016/j.solener.2020.11.053.

Offergeld, Matthias; Röger, Marc; Stadler, Hannes; Gorzalka, Philip; Hoffschmidt, Bernhard (2019): Flux density measurement for industrial-scale solar power towers using the reflection off the absorber. In : SolarPACES 2018: International Conference on Concentrating Solar Power and Chemical Energy Systems. SolarPACES 2018: International Conference on Concentrating Solar Power and Chemical Energy Systems. Casablanca, Morocco, 2–5 October 2018: AIP Publishing (AIP Conference Proceedings), p. 110002. DOI: 10.1063/1.5117617.

Osuna, Rafael; Olavarría, Rafael; Morillo, Rafael; Sánchez, Marcelino; Cantero, Felipe; Fernández-Quero, Valerio et al. (2006): PS10, Construction of a 11MW solar thermal tower plant in Seville, Spain. In : SolarPACES Conference 2006.

Pacheco, James E.; Bradshaw, Robert W.; Dawson, Daniel B.; De la Rosa, Wilfredo; Gilbert, Rockwell; Goods, Steven H. et al. (2002): Final Test and Evaluation Results from the Solar Two Project. Sandia National Laboratories. Albuquerque, New Mexico. DOI: 10.2172/793226.

Popp, R.; Flesch, R.; Konrad, T.; Jassmann, U.; Abel, D. (2019): Control-Oriented Model of a Molten Salt Solar Power Central Receiver. In : 2019 18th European Control Conference (ECC). 2019 18th European Control Conference (ECC), pp. 2295–2300. DOI: 10.23919/ECC.2019.8795914.

Popp, Rudolf; Iding, Kevin; Schwarzbözl, Peter; Konrad, Thomas; Abel, Dirk (2023): A Comparison Between Model Predictive and PID-Based Control of a Molten Salt Solar Tower Receiver. In *AIP Conference Proceedings*. DOI: 10.1063/5.0148728.

Puppe, Michael; Giuliano, Stefano; Frantz, Cathy; Uhlig, Ralf; Flesch, Robert; Schumacher, Ralph et al. (2018): Techno-economic optimization of molten salt solar tower plants. In *AIP Conference Proceedings* 2033 (1), p. 40033. DOI: 10.1063/1.5067069.

Relloso, S.; García, E. (2015): Tower technology cost reduction approach after Gemasolar experience. In *Energy Procedia* 69, pp. 1660–1666. DOI: 10.1016/j.egypro.2015.03.125.

Relloso, Sergio (2019): Noor III 150 MW Molten Salt Tower: 1st Year of Commercial Operation. SENER. Casablanca, 2019.

Relloso, Sergio; Gutiérrez, Yolanda (2016): SENER molten salt tower technology. Ouarzazate NOOR III case. In : Proceedings of the SolarPACES Conference 2016. SolarPACES. Abu Dhabi. DOI: 10.1063/1.4984384.

Richter, Pascal; Speetzen, Nils (2022): Accelerated aiming strategy in central receiver systems using integer linear programming. In : SolarPACES 2020: 26th International Conference on Concentrating Solar Power and Chemical Energy Systems. SOLARPACES 2020: 26th International Conference on Concentrating Solar Power and Chemical Energy Systems. Freiburg, Germany, 28 September–2 October 2020: AIP Publishing (AIP Conference Proceedings), p. 30018. DOI: 10.1063/5.0085711.

Rodriguez-Sanchez, M. R.; Sanchez-Gonzalez, A.; Marugan-Cruz, C.; Santana, D. (2015): Flow patterns of external solar receivers. In *Solar Energy* 122, pp. 940–953. DOI: 10.1016/j.solener.2015.10.025.

Rodríguez-Sánchez, M. R.; Soria-Verdugo, Antonio; Almendros-Ibáñez, José Antonio; Acosta-Iborra, Antonio; Santana, Domingo (2014): Thermal design guidelines of solar power towers. In *Applied Thermal Engineering* 63 (1), pp. 428–438. DOI: 10.1016/j.applthermaleng.2013.11.014.

Röger, Marc; Herrmann, Patrik; Ulmer, Steffen; Ebert, Miriam; Prahl, Christoph; Göhring, Felix (2014): Techniques to Measure Solar Flux Density Distribution on Large-Scale Receivers. In *J. Sol. Energy Eng* 136 (3), p. 181. DOI: 10.1115/1.4027261.

Sánchez-González, Alberto; Rodríguez-Sánchez, María Reyes; Santana, Domingo (2020): Allowable solar flux densities for molten-salt receivers: Input to the aiming strategy. In *Results in Engineering* 5, p. 100074. DOI: 10.1016/j.rineng.2019.100074.

Sani, Alessandro; Maggi, Andrea; Losito, Matteo (2018): 24h dynamic simulation of a CSP solar tower demo plant. In *AIP Conference Proceedings* 2033 (1), p. 210016. DOI: 10.1063/1.5067218.

Sanitjai, S.; Goldstein, R. J. (2004): Forced convection heat transfer from a circular cylinder in crossflow to air and liquids. In *International Journal of Heat and Mass Transfer* 47 (22), pp. 4795–4805. DOI: 10.1016/j.ijheatmasstransfer.2004.05.012.

Scheuerer, M.; Scheuerer, G. (1992): Two-Fluid Model Simulation of Two-Phase Flow Problems Using a Conservative Finite-Volume Method 1992, pp. 310–315. DOI: 10.1615/ICHMT.1992.ExpSystComputSimEnergEngin.510.

Schmidt, Achim (2019): Technical Thermodynamics for Engineers. Cham: Springer International Publishing. DOI: 10.1007/978-3-030-20397-9.

Schneider, Wolfgang; Heinrich, Berthold (2017): Praktische Regelungstechnik Effektiv lernen durch Beispiele. Wiesbaden: Springer Fachmedien Wiesbaden, 2017.; Imprint: Springer Vieweg. Available online at http://lobid.org/resources/HT019314093. DOI: 10.1007/978-3-658-16993-0.

Schöttl, Peter; Bern, Gregor; van Rooyen, De Wet; Flesch, Jonathan; Fluri, Thomas; Nitz, Peter (2018): Efficient modeling of variable solar flux distribution on Solar Tower receivers by interpolation of few discrete representations. In *Solar Energy* 160, pp. 43–55. DOI: 10.1016/j.solener.2017.11.028.

Schroedter-Homscheidt, M.; Wilbert, S. (2017): Methods to provide meteorological forecasts for optimum CSP system operations. In Peter Heller (Ed.): The performance of concentrated solar power (CSP) systems. Analysis, measurement and assessment, vol. 93. Duxford, Cambridge, MA, Kidlington: Elsevier (Woodhead Publishing series in energy), pp. 253–281. DOI: 10.1016/B978-0-08-100447-0.00008-0.

Schwager, Christian; Angele, Florian; Nouri, Bijan; Schwarzbözl, Peter; Teixeira Boura, Cristiano José; Herrmann, Ulf: Impact of DNI Forecast Quality on Performance Prediction for a Commercial Scale Solar Tower. Application of Nowcasting DNI Maps to Dynamic Solar Tower Simulation. In : SolarPACES Conference Proceedings, 1. DOI: 10.52825/solarpaces.v1i.675.

Schwager, Christian; Angeley, Florian; Schwarzbözl, Peter; Boura, Cristiano José Teixeira; Herrmann, Ulf (2023): Model predictive assistance for operational decision making in molten salt receiver systems. In *AIP Conf. Proc.* 2815 (1), p. 30020. DOI: 10.1063/5.0151514.

Schwager, Christian; Boura, Cristiano J. Teixeira; Flesch, Robert; Alexopoulos, Spiros; Herrmann, Ulf (2019): Improved efficiency prediction of a molten salt receiver based on dynamic cloud passage simulation. In *AIP Conf. Proc.* 2126 (1), p. 30054. DOI: 10.1063/1.5117566.

Schwager, Christian; Flesch, Robert; Schwarzbözl, Peter; Herrmann, Ulf; Teixeira Boura, Cristiano José (2022): Advanced two phase flow model for transient molten salt receiver system simulation. In *Solar Energy* 232, pp. 362–375. DOI: 10.1016/j.solener.2021.12.065.

Schwarzbözl, Peter; Pitz-Paal, Robert; Schmitz, Mark (2009): Visual HFLCAL - A Software Tool for Layout and Optimisation of Heliostat Fields. In : SolarPACES Conference 2009. Available online at https://elib.dlr.de/60308/1/11354-Schwarzbozl.pdf.

Siemens AG (2022): Control System. Available online at https://www.siemens-energy.com/global/en/offerings/power-generation/sppa-t3000.html.

Sirch, T.; Bugliaro, L.; Zinner, T.; Möhrlein, M.; Vazquez-Navarro, M. (2017): Cloud and DNI nowcasting with MSG/SEVIRI for the optimized operation of concentrating solar power plants. In *Atmospheric Measurement Techniques* 10 (2), pp. 409–429. DOI: 10.5194/amt-10-409-2017.

SolarPACES Network (2021): CSP Projects Around the World. Available online at https://www.solarpaces.org/csp-technologies/csp-projects-around-the-world/.

Sötz, Veronika Anna; Bonk, Alexander; Bauer, Thomas (2020): With a view to elevated operating temperatures in thermal energy storage - Reaction chemistry of Solar Salt up to 630°C. In *Solar Energy Materials and Solar Cells* 212, p. 110577. DOI: 10.1016/j.solmat.2020.110577.

STEAG Energy Services GmbH (2020): Universal Plant Design and Optimization. Fact Sheet, checked on 1/13/2022.

STEAG Energy Services GmbH (2022): Smart solutions for smart operations. Available online at https://www.steag-systemtechnologies.com/en/it-solutions/optimization.

Uhlig, Ralf; Frantz, Cathy; Flesch, Robert; Fritsch, Andreas (2018): Stress analysis of external molten salt receiver. In *AIP Conference Proceedings* 2033 (1), p. 40040. DOI: 10.1063/1.5067076.

Uhlig, Ralf; Frantz, Cathy; Fritsch, Andreas (2016): Effects of vertically ribbed surface roughness on the forced convective heat losses in central receiver systems. In *AIP Conference Proceedings* 1734 (1), p. 30036. DOI: 10.1063/1.4949088.

van Zwieten, J.S.B.; Sanderse, B.; Hendrix, M.H.W.; Vuik, C.; Henkes, R.A.W.M. (2015): Efficient Simulation of One-Dimensional Two-Phase Flow with a New High-Order Discontinuous Galerkin Method. DELFT UNIVERSITY OF TECHNOLOGY.

Vant-Hull, Lorin L. (2002): The Role of "Allowable Flux Density" in the Design and Operation of Molten-Salt Solar Central Receivers. In *J. Sol. Energy Eng* 124 (2), pp. 165–169. DOI: 10.1115/1.1464124.

Vij, A. K.; Dunn, W. E. (1996): Modeling of Two-Phase Flows in Horizontal Tubes.

Vinnemeier, Philipp (2018): Model-Based Optimal Operation of Solar Thermal Power Cycles. Dissertation. RWTH Aachen University. DOI: 10.18154/RWTH-2018-230485.

Vortmeyer, Dieter; Kabelac, Stephan (2013): K2 Sichtfaktoren. In VDI e.V. (Ed.): VDI-Wärmeatlas. Berlin, Heidelberg: Springer Berlin Heidelberg, pp. 1097–1114. Available online at https://link.springer.com/referenceworkentry/10.1007/978-3-642-19981-3_69. DOI: 10.1007/978-3-642-19981-3_69.

W.Ezzat, Akram; W. Zghaer, Hassan (2013): Forced Convection Heat Transfer around Heated Inclined Cylinder. In *IJCA* 73 (8), pp. 5–11. DOI: 10.5120/12759-8631.

Wang, Shuang; Asselineau, Charles-Alexis; Pye, John; Coventry, Joe (2022): An efficient method for aiming heliostats using ray-tracing. In *AIP Conference Proceedings* 2445 (1), p. 120023. DOI: 10.1063/5.0085672.

Yasser, Zeyad; Glumm, Detlef; Schmitz, Mark; Schroedter-Homscheidt, Marion (2020): Forecasting of power production of a parabolic trough plant using EO and NWP data. In *AIP Conference Proceedings* 2303 (1), p. 160009. DOI: 10.1063/5.0028950.

Zavoico, Alexis B. (2001): Solar Power Tower - Design Basis Document. San Francisco.

Appendix

A Operating Modes and Transitions Details

Daily startup:

- During **night preservation (0)** mode the system is shutdown. Only filled pipes are heat traced to prevent freezing.
- When night preservation is active, the `humanOperator` can initiate the startup routine with transition **0-a** by commanding the `modeOperator` to pump startup and the field control to standby.
- During **pump startup (1),** the `modeOperator` starts the receiver pumps, activates the `inletVesselLevelController` and confirms the operating mode after the pumps reach the minimum mass flow rate. The pump bypass opens automatically since any flow out of the inlet vessel is blocked. The `heliostatField` confirms after 60 s to mimic the heliostats being tracked to the standby aim points.
- When pump startup is confirmed, the `humanOperator` performs transition **1-a** by commanding the `modeOperator` to standby mode.
- During **Standby (2)** the `modeOperator` opens the main drain valves allowing HTF to bypass the receiver, activates the `inletVesselPressureController`, sets both flow path controllers to 50 % mass flow control, activates the `outletVesselLevelController` and activates heat tracing for the remaining drained pipes. The HTF now circulates through the main drain lines (one for each flow path) into the downcomer and back into the cold storage tank. When mass flow rate in the riser has reached its set point, the `modeOperator` confirms the operating mode. All heliostats aim at the standby aim points, i.e. zero flux on the receiver.

- When both control units have confirmed standby, the `humanOperator` performs transition **2-a** into preheat mode by commanding the `heliostatField` to gentle warming mode.
- During **preheat (3)** the `heliostatField` performs gentle warming, i.e. it controls the back wall temperatures of the empty absorber tubes by constantly adjusting the flux density for each panel, while the temperature set point is ramped up at a constant rate. The receiver remains on standby.
- When all preheated pipes and tube have reached certain temperature thresholds, the `humanOperator` initiates the receiver flood withtransition **3-a** by setting the receiver mode to flood.
- During **flood (4)** the `modeOperator` raises the mass flow set point for each flow path to 100 % and opens all drain and vent valves of this flow path as soon as the mass flow rate has reached its set point. Simultaneously, the main drain valve is closed to stop the bypass flow. When the completion of the flood is detected by differential pressure sensors in the upper manifold and temperature sensors below the vent valves, the `modeOperator` closes all drain and vent valves and opens the isolation valves at the inlet and outlet of each flow path to establish serpentine flow. Then the `modeOperator` confirms the flood.
- When flood is confirmed, the `humanOperator` triggers transition **4-a** into ramp-up mode, sets the receiver mode to fixed flow and the field mode to temperature ramp.
- During **ramp-up (5)**, when commanded into fixed flow mode the `modeOperator` sets the set points for the level controllers to nominal values and switches the flow path controller to clear-sky mass flow control, i.e. the mass flow rate that is required at the time to reach nominal outlet temperature at clear sky conditions. At the same time, the `heliostatField` performs the temperature ramp by fading from gentle warming to optimized flux density distribution.

- When the outlet temperature of each flow path has reached a certain threshold, the `humanOperator` triggers transition **5-a** into filled cloud protection mode by setting the field mode to optimized aiming. The receiver mode remains in fixed flow.
- During **filled cloud protection (6)** mode, the `heliostatField` is in optimized aiming mode and therefore produces unfiltered flux density distributions with linear interpolation between each time step according to the flux file. The flow path controllers are still set to clear-sky mass flow rate.
- When filled cloud protection is confirmed by the `heliostatField`, the `humanOperator` triggers transition **6-a** into normal operation mode while setting the receiver mode to normal operation as well.
- Going into **normal operation (7)** the `modeOperator` switches the flow path controller to temperature control and ramps their set point from the current outlet temperature up to the nominal value. Normal operation is then confirmed.

Daily Shutdown:

- When normal operation is active, the `humanOperator` can initiate the shutdown routine with transition **7-a** by commanding the `modeOperator` to fixed flow.
- During **filled cloud protection (6)**, after the `modeOperator` has switched the flow path controllers to clear-sky mass flow control it confirms fixed flow mode.
- When fixed flow is confirmed, the `humanOperator` triggers transition **6-b** into ramp down by commanding the `heliostatField` to temperature ramp.
- During **ramp down (8)** the `heliostatField` notices that it commanded from optimized aiming to temperature ramp and therefore

fades from the current optimized flux density distribution to the gentle warming flux density distribution.

- When the outlet temperature of each flow path has dropped below a certain threshold, the `humanOperator` triggers transition **8-a** into drainage by commanding the `modeOperator` to drainage mode and the `heliostatField` to gentle warming mode.
- During **drainage (9)** the `heliostatField` immediately switches from the current (mixed) flux density distribution to the one for gentle warming to avoid overheating. The `modeOperator` lowers the inlet vessel level set point to avoid overfilling. Simultaneously, serpentine flow is stopped by the isolation valves while the main drain valves open to start the bypass flow. At the same time the flow path controller is set to half of the current value. When all valves have set and the inlet vessel level has reached the set point, the `modeOperator` sets the flow path controllers 1 % mass flow rate (not zero for numerical stability). Subsequently, when the new mass flow rate set point is reached, all drain and vent valves open (only partially to avoid low pressure in main drain line) and the vent lines are pressurized with compressed air to force the HTF out of the receiver panels. When the differential pressure sensors in the manifolds detect that the panels are approx. 90 % empty, the `modeOperator` partially closes the vent and drain valves to compensate for some panels being drained quicker due to less flow resistance. When the sensors detect that the panels are fully drained, all drain valves are closed and the pressure in the vent lines is released. Simultaneously, the `modeOperator` raises the outlet vessel set point to allow for quicker drainage and to avoid the outlet vessel running empty during the next flood. As soon as all valves have set, the `modeOperator` confirms the flood.
- When flood is confirmed, the `humanOperator` triggers transition **9-a** into night preservation mode and commands the same for field mode and receiver mode.

Table 0-1: Detailed table of all operating modes

Operating Mode	recMode	fieldMode	BPV2 (inlet valve)	BPVx (outlet valve)	DV1-3 (drain valves)	DVx (main drain valve)	VV1-8 (vent valves)	ISVx (outlet vessel valve)	FPCMode (FP controller)	LvCMode (inlet ves. level contr.)	PrCMode ((inlet ves. press. contr.)	DCCMode (outlet ves. Level contr.)	Heat tracing	Selection station	lev_inVes_set [-]	lev_outVes_set [-]	p_recVent_set [barg]	p_inVes_set [barg]	T_out_set [°C]
0 Night preservation	0	0	0	1	0	0	1	1	1	0	0	0	0	0	0.5	0.5	0.5	15	550
1 Pump startup	1	1	0	1	0	0	1	1	1	1	0	0	0	0	0.5	0.5	0.5	15	550
2 Standby	2	1	0	1	0	1	1	1	0.5	1	1	1	1	0	0.5	0.5	0.5	15	550
3 Preheat	2	2	0	1	0	1	1	1	0.5	1	1	1	1	0	0.5	0.5	0.5	15	550
4 Flood	3	2	1	1	0	0	0	1	1	1	1	1	1	0	0.5	0.5	0.5	15	550
5 Ramp up	4	3	1	1	0	0	0	1	2	1	1	1	1	1	0.7	0.21	0.5	15	550
6 Filled cloud protection	4	4	1	1	0	0	0	1	2	1	1	1	1	1	0.7	0.21	0.5	15	550
7 Normal operation	5	4	1	1	0	0	0	1	3	1	1	1	1	1	0.7	0.21	0.5	15	565
8 Ramp down	4	3	1	1	0	0	0	1	2	1	1	1	1	1	0.7	0.21	0.5	15	550
9 Drainage	6	2	0	0	0	0	1	1	0.01	1	1	1	1	0	0.5	0.5	0.5	15	550
10 Drained cloud protection	7	2	0	1	0	0	1	1	0.01	1	1	1	1	0	0.5	0.5	0.5	15	550

Table 0-2: Detailed table of all transitions for daily startup

Transition	Operating Mode	Condition	RecMode_set	recMode	fieldMode_set	fieldMode	BPV2 (inlet valve)	BPVx (outlet valve)	DV1-3 (drain valves)	DVx (main drain valve)	VV1-8 (vent valves)	ISVx (outlet vessel valve)	FPCMode (FP controller)	LvCMode (inlet ves. level contr.)	PrCMode ((inlet ves. press. contr.)	DOCMode (outlet ves. Level contr.)	Heat tracing	Selection station	lev_inVes_set [-]	lev_outVes_set [-]	p_recVent_set [barg]	p_inVes_set [barg]	T_out_set [°C]
	Night Preservation		0	0	0	0	0	1	0	0	1	1	1	0	0	0	0	0	0.5	0.5	0.5	15	550
0-a			1	1	1	0	0	1	0	0	1	1	1	0	0	0	0	0	0.5	0.5	0.5	15	550
	Pump Startup	60s delay	1	1	1	1	0	1	0	0	1	1	1	1	0	0	0	0	0.5	0.5	0.5	15	550
1-a		mf_pumps>=0.99*mf_min	2	1	1	1	0	1	0	1	1	1	0.5	1	1	1	1	0	0.5	0.5	0.5	15	550
	Standby	mf_riser >=0.99*mf_n *FPCMode	2	2	1	1	0	1	0	1	1	1	0.5	1	1	1	1	0	0.5	0.5	0.5	15	550
2-a		reached fieldMode and recMode	2	2	2	1	0	1	0	1	1	1	0.5	1	1	1	1	0	0.5	0.5	-	15	550
	Preheat	60s delay	2	2	2	2	0	1	0	1	1	1	0.5	1	1	1	1	0	0.5	0.5	-	15	550
3-a		min(T_back_min) >=290°C and min(T_int_min) >=0.99*290°C	3	2	2	2	0	1	0	1	1	1	1	1	1	1	1	0	0.5	0.5	-	15	550
		mf_riser>=0.99*mf_n *FPCMode	3	2	2	2	0	1	0.2	0	0.5	1	1	1	1	1	1	0	0.5	0.5	-	15	550
	Flood	min(dp_pass)>= dp_stopFlood and min(T_manTop) >=285°C	3	3	2	2	1	1	0	0	0	1	1	1	1	1	1	0	0.5	0.5	-	15	550
4-a	Ramp Up	recMode confirmed and BPV2=1	4	4	3	3	1	1	0	0	0	1	2	1	1	1	1	1	0.7	0.21	-	15	550
5-a	Filled Cloud Protection	min(T_out)>= 550°C	4	4	4	4	1	1	0	0	0	1	2	1	1	1	1	1	0.7	0.21	-	15	550
6-a	Normal Operation	Modes confirmed	5	5	4	4	1	1	0	0	0	1	3	1	1	1	1	1	0.7	0.21	-	15	565

Table 0-3: Detailed table of all transitions for daily shutdown

Transition	Operating Mode	Condition	RecMode_set	recMode	fieldMode_set	fieldMode	BFV2 (inlet valve)	BFVx (outlet valve)	DV1-3 (drain valves)	DVx (main drain valve)	VV1-8 (vent valves)	ISVx (outlet vessel valve)	FPCMode (FP controller)	LvCMode (inlet ves. level contr.)	PrCMode ((inlet ves. press. contr.)	DOCMode (outlet ves. Level contr.)	Heat tracing	Selection station	lev_inVes_set [-]	lev_outVes_set [-]	p_recVent_set [barg]	p_inVes_set [barg]	T_out_set [°C]
	Normal Operation		5	5	4	4	1	1	0	0	0	1	3	1	1	1	1	1	0.7	0.21	-	15	565
7-a	Filled Cloud Protection	modes confirmed	4	4	4	4	1	1	0	0	0	1	2	1	1	1	1	1	0.7	0.21	-	15	550
6-b	Ramp Down	modes confirmed	4	4	3	3	1	1	0	0	0	1	2	1	1	1	1	1	0.7	0.21	-	15	550
8-a		max(T_out) <=400°C	4	4	2	3	1	1	0	0	0	1	2	1	1	1	1	1	0.7	0.21	0.5	15	550
		60s delay	4	4	2	2	1	1	0	0	0	1	2	1	1	1	1	1	0.7	0.21	0.5	15	550
		fieldMode confirmed	6	4	2	2	0	0	0	1	0	1	pre/ 2	1	1	1	1	1	0.5	0.21	0.5	15	550
		reached levels	6	4	2	2	0	0	0	1	0	1	0.01	1	1	1	1	0	0.5	0.21	0.5	15	550
		reached mflow	6	4	2	2	0	0	1	1	1	1	0.01	1	1	1	1	0	0.5	0.21	7	15	550
		min(dp_pass)<= 0.1*dp_stopFlood	6	4	2	2	0	0	0.5	0.5	1	1	0.01	1	1	1	1	0	0.5	0.21	7	15	550
		max(dp_pass)<= 0.01*dp_stopFlood	6	4	2	2	0	0	0	0	1	1	0.01	1	1	1	1	0	0.5	0.5	0.5	15	550
	Drainage	30s delay	6	6	2	2	0	0	0	0	1	1	0.01	1	1	1	1	0	0.5	0.5	0.5	15	550
9-a	Night Preservation	modes confirmed	0	0	0	0	0	1	0	0	1	1	1	0	0	0	0	0	0.5	0.5		15	550

B Scenarios

B.1 Artificial clouds

The following scenarios are based on artificial cloud shapes moving across the heliostat field. The full scenario names comprise average cloud size, cloud size deviation, average cloud coverage, random points density factor, shape factor (fracturing), cloud velocity y component, cloud velocity x component, standard deviation of cloud velocity, random seed value, time before clouds arrive at heliostat field, time step size. These scenarios consider clouds as opaque. Hence, abrupt transitions between sun and shade are possible.

B.1.1 Sc_7750

Full name: Sc_7000m_700m_50%_0.05_1.5_+10+0_10%_1_1800s_30s

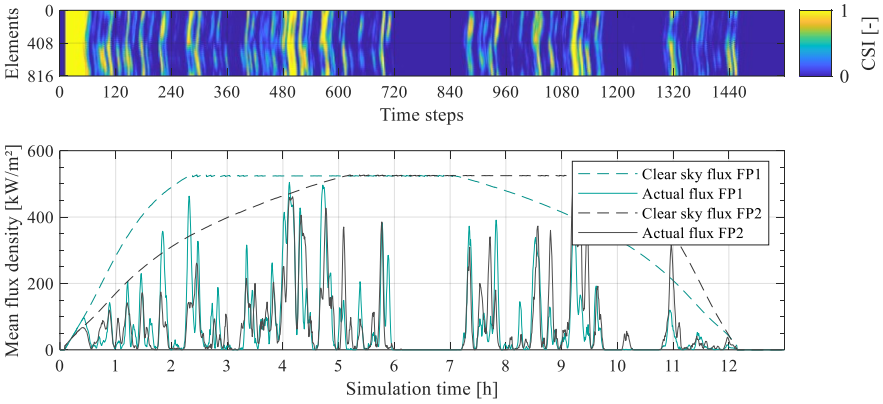

Figure 0-1: CSI (clear sky index) distribution along the receiver circumference and over time (top) as well as mean flux density for each receiver flow path over time (bottom)

B.1.2 Sc_7710

Full name: Sc_7000m_500m_10%_0.05_2_+10+0_1%_1_3600s_10s

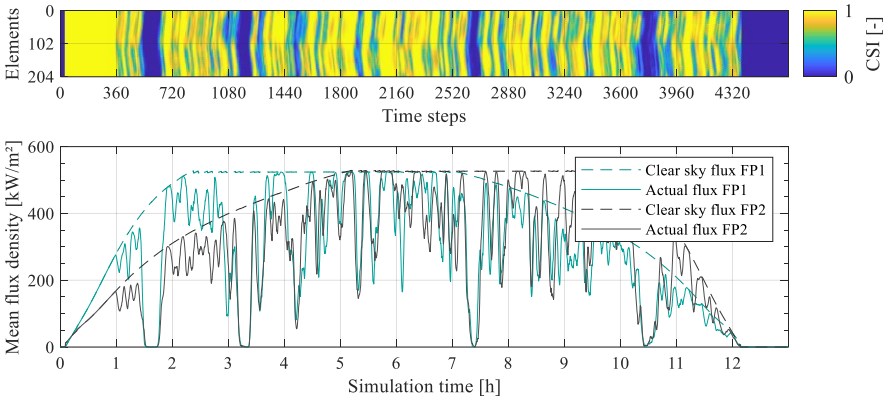

Figure 0-2: CSI (clear sky index) distribution along the receiver circumference and over time (top) as well as mean flux density for each receiver flow path over time (bottom)

B.2 PSA cloud camera measurement based

The following scenarios are based on DNI maps from an ASI-based nowcasting system without including forecasted data (only lead time 0). The scenario name includes the date of record in the format yymmdd. The suffix “reaBlur” indicates, that blurriness and translucent shading is considered in the ray-tracing.

B.2.1 Sc_PSA_190906_realBlur

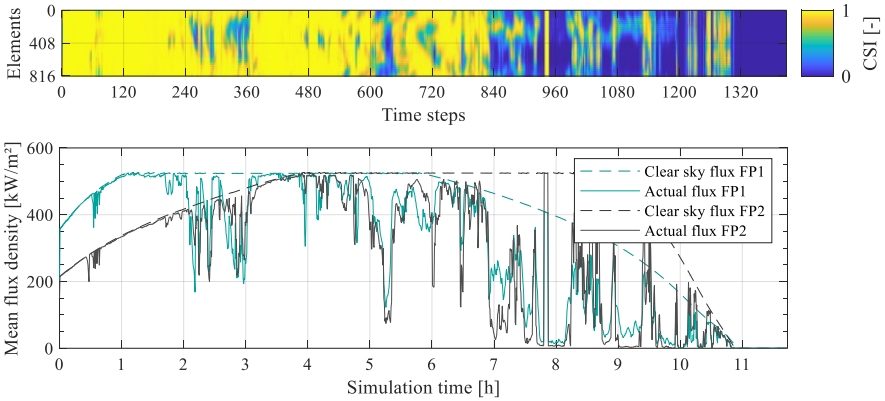

Figure 0-3: CSI (clear sky index) distribution along the receiver circumference and over time (top) as well as mean flux density for each receiver flow path over time (bottom)

B.2.2 Sc_PSA_191021_realBlur

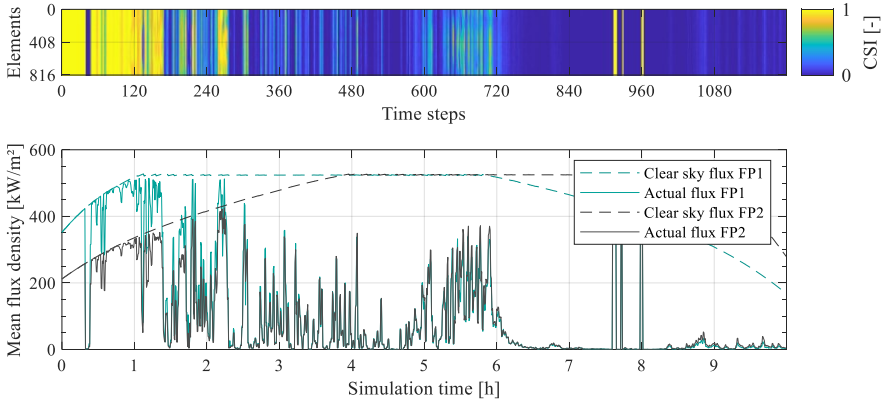

Figure 0-4: CSI (clear sky index) distribution along the receiver circumference and over time (top) as well as mean flux density for each receiver flow path over time (bottom)

B.2.3 Sc_PSA_191101_realBlur

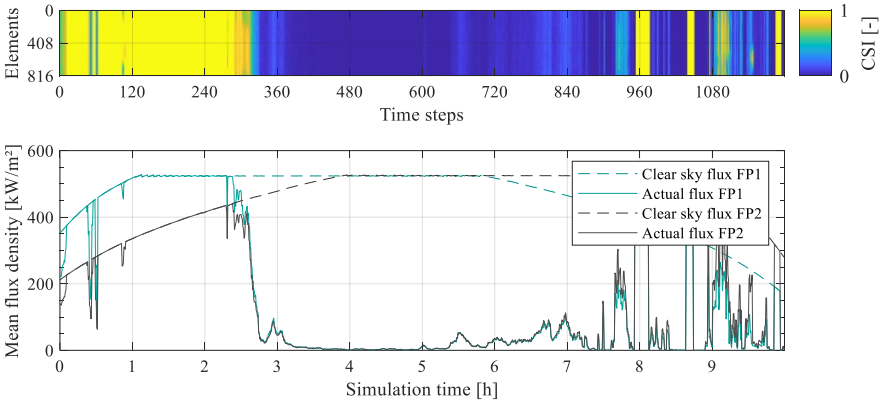

Figure 0-5: CSI (clear sky index) distribution along the receiver circumference and over time (top) as well as mean flux density for each receiver flow path over time (bottom)

B.2.4 Sc_PSA_191114_realBlur

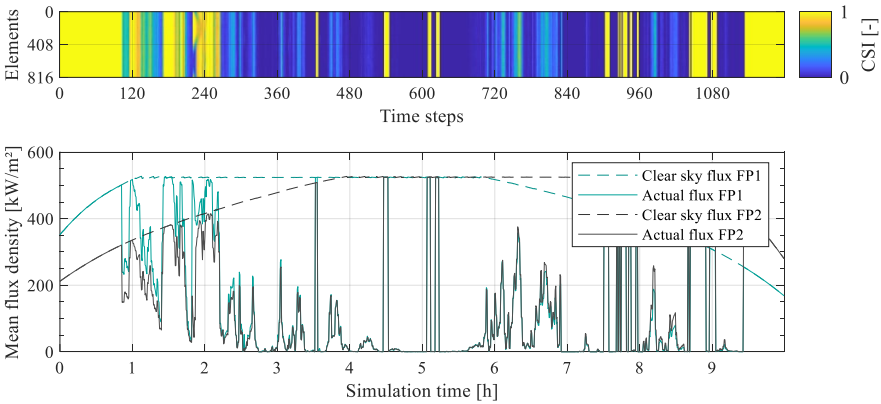

Figure 0-6: CSI (clear sky index) distribution along the receiver circumference and over time (top) as well as mean flux density for each receiver flow path over time (bottom)

B.2.5 Sc_PSA_191126_realBlur

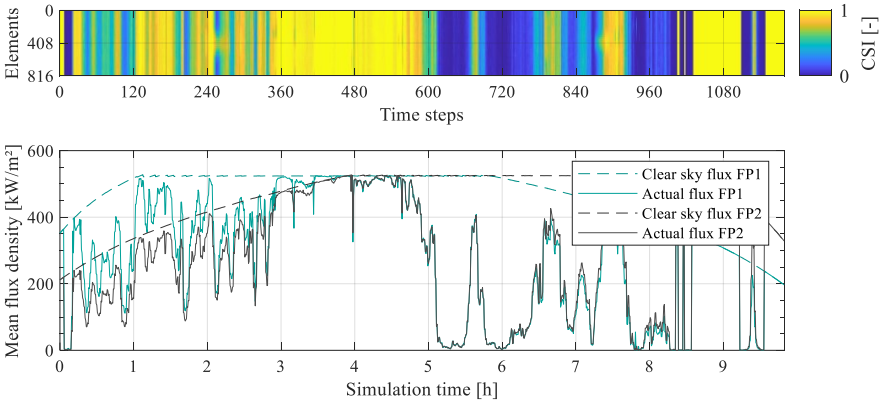

Figure 0-7: CSI (clear sky index) distribution along the receiver circumference and over time (top) as well as mean flux density for each receiver flow path over time (bottom)

B.3 Other scenarios

B.3.1 Sc_Clear_10s

This scenario is based on a clear-sky without any disturbances. The time steps size is 10 s.

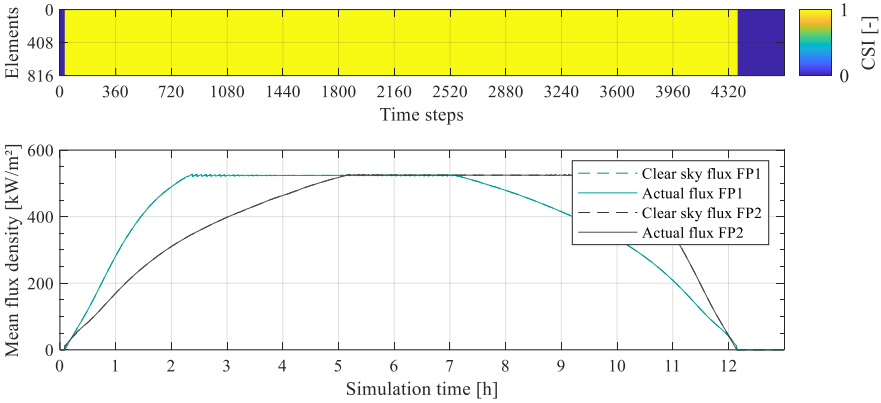

Figure 0-8: CSI (clear sky index) distribution along the receiver circumference and over time (top) as well as mean flux density for each receiver flow path over time (bottom)

B.3.2 Sc_Clear_10s_-80%-50%_0800-1000

This scenario is based on the clear-sky scenario, but with two abrupt and homogeneous shading sequences. The entire heliostat field is considered to shaded by 80 % during the third hour and by 50 % during the fourth hour of the scenario.

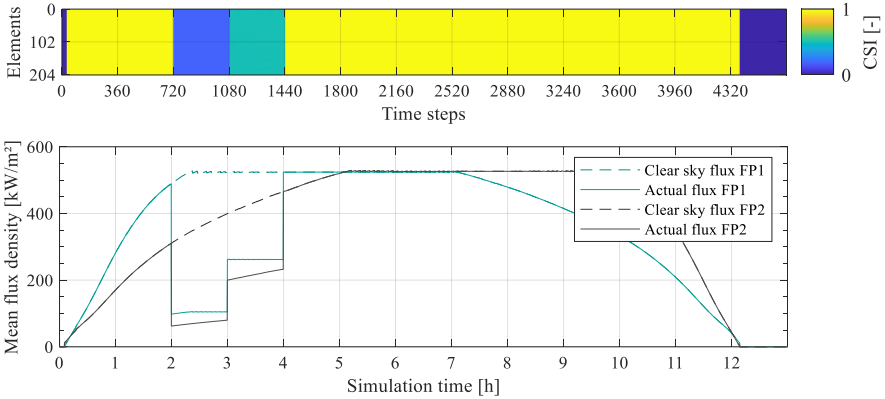

Figure 0-9: CSI (clear sky index) distribution along the receiver circumference and over time (top) as well as mean flux density for each receiver flow path over time (bottom)

C Additional OAS Test Results

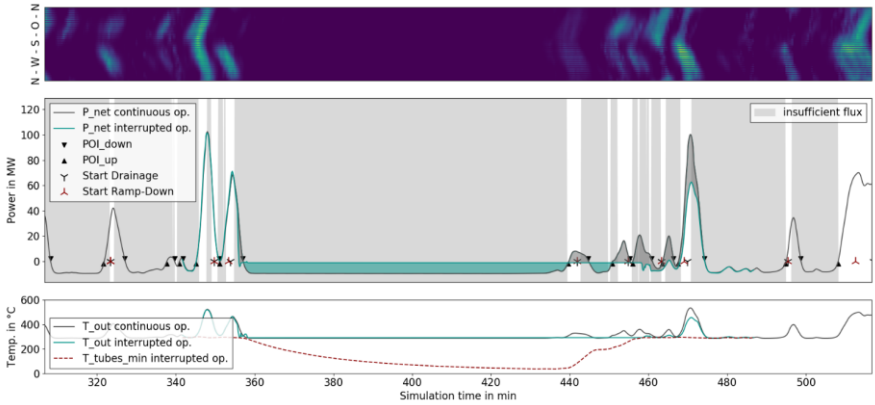

Figure 0-10: OAS test results for POI 22 in scenario Sc_7750 saving 6.35 MWh_{el}

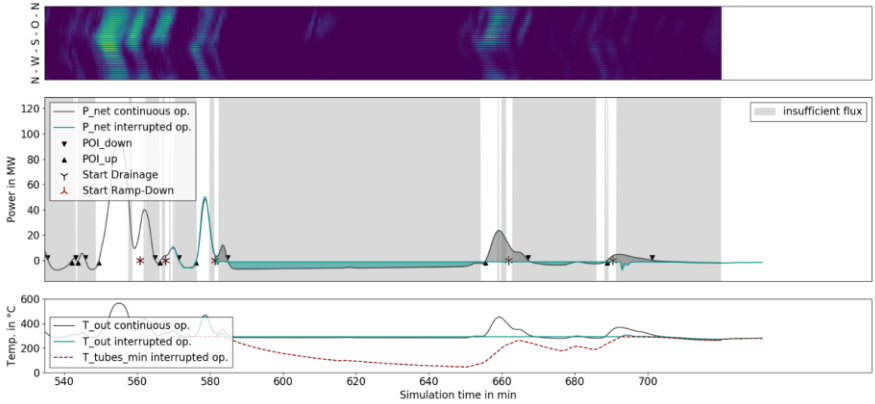

Figure 0-11: OAS test results for POI 36 in scenario Sc_7750 saving 1.9 MWh_{el}

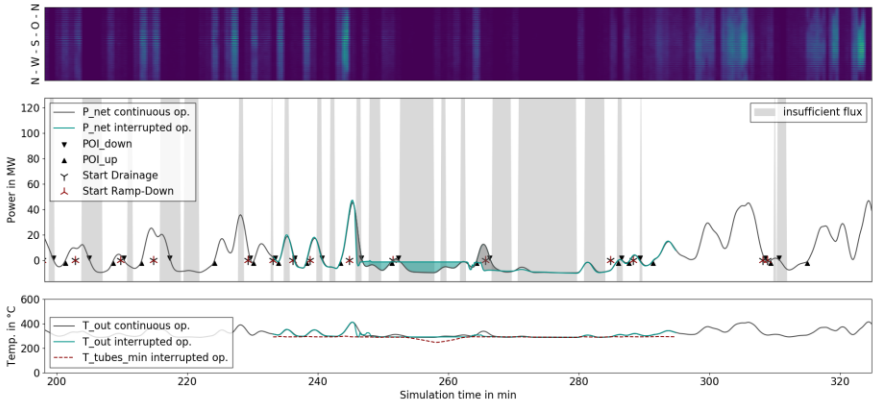

Figure 0-12: OAS test results for POI 15 in scenario Sc_PSA_191021_realBlur saving 0.36 MWh_{el}

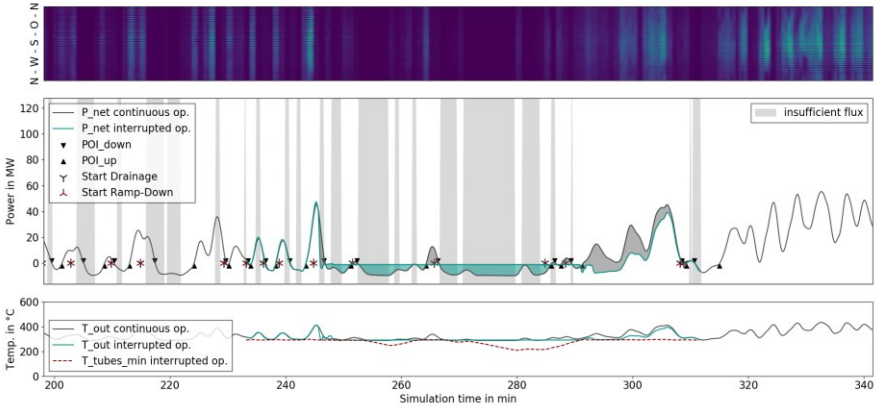

Figure 0-13: OAS test results for POI_{down} 15 and POI_{up} 16 in scenario Sc_PSA_191021_realBlur costing 0.36 MWh_{el}

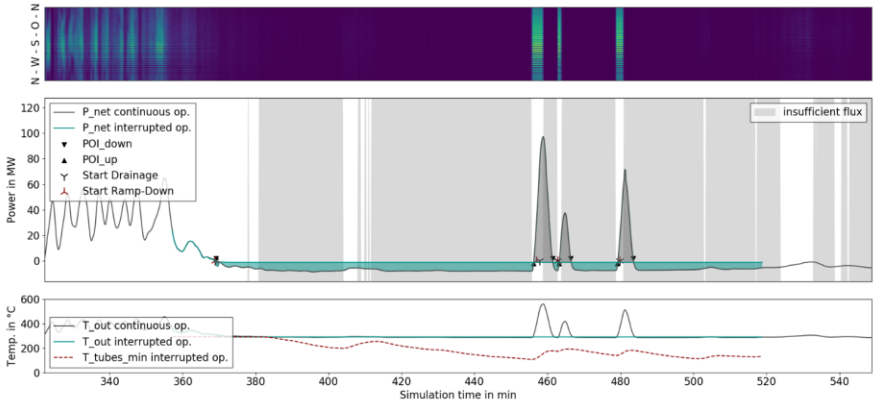

Figure 0-14: OAS test results for POI 22 in scenario Sc_PSA_191021_realBlur saving 4.71 MWh_{el}

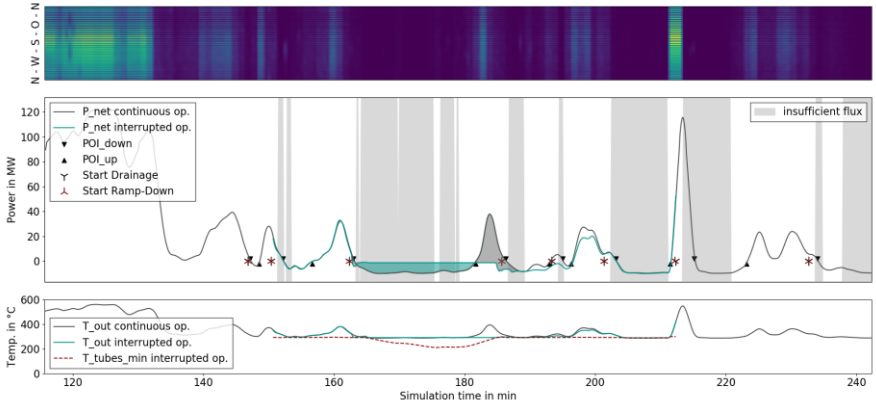

Figure 0-15: OAS test results for POI 2 in scenario Sc_PSA_191114_realBlur saving 0.41 MWh_{el}

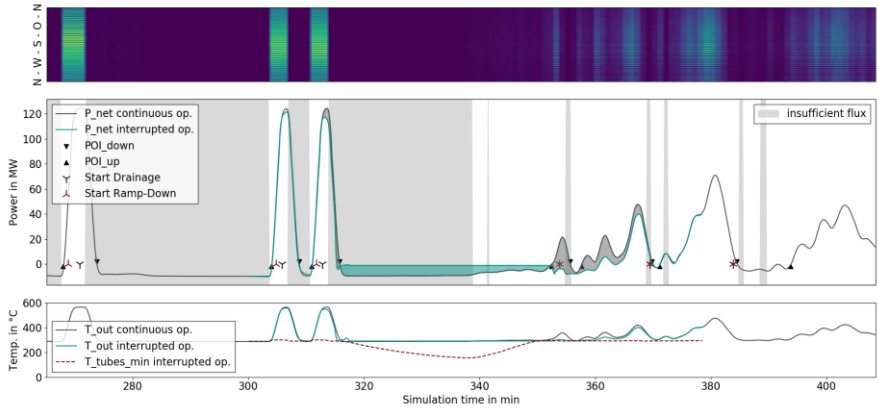

Figure 0-16: OAS test results for POI 10 in scenario Sc_PSA_191114_realBlur saving 0.87 MWh_{el}

D Mathematical Derivations

D.1 Integration of radiation losses

$$\dot{Q}_{\text{radLoss}} = \epsilon_{\text{abs}}\ \sigma\ A_{\text{abs}}\ \frac{\int_0^{l_{\text{rad}}} (T(x)^4 - T_{\text{amb}}^4)\ dx}{l_{\text{rad}}} \tag{0.1}$$

$$T(x)^4 = \left(\underbrace{\frac{T_{\text{fr,out}} - T_{\text{fr,in}}}{l_{\text{rad}}}}_{A}\ x + \underbrace{T_{\text{fr,in}}}_{B} \right)^4 \tag{0.2}$$

$$\Leftrightarrow T(x)^4 = \left(\underbrace{A^2x^2}_{C} + \underbrace{2AxB + B^2}_{D} \right)^2 \tag{0.3}$$

$$\begin{aligned} \Leftrightarrow T(x)^4 &= C^2 + 2CD + D^2 \\ &= A^4x^4 + 2A^2x^2(2AxB + B^2) + (2AxB + B^2)^2 \\ &= A^4x^4 + 4A^3x^3B + 2A^2x^2B^2 + 4A^2x^2B^2 + 4AxB^3 + B^4 \\ &= A^4x^4 + 4A^3x^3B + 6A^2x^2B^2 + 4AxB^3 + B^4 \end{aligned} \tag{0.4}$$

$$\Rightarrow \frac{\dot{Q}_{\mathrm{radLoss}}}{\epsilon_{\mathrm{abs}}\,\sigma\,A_{\mathrm{abs}}} =$$

$$\frac{\frac{1}{5}A^4x^5 + A^3Bl_{\mathrm{rad}}^4 + 2A^2B^2l_{\mathrm{rad}}^3 + 2AB^3l_{\mathrm{rad}}^2 + B^4l_{\mathrm{rad}} - T_{\mathrm{amb}}^4\,l_{\mathrm{rad}}}{l_{\mathrm{tube,rad}}} \tag{0.5}$$
$$= \frac{1}{5}A^4l_{\mathrm{rad}}^4 + A^3Bl_{\mathrm{rad}}^3 + 2A^2B^2l_{\mathrm{rad}}^2 + 2AB^3l_{\mathrm{rad}} + B^4 - T_{\mathrm{amb}}^4$$

$$\begin{aligned}\Leftrightarrow \frac{\dot{Q}_{\mathrm{radLoss}}}{\epsilon_{\mathrm{abs}}\,\sigma\,A_{\mathrm{abs}}} = \frac{1}{5}\left(T_{\mathrm{fr,out}} - T_{\mathrm{fr,in}}\right)^4 + \left(T_{\mathrm{fr,out}} - T_{\mathrm{fr,in}}\right)^3 T_{\mathrm{fr,in}} \\ + 2\left(T_{\mathrm{fr,out}} - T_{\mathrm{fr,in}}\right)^2 T_{\mathrm{fr,in}}^2 + 2\left(T_{\mathrm{fr,out}} - T_{\mathrm{fr,in}}\right) T_{\mathrm{fr,in}}^3 \\ + T_{\mathrm{fr,in}}^4 - T_{\mathrm{amb}}^4\end{aligned} \tag{0.6}$$

$$T_{\mathrm{fr,out}} - T_{\mathrm{fr,in}} = \Delta T_{\mathrm{fr}} = \Delta T_{\mathrm{fluid}} = T_{\mathrm{out}} - T_{\mathrm{in}} \tag{0.7}$$

$$T_{\mathrm{fr,in}} = T_{\mathrm{in}} + T_{\mathrm{front}} - T_{\mathrm{fluid}} \tag{0.8}$$

$$\begin{aligned}\Rightarrow \dot{Q}_{\mathrm{radLoss}} &= \epsilon_{\mathrm{abs}}\,A_{\mathrm{abs}}\,\sigma\left[\frac{1}{5}\,\Delta T_{\mathrm{fr}}^4 + \Delta T_{\mathrm{fr}}^3\,T_{\mathrm{f,in}} + 2\,\Delta T_{\mathrm{fr}}^2\,{T_{\mathrm{fr,in}}}^2\right. \\ &\quad \left. + 2\,\Delta T_{\mathrm{fr}}\,{T_{\mathrm{fr,in}}}^3 + {T_{\mathrm{fr,in}}}^4 - T_{\mathrm{amb}}^4\right] \\ &= \epsilon_{\mathrm{abs}}\,A_{\mathrm{abs}}\,\sigma\left[\frac{1}{5}\,\Delta T_{\mathrm{fluid}}^4 + \Delta T_{\mathrm{fluid}}^3\,T_{\mathrm{fr,in}} + 2\,\Delta T_{\mathrm{fluid}}^2\,T_{\mathrm{fr,in}}^2\right. \\ &\quad \left. + 2\,\Delta T_{\mathrm{fluid}}T_{\mathrm{fr,in}}^3 + T_{\mathrm{fr,in}}^4 - T_{\mathrm{amb}}^4\right]\end{aligned} \tag{0.9}$$